

Development and Modelling of Expansion Tubes

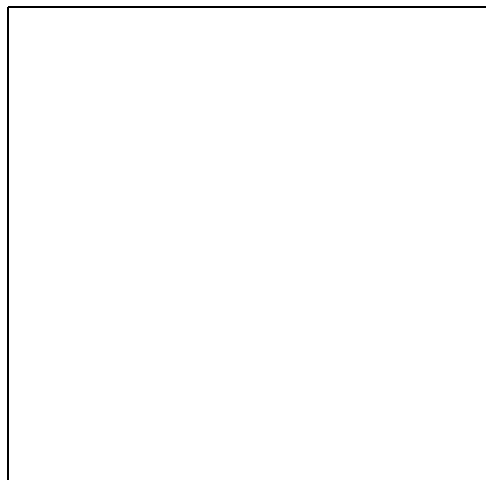
Michael P. Scott

A THESIS SUBMITTED FOR THE DEGREE OF
DOCTOR OF PHILOSOPHY



Division of Mechanical Engineering,
School of Engineering,
The University of Queensland,
Australia.

June, 2006



Statement of Originality

I hereby declare that this submission is my own work and to the best of my knowledge it contains no material previously published or written by another person, nor material which to a substantial extent has been accepted for the award of any other degree or diploma at UQ or any other educational institution, except where due acknowledgement is made in the thesis. Any contribution made to the research by colleagues, with whom I have worked at UQ or elsewhere, during my candidature, is fully acknowledged.

I also declare that the intellectual content of this thesis is the product of my own work, except to the extent that assistance from others in the project's design and conception or in style, presentation and linguistic expression is acknowledged.

Michael P. Scott

Abstract

The accurate simulation of flow conditions encountered by aircraft is imperative to the development of aeronautics and astronautics. Test flights are expensive and time consuming, thus, ground based test facilities provide the majority of data in new flight regimes. A mixture of analytical studies, Computational Fluid Dynamics (CFD), experimental results from ground based test facilities and actual atmospheric flights are required to obtain important design parameters. Coupled with this need for aerodynamic information, is a constant desire to simulate higher flow speeds. Expansion tubes provide an option for testing aeroshells such as the new Crew Exploration Vehicle (CEV) or the high enthalpy end of scramjet flight regime. A unique opportunity already exists in which the fabricated hardware for the RHYFL shock tunnel could be utilized to create the world's largest expansion tube, RHYFL-X. This thesis continues a project which attempted to investigate if RHYFL-X would be a beneficial experimental tool.

This thesis began by installing and commissioning a new single-stage, free-piston driver for the X2 expansion tube located at the University of Queensland. The new configuration provided a smaller scale version of the RHYFL-X expansion tube on which testing could be performed. It also provided a number of advantages which would lead to increased performance in the X2 facility. Once installation was complete, a series of experiments was conducted to ensure that the new driver configuration was operating correctly and to determine the capabilities of it. Four conditions were examined. Two air conditions which produced secondary shock speeds of 8.14 km/s and 8.61 km/s, a condition to simulate the entry into the Titan atmosphere at 5.51 km/s and another condition to simulate entry into the Jovian atmosphere at 10.2 km/s. Numerical one-dimensional models were examined along with hybrid simulations, which used the one-dimensional model up to rupture of the secondary diaphragm and then coupled this to an axisymmetric simulation of the

acceleration tube. The results from these numerical simulation models compared well to the experiments and showed that the new driver provided a significant increase in the stagnation pressures that could be generated in the expansion tube over the old two-stage, free-piston driver.

There have been claims in previous studies that an expansion tube nozzle would not only increase the core flow diameter but also the steady time available for testing. However, this claim has never been physically demonstrated. A full-capture, contoured, shock-free nozzle was designed for the new X2 configuration. The design code for the nozzle incorporated a flow solver for the Parabolized Navier-Stokes (PNS) equations coupled to a Nelder-Mead optimization algorithm. A 1.4m nozzle was installed at the end of the acceleration tube and a series of experiments conducted. CFD simulations similar to the hybrid method mentioned above were conducted with the nozzle attached. The experiments again matched well with the numerical models. The results indicated that the addition of the nozzle produced a larger core flow diameter and longer test time as had been claimed. However, the improvements were not as significant as predicted by the axisymmetric simulations. Extremely large boundary layers were formed but sufficient core flow was still generated to enable the testing of models.

Both the addition of a single-stage, free-piston driver and a contoured nozzle has significantly increased the capabilities of the X2 expansion tube. The numerical models that are used in this thesis provide an excellent basis for the prediction of the flow that can be generated in the X-series of expansion tubes located at the University of Queensland. Following the success of this project, the larger X3 expansion tube located at the University of Queensland is going to be refurbished with a single-stage, free-piston driver and a nozzle.

Acknowledgments

Firstly, I would like to thank my two supervisors, Peter and Richard. You have both helped and taught me a great deal and I appreciate it immensely. I hope one day I have a red beard as cool as yours PJ (I've tried a few times now) and I'll always continue to support you that socks and sandals are a good fashion statement. I would also like to say thank you to David Mee for the numerous questions he answered along the way.

A big thank you to Dave and Brian who helped so much down in the lab. I would still be waiting, if you guys hadn't made so many things up and hadn't helped installing the new driver and nozzle.

To my fellow room mates in room 215; Reidy, Rozza and Nick; thanks for putting up with me and all the help you have given me along the way. I'm not quite sure how we never got in more trouble. If doing a PhD hasn't turned you nuts then I am sure sharing a room with me has. I think we should face the fact though, that I'm really not a nerd like you 3 other guys. Thanks to Denman and many of the other postgrads as well for helping. Special thanks to Rowan for all the finite-rate work and the thousands of other things.

To my mum and dad, I appreciate all that you have done for me. To all my other family members and friends who have helped me throughout the journey, I say thank you. To my grandfather, Geoff, you didn't quite get to see me finish but I'm sure you're watching somewhere. To him and everyone else I say, yes I'm done, so you can stop asking.

Contents

Statement of Originality	i
Abstract	ii
Acknowledgments	iv
List of Tables	x
List of Figures	xvii
Nomenclature	xx
1 Introduction	1
1.1 Propulsion Systems	1
1.2 Space Exploration	3
1.3 Experimental, Computational and Analytical Methods in High Speed Aero- dynamics	4
1.4 The RHYFL Shock Tunnel	6
1.5 Converting RHYFL to an Expansion Tunnel	7
1.6 Aims and Contribution of This Thesis	9
1.7 Thesis Outline	10
2 The Development of Impulse Flow Facilities	12
2.1 A Brief Introduction to Shock Tubes and Shock Tunnels	13
2.2 Impulse Facility Drivers	14
2.2.1 Detonation Driver	15
2.2.2 Free-Piston Driver	15

2.3	The Background of Expansion Tubes	18
2.3.1	Initial Research	20
2.3.2	The Renaissance of Expansion Tubes	24
2.3.3	The Latest Progress in Expansion Tube Work	26
2.3.4	Review of Previous Expansion Tube Nozzles	27
2.4	Summary	32
3	One-Dimensional and Axisymmetric Modelling	34
3.1	One-Dimensional Code and Geometry	35
3.2	One-Dimensional Numerical Simulations	36
3.2.1	Initial Condition	36
3.2.2	Optimal Compression Ratio	37
3.2.3	Optimal Piston Mass and Reservoir Fill Pressure	41
3.2.4	Fill Pressures for the Shock and Acceleration Tubes	42
3.2.5	L1d Verification	44
3.3	Examination of the Air Condition	46
3.4	Final Modified One-Dimensional Simulations	53
3.4.1	Air Condition 1	55
3.4.2	Air Condition 2	57
3.4.3	Titan Condition	59
3.4.4	Jupiter Condition	62
3.5	Axisymmetric Simulations of the Acceleration Tube	67
3.5.1	Air Condition 1	68
3.5.2	Air Condition 2	87
3.5.3	Titan Condition	87
3.5.4	Grid Refinement Study	89
3.6	Summary	101
4	The New X2 Expansion Tube Hardware	103
4.1	The Old Driver	103
4.2	The New Driver	105
4.3	X2 Experimental Results	112
4.3.1	Blanked Off Tests	112

4.3.2	Air Conditions	112
4.3.3	Titan Condition	128
4.3.4	Jupiter Condition	131
4.3.5	Higher Burst Pressure	133
4.3.6	Higher Compression Ratio	133
4.4	Summary	134
5	Design of a Hypersonic Nozzle	137
5.1	Design Methods	137
5.2	Current Nozzle Design	139
5.2.1	Skimmer vs Full Capture Nozzles	139
5.2.2	Conical vs Contoured Nozzles	140
5.2.3	Method Of Characteristics (MOC)	140
5.2.4	Optimized Design Profile	141
5.3	Manufacture and Installation	145
5.4	Comparison of Nozzle Simulations and Experiments	150
5.4.1	Experiments with the Nozzle Attached	150
5.4.2	Axisymmetric Simulations	151
5.4.3	Air Condition 1	152
5.4.4	Air Condition 2	161
5.4.5	Titan Condition	171
5.5	Examination of the Hypersonic Nozzle	173
5.6	Summary	184
6	Conclusions and Recommendations	186
6.1	The Modified X2 Expansion Tube	186
6.2	Expansion Tube Modelling	188
6.3	Hypersonic Nozzles for Expansion Tubes	191
	Bibliography	193
A	L1d Input Files	207
A.1	air_condition_1.Lp	208
A.2	modified_air_condition_1.Lp	209

B	Finite-Rate Chemistry Input File	211
B.1	air_he.chm	212
C	MB_CNS Input File	213
C.1	x2_air_condition_1_with_nozzle_grid_3.sit	214
D	SM_3D⁺ Input File	220
D.1	x2_nozzle_laminar_with_non_uniform_inflow.py	221
D.2	wall_definition.py	224
D.3	roberts.py	226
D.4	bezier.py	227
E	Technical Drawings	229

List of Tables

1.1	Specifications for the RHYFL shock tunnel	6
3.1	Robert Palmer’s Condition 7	38
3.2	L1d results for the new X2 configuration and experimental results for the old X2 configuration	38
3.3	Initial conditions held constant for the varying compression ratio simulations	40
3.4	Initial conditions held constant for the varying piston mass simulations . .	42
3.5	L1d results with varying piston masses	43
3.6	Test gas properties for varying fill pressures in the shock and acceleration tubes for the full simulations	44
3.7	Test gas properties for varying fill pressures in the shock and acceleration tubes without the modelling of the compression process	45
3.8	L1d and experimental results for the old X2 configuration	46
3.9	Initial conditions for the one-dimensional simulation of the target condition	47
3.10	Summary of the L1d flow properties for Air Condition 1	57
3.11	Summary of the L1d flow properties for Air Condition 2	59
3.12	Summary of the L1d flow properties for the Titan condition	65
3.13	Number of cells used in the acceleration tube for each grid of the axisym- metric simulations	90
3.14	Summary of the properties at the acceleration tube exit for the grid refine- ment study for Air Condition 1	92
3.15	Summary of the properties at the acceleration tube exit for the grid refine- ment study for Air Condition 2	97
4.1	Fill conditions for the Air Condition 1 experiments	115
4.2	Fill conditions for the Air Condition 2 experiments	115

4.3	Location of the flush mounted static pressure transducers	116
4.4	Summary of the flow properties at the acceleration tube exit for Air Condition 1	118
4.5	Summary of the flow properties at the acceleration tube exit for Air Condition 2	119
4.6	Shot-to-shot variation in the flow properties for the air conditions	120
4.7	Noise levels in the experiments for the air conditions	121
4.8	Fill conditions for the Titan experiments	129
4.9	Summary of the flow properties at the acceleration tube exit for the Titan condition	130
4.10	Fill conditions for the Jupiter experiments	132
4.11	Summary of the flow properties at the acceleration tube exit for the Jupiter condition	132
4.12	Fill conditions for the higher burst pressure experiments	133
4.13	Fill conditions for the higher compression ratio experiments	134
5.1	Nozzle co-ordinates from IMOC	141
5.2	Bezier points for the optimized turbulent profile	145
5.3	Sample of the nozzle co-ordinates for the final design	147
5.4	Bezier points for the final design	148
5.5	Number of cells for each grid of the axisymmetric nozzle simulations	152
5.6	Summary of the flow properties at the nozzle exit for Air Condition 1	160
5.7	Summary of the flow properties at the nozzle exit for Air Condition 2	170
5.8	Summary of the flow properties at the nozzle exit for the Titan condition	177
E.1	List of technical drawings	229

List of Figures

1.1	An artistic rendition of the X-30 NASP. Taken from [1].	2
1.2	An artistic rendition and the layout of the RHYFL shock tunnel. Taken from [2].	7
1.3	The proposed RHYFL-X facility with a nozzle. Taken from [3].	8
2.1	Flow in a shock tube	14
2.2	Layout of various stages of a free-piston driver	16
2.3	Layout of various stages of a compound free-piston driver	17
2.4	Layout of a double-diaphragm, free-piston driven expansion tube	18
2.5	Comparison of a single and double-diaphragm driver. Adapted from [4]. . .	19
2.6	Layout and x-t diagram for an expansion tube	20
2.7	Layout of the Langley expansion tube/tunnel. Taken from [5].	30
3.1	Geometry for the L1d simulations including the compression process	36
3.2	Static and Pitot pressure traces from L1d at the end of the acceleration tube for the new X2 configuration	38
3.3	Mach number trace from L1d at the end of the acceleration tube for the new X2 configuration	39
3.4	Primary and secondary shock speeds for the varying compression ratios . .	41
3.5	Piston velocity from L1d for the final simulation including the compression process	43
3.6	Geometry for the L1d simulations of the old X2 configuration	46
3.7	An x-t diagram from L1d for the air condition	48
3.8	Static pressure from L1d at 5.75 m along the tube	50
3.9	Static pressure from L1d towards the end of the shock tube	50

3.10	Comparison of experimental and numerical static pressure traces in the shock tube	51
3.11	Properties from L1d at the end of the acceleration tube for the simulation including the compression process	52
3.12	Temperature of the slug of gas just before primary diaphragm rupture . . .	54
3.13	Geometry for the final modified one-dimensional simulations	55
3.14	Comparison of experimental and numerical static pressure traces in the shock tube for Air Condition 1	56
3.15	Static pressure from L1d towards the end of the shock tube for Air Condition 1	56
3.16	Properties from L1d at the end of the acceleration tube for Air Condition 1	58
3.17	Properties from L1d at the end of the acceleration tube for Air Condition 2	60
3.18	Comparison of experimental and numerical static pressure traces in the shock tube for the Titan condition	62
3.19	Static pressure from L1d towards the end of the shock tube for the Titan condition	62
3.20	An x-t diagram from L1d for the Titan condition	63
3.21	Properties from L1d at the end of the acceleration tube for the Titan condition	64
3.22	Properties from L1d at the end of the acceleration tube for the Jupiter condition	66
3.23	Geometry for the MB_CNS simulations	68
3.24	Properties from MB_CNS at the end of the acceleration tube for Air Condition 1. For the laminar simulation with equilibrium chemistry.	69
3.25	Profiles from MB_CNS across the acceleration tube exit for Air Condition 1. For the laminar simulation with equilibrium chemistry.	72
3.26	Profiles from MB_CNS across the acceleration tube exit for Air Condition 1. For the turbulent simulation with equilibrium chemistry.	73
3.27	Propagation of the flow in the acceleration tube for the laminar case: part 1	74
3.28	Propagation of the flow in the acceleration tube for the laminar case: part 2	75
3.29	Propagation of the flow in the acceleration tube for the laminar case: part 3	76
3.30	Propagation of the flow in the acceleration tube for the laminar case: part 4	77
3.31	Propagation of the flow in the acceleration tube for the turbulent case: part 1	78

3.32	Propagation of the flow in the acceleration tube for the turbulent case: part 2	79
3.33	Propagation of the flow in the acceleration tube for the turbulent case: part 3	80
3.34	Propagation of the flow in the acceleration tube for the turbulent case: part 4	81
3.35	Pressure and temperature from L1d along the shock tube	84
3.36	Properties from MB_CNS at the end of the acceleration tube for Air Condition 1 comparing the different MB_CNS models. Taken at a radial distance of 24 mm from the centreline.	86
3.37	Species fractions from MB_CNS at the end of the acceleration tube for Air Condition 1	87
3.38	Properties from MB_CNS at the end of the acceleration tube for Air Condition 2. For the laminar simulation with equilibrium chemistry.	88
3.39	Profiles from MB_CNS across the acceleration tube exit for Air Condition 2. For the laminar simulation with equilibrium chemistry.	89
3.40	Profiles from MB_CNS across the acceleration tube exit for Air Condition 2. For the turbulent simulation with equilibrium chemistry.	90
3.41	Properties from MB_CNS at the end of the acceleration tube for Air Condition 2 comparing the different MB_CNS models. Taken at a radial distance of 24 mm from the centreline.	91
3.42	Species fractions from MB_CNS at the end of the acceleration tube for Air Condition 2	92
3.43	Properties from MB_CNS at the end of the acceleration tube for the Titan condition. Taken at a radial distance of 24 mm from the centreline.	93
3.44	Profiles from MB_CNS across the acceleration tube exit for the Titan condition	94
3.45	Contours of the log of density at t=0.8 ms for the Titan condition. t=0 ms when the shock wave enters the acceleration tube	94
3.46	Properties from MB_CNS at the end of the acceleration tube for Air Condition 1. Varying grid resolutions for the laminar simulations.	95
3.47	Properties from MB_CNS at the end of the acceleration tube for Air Condition 2. Varying grid resolutions for the laminar simulations.	96
3.48	Convergence of the shock speeds for different grid resolution for the two air conditions for the laminar simulations.	97

3.49	Convergence of the shock speeds for different grid resolution for the two air conditions for the turbulent simulations.	98
3.50	Properties from MB_CNS at the end of the acceleration tube for Air Condition 1. Varying grid resolutions for the turbulent simulations.	99
3.51	Properties from MB_CNS at the end of the acceleration tube for Air Condition 2. Varying grid resolutions for the turbulent simulations.	100
4.1	Schematic of the old X2 configuration. Taken from [6].	104
4.2	Schematic of the new X2 expansion tube	106
4.3	Layout of the new X2 expansion tube	107
4.4	The new X2 expansion tube	107
4.5	The new X2 compression tube	108
4.6	The new X2 piston launching station	109
4.7	The new X2 piston	109
4.8	The new X2 couplings	110
4.9	Section view of the X2 primary diaphragm station and the new couplings .	110
4.10	The new X2 buffer assembly	111
4.11	The new X2 shock tube frame	111
4.12	Pressure traces in the driver section for the blanked off tests	113
4.13	Schematic of the pressure transducer locations	115
4.14	Pitot pressure rake at the acceleration tube exit plane	116
4.15	Shielded PCB pressure transducer arrangement. Taken from [7].	116
4.16	Comparison of the experimental and computational static pressures at the acceleration tube exit for Air Condition 1	124
4.17	Comparison of the experimental and computational Pitot pressures at the acceleration tube exit for Air Condition 1	124
4.18	Comparison of the experimental and computational static pressures at the acceleration tube exit for Air Condition 2	125
4.19	Comparison of the experimental and computational Pitot pressures at the acceleration tube exit for Air Condition 2	125
4.20	Comparison of the experimental and computational static pressures at the acceleration tube exit for the Titan condition	130

4.21	Comparison of the experimental and computational Pitot pressures at the acceleration tube exit for the Titan condition	131
4.22	Static and Pitot pressure at the acceleration tube exit for the Jupiter condition	132
5.1	Lag between the actual characteristic and the MOC/BL design caused by large boundary layers. Adapted from [8].	138
5.2	Profiles of various nozzle designs	143
5.3	Properties from SM_3D ⁺ at the nozzle exit	146
5.4	Mach number from SM_3D ⁺ along the centreline of the nozzle	146
5.5	Mach number and flow angle from SM_3D ⁺ across the nozzle exit plane . .	147
5.6	Section 1 of the nozzle before painting	148
5.7	Section 2 of the nozzle before painting	148
5.8	Section 3 of the nozzle before painting	149
5.9	The 3 sections of the nozzle	149
5.10	The installed nozzle and frame - view 1	149
5.11	The installed nozzle and frame - view 2	150
5.12	Pitot pressure rake at the nozzle exit plane	151
5.13	Properties from MB_CNS at the nozzle exit for Air Condition 1. Varying grid resolutions for the laminar simulations.	153
5.14	Properties from MB_CNS at the nozzle exit for Air Condition 2. Varying grid resolutions for the laminar simulations.	154
5.15	Properties from MB_CNS at the nozzle exit for Air Condition 1. Varying grid resolutions for the turbulent simulations.	155
5.16	Properties from MB_CNS at the nozzle exit for Air Condition 2. Varying grid resolutions for the turbulent simulations.	156
5.17	Properties from MB_CNS at the nozzle exit for Air Condition 1 comparing the different MB_CNS models.	162
5.18	Static and Pitot pressures from the experiments at the nozzle exit for Air Condition 1	163
5.19	Pitot pressures from the experiments at the nozzle exit for Air Condition 1	163
5.20	Species fractions from MB_CNS at the nozzle exit for Air Condition 1 . . .	164

5.21	Comparison of the experimental and computational Pitot pressure profiles at the nozzle exit for Air Condition 1	164
5.22	Mach number profiles from MB_CNS across the nozzle exit for Air Condition 1	165
5.23	Temperature profiles from MB_CNS across the nozzle exit for Air Condition 1	165
5.24	Propagation of the flow in the nozzle for the turbulent case: part 1	166
5.25	Propagation of the flow in the nozzle for the turbulent case: part 2	167
5.26	Propagation of the flow in the nozzle for the turbulent case: part 3	168
5.27	Propagation of the flow in the nozzle for the turbulent case: part 4	169
5.28	Properties from MB_CNS at the nozzle exit for Air Condition 2 comparing the different MB_CNS models.	172
5.29	Species fractions from MB_CNS at the nozzle exit for Air Condition 2	173
5.30	Static and Pitot pressures from the experiments at the nozzle exit for Air Condition 2	173
5.31	Pitot pressures from the experiments at the nozzle exit for Air Condition 2	174
5.32	Comparison of the experimental and computational Pitot pressure profiles at the nozzle exit for Air Condition 2	174
5.33	Mach number profiles from MB_CNS across the nozzle exit for Air Condition 2	175
5.34	Temperature profiles from MB_CNS across the nozzle exit for Air Condition 2	175
5.35	Properties at the nozzle exit for the Titan condition with a comparison of the experimental and computational pressures	176
5.36	Comparison of the experimental and computational Pitot pressures at the nozzle exit for the Titan condition	177
5.37	Comparison of the experimental and computational Pitot pressure profiles at the nozzle exit for the Titan condition	178
5.38	Profiles from MB_CNS across the nozzle exit for the Titan condition	178
5.39	An x-t diagram constructed from the equilibrium, turbulent simulation of Air Condition 1	181
5.40	A x-t diagram in the nozzle constructed from the equilibrium, turbulent simulation of Air Condition 1	181
5.41	Pitot pressure time history along the nozzle for Air Condition 1: part 1 . . .	182

5.42 Pitot pressure time history along the nozzle for Air Condition 1: part 2 . . .	183
5.43 The boundary layer growth at the acceleration tube exit	183

Nomenclature

γ	ratio of specific heats, C_p/C_v
λ	compression ratio
μ	coefficient of friction
ϕ_θ	weighting parameter for the flow angle
ϕ_M	weighting parameter for the Mach number
ρ	density, kg/m^3
θ	flow angle
k	polytropic index for an isentropic process
n	polytropic index
p, P	pressure, Pa
R	specific gas constant, $(\text{J}/\text{kg}\cdot\text{K})$
T	temperature, K
U	shock speed, m/s
v, V	volume, m^3
A	area, m^2
a	speed of sound, m/s
C_p	specific heat (constant pressure), $\text{J}/(\text{kg}\cdot\text{K})$

C_v	specific heat (constant volume), J/(kg.K)
F	force, N
f	friction coefficient
H	total enthalpy, MJ/kg
h	enthalpy, MJ/kg
h	heat transfer coefficient, W/m ² k
M	Mach number
N	number of cells in the core flow
Pr	Prandtl number
St	Stanton number
u	velocity, m/s

Subscripts

1	test gas in initial state
10	accelerator gas in initial state
5	fully expanded test gas
D^*	initial driver state
Df	peak driver state
p	Pitot

Acronyms

BL	Boundary Layer
BRL	Ballistic Research Laboratory
C-J	Chapman-Jouget

CEA	Chemical Equilibrium with Applications
CEV	Crew Exploration Vehicle
CFD	Computational Fluid Dynamics
CPU	Central Processing Unit
EELV	Evolved Expendable Launch Vehicle
ESA	European Space Agency
MARIAH	MagnetoHydrodynamic Accelerator Research Into Advanced Hypersonics
MHD	MagnetoHydroDynamic
MOC	Method Of Characteristics
MPI	Message Passing Interface
NASA	National Aeronautics and Space Administration
NASP	National AeroSpace Plane
NC	Numerically Controlled
PNS	Parabolized Navier-Stokes
RDHWT	Radiantly Driven Hypersonic Wind Tunnel
RHYFL	Rocketdyne HYpersonic Flow Laboratory
SID	Shock-Induced Detonation
SSTO	Single-Stage To Orbit
UHP	Ultra-High-Pressure
UQ	University of Queensland
USSR	Union of Soviet Socialist Republics
US	United States
x-t	distance-time

CHAPTER 1

Introduction

In the past century many significant milestones have been reached in the aerospace field. On December 17th 1903, the Wright brothers began a new era for mankind when they completed the first powered flight. A relatively short time progressed before Capt. Charles E. Yeager piloted the Bell XS-1 on October 14th 1947, to a speed greater than that of the speed of sound. In 1955, the North American Aircraft Corporation began production of the X-15, the first manned hypersonic airplane [9]. These were just three events out of a plethora of events in aeronautics and astronautics. They help to illustrate the constant aspirations to fly to further destinations and at faster speeds. The advances in commercial air flight as well as missions to space to explore the universe coupled with the demand for military applications means there is a constant improvement in aerodynamic vehicles. With this comes the need for aerothermodynamic data to assist in the development.

1.1 Propulsion Systems

All aircraft require a propulsion mechanism to produce flight, with different types used depending on the requirements. Air-breathing systems are comprised of reciprocating piston engines, turbojets, turbofans and ramjets. These systems are used for subsonic flight such as commercial applications and low supersonic flight (below approximately Mach 3) as in military fighter planes. Another air-breathing concept which has been investigated since the 1960s and is still in the research stage, is the supersonic combustion ramjet or scramjet. The high cost of space exploration has caused stagnation in the astronautics field as explained below. Scramjets would help alleviate financial problems



Figure 1.1: An artistic rendition of the X-30 NASP. Taken from [1].

which usually stem from the need to carry both fuel and oxygen into space. Work in this area is at the forefront of propulsion research today and it is capable of transforming future hypersonic transportation.

An artistic rendition of a scramjet concept vehicle is shown in Figure 1.1. The Single-Stage To Orbit (SSTO) reusable launch vehicle would involve a highly integrated frame and air-breathing system. The aim of such an undertaking would be to build a plane which could take off horizontally from a runway, fly into orbit and then return to land on a runway. With the creation of such a craft, access to space would become much more readily available and travel times for commercial flights across the globe could be dramatically reduced. This is still futuristic technology and the plans of the National AeroSpace Plane (NASP) project as described below, were not realistic at the time they were undertaken. A great amount of work and development is still necessary before scramjet aircraft come to fruition. The development process is moving forward as the recent flights of the X-43 and Hyshot have demonstrated [10, 11].

Rockets are another propulsion system and are the only option available to gain access into space at the present time. They produce high thrust and are thus suitable for accelerating to hypersonic speeds. Their use has been extensive but they require oxidizer to be carried on board. This is a large percentage of the weight for a vehicle. For the Space Shuttle main engines, the oxygen takes up 30% of the total weight. This increases the thrust needed for take-off and thus larger rockets are required, this in turn increases

the cost.

High speed flight is a very complex field. Though there has been a lot of successful work on developing propulsion systems, as well as all aspects of aircraft design, more research is required. For all the large advances which have been made, recently the direction of the aerospace industry has been unfocused, mainly due to costs.

1.2 Space Exploration

Manned space exploration requires a heavy lift launch vehicle driven by a propulsion system and preferably the craft is reusable, or partially reusable, to reduce costs. In the 1960s, NASA's direction veered from the reusable rocket type planes, such as the X-15, to concentrate on competing with the USSR in sending men into space. Designs involved using non-reusable command modules propelled by large multi-stage rockets. In October 1957, Sputnik 1 was the first artificial Earth satellite launched and in July 1969, the Apollo 11 capsule carried the first men to the Moon. Following this, the United States focus shifted back towards a vehicle capable of flying to and from space [12]. The first partially reusable spacecraft, the Space Shuttle was launched in 1981. It has been operational since that time and will not be retired until the International Space Station is completed some time before 2010. The Space Shuttle Orbiter is old technology and a deficiency in the current range of space vehicles was highlighted when the fleet was grounded after the Columbia accident on February 1st 2003. Even though in this time the Chinese flew their first manned mission into space in the Shenzhou 5, the world was reliant on the non-reusable Russian Soyuz launch vehicle to reach the International Space Station. The only other heavy launch system in the United States at the current time is the Evolved Expendable Launch Vehicle (EELV) which is not designed for manned flight.

Recently, Project Constellation and the Crew Exploration Vehicle (CEV) was announced as the successor to the Space Shuttle [13]. It is a capsule style design, similar to those which were used in travelling to the Moon. The CEV will be capable of Earth orbit and manned interplanetary flight. The stated goals are to return to the Moon and construct outposts in order to reach Mars. In five years from now the vehicle is to be ready to ferry supplies and people to the International Space Station. A return to the Moon will occur in 2018. However, this announcement caused the cancellation of the

X-43B to focus on Project Constellation. In the last forty-five years, billions of dollars have been poured into hypersonic flight projects, (involving both scramjets and rocket propulsion systems), which have been cancelled before completion. Some of these were:

- The follow up to X-15 in the early 1960s, the X-20 or Dyna-Soar which was cancelled in 1963.
- The X-30 or NASP project which was initiated in the late 80s and aborted in 1993.
- Both the X-33 and X-34 planes which were scrapped in early 2001.

This exposes oscillations in the focus of space exploration and highlights the necessity to keep research moving forward. There is a need for research into both air-breathing systems and blunt body reentry capsules. Whatever direction hypersonic flight takes, aerodynamic data is essential for the design of the vehicles. This data can be provided through a combination of computational, experimental and analytical studies.

1.3 Experimental, Computational and Analytical Methods in High Speed Aerodynamics

Actual atmospheric test flights for reproducing flow conditions experienced by vehicles, though vital for development of aeronautics and astronautics, are expensive, time consuming and impractical at times. This limits the amount of data that can be obtained with them and other options are required. These methods are analytical studies, Computational Fluid Dynamics (CFD) and sub-scale model experiments in ground based flow facilities.

Analytical solutions for aerodynamic flows exist for only a handful of cases and are generally complex with a lot of simplifying assumptions needed in order to arrive at a solution.

CFD provides an option, which is inexpensive, obtains a complete set of results in a flow field and is suitable for almost all complexity of problems. However, numerical solutions use mathematical models to depict reality and these models may not accurately describe what they are meant to. In aerodynamics there are primarily two areas that

CFD is used. These are simulating the flow around a vehicle to ascertain data pertinent to its design or reproducing the flow in ground based test facilities to estimate the flow conditions generated in them. In this thesis, CFD is utilized in the second way. The main aim being to calculate the freestream test properties experienced by a scale-model vehicle in an expansion tube. Generally in CFD, modelling assumptions are made to simplify the problem and reduce the computational resources required. This is no different in hypersonic flow where phenomena such as viscous interaction and high-temperature effects, as well as other flow phenomena such as turbulence, can create numerical models which are extremely complex and time consuming. Simplifying assumptions about these effects can be made, but this may lead to flow which is different to that in the real case. How, or by what percentage, the phenomena change certain properties can be uncertain. Furthermore, the phenomena can be coupled to each other and it is even harder to determine their individual effects. Therefore, even though a solution may be precisely obtained from a computational program, the results may be not physically valid. For this reason, the results from numerical methods must be examined and compared to experimental solutions, in order to validate them.

Ground based test facilities that are used to obtain experimental results are diverse. Wind tunnels provide an option to test scale or full size models of aircraft or simply single components. Wind tunnels have been around for some time and their history is discussed in detail in Chapter 2. They provide important design parameters for vehicles such as lift, drag and heat loads in flows that are similar in characteristics to those in true flight. Similarity with full scale flight is achieved by matching certain flow properties such as Reynolds number or the binary scaling parameter. With the advances in aerodynamic vehicles comes a need to continually improve test facilities to simulate the appropriate flight conditions. In the highest flow regime of aeroshells and scramjets, there are opportunities for new and improved wind tunnels.

Experimental, ground based investigations are expensive, often do not have the correct scale or boundary conditions, contain measurement errors and only provide select data. Impulse facilities such as expansion tubes are inherently sensitive due to their high speed nature. Unsteadiness caused by such things as rupturing diaphragms and noise in measured signals can make it difficult to reproduce results. The leading means of research into possible flight configurations is to combine computational models, experiments and

Table 1.1: Specifications for the RHYFL shock tunnel

Specification	RHYFL Value
Compression tube length	47 m
Compression tube diameter	61 cm
Shock tube length	31 m
Shock tube diameter	20 cm
Piston length	1.8 m
Piston weight	1750 kg
Total weight	725000 kg
Operating pressure	255 MPa
Operating temperature	5000 K

atmospheric flight tests.

1.4 The RHYFL Shock Tunnel

One impulse type wind tunnel, the Rocketdyne HYpersonic Flow Laboratory, or RHYFL free-piston shock tunnel, was designed in the late 1980s as part of the NASP program. This program attempted to bring to reality a hypersonic, air-breathing, SSTO vehicle like that described in Section 1.1. The RHYFL facility, shown in Figure 1.2, was to be the largest of its kind in the world, capable of producing flows which would have replicated NASP flights in the highest Mach number region. In addition to this, RHYFL possessed the capability of testing full scale components which would have been a significant advantage. Even though results that sufficiently simulate flow phenomena can be obtained by using a sub-scale model with a matching Reynolds number based on a characteristic length. Such scale model data would still not be acceptable as design validation for vehicles such as scramjets, when combustion kinetics and turbulent compressible flows are present [14]. Some of the specifications of the original RHYFL shock tunnel can be seen in Table 1.

Despite the prospects this facility would have provided, the project was abandoned in 1991. This was after the fabrication of the major hardware components and was due to the cancellation of the NASP program. The components of RHYFL were placed into storage, where they remain. Since that time it has been proposed that the manufactured hardware of the RHYFL shock tunnel could be used to build an expansion tube, termed

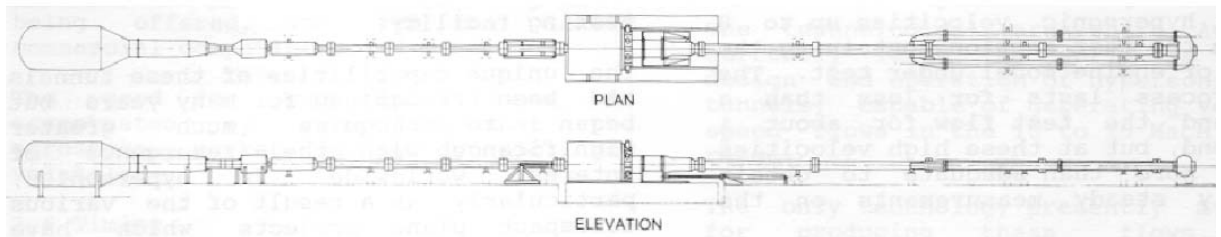
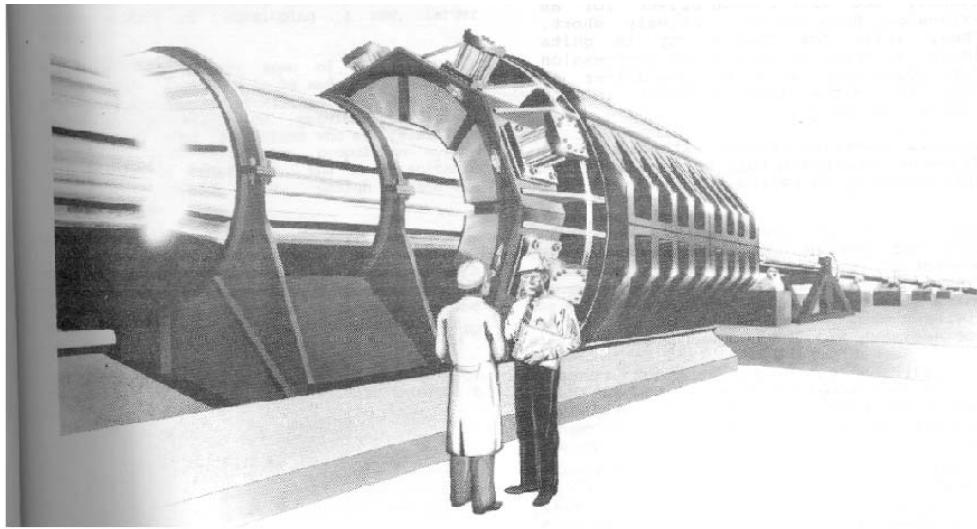


Figure 1.2: An artistic rendition and the layout of the RHYFL shock tunnel. Taken from [2].

RHYFL-X [15]. If the opportunity of transforming the RHYFL shock tunnel was taken, it would mean a facility would exist that would be capable of producing test conditions with large total enthalpies and total pressures experienced in the highest speed of atmospheric flight [16]. This range of flight conditions is currently unavailable in ground based testing facilities.

1.5 Converting RHYFL to an Expansion Tunnel

This section is a summary and evaluation of a previous study performed by Stewart [16] at the University of Queensland. The current study is essentially a continuation and expansion of Stewart's PhD work which looked at the feasibility of turning the manufactured components of the RHYFL shock tunnel into an expansion tube. The discussion of what was attempted and achieved leads directly into this thesis.

The initial stage of Stewart's investigation involved running CFD simulations of the proposed RHYFL-X facility. From this data, performance predictions were obtained. To

1.5. CONVERTING RHYFL TO AN EXPANSION TUNNEL

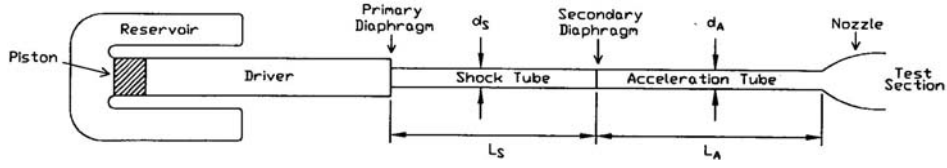


Figure 1.3: The proposed RHYFL-X facility with a nozzle. Taken from [3].

provide some confidence in the numerical results obtained for the RHYFL-X expansion tube, a computational simulation of the existing X2 expansion tube was compared against experimental results. It was found that the one-dimensional and two-dimensional axisymmetric approaches used were sufficient in capturing the dominant flow characteristics of the X2 facility. It was also reasoned that, due to the size of the proposed RHYFL-X facility, the discrepancies obtained in the X2 investigation, which were due to viscous effects and three-dimensional phenomena, would be less significant in the RHYFL simulations. The conclusion reached was that the RHYFL-X expansion tube would be able to generate high total pressures, in the order of tens gigapascals, at the expense of simulation time relative to the RHYFL shock tunnel. It was stated that this would make the RHYFL-X expansion tube the premier scramjet test facility in the world, in that it could replicate the total enthalpies and pressures experienced in high speed atmospheric flight, while testing entire scramjet models [16].

The study of the conversion of the RHYFL shock tunnel into an expansion tube continued with a look at the design of two nozzles to be situated on the end of the acceleration tube as shown in Figure 1.3. This would allow the flow to be expanded to a larger test core diameter. A Method Of Characteristics (MOC) procedure was utilized in the design of the nozzles so that no major shocks developed due to their contour. The unexpected outcome from the results was, that while the nozzle expanded the test flow to the appropriate free-stream conditions, not only did it increase the diameter of the test core flow but it also increased the steady flow time suitable for testing. This finding was extremely promising because of the short test times that are usually associated with expansion tubes. However, at the conclusion of Stewart's thesis, all of the facility performance results were from computer simulations.

To check if the test times obtained within the RHYFL-X facility would be long enough for steady flow conditions to establish within a scramjet model, experiments were conducted in the X3 expansion tube. Heat transfer measurements were used to find the time

taken to reach steady state as viscous properties are still establishing when the pressure reaches steady state. The measurements suggested that for flight speeds of about 5 km/s, scramjet engines around one to two metres in length could be tested [16].

1.6 Aims and Contribution of This Thesis

The motivation of this project was to help determine what experimental conditions could really be produced by the RHYFL-X facility and if these conditions would be suitable for testing scramjets and aeroshells. If sufficient test times, core flow diameter and appropriate free stream conditions could be generated then the proposed RHYFL-X expansion tube would be a valuable tool for hypersonic flight research.

The broad aim of this thesis was to continue the development of high-enthalpy wind tunnels, specifically expansion tubes. This was achieved by:

1. The installation and commissioning of a new single-stage, free-piston driver on the X2 expansion tube. Design work for this driver was done by Richard Morgan. This modification provided a smaller scale version of the proposed RHYFL-X expansion tube and provided increased performance when compared to the old X2 two-stage piston configuration. When X2 was operational a series of experiments was performed to test the capabilities of it.
2. CFD modelling of the new X2 configuration with the one-dimensional code, L1d and the axisymmetric code, MB_CNS. The results were compared to the experimental values and with adequate agreement the experiments would validate the CFD. Similar methods to those shown here have been used before to model expansion tubes but the continual development of them is required to more accurately predict flow conditions and help understand the flow phenomena. This leads to improved operation of the experimental facility and more consistent performance.
3. The design, construction and installation of a full-capture, shock-free, contoured nozzle for the new arrangement of the X2 expansion tube. The design methods utilized a parabolized Navier-Stokes solver coupled with a Nelder-Mead optimization algorithm. Such a procedure was novel for the design of an expansion tube nozzle.

4. Once the nozzle was attached to X2 a series of experiments was conducted.
5. CFD modelling, using MB_CNS, of the X2 facility with the nozzle attached. This assisted in providing an understanding of the flow within the tube. Validation of the numerical simulation was undertaken by matching the simulation data to experiments. The findings confirmed Stewart's previous computational work in which it was shown that the addition of a nozzle on an expansion tube would increase the core flow diameter and also increase the steady test time.

1.7 Thesis Outline

Chapter 2 presents a review of impulse flow machines that are used to simulate hypersonic flight. It begins with an overview of the various facilities and the range of conditions over which they operate. The development of expansion tubes is analysed comprehensively as furthering the development is a significant element of the thesis. Previous investigations pertaining to expansion tube nozzles are summarised to convey what they achieved and what problems were encountered. From this information, the basis for the design of the new nozzle for the X2 expansion tube at the University of Queensland was formed.

Chapter 3 examines one-dimensional and axisymmetric modelling of the X2 expansion tube with the new single-stage, free-piston driver attached. The work looks towards an initial condition for testing and demonstrates the benefits of the new arrangement. It also provides an optimal compression ratio, piston mass and reservoir fill pressure for the facility. Final one-dimensional simulations for four different conditions are presented. Hybrid axisymmetric simulations of the acceleration tube are also discussed. These numerical results supplied a basis for comparison with the experiments once the hardware was completed.

Chapter 4 describes the changes that were made in the implementation of the new configuration of X2. It outlines the layout of the new piston launcher, piston, compression tube and couplings that were fabricated to connect the old tube to the new parts. Preliminary experiments show that the single-stage driver is capable of attaining the pressures required for rupture of the primary diaphragm. The one-dimensional and axisymmetric simulations of the expansion tube from the previous chapter are compared to the

experiments for each condition.

Chapter 5 explains the design, construction and installation of the full-capture, contoured nozzle. It discusses the parabolized Navier-Stokes solver and the Nelder-Mead optimization algorithm used in the nozzle design. The advantages of this method over the conventional Method of Characteristics are given. The experiments in the X2 expansion tube with the new nozzle attached are compared to axisymmetric models and the results examined. A comparison of the expansion tube, with and without the nozzle, is presented to demonstrate the effects of the nozzle. At the nozzle exit, the core flow diameter was approximately 50% of the 201.8 mm. This was an increase from the 60 mm at the acceleration tube exit. The addition of nozzle was also shown to double the test time to 110 μ s.

Chapter 6 presents the conclusions and recommendations from the work.

CHAPTER 2

The Development of Impulse Flow Facilities

The advent of World War II expedited the development of hypersonic experimental facilities. Supersonic wind tunnels were established in Germany to test rocket missiles. In an attempt to advance the knowledge base and capabilities of missiles, an interest into the hypersonic flow regime was promoted. In 1945, at the end of the war, hypersonic research picked up from where the German research had left off. Through the following fifty years the need for more in-depth and wider knowledge into hypersonic flow has increased. The progress in commercial air travel, high technology weaponry and space flight have all influenced the development of ground based test facilities.

Initial hypersonic facilities were continuous flow or intermittent type machines with test times in the order of 10 seconds or longer. They were similar to the earlier supersonic tunnels and thus were restricted in total enthalpy and pressures to flows with speeds below Mach 12 [17]. The higher speed requirements of wind tunnels have generated issues which impact on their design. Continuous test tunnels require enormous amounts of power to operate at speeds above Mach 8, thus short duration pulse facilities are utilized. The available test time depends on the facility and they range in the order of $10\ \mu\text{s}$ to 10 ms. Other problems exist, when simulating higher regime flight, such as structural and heating loads. Wind tunnel material cannot be exposed for prolonged periods to the extreme conditions, predominantly the high temperatures of the contained gases.

Researchers are always attempting to develop new types of facilities which can overcome the limitations of current capabilities. In the early 1990s, the United States (US) Air

Force and NASA began to examine a perceived gap in the US hypersonic test facilities for air-breathing propulsion systems above Mach 8 [18]. From this deficiency, an investigation into the use of MagnetoHydroDynamics (MHD) for hypersonic wind tunnels was started. The project called MHD Accelerator Research Into Advanced Hypersonics (MARIAH) expanded on previous work in the area. Just prior to this time, the Radiantly Driven Hypersonic Wind Tunnel (RDHWT) was proposed at Princeton University. It used one of three methods; laser, electron beam or microwave to add thermal energy to supersonic flow. In October 1997 these two programs were merged to form RDHWT/MARIAH II. The aim of this venture is to construct a medium-scale hypersonic wind tunnel with Mach 8-15 true enthalpy/entropy test conditions with run times in the order of a second. The project still has to provide solutions to challenging problems such as an Ultra-High-Pressure (UHP) air supply operating to 2 GPa, supersonic thermal energy addition and MHD augmentation. This will take time, as with many new and promising ideas. Even with the success of this project, it still does not allow testing for vehicles such as blunt bodies capsules used during planetary entry and Earth reentry.

There are many other facility types such as arc jet tunnels, hot shot tunnels, Ludwig tube tunnels and gas guns which are not dealt with in this thesis, however, they all have their advantages and uses. Information describing these facilities can be found in Lukasiewicz [17] and extensively throughout the aerospace literature. Collectively these facilities fall short of being able to simulate atmospheric flight conditions in the very high Mach number range. They are limited in either total pressure and total temperature, or both. The best option, at the current time, for the ground based simulation of very high speed flow is the class of test facilities based on shock and expansion tubes.

2.1 A Brief Introduction to Shock Tubes and Shock Tunnels

A shock tube is essentially two chambers of gas, one high pressure and one low pressure, separated by a diaphragm. A picture of a shock tube and the wave motion produced is shown in Figure 2.1. Upon rupture of the diaphragm a shock wave propagates into and processes the gas in the lower pressure region. This compresses and heats the gas in

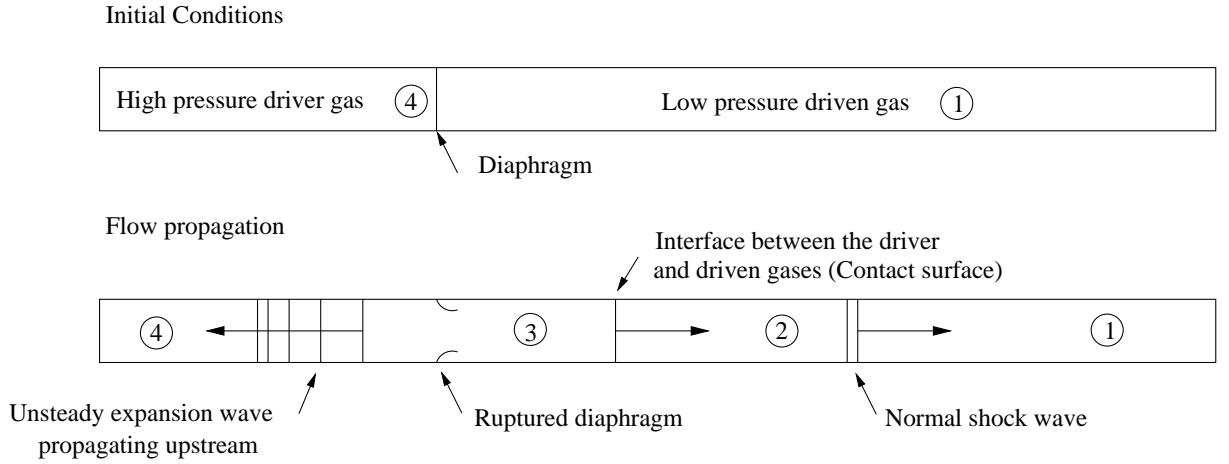


Figure 2.1: Flow in a shock tube

region 1 and induces a mass motion. An unsteady expansion fan propagates upstream into region 4, providing a pressure gradient that accelerates the gas from state 4 to state 3.

The concept for a shock tube was proposed by Vieille [19] in 1899. An in-depth coverage of the research conducted into shock tubes following this, can be found in Lukasiewicz [17]. Despite the copious amount of research performed, it was not until the 1940s at Princeton University that the basis of shock tube operation was properly established [20]. In 1951, a diverging section was placed before the test section to form the first shock tunnel [21]. A detailed examination of the modifications that could be made to a shock tube was presented by Hertzberg et al. [22].

Since that time, the reflected shock tunnel has been the main testing tool for high speed experimental studies. A list of some of the facilities currently operational and an in-depth coverage of shock tunnel theory can be found in Goozee [23]. Despite the capabilities of shock tunnels, they still possess a restriction in their speed simulation prospects.

2.2 Impulse Facility Drivers

The driver is the mechanism that provides the source of energy for a wind tunnel to increase the pressure and temperature of the gas. For an impulse facility high performance in the driver equates to increasing the strength of the shock wave in the driven tube. The main limitation which generally exists is the pressure which the the driver section can

contain. Like all things, the variants have their advantages and disadvantages. Factors such as cost, performance, fabrication requirements, safety and ease of operation will determine the appropriate driver. Throughout the 1960s and 1970s many drivers were examined for shock tubes and shock tunnels. The varying types were light gas drivers, electrically heated drivers, combustion drivers and compression drivers. The two main drivers used worldwide on expansion tubes at the present time are free-piston drivers and detonation drivers.

2.2.1 Detonation Driver

Typical combustion drivers use the ignition of hydrogen and oxygen in helium to create a high temperature gas. Instead of the deflagrative process used in combustion drivers, detonation drivers release energy via a detonation wave that propagates down the tube. This free running Chapman-Jouget (C-J) wave increases the pressure and temperature of the driver gas which in turn is used to drive the shock wave down the shock tube [24, 25, 26, 27]. A detonation driver can be run with both a forward and backward running detonation wave. The advantages of this type of driver is that it is cheap, simple and the obtainable pressures are only restricted by the driver vessel design. However, the range of driver gases are limited and this affects the speed of sound that can be generated in the driver gas.

2.2.2 Free-Piston Driver

The processes in a single-stage, free-piston driver [28] are shown in Figure 2.2. Upon release of the piston, a high pressure reservoir of gas pushes it down the tube compressing the driver gas to a high temperature and pressure. Once the driver gas slug reaches the burst pressure of the primary diaphragm the material ruptures, allows the sudden expansion of the driver gas and sends a shock wave down the shock tube. Great flexibility in tailoring conditions is possible in a free-piston driver. Through the varying combination of driver gas and compression ratio, a range of driver gas speed of sound at primary diaphragm rupture is achievable. When compared to other drivers, the free-piston driver provides high facility performance because it is capable of producing high shock speeds and a large range of stagnation enthalpies [29]. The major downfall of this configuration

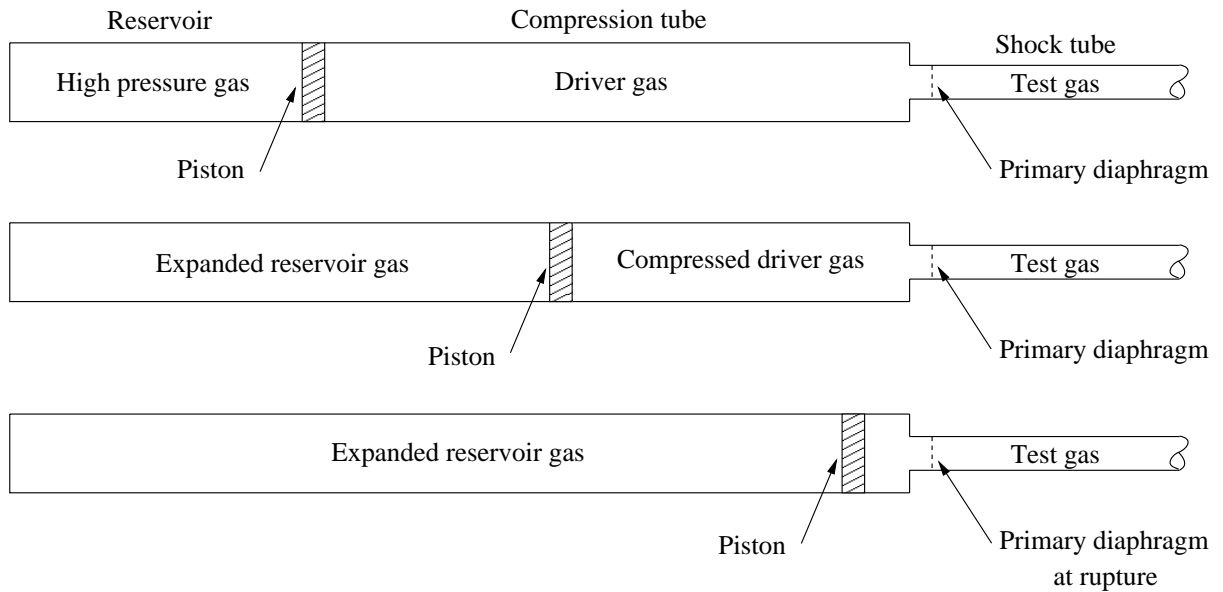


Figure 2.2: Layout of various stages of a free-piston driver

is the need to handle and control the motion of a heavy piston.

One constraint is that the piston's velocity at rupture of the primary diaphragm must be sufficient to maintain driver gas pressure [30]. A large area ratio is usually employed at the primary diaphragm station so that this velocity is manageable. If the speeds are too high, the impact speeds of the piston on the buffer can be detrimental. Furthermore, an adequate volume of driver gas is necessary to drive the test gas as well as prevent attenuation of the primary shock wave. Attenuation is caused by the reflected unsteady expansion wave catching up to and weakening the shock wave. Single-stage, constant area drivers can require impractical lengths of compression tube to avoid this. This is another reason for a large area ratio between the driver and driven tubes. On large scale facilities this can create high capital expenditure because of material and construction costs and has led to the development of the two-stage or compound, free-piston driver.

Two-Stage Piston Driver

As stated by Morgan [31], in a two-stage driver configuration, the initial compression occurs in a large diameter tube where the pressures are low and the swept volume is high. Work is performed by the reservoir gas on the piston but there is little compression work done on the driver gas. In the second stage most of the reservoir work has been transferred to the piston which is compressing the driver gas at high pressure but with

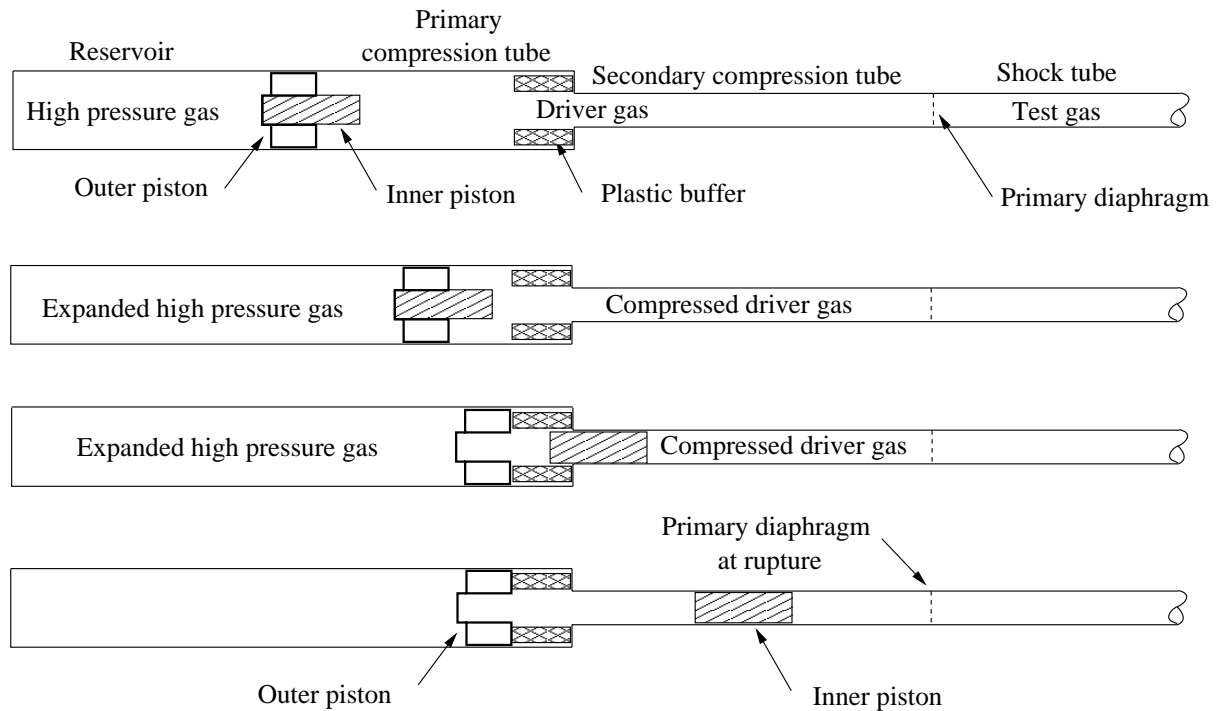


Figure 2.3: Layout of various stages of a compound free-piston driver

small swept volume. This results in a rapid pressure rise. This process is best completed in a small bore, high pressure tube. Two pistons are required for the two tubes as shown in Figure 2.3. The first stage (outer) piston is lightweight and acts as a carrier for the secondary (inner) piston which is heavy and stores most of the energy from the early part of the reservoir expansion.

The advantages of this design are that it reduces the length of the facility and decreases the cost. This reduction in cost is at a sacrifice in performance. The lower costs are because the low pressures in the first stage mean a thinner walled tube can be used for the large diameter section while the high pressures are contained in a relatively small diameter tube [32].

Double Diaphragm Driver

Another variant of an impulse facility driver that has been coupled with a free-piston compressor is the double diaphragm or compound driver. It was first proposed by Henshall [33] and has since been examined further on shock and expansion tubes by the group at the University of Queensland [34, 35, 36, 4, 37]. The driver is comprised of two regions

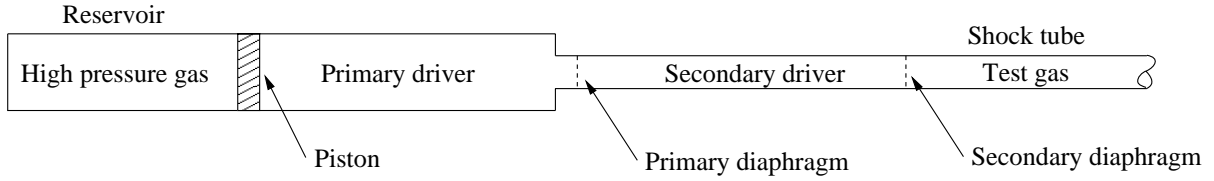


Figure 2.4: Layout of a double-diaphragm, free-piston driven expansion tube

separated by a diaphragm as illustrated in Figure 2.4. When the primary diaphragm ruptures, a shock wave propagates down the secondary driver tube. From here, two methods exist for operating a double diaphragm driver. In the first, the shock arrival at the secondary diaphragm causes it to burst. The gas that follows the shock down the shock tube has an elevated temperature and velocity thus increasing the driver performance. Alternatively, the secondary diaphragm can be of sufficient thickness so that the shock wave is reflected back upstream processing the gas further. The secondary diaphragm is then ruptured by external means. This results in stationary driver gas with an increased temperature and hence greater driver performance. Of these two methods, the former is the one that has been predominantly implemented on expansion tubes and is referred to as a super-orbital expansion tube.

Morgan [4] presents the performance benefits of a compound driver on a free-piston driven expansion tube. The results are plotted in Figure 2.5. The driver equivalent flow Mach number is defined as the speed behind the shock wave in the test gas normalized by the speed of sound in the driver at diaphragm rupture. The pressure of the processed test gas is given as p_2 and p_4 is the diaphragm burst pressure. A significant pressure ratio advantage is seen in the compound arrangement for driver equivalent flow Mach numbers above Mach 2. Below this value there is little or no benefit in the pressure ratio and as there is a loss in test time, the single diaphragm arrangement is a superior option. Thus, only when targeting the higher speed regime is a compound driver useful on an expansion tube.

2.3 The Background of Expansion Tubes

Shock tunnels are limited in the total enthalpy which they can simulate because all the energy is added across a shock wave. In a reflected shock tunnel, high temperature and pressure gas must be contained in the stagnation region before the flow can be steadily

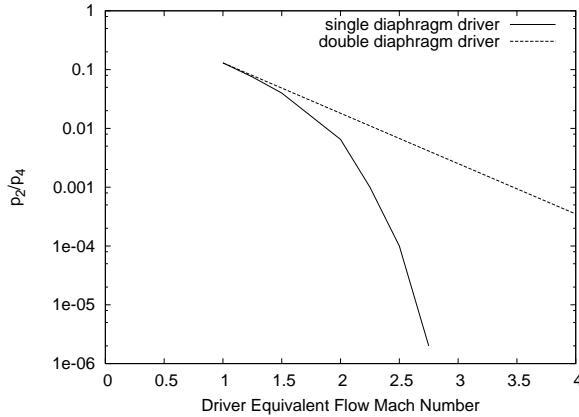


Figure 2.5: Comparison of a single and double-diaphragm driver. Adapted from [4].

expanded through a supersonic nozzle. This results in energy losses through radiative cooling. For a non-reflected tunnel, highly dissociated and ionized plasmas are created in large velocity flows, which makes them unsuitable for simulating free-flight conditions. As a consequence of this, shock tunnels are constrained to velocities such as those used in Earth orbit flights [4].

An expansion tube is essentially the substitution of the nozzle at the end of a shock tunnel with another constant area tube so that two shock tubes are located in series. This replaces the steady expansion of the test gas in the nozzle with an unsteady expansion that travels the length of the second tube. The result is that more energy is added to the fully expanded part of the test flow. Higher pressure and velocity conditions can be achieved without increasing the needed tube wall thickness. This is possible because the large stagnation conditions never physically occur and hence do not have to be contained.

The layout and operation of an expansion tube is depicted in Figure 2.6 along with a distance-time ($x-t$) diagram. Upon rupture of the primary diaphragm, in this instance initiated by a free-piston driver, a shock wave travels down the shock tube processing the test gas. When the shock arrives at the thin secondary diaphragm, the diaphragm bursts allowing a strong shock wave to propagate through the acceleration gas. An unsteady expansion, moving downstream in a laboratory frame of reference, propagates upstream through the test gas. Trimpi [38] explains that, for a steady expansion, the total enthalpy change of the flow is $dH = 0$, while for a non-steady case it is $dH = -(M - 1)dh$. When $M \gg 1$ there is a total energy multiplication effect in the non-steady case as seen in this equation. However, this advantage is at the expense of test time which is reduced due

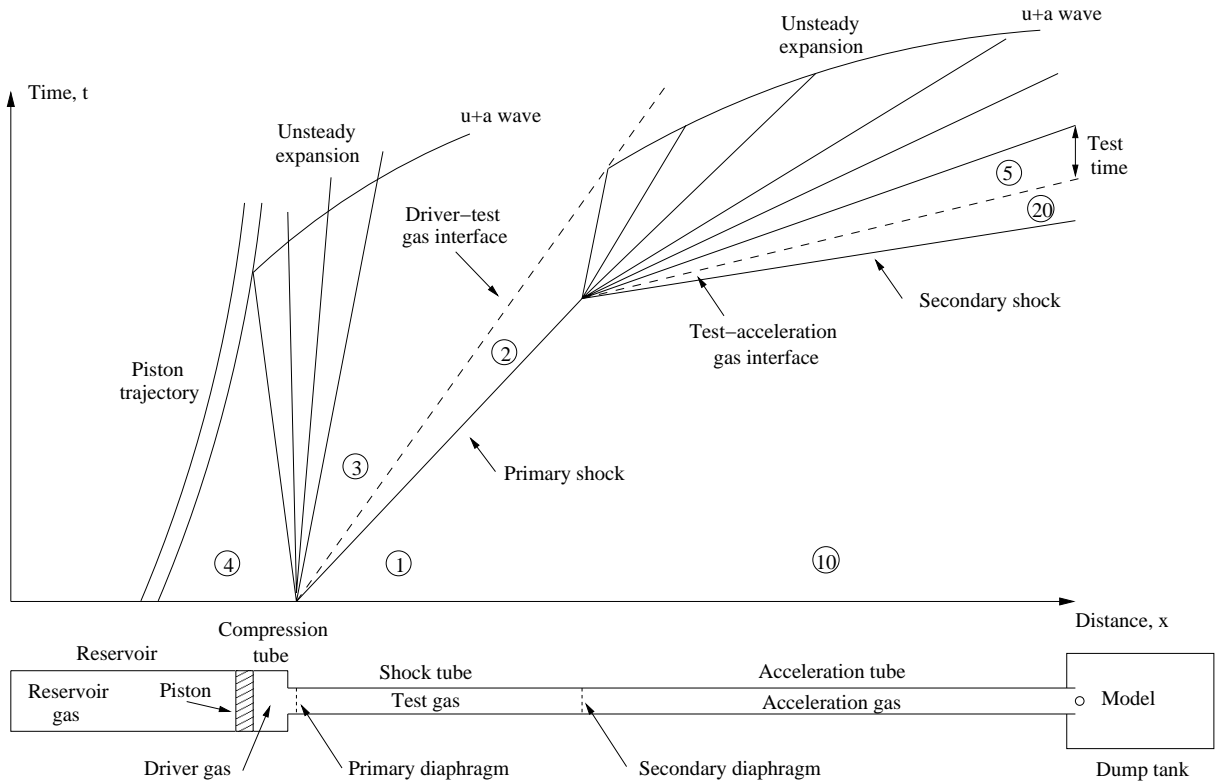


Figure 2.6: Layout and x-t diagram for an expansion tube

to the unsteady processing of the gas and the complex wave motion. Thus, expansion tubes are better suited to testing bluff bodies than air-breathing propulsion systems when long duration test flows are required. Furthermore, model sizes at the current time are restricted as the core flow diameter is limited to the size of the acceleration tube.

2.3.1 Initial Research

Resler and Bloxsom [39] are accredited with first proposing the concept for an expansion tube in 1952. The authors claimed that replacing the steady expansion of a shock tunnel with an unsteady expansion, would produce a very high Mach number flow, with a large Reynolds number. In 1953, Bernstein [40] independently wrote calculations about a similar arrangement, to generate test gas with a high Mach number and static temperature. The paper by Hertzberg et al. [22] in 1955, examined a number of modifications to a shock tube, to determine the best method of hypersonic testing. One configuration was the non-steady expansion method as described by Resler and Bloxsom. It was stated that the addition of a second shock tube section would provide the advantage of high Reynolds

number and temperature, but at a sacrifice of test time.

A reasonably detailed theoretical analysis was performed by Trimpi [38] in 1962, the first to call the apparatus an expansion tube. The study considered both perfect gas and real air in equilibrium with the assumptions of idealized diaphragm rupture, centred expansion waves and continuum flow. Trimpi identified that an expansion tube would possess numerous advantages over a reflected and non-reflected shock tunnel. It would generate velocities twice those of a shock tunnel for the same initial conditions. Pressures with values of several orders of magnitude lower would only have to be contained as the flow is never stagnated. Furthermore, the test gas would be less dissociated and the slower rate of the expansion process would allow the various energy modes a greater possibility to remain in equilibrium. The conclusion reached, was that the expansion tube, when compared to any other experimental device, had a superior theoretical potential for replicating hypersonic flight. Trimpi established that expansion tubes would require a large diameter for the acceleration tube as boundary layers can become large and in effect eliminate a core flow diameter. He recognized that the non-ideal secondary diaphragm rupture was important in attaining a suitable test time as the test gas is located close to the diaphragm at rupture. Lastly it was noted that investigation into interface mixing and shock wave attenuation was needed and that the extent to which the theory would deviate from reality was unknown.

Additional theoretical research was carried out in the 1960s but this involved expansion tubes with nozzles attached. These studies are discussed in Section 2.3.4. Nevertheless, in the mid 1960s, numerous institutes performed experimental work to further examine the prospects of expansion tubes.

Experimental Research

At the NASA Langley Research Center, a shock tube was converted to an expansion tube [41]. It consisted of a constant diameter 3.75 inch (9.5 cm) tube, with room temperature hydrogen gas as the driver, pressurized to 100 atmospheres (10.1 MPa). The test gas was air with a fill pressure of 22 torr (2.9 kPa) and the acceleration gas was helium with a fill pressure ranging from 10^{-2} to 2 torr (13.3 to 266.7 Pa). The results were compared to the one-dimensional, inviscid theory presented by Trimpi [38] and it was stated that the differences which existed were moderate and tolerable. Consideration was taken for the

problems of flow attenuation, secondary diaphragm rupture, flow turbulence, interface mixing, boundary layer thickness, thermal non-equilibrium and test time. No answers were given to these quandaries but it was considered that they were not serious enough to detract from expansion tube capabilities.

Givens et al. [42] conducted experiments on a facility with a combustion driver which could attain an after-burn pressure of 200 atmospheres (20.2 MPa). The expansion tube was a constant diameter of 17 cm and the driven section contained air at a pressure of 155 mm Hg (20.7 kPa) while the acceleration tube contained helium at a pressure of 115 μ m Hg (15.3 Pa). This arrangement was able to generate conditions of a velocity of 7.5 km/s, a test time of 100 μ s and a free-stream to standard atmospheric density ratio of 0.004. The authors identified a test flow possessing varying properties which was attributed to severe contamination from the secondary diaphragm and the walls. Suggestions given to reduce the level of contamination were:

- the removal of the secondary diaphragm prior to the shock arrival,
- the construction of the tube walls with glass and
- the shortest possible acceleration tube to prevent mixing of the boundary layer and the test gas.

The design characteristics of the Ballistic Research Laboratory (BRL) expansion tube were discussed by Spurk [43]. The test section had a diameter of 6.426 inches (16.3 cm) and they examined flows at velocities of 10000 to 20000 ft/s (3050 to 6070 m/s). The paper focused on presenting results for the experiments that were completed. The performance of the expansion tube and its potential as a hypersonic testing tool were not assessed.

The Work at NASA Langley

Following the extensive theoretical research completed in the 1960s, NASA Langley shifted their focus to constructing an expansion tube. This was to verify that the expansion tube concept was realistically capable of generating hypersonic flows that were suitable for experimental testing. Initially, a pilot facility was created from an existing shock tunnel and this was discussed in Section 2.3.1. Further investigation was presented in the report by Jones and Moore [44]. They found that the flow properties were of the same order of

magnitude as the theory and while examination was required for the discrepancies that existed, it was concluded that the expansion tube would be able to produce flows suitable for high velocity research. The NASA Langley pilot facility operated for approximately ten years and even though in that time no complete answers were provided to some of the problems encountered and no explanations were given for the discrepancies with the theory, the results were still promising and the expansion tube was considered a feasible testing tool for hypersonic vehicles. It could produce a few flow conditions in the range of 7 to 9 km/s.

In the late 1960s, NASA Langley built a larger, 15 cm diameter, machined walled, arc-driven expansion tube, capable of reaching higher pressures than the pilot facility. While numerous studies were performed on this facility, the results predominantly produced similar findings. The early experiments by Moore [45] used both heated and unheated helium as the driver gas with air as the test gas. The preliminary investigation yielded flows with interface velocities of 5 to 6 km/s, Pitot pressure surveys that indicated a test core diameter of approximately half the acceleration tube diameter and test times of 200 to 400 μ s. At lower interface velocities, a dip in the Pitot pressure prior to the arrival of the expansion fan at the test section existed thereby reducing the test time by approximately half. The thermochemical state of the flow was unable to be predicted from simple expansion tube theory. A comparison of the experimental wall static pressures to the theoretical values indicated a thermochemical equilibrium expansion. However, a similar comparison of the predicted Pitot pressures showed a thermochemical non-equilibrium expansion.

Miller's article in 1974 [46] centred on the flow properties of the Langley expansion tube. Using helium, argon, air and carbon dioxide as test gases, the experiments indicated that a sufficient test time was generated with a core flow of approximately half the tube diameter. Attenuation was seen in the flow when argon, air and carbon dioxide were used but not for helium. A comparison of the flow quantities for the predicted and measured values indicated that the expansion was in thermochemical equilibrium. An examination of blunt bodies with test gases of helium, air and carbon dioxide with free stream velocities between 5 and 7 km/s further stated that good repeatability was attained with a core flow of half the tube diameter [47, 48].

In 1975, Miller and Moore [49] looked at the establishment of quasi-steady flow about

a test model. Due to the short test time of the expansion tube it was unknown if a steady flow would develop. It was found that for two-thirds of the $250\ \mu\text{s}$ test period a steady state existed. Similar findings were again described by Miller [50, 51]. Using unheated helium driver gas together with helium, air and carbon dioxide as test gases, a good quality flow that was repeatable for different experiments was produced. It had a 200 to $300\ \mu\text{s}$ test times which was sufficient for testing blunt axisymmetric and two dimensional models. However, for a given test gas the range of operating conditions was limited to a given flow condition. Therefore different test gases were necessary to obtain different conditions.

The paper by Shinn and Miller [52] gave an optimum operating condition with helium test gas and a test time of $300\ \mu\text{s}$. The shock tube fill pressure was 3.45 kPa, the acceleration tube fill pressure was 16 Pa and the secondary diaphragm thickness was $6.35\ \mu\text{m}$. They examined the effect of tube wall boundary layer growth and finite diaphragm opening time through the variation of shock and acceleration tube gas pressure and secondary diaphragm thickness. The core flow diameter was again half the tube diameter. The large tube wall boundary layer was found to cause the dip in Pitot pressure seen in the test time.

A summary of the development and operation of the Langley expansion tube over the previous ten years was given in 1983 [5]. It was recognised that contrary to theory, only a single flow condition in terms of Mach number and Reynolds number, sufficient for model testing, could be produced for a test gas. The facility was deactivated in 1980 and decommissioned in January 1983 due to financial and resource issues. At the time there were no other active expansion tubes in the USA.

2.3.2 The Renaissance of Expansion Tubes

In 1987 [53], the TQ shock tube at the University of Queensland was converted to a free-piston driven expansion tube now referred to as X1. A grant was provided by NASA so that a series of experiments could be conducted to determine the range of test conditions. It was thought that the free-piston driver would offer a wider range as opposed to the arc-driven Langley expansion tube.

Preliminary experiments by Paull et al. [54] demonstrated that the Pitot pressure mea-

surements were qualitatively similar to those discussed in Section 2.3.1, from the Langley facility. The Pitot pressure measurements also revealed additional operating conditions existed for a test gas of air. However, test times were shorter than those predicted by theory and this was partially caused by driver gas contamination and expansion waves reflecting from the driver/test gas interface.

The study by Gourlay [55] examined the problems that were being experienced in the test period. Large perturbations in the pressure were disturbing the steady test time. If the cause of this was determined it would assist in establishing a broader range of operating conditions. The theory postulated behind the disturbances was that once the primary shock had passed through the test gas the driver and test gases mixed producing regions of less dense gas referred to as “blobs”. These “blobs” could separate from the contact surface due to Rayleigh-Taylor instabilities and then overtake the interface due to boundary layer entrainment effects. Once they had passed through the unsteady expansion they would then cause the perturbations in the test flow. However no “blobs” of gas were observed. The final conclusion given was that the fill pressures could be scaled to give the same flow conditions so they should be chosen such that the maximum test time was obtained.

Paull and Stalker [56] further focused on the test flow disturbances that had been limiting expansion tubes. It was realized that the steady test time was ended by either the arrival of the tail of the unsteady expansion or the head of the unsteady expansion after it had been reflected from the driver/test gas interface. This was seen clearly in the numerical simulations of the Shinn and Miller experiments [57]. However, for small expansion ratios, additional disturbances were observed in the test gas which may have been reducing the test time. Similar disturbances to these were seen in the driver gas. In the study, the disturbances were modelled as first-order lateral acoustic waves and it was established that the waves first created in the driver gas, limited the test time by penetrating the driver/test gas interface and eventually arriving in the test gas where they remained to interrupt the test time. This problem could be rectified by eliminating the waves entering the test gas by having a sufficient increase in the speed of sound from the expanded driver gas to the test gas at the driver/test gas interface. The findings suggested that unless some means of prevention of the waves could be discovered, expansion tubes could only be expected to operate successfully when the Mach number of the driver gas at the interface exceeded critical values, in the range of 4 to 5 from these experiments.

As part of the NASP program, the NASA Langley six inch expansion tube was moved to GASL and renamed HYPULSE. Installation began in October 1987 and the first experiment was conducted in March 1989 [58]. The work from the University of Queensland had shown that with blends of air (nitrogen), argon and helium as the driver gas [59] most conditions could be achieved. It was also planned to install a free-piston driver to increase the operational capabilities.

2.3.3 The Latest Progress in Expansion Tube Work

In 1994 Erdos et al. [60] determined that an increased in the test envelope of the HYPULSE shock-expansion tube was possible without a free-piston driver. By changing the driver gas composition the speed of sound of the driver gas could be altered. This was determined to be the major factor in obtaining a wide range of total enthalpies. It was also concluded that the vital factor in avoiding flow disturbances in their experiments, was to restrict the Reynolds number so that transition did not occur in the test gas. Through these means the operating range for expansion tubes could be widened.

Following this a Shock-Induced Detonation (SID) driver was placed on the facility and experiments were conducted in order to increase the test pressures [61]. Test flow was qualitatively similar to conventional drivers but there was a twenty times increase in pressure at some enthalpies when compared to a conventional light-gas driver.

At the University of Queensland further studies on X1 [62, 7] concentrated on what conditions could be achieved and if these were beneficial for testing models. Quasi-steady flows were generated with argon and air test gas at flow velocities above 9 km/s. From here, the emphasis turned to free-piston driven, super-orbital expansion tubes. This triple diaphragm design was discussed previously. The first paper presenting preliminary findings from the X1 super-orbital expansion tube was in 1991 [34]. Neely and Morgan [35] continued to demonstrate the concept and Neely also conducted studies [63].

By the middle of 1995 a larger expansion tube, X2, was designed and constructed [64] at the University of Queensland. Commissioning took place at the end of 1995. The X2 expansion tube consisted of a two-stage, free-piston driver. This compound piston was implemented to reduce the cost of the facility and was also a prototype for the larger X3 expansion tube which was to be constructed [65]. Palmer [66] was one of the first to

complete experiments in X2. At the start of 2004 a new driver was installed on X2 as the old compound piston was no longer required. This change is discussed in Chapter 4.

The most recent member of the series of expansion tubes at the University of Queensland is the X3 expansion tube [31, 67, 68]. The commissioning tests for this facility were conducted in January 2001 with the first experiments conducted in May 2001 [69].

The JX-1 free-piston driven expansion tube was installed at Tohoku University. Details of the design and performance were given by Sasoh et al. [70]. The facility targeted conditions suitable for modelling the MUSES-C reentry vehicle [71] and could achieve a stagnation enthalpy of 40 MJ/kg.

2.3.4 Review of Previous Expansion Tube Nozzles

An expansion tunnel is the name given to an expansion tube with an area change in the shock or acceleration tube or a nozzle at the end of the acceleration tube. The unsteady expansion is either followed by or partially replaced with a steady expansion. This increases the core flow of the facility but total enthalpy and pressure are lost through the area change. The first examination of area changes in expansion tubes began around the same time as the first comprehensive theoretical study of an expansion tube was conducted by Trimpi in 1962 [38]. Since that time a small number of researchers have examined area changes in expansion tubes, with the majority concentrating on nozzles situated at the end of the acceleration tube. Despite these investigations there has been limited success and until the end of 2005 no facility operated continuously with a nozzle attached.

Hypersonic nozzle design has been examined comprehensively throughout aerospace history. After the end of the Second World War hypersonic tunnels were operated with axisymmetric nozzles attached. A great amount of effort was placed on the nozzle design as the facilities were dependent on the steady, isentropic expansion in the convergent-divergent nozzle to produce uniform test flow as well as accelerate the gas to the desired speed. Initial designs were similar to the two-dimensional approach utilized for supersonic nozzles. These though were not used above Mach 10. The design methods shifted towards axisymmetric nozzles and these were then used for facilities above Mach 6 [17]. The first use of a nozzle on an impulse facility was in 1951 when Hertzberg [21] placed a diverging

section before the test section of a shock tube.

After Resler and Bloxson [39] first proposed the expansion tube concept in 1952, Hertzberg et al. [22] mentioned the possibility of a modification of adding a nozzle to an expansion tube. Trimpi also mentioned the possibility of a steady expansion following the unsteady expansion in an expansion tube in 1962 [38]. It was not until 1965 that two research groups performed work on area changes in expansion tubes.

The first group which looked at the expansion tube nozzle were Trimpi and Callis [72] in 1965. They conducted a perfect gas analysis of a nozzle positioned at the end of the acceleration tube with a diaphragm placed between. This configuration was referred to as an expansion tunnel. The results indicated that there would be an increase in test time, a larger initial test gas slug length, a higher efficiency and reduced secondary diaphragm bursting problems. It was stated that a nozzle, if constructed, would need to be reasonably long. They concluded that they believed the advantages of an expansion tunnel outweighed the disadvantages.

Callis [73] continued this work with a perfect gas analysis of area changes, referred to as nozzles, after the primary and secondary diaphragms to try to eliminate two problems mentioned by Trimpi [38]. These were diaphragm opening problems and viscous effects in the acceleration tube which caused large boundary layers. The use of an area change would increase the diameter of the tube at the test section and mitigate the effect of the large boundary layers. This would also allow smaller diaphragms that would be able to open quicker, producing more ideal wave systems. Three configurations were investigated. Configuration I had a nozzle immediately downstream of the primary diaphragm with the pressure and velocity of the driver gas at the nozzle exit matched identically to the values in the shock initiated flow. This required extreme driver pressures. Configuration II was physically the same as I but was operated in an over-expanded mode. It required large driver pressures and generated a small operating regime. Configuration III was a nozzle located downstream of the secondary diaphragm. It was the most feasible option but due to the short nozzle lengths required in order to ensure the availability of testing time, strong re-compression shock waves emerged disrupting any useful test flow. The three configurations were rejected and the arrangement given by Trimpi and Callis [72] was suggested as a better option.

Callis [74] followed this report with an analysis of a calorically perfect gas through conical nozzles. A method of axisymmetric irrotational characteristics was utilized because a one-dimensional approach would have been inadequate. The design was a skimmer or scoop type conical nozzle. A skimmer nozzle has an inlet diameter which is smaller than the end of the acceleration tube and this removes the boundary layers providing uniform flow. A range of solutions for varying nozzle half-angles and inlet Mach numbers was determined. It was established that the method provided a means of generating transition contours and evaluating the resulting shock free flow. Trimpi [75] produced a theoretical investigation of simulations in expansion tubes and tunnels but was not concerned with the comparison of the two.

Not long after Trimpi and Callis' first report [72], Norfleet et al. [76], in November 1965, presented a report looking at an abrupt area change at the secondary diaphragm. They named the facility a modified expansion tube. The experimental results showed that flow disturbances of sufficient magnitude precluded any meaningful aerodynamic testing. The possible source of these disturbances was from the secondary diaphragm. In 1966, Norfleet and Loper [77] presented an analysis of an expansion tunnel with several varying area ratios assuming thermodynamic and chemical equilibrium. They reasoned that an expansion tunnel provided a velocity loss which for a given driver could be large but only became critical when the driver had limited potential. In contrast to this there was an increase in the test gas slug length parameter, which is defined as the test gas slug length at time of rupture of the secondary diaphragm divided by the acceleration tube length.

A skimmer nozzle was designed for the NASA Langley Expansion tube by Miller in the mid 1970s [78]. The layout of this facility is pictured in Figure 2.7. In 1983 he looked at the preceding ten years worth of operating experience on the NASA Langley Expansion tube with and without a nozzle [5]. The configuration with the nozzle attached was termed the expansion tunnel. In 1975 the facility was converted to the tunnel arrangement by placing a 10° , conical scoop nozzle at the end of the acceleration tube. Two years later the facility was converted back to its original arrangement. Miller concluded that the preferred option was to operate without a nozzle. The expansion tunnel produced flow with a low Reynolds number of 1.6×10^4 /m and an annular shock in the exit flow. This illustrated the non-uniform nature of the flow. As stated before, the NASA Langley expansion tube was deactivated in January 1983 due to financial and resource issues.

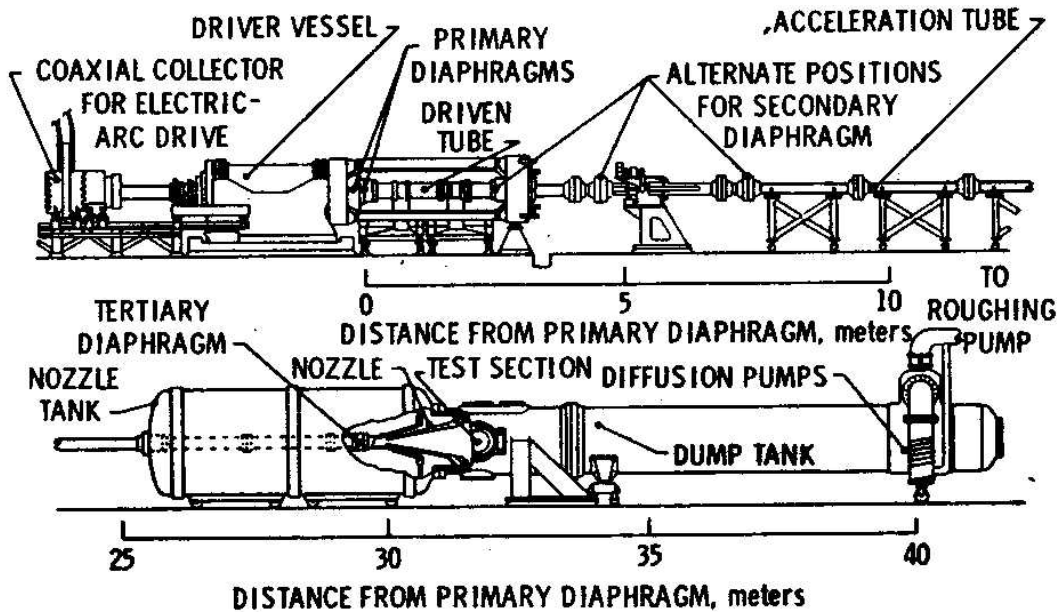


Figure 2.7: Layout of the Langley expansion tube/tunnel. Taken from [5].

In 1994, Leyva [79] studied area changes located after the primary and secondary diaphragms. The paper described the changes as divergent conical nozzles. It stated that the addition of a nozzle could increase scale and test time while concluding that more work was required to obtain accurately the test times available. A more comprehensive study would also have provided the optimum area ratios to produce the maximum test slug length.

In 1996, Bakos et al. [80] presented the design for a full capture nozzle for the HY-PULSE expansion tube at GASL. A full capture nozzle has an inlet diameter equal to the diameter of the end of the acceleration tube. This means that the inflow is non-uniform but the problems of a skimmer type nozzle (with the leading edge producing shocks and the larger area ratio causing a lower Reynolds number at the exit) are not encountered. The specifications for the nozzle only required that the flow be expanded from a Mach number of 4.77 to 6.4 with an exit diameter of 30 cm. It was determined that the flow from the nozzle was far from uniform even though the wall contours were designed to make it uniform.

The thesis by Sudnitsin [81] in 2000 involved the construction of a steady expansion

2.3. THE BACKGROUND OF EXPANSION TUBES

nozzle to be situated at the end of the acceleration tube of the X1 facility at the University of Queensland. The goal was to increase the core flow diameter. A conical nozzle of 8° half angle with an area ratio of 9 was installed. The results indicated that the nozzle produced uniform test flow with an increased core flow area. The starting process had minimal effect on the test flow and when a diaphragm was placed at the nozzle throat, the test time increased. The static pressures generated were very low and not long after the conversion to a expansion tunnel, the nozzle was removed.

Recently, Chue et al. [82] designed another nozzle for the HYPULSE expansion tube. The specifications for this nozzle were that it was to increase the test core size from 15 cm to 30 cm while having a Reynolds number of at least $9.8 \times 10^5 / \text{m}$, a nozzle entrance pressure of 1 atm with a total enthalpy of 21 MJ/kg and a velocity of 6 km/s. A limitation existed in that the length of the nozzle was constrained to fit in the existing test section of the facility. Further to this, the nozzle was kept as short as possible so that the useful test time was not decreased by the flow establishment process and because hypersonic boundary layers can become large in long nozzles thus reducing the core flow diameter. The effects of both skimmer and full capture nozzles were examined along with contoured and conical walls. Contoured nozzles should lead to uniform exit flow but, at non-design operating conditions, are more susceptible to flow non-uniformities because they rely upon wave cancellation, which is only precisely achieved at one condition. Conical nozzles are easier to design and are less sensitive to off design conditions but have a diverging and expanding flow at the exit. The motivation for Chue's work was that the previous nozzles [78, 80] were deemed inadequate.

The method of characteristics was used, with the skimmer option being examined first, followed by the examination of the full capture option. Three arrangements were analyzed, with the first being fully contoured, to produce completely uniform flow at the nozzle exit. The length necessary for the nozzle was 8.08 m, which was too long and in addition to this, compression waves and shocks of significant magnitude to destroy the flow uniformity were formed. The second design was a conical nozzle with either a half angle of 5.71° , 8° or 10° . For the 5.71° and 8° nozzles the leading edge shock destroyed any uniformity in the flow. Compression waves were seen in the 10° nozzle and when a non-uniform inflow was implemented the flow became unsatisfactory. The last option consisted of a contoured inlet, followed by a conical profile. It was hoped that this nozzle

would reduce the compression waves which had been seen to disturb the flow in the previous alternatives. This design was chosen with a full capture approach due to the fact that it gave a larger core flow diameter. Even though the nozzle was designed and constructed for an operating condition with a total enthalpy of 21 MJ/kg, it was believed that the nozzle would operate adequately over a enthalpy range of 8 to 30 MJ/kg [82].

Work in the LENS facility involved the use of a hypersonic nozzle attached to an expansion tube [83, 84]. Very little is presented in these papers about the details of the nozzle characteristics. The main emphasis by Holden et al. is the flow over a double cone configuration tested in the tube, with flow conditions generated in the tube also presented. Nompelis et al. [84] concentrate on comparing experimental results to numerical simulations for the flow produced in the facility. As is done in the present thesis, the numerical simulations are used to examine turbulent effects as well as finite-rate chemistry effects. It is concluded that in the condition that is focused on, only a small amount of vibrational non-equilibrium energy is present, but turbulent effects should be included. They obtained reasonable accuracy between the computational and experimental results but did not obtain a complete quantitative agreement between the two methods.

2.4 Summary

In the past fifty years hypersonic ground based test facilities have progressed considerably. From the first designs in hypersonic facilities, the focus has moved to impulse tubes for higher speeds. A gap still remains in testing capabilities at the highest speed flow regimes. Expansion tubes partially fill this void and at present, are the only machines capable of replicating the conditions experienced in flight above Earth orbital velocities. Their disadvantages lie in the relatively small test time and core flow diameter they produce. While other ideas for future facilities must be created for further advances in flight, the problems associated with expansion tubes need to be addressed at the present time. The addition of a contoured, shock free nozzle at the end of the acceleration tube in an expansion tube was proposed to rectify some of these shortcomings. Despite the previous work that had been conducted on expansion tube nozzles they had not provided great benefits. It was hoped that an improved design method would take advantage of the compensating effects of boundary layer growth at the nozzle throat and the downstream

part of the unsteady expansion. The ultimate test as to whether a flow straightening nozzle would succeed, was the construction and trial of a nozzle on the X2 facility as presented in Chapter 5.

CHAPTER 3

One-Dimensional and Axisymmetric Modelling

One of the main aims of this thesis was to examine the performance of a hypersonic nozzle for the X2 expansion tube. Before the nozzle was installed, X2 was upgraded with a new single-stage, free-piston driver. In this chapter, the term new configuration, refers to X2 with the single-stage, free piston driver attached. The term old configuration refers to X2 when the two-stage, free-piston driver was installed. The new facility provided a small scale model of the proposed RHYFL-X expansion tube on which the contoured nozzle could be tested. The details of the new driver are discussed in Chapter 4.

Presented in this chapter is one-dimensional and axisymmetric modelling of X2. The initial aim of this analysis was to develop a target condition for experimental testing in the new tube configuration as well as for the design of the nozzle. More importantly the numerical results provided a comparison to the experiments. The experimental values are used to validate the numerical work which can then in turn be used to provide an in-depth description of the flow in the tube. The core flow properties at the acceleration tube exit are the main information required so that when a model is tested in the facility the conditions it experiences are known. Though the modelling techniques used in this thesis have been previously utilized in modelling expansion tubes, code development is essential to continue providing a better understanding and estimation of expansion tube flows. This work, along with work by Jacobs [85] on the X3 expansion tube, are the first axisymmetric, finite-rate chemistry simulations performed on expansion tubes at the

University of Queensland. Earlier numerical simulations, performed in collaboration with McIntyre et al. [86], used equilibrium chemistry.

3.1 One-Dimensional Code and Geometry

CFD simulations using the quasi-one-dimensional transient code, L1d [87], were performed on the new X2 expansion tube. The code incorporated a Lagrangian perspective for the gas dynamics. The flow domain is comprised of regions of gas and these gas slugs are further separated into a number of fixed mass cells. These elements of fixed mass are tracked throughout time. Essentially, L1d operates via a time-stepping loop advancing the state of the system by a small increment of time, once the initial boundary conditions have been specified. Pressures and velocities are calculated between the gas regions by tracing the interfaces that exist there. At the beginning of the time step the flow state is interpolated from the cell centres on either side of the interface, then during a time step a Riemann solver is applied. Pistons and diaphragms can be included to separate the gas slugs. Their effect is handled through the appropriate boundary conditions. A diaphragm has a reflective boundary condition until the adjoining interface reaches the specified burst pressure at which time the diaphragm is removed and the gas slug interfaces begin to interact. For a piston, the mass, diameter and length are specified and point-mass dynamics are used to model its motion. Though only one spatial co-ordinate is resolved the code allows the gradual variation of the tube wall diameter. Greater detail about the governing equations is given by Jacobs [88].

The numerical methods in this thesis incorporate viscous, laminar flow and equilibrium chemistry unless otherwise stated. Viscous effects are approximated in L1d by the application of engineering correlations while the thermodynamic and transport properties for the thermally perfect gases are calculated using a look up table generated by the CEA (Chemical Equilibrium with Applications) program given by Gordon and McBride [89].

The entire arrangement of the new X2 expansion tube, including the compression process was modelled. The computational geometry is shown in Figure 3.1. The diameter of the slugs of gas and the setup of the geometry in L1d can be seen in the input file in Appendix A. The domain consists of four gas slugs, a piston and two diaphragms as in the real facility. Head loss from the area transitions is taken into account in the code with

3.2. ONE-DIMENSIONAL NUMERICAL SIMULATIONS

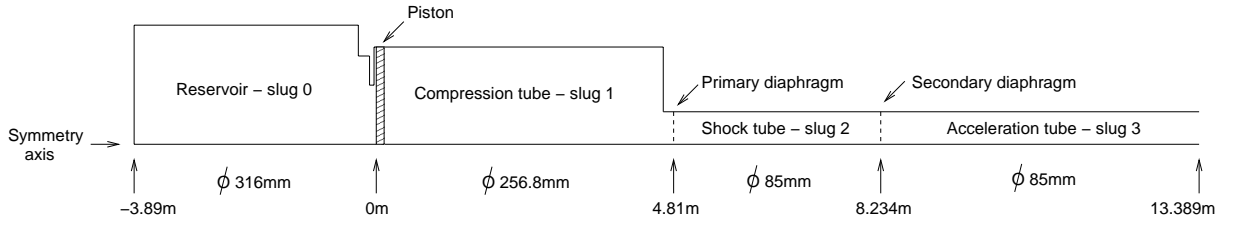


Figure 3.1: Geometry for the L1d simulations including the compression process

head loss factors for sudden area changes as tabulated for internal incompressible viscous flow [90]. The pressure loss is distributed over a finite length on the high-speed side of the contraction or expansion. A somewhat arbitrary viscous loss coefficient of 0.5 was calculated for the piston launching station. Though the contraction diameter ratio gives a value of 0.35 this value was slightly increased due to the geometry of the piston launcher. Extra losses will be encountered as the flow travels through the slots in the launcher. The effects of this are presented later. A value of 0.35 was set for the contraction located just before the primary diaphragm. It was assumed that the piston was 25 kg as it was not fabricated when the initial modelling was undertaken. The friction force on the piston was $F = \mu A_{seal} P_{front}$ where μ is the coefficient of friction on the piston (taken to be 0.4), A_{seal} is the contact area of the chevron seal with the tube wall and P_{front} is the pressure on the front of the piston. A hold time of $10\mu s$ was placed on both the primary and secondary diaphragms from the instant that the rupture pressure was reached until the diaphragm bursts. This was done as even the thinnest of diaphragm materials requires a finite time to rupture and will have sufficient inertia to cause a shock wave to be reflected back upstream.

3.2 One-Dimensional Numerical Simulations

3.2.1 Initial Condition

The initial numerical simulation concentrated on an operating condition that was similar to the old X2 Condition 7 presented in Palmer's thesis [66]. This condition had a secondary shock speed of 9 km/s and the filling properties are shown in Table 3.1. Most of the early one-dimensional work in this thesis was run on a single Intel Xeon 2.0 GHz processor on the Gemini2 machine located at the University of Queensland. The present simulation took 22.5 CPU (Central Processing Unit) hours to complete.

The L1d results indicated that the new configuration would produce higher shock speeds, test times, test gas pressures and temperatures when compared to the old configuration. The values for these variables can be seen in Table 3.2. Despite this table comparing the old configuration experimental results and the new configuration computational results, it still provides an approximate indication of the relevant capabilities of the two arrangements. Later in this chapter, computational models for the old arrangement are presented to ensure that L1d was providing an accurate estimation of the freestream thermodynamic properties. Furthermore, once the expansion tube was operational, the CFD simulations for the new tube were compared to the corresponding experimental values. This is also presented later in the thesis.

The static and Pitot pressure traces at the end of the acceleration tube from the one-dimensional simulations are shown in Figure 3.2. The test pressures for this simulation were taken to be the values immediately following the jumps seen in the plots. The steady increase that appears in the pressure throughout the test period was attributed to the one-dimensional approach of the code. In one-dimension, a pressure gradient is required over time to push the gas down the tube against shear stresses that are acting on the gas at the wall. In reality, boundary layers exist which facilitate in pushing the inviscid core and thus little increase in pressure occurs over the test period in an experiment. As would be expected this increase is not seen in inviscid simulations. In Figure 3.3 the Mach number trace at the end of the acceleration tube is pictured. Here it can be seen that there is no significant change in the property during the steady test time.

With an estimation of the capabilities of the new facility the next step was to examine parameters which could be varied in the machine so that a target condition could be determined.

3.2.2 Optimal Compression Ratio

The old Condition 7 in the modified X2 expansion tube had a compression ratio, assuming isentropic compression, of 41.67. This is derived for an isentropic process, $pv^k = \text{constant}$ and for a driver gas of helium $k = \gamma = 1.667$. From this

$$\text{Pressure ratio} = \frac{P_{Df}}{P_{D*}} = \frac{24 \times 10^6}{48 \times 10^3} = 500 \quad (3.1)$$

3.2. ONE-DIMENSIONAL NUMERICAL SIMULATIONS

Table 3.1: Robert Palmer's Condition 7

Reservoir fill pressure	1.55 MPa
Compression tube fill pressure	48 kPa
Shock tube fill pressure	2.5 kPa
Acceleration tube fill pressure	3.1 Pa
Primary diaphragm burst pressure	24 MPa
Secondary diaphragm burst pressure	45 kPa
Reservoir gas	Air
Driver gas	Helium
Test gas	Air
Acceleration tube gas	Air

Table 3.2: L1d results for the new X2 configuration and experimental results for the old X2 configuration

Condition	Old Configuration	New Configuration
Test gas static pressure, P_5	3.4 kPa	4.0 kPa
Test gas Pitot pressure, P_{p5}	260 kPa	360 kPa
Test gas temperature, T_5	3877 K	5000 K
Test time	$40 \mu\text{s}$	$65 \mu\text{s}$
Primary shock speed, U_1	4.8 km/s	5.5 km/s
Secondary shock speed, U_{10}	9 km/s	12 km/s

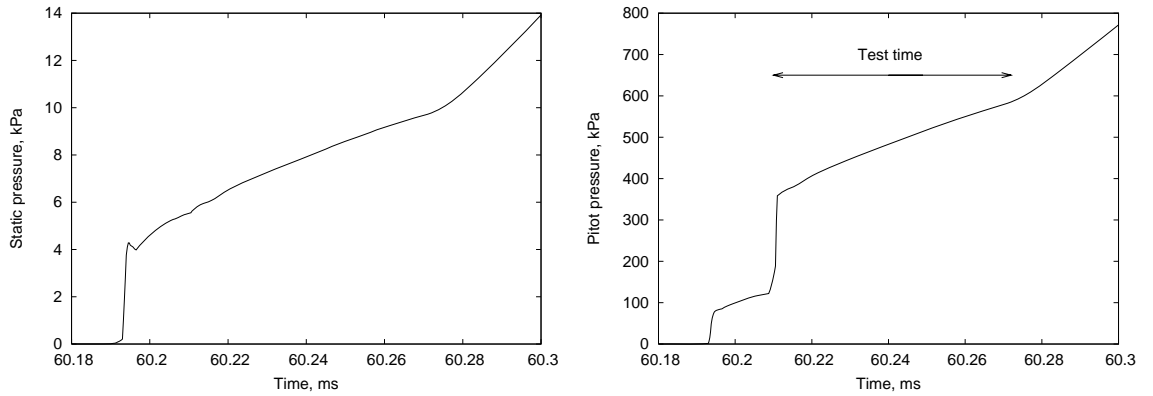


Figure 3.2: Static and Pitot pressure traces from L1d at the end of the acceleration tube for the new X2 configuration

3.2. ONE-DIMENSIONAL NUMERICAL SIMULATIONS

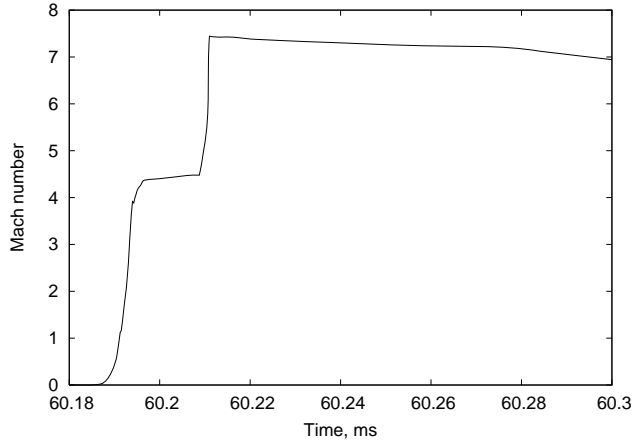


Figure 3.3: Mach number trace from L1d at the end of the acceleration tube for the new X2 configuration

$$\lambda = 500^{\frac{1}{1.667}} = 41.67 \quad (3.2)$$

where P_{Df} is the primary diaphragm burst pressure, P_{D*} is the driver gas fill pressure and λ is the compression ratio.

From the one-dimensional simulation the initial driver gas volume is 0.224 m^3 while the final driver gas volume just before primary diaphragm rupture is $5.285 \times 10^{-3} \text{ m}^3$. This equates to a compression ratio from L1d of 42.4. This is a 2% difference from the isentropic value and suggests that the code is modelling this part of the compression process extremely well. This accuracy was seen consistently throughout the simulations which are discussed here, even those involving different compression ratios.

The new configuration of X2 allows compression ratios up to a value of 60.2. This is a decrease in what could be achieved in the old compound piston configuration. However, the initial volume of driver gas in the old configuration was $7.8 \times 10^{-2} \text{ m}^3$ so the compression ratios for the different arrangements cannot be directly related. To determine the effects of a different compression ratio in the new expansion tube, a series of simulations were run with everything held constant except for the compression ratio and reservoir fill pressure. Table 3.3 shows the values held constant in the simulations. The reservoir fill pressure is coupled with the compression ratio such that it needs to be scaled to ensure the piston is being driven as hard as possible while impacting on the buffer only after it has released the majority of its energy. Initially, the reservoir pressure was scaled with the same ratio as the driver gas fill pressure for each specific case divided by 48 kPa. This

3.2. ONE-DIMENSIONAL NUMERICAL SIMULATIONS

Table 3.3: Initial conditions held constant for the varying compression ratio simulations

Shock tube fill pressure	2.5 kPa
Acceleration tube fill pressure	3.1 Pa
Primary diaphragm burst pressure	24 MPa
Secondary diaphragm burst pressure	45 kPa
Reservoir gas	Air
Driver gas	Helium
Test gas	Air
Acceleration tube gas	Air
Piston mass	25kg

value of 48 kPa is the driver gas fill pressure from the first simulation discussed above. For this series of experiments the piston mass was 25 kg. This number is inconsequential as the simulations are simply examining the effect of changing compression ratio. A range of compression ratios from 30 to 60 were examined.

Illustrated in Figure 3.4 is that both the primary and secondary shock speeds gradually increased with increasing compression ratio. This is consistent with what should occur in theory. A higher compression ratio produces higher driver slug gas temperatures before primary diaphragm rupture. A stronger shock is then produced in the shock tube as governed by the shock tube relations. However, as the compression ratio is increased a smaller final slug length and thus volume of driver gas is yielded. This results in the shock wave not been driven as hard down the full length of the shock tube and lower flow properties are generated at the end of the acceleration tube. These two counteracting effects meant the core flow test time, Pitot pressure, static pressure and density were relatively independent of the compression ratio. At the highest compression ratio, a low reservoir fill pressure, below 1 MPa was required to drive the piston. A compression ratio of 40 was chosen as the starting point for the experiments because little was gained, except a slight increase in shock speed, from the higher compression ratios. It also provides leeway to drive the piston harder if needed. Once the tube was operational a higher compression ratio could be experimentally investigated.

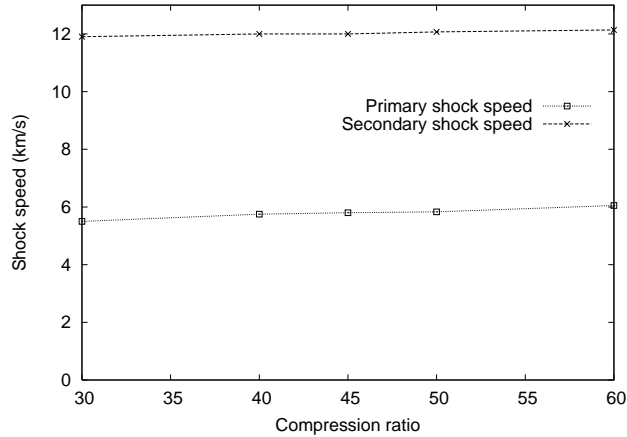


Figure 3.4: Primary and secondary shock speeds for the varying compression ratios

3.2.3 Optimal Piston Mass and Reservoir Fill Pressure

At the time of the undertaking of the one-dimensional numerical study, the piston was the single remaining component of the new driver which was not fabricated. The ideal situation would be to make the piston as heavy as possible and drive it as hard as possible, thus obtaining higher temperatures in the driver gas before primary diaphragm rupture and consequently, a stronger primary shock wave. The choice of piston mass is not that simple, in that the design, similar to the varying compression ratio, must ensure that a soft impact of the piston on the buffer occurs. This requires an appropriate reservoir fill pressure which means that the selection of the piston mass and reservoir fill pressure are coupled.

Three outcomes exist for the choice of the reservoir pressure. If the reservoir pressure is too high, the piston will be driven too hard and will impact on the buffer with a large velocity. This will mean that not all of the energy will have been added to the flow and will cause the excess energy to be absorbed by the buffer. The best instance is when the piston is driven with a pressure so that it hits with zero velocity or as close to zero as possible. Finally, if the reservoir pressure is too low the piston will experience reverse motion then travel forward again and hit the buffer. In this instance the piston could be driven harder initially.

To obtain an optimal piston mass, simulations with varying values were conducted. The variables held constant are shown in Table 3.4. As stated above the piston mass and reservoir fill pressure are coupled. If the reservoir fill pressure is held constant the same

Table 3.4: Initial conditions held constant for the varying piston mass simulations

Shock tube fill pressure	10 kPa
Acceleration tube fill pressure	12.4 Pa
Primary diaphragm burst pressure	24 MPa
Secondary diaphragm burst pressure	45 kPa
Reservoir gas	Air
Driver gas	Helium
Test gas	Air
Acceleration tube gas	Air
Compression ratio	40

amount of energy is available and a heavier piston will merely reach a lower speed while producing the same final driver gas slug conditions. Consequently, the reservoir pressure was varied in each different piston mass simulations until the lowest piston velocity was achieved at buffer impact. The results revealed that the flow conditions experienced minimal effect with changing piston mass and appropriate reservoir fill pressure. The test conditions obtained are shown in Table 3.5. The changes from each simulation were small so the decision was made to continue with the original design of a total piston mass of 35 kg. This value is approximately the same weight as the two combined pistons in the old compound piston driver. It is also light enough for one person to manually handle which allows for ease of operation.

The optimal reservoir fill pressure with a piston mass of 35 kg was 1.56 MPa, just above the initial 1.55 MPa. The resulting piston velocity profile is shown in Figure 3.5. The maximum piston velocity was 89.8 m/s, while the impact velocity was 13.3 m/s. This equates to about 2 percent of the piston’s initial energy being absorbed by the buffer upon impact. This condition was chosen as it produced the lowest impact velocity of all the conditions examined. Further investigation is unwarranted as differences arose in the reservoir fill pressure in the experiments. This is discussed in section 4.3.2.

3.2.4 Fill Pressures for the Shock and Acceleration Tubes

With the compression ratio and piston mass determined, the next modelling focused on increasing the pressure in the shock and acceleration tubes. The aim of this was to

3.2. ONE-DIMENSIONAL NUMERICAL SIMULATIONS

Table 3.5: L1d results with varying piston masses

Piston mass (kg)	Static pressure (kPa)	Pitot pressure (kPa)	Test time (μ s)	Density (kg/m^3)	Primary shock speed (m/s)	Secondary shock speed (m/s)
15	11.8	713	118	9.1	4660	9750
25	12.5	763	108	9.2	4750	9975
27.5	12.2	775	100	9.2	4665	10000
30	12.2	775	117	9.4	4750	10075
50	12.5	744	103	9.0	4730	10000

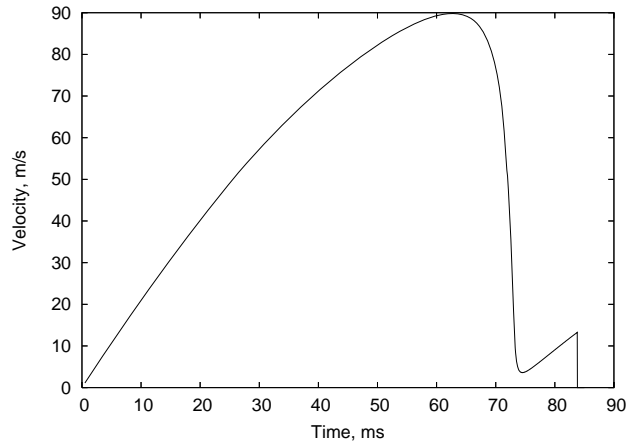


Figure 3.5: Piston velocity from L1d for the final simulation including the compression process

obtain an initial condition with higher test gas densities while achieving similar shock speeds to Palmer’s Condition 7 in the old two-stage driver arrangement. The primary and secondary shock speeds for this were approximately 4.8 km/s and 9 km/s respectively. For the present study, a slightly slower secondary shock speed of 8.5 km/s was targeted.

Initially, both pressures in the shock and acceleration tubes were scaled by a factor of 2 and then 4. It was found that when the pressures were doubled, the shock speeds were 5.3 km/s and 11.2 km/s, which were still too high. Increasing the pressures by a factor of 4 reduced the shock speeds further and the values for the properties can be seen in Table 3.6. To determine how much the effects of varying the fill pressures would change the test properties, a range of conditions were simulated. The results for these tests can be seen in Table 3.7. For these 9 analyses, only downstream of the primary diaphragm was modelled, in order to decrease computational time. Due to the conditions upstream of

3.2. ONE-DIMENSIONAL NUMERICAL SIMULATIONS

Table 3.6: Test gas properties for varying fill pressures in the shock and acceleration tubes for the full simulations

Shock and acceleration tube fill pressures (kPa, Pa)	Static pressure (kPa)	Pitot pressure (kPa)	Test time (μ s)	Density (kg/m^3)	Primary shock speed (m/s)	Secondary shock speed (m/s)
7.5, 25	26.25	1171	50	0.015	4963	9666
7.5, 35	35.83	1400	37	0.02	4973	9365
10.0, 12.4	12.5	762.5	108	0.009	4750	9975
9.6, 43	35.0	1500	60	0.023	4780	8530

the primary diaphragm being identical to the cases discussed at the start of the section, the values from these previous simulations for the pressure, temperature and slug gas length, just before primary diaphragm rupture were used. Full simulations, including the compression process, were made for the cases when the shock tube fill pressure was 7.5 kPa and when the acceleration tube fill pressures were 25 Pa and 35 Pa. When the full simulations were compared to the values in Table 3.7, the only differences observed were that the condensed simulations tended to underestimate shock speeds by at the most 5% and overestimate test times by approximately 10-20%. The shock and acceleration tubes pressures chosen for the initial target condition in X2 were 9.6 kPa and 43 Pa. The full simulation of this configuration produced the results shown in Table 3.6. This condition is discussed further in Section 3.3 and the properties presented here will change in the experiment for reasons which will be discussed.

3.2.5 L1d Verification

As stated previously, the CFD results for the new X2 expansion tube with the single-stage driver were being compared to the experiments for the old configuration which is not technically appropriate. To ensure that the new configuration was giving increased performance L1d simulations of the old configuration were run. Due to the complexities of the two-stage piston arrangement, only downstream of the primary diaphragm was examined. The geometry is shown in Figure 3.6. Due to the fact that the compression process was not modelled the properties for the slug of gas before the shock tube were

3.2. ONE-DIMENSIONAL NUMERICAL SIMULATIONS

Table 3.7: Test gas properties for varying fill pressures in the shock and acceleration tubes without the modelling of the compression process

Shock and acceleration tube fill pressures (kPa, Pa)	Static pressure (kPa)	Pitot pressure (kPa)	Test time (μ s)	Density (kg/m ³)	Primary shock speed (m/s)	Secondary shock speed (m/s)
2.5, 15	17.62	857.1	58.3	0.01	5666	10483
2.5, 25	26.11	1144.4	40	0.015	5664	9976
2.5, 35	34.38	1375	25.5	0.019	5666	9598
5.0, 15	17.92	842.9	64.7	0.01	5185	10169
5.0, 25	27.08	1157.1	58.8	0.015	5186	9668
5.0, 35	35.0	1385.7	42.8	0.02	5182	9293
7.5, 15	17.08	800	65.5	0.01	4875	9905
7.5, 25	26.25	1100	55.9	0.015	4865	9386
7.5, 35	33.3	1300	50	0.019	4877	9142

required explicitly. The temperature and pressure were assumed to be uniform in the slug. The pressure was set to equal the diaphragm burst pressure, the length of the slug was obtained from experimental tests and the bulk temperature method [64] was used to obtain the driver gas temperature. For the bulk temperature method the compression process is assumed to be polytropic and is expressed by equation 3.3.

$$\frac{P_{Df}}{P_{D*}} = \lambda^n \quad (3.3)$$

Here P_{Df} was the peak pressure which was equal to the burst pressure, P_{D*} was the initial driver fill pressure and λ was the compression ratio. Assuming a perfect gas, the equation of state was $P = \rho RT$ and equation 3.3 became

$$\frac{T_{Df}}{T_{D*}} = \lambda^{n-1} \quad (3.4)$$

Therefore the slug of gas was set at a pressure of 24 MPa and a temperature of 2300K. The simulation produced similar results to the experiments conducted by Palmer [66] for the static pressure and shock speeds. This is shown in Table 3.8. One discrepancy discerned between the equilibrium viscous simulation and the experiments was that the Pitot pressure and temperature were significantly different. This was attributed to the one-dimensional approach of the code. Modelling issues in L1d are discussed later and

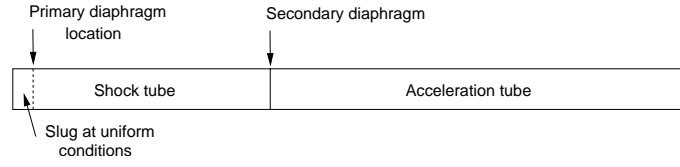

Figure 3.6: Geometry for the L1d simulations of the old X2 configuration

Table 3.8: L1d and experimental results for the old X2 configuration

	Equilibrium, inviscid	Equilibrium, viscous	Experiments
Test gas static pressure, p_5	4.2 kPa	3.4 kPa	3.4 kPa
Test gas Pitot pressure, p_{p5}	344 kPa	160 kPa	260 kPa
Test gas temperature, T_5	3667 K	4545 K	3110 or 3877 K
Test time	62 μ s	40 μ s	40 μ s
Primary shock speed, U_1	4858 km/s	4685 km/s	4800 km/s
Secondary shock speed, U_{10}	11003 km/s	9146 km/s	9000 km/s

it will be shown that it estimates static pressure and shock speeds reasonably well while producing errors in temperature and Pitot pressure. A more in-depth comparison could not be provided due to the lack of availability of more experimental data in the old arrangement. The reasonable agreement between the experiments and CFD for the old configuration suggest that, at worst, the old configuration static pressure was roughly 3.4 kPa and the shock speeds are roughly 4.7-4.8 km/s and 9.0-9.1 km/s. Comparing the two numerical models shows a marked increase in these properties. It is noted that the one-dimensional CFD does not provide perfect estimates but there is still sufficient evidence to assume the new arrangement would give increased performance. The experiments in Chapter 4 will definitively show and support this statement.

3.3 Examination of the Air Condition

This section presents the results from the final full simulation of the target condition in the new X2 configuration. The initial conditions are illustrated in Table 3.9. It took 23.7 Central Processing Unit (CPU) hours to run on a single processor of the Blackhole Linux cluster located at the University of Queensland. This machine is comprised of 93 dual processor AMD Opteron (2.2 and 2.4 GHz) nodes.

Table 3.9: Initial conditions for the one-dimensional simulation of the target condition

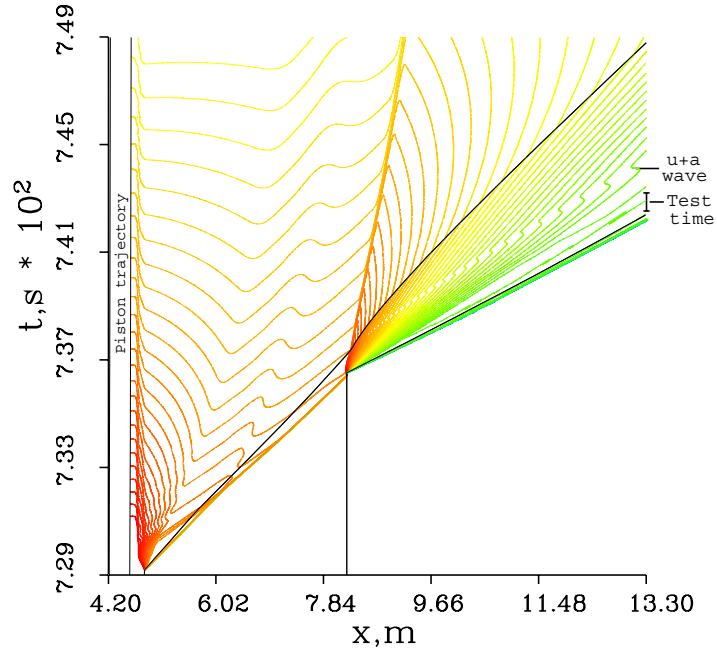
Reservoir fill pressure	1.56 MPa
Compression tube fill pressure	48 kPa
Shock tube fill pressure	9.6 kPa
Acceleration tube fill pressure	43 Pa
Primary diaphragm burst pressure	24 MPa
Secondary diaphragm burst pressure	Approx. 12 kPa
Reservoir gas	Air
Driver gas	Helium
Test gas	Air
Acceleration tube gas	Air
Compression ratio	40
Piston mass	35 kg

The set up file in L1d is referred to as an “Lp” file and the relevant one for this simulation is given in Appendix A. The computational domain was comprised of 300 cells in the reservoir gas, 550 cells in the driver gas, 1500 in the test gas and 600 cells in the acceleration gas. The cells in the grid were clustered towards the diaphragm in the shock and acceleration tubes. This meant the test gas was clustered at both ends and the acceleration gas was clustered towards the secondary diaphragm. An adaptive grid was used in the acceleration tube gas to prevent “crushed” cells from decreasing the time step and stalling the calculation. If a cell become too small it was merged with its neighbouring cell and if a cell become too large it was split into a number of cells.

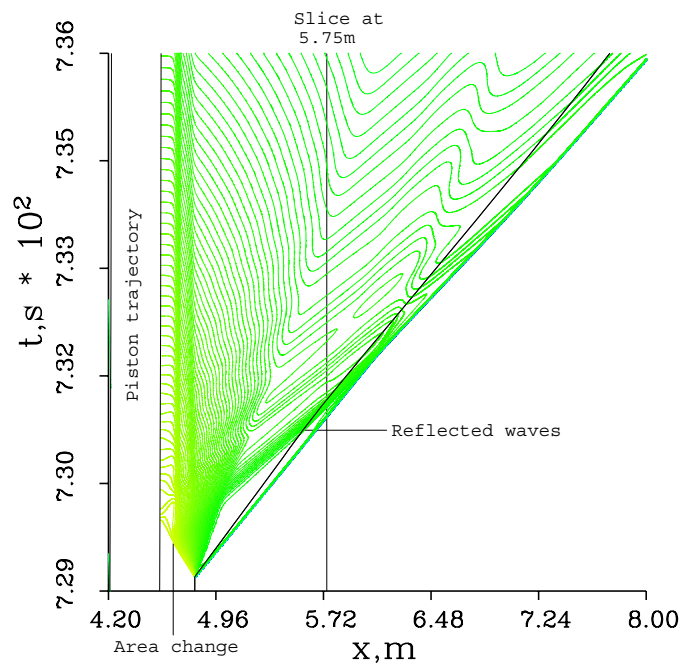
Figure 3.7 is comprised of two x-t diagrams showing contours of the log of pressure. The solid black lines indicate the interfaces between the slugs of gas. The starting reference time is the commencement of the simulation which is upon piston release. The distances along the tube match those from Figure 3.1.

The effect of the new driver configuration on the primary shock wave can be seen in Figure 3.7(a). When the primary diaphragm ruptures, disturbances created by the metal bursting travel back upstream. When these waves reach the area change they effectively see a larger amount of gas and are partially reflected downstream. These waves catch up to the primary shock at approximately 5.5m along the tube. Taking a slice throughout time at a distance of 5.75m along the tube, the effect of the reflected waves can be seen.

3.3. EXAMINATION OF THE AIR CONDITION



(a) Over the entire tube



(b) Zoomed into the shock tube region

Figure 3.7: An x-t diagram from L1d for the air condition

Looking at Figure 3.8, a large compression immediately follows the shock wave. This is labelled 1 and is caused by the waves reflected off the area change. The initial jump in shock tube pressure caused by the shock wave is fractionally above 2 MPa, which is close to the 2.2 MPa predicted by the shock tube relations for flow of a calorically perfect gas in a shock tube. There is also a slight jump in pressure labelled 2 in Figure 3.8. This jump in pressure is also caused by more waves reflecting as they hit the area change. Typically in an expansion tube with no area ratio at the primary diaphragm, the upstream edge or head of the unsteady expansion reflects off the front surface of the piston. The u+a wave that is formed catches up to and attenuates the primary shock. However, because of the large area change this does not occur and instead there is an increase in pressure brought about by the large volume of driver gas pushing the shock tube gas harder. This benefits the flow by increasing the shock speed. This feature is due to the design of the facility and will occur at all conditions. The pressures in the second half of the shock tube that drive the shock wave remain at a level similar to that given by the normal shock relations and do not contain the large jump in pressure after the shock wave passes. This can be seen in Figure 3.9. The locations st1, st2 and st3 correspond to the pressure transducers in the actual tunnel and are at a distance of 7.382 m, 7.614 m and 7.845 m respectively. Whenever mentioned in this thesis, these locations refer to these positions. If an insufficient driver length was present to push the shock wave down the tube there would be a decrease in the static pressure levels as one moved down the shock tube. However a constant level of about 2.4 MPa and no reduction in the amount of steady pressure is shown in Figure 3.9. The large area ratio, as discussed above, facilitates in producing this behaviour.

The shock tube static pressure traces from L1d along the tube with a comparison to experiments and inviscid simulations are plotted in Figure 3.10. Three experimental shots were selected to demonstrate repeatability. The shock tube pressures from all the experiments consistently provided excellent agreement from shot to shot. It would be superfluous to put more shots in this plot and would make the figure indecipherable. The inviscid simulation pressure is higher than the viscous simulation as expected. Comparing the viscous one-dimensional simulation to the experiments shows that the initial jump in the shock wave pressure is off by approximately 20%. The viscous L1d level is approximately 2.4 MPa compared to 2 MPa for the experiments. Furthermore the shock

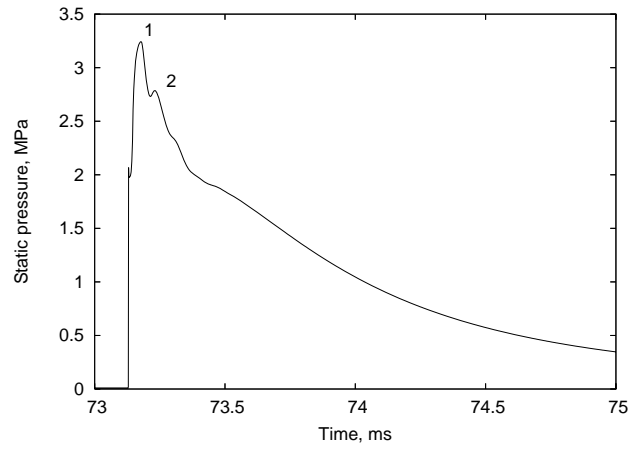


Figure 3.8: Static pressure from L1d at 5.75 m along the tube

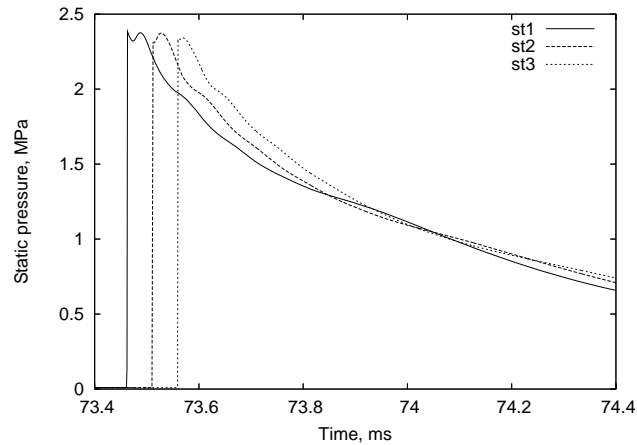
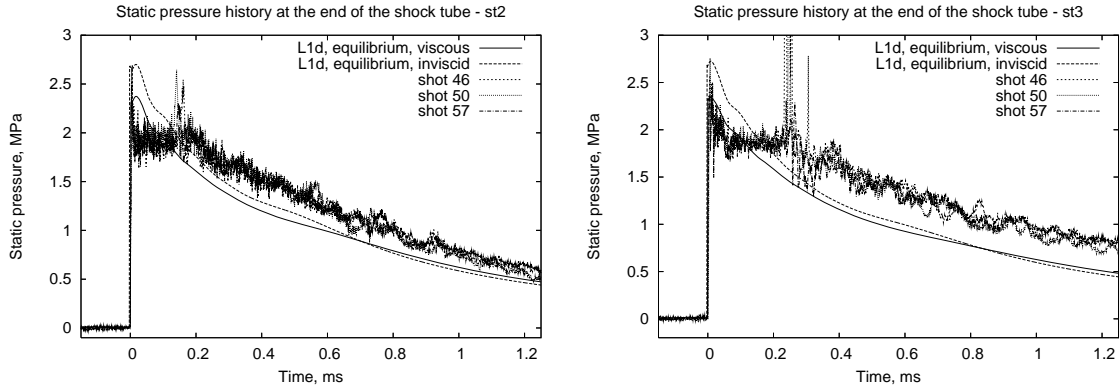


Figure 3.9: Static pressure from L1d towards the end of the shock tube

speeds from the experiments were 4.46 km/s compared to 4.78 km/s from the simulation. This is an error of 6.5% and represents a large amount of extra energy in the numerical results. The decay rates in the static pressure are fairly similar from the two methods which would suggest that the length of the slug of driver gas before primary diaphragm rupture is close to correct in the simulation. The only other two variables which influence the shock tube static pressure levels are pressure and temperature of the slug of driver gas preceding primary diaphragm rupture. The pressure is set by the thickness of the metal diaphragm which in this case is 1.6mm cold rolled steel. The corresponding burst pressure for a diameter of 85 mm is 24 MPa. This would then imply that the temperature of the slug of gas before rupture in the numerical simulations is too high. To overcome this problem modified simulations were performed and are discussed in the next section (Section 3.4).



(a) At a distance of 7.614 m along the tube (b) At a distance of 7.845 m along the tube

Figure 3.10: Comparison of experimental and numerical static pressure traces in the shock tube

At the downstream end of the facility, towards the exit of the acceleration tube, a slight attenuation of the secondary shock wave can be seen in Figure 3.7. The test time is ended by the arrival of the unsteady expansion which propagates when the secondary diaphragm bursts. The u+a wave from the driver-test gas interface comes through at a later time around 0.744 ms.

The test flow conditions at the end of the acceleration tube for this simulation which were given in Table 3.6 are plotted in Figure 3.11. In addition to a fully viscous one-dimensional model, a fully inviscid one-dimensional model was created. The comparison between the inviscid and viscous simulations is shown in these graphs. The graphs have been shifted in time so that the shock arrives at 0 ms in both simulations. The inviscid shock speeds were 5.15 km/s for the primary shock wave and 10.44 km/s for the secondary shock wave. This compared to the viscous shock speeds of 4.78 km/s and 8.53 km/s. As the inviscid simulation has no wall shear stresses, there are no velocity gradients in the expanded test gas. This results in higher pressure flow properties. Some thermodynamic properties such as Pitot pressure are different by more than 50% and even static pressure and the shock speeds are significantly different. In expansion tubes, the viscous effects are too important to ignore in the acceleration tube and there is little point conducting inviscid simulations of any kind to predict the core flow properties. In Section 3.4.1, an inviscid simulation in the modified one-dimensional simulation of the first air condition presented below will be shown to further support this argument and then no inviscid simulations will be dealt with again in this thesis.

3.3. EXAMINATION OF THE AIR CONDITION

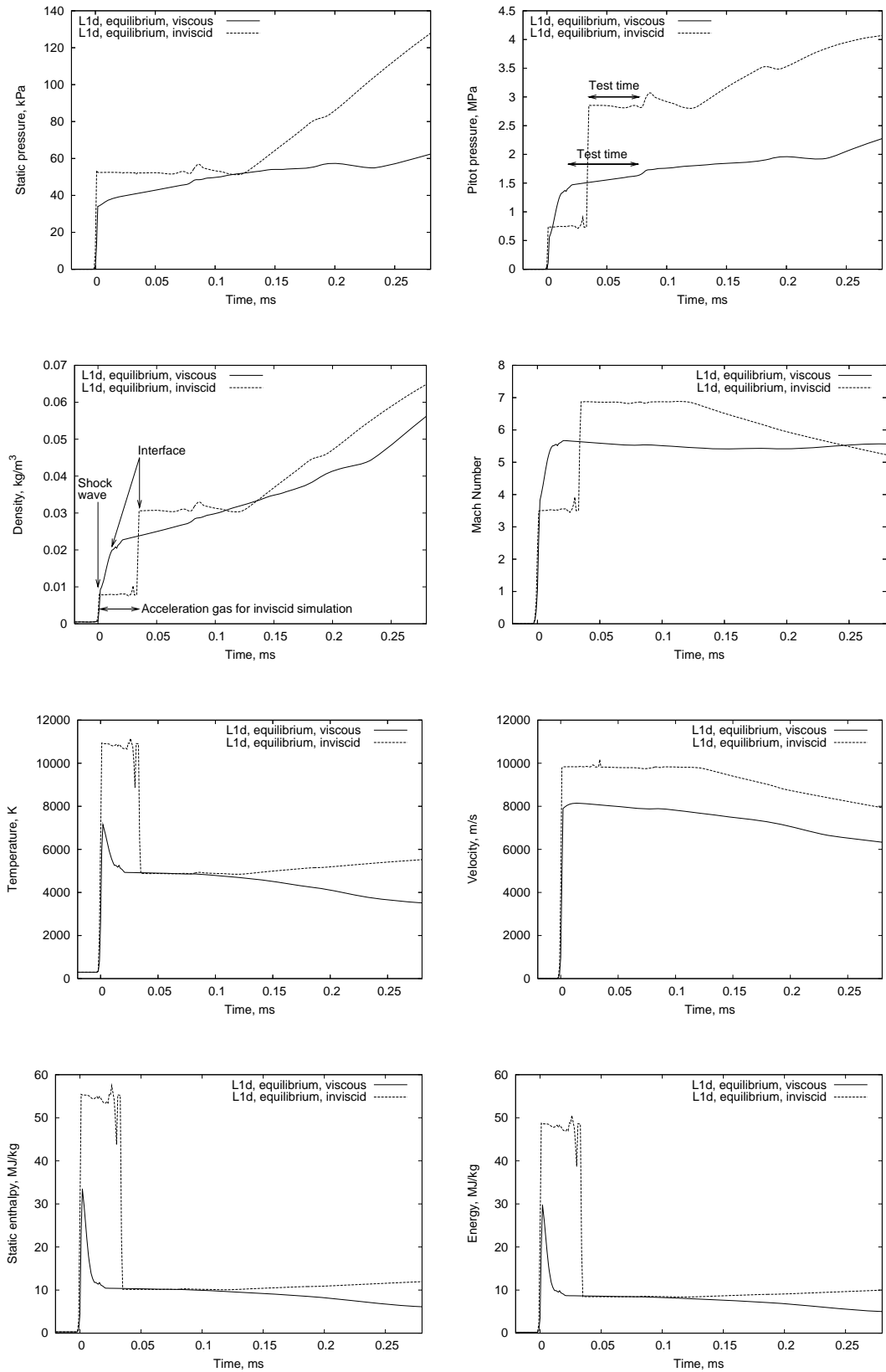


Figure 3.11: Properties from L1d at the end of the acceleration tube for the simulation including the compression process

3.4 Final Modified One-Dimensional Simulations

As described before, the one-dimensional simulation including the compression process estimated a temperature in the slug of driver gas just before primary diaphragm rupture that was too high. The temperature in the section of the tube near the primary diaphragm from that simulation is shown in Figure 3.12. The driver gas in this simulation is comprised of 100% helium and reaches approximately 3500 K. This is close to the value of 3560 K calculated when an isentropic compression process is assumed. However, the isentropic temperature would also be an overestimate as it does not include heat losses in the tube.

Doolan [64] and Stewart [16] both performed previous studies on X2 using L1d to simulate the flow. However they both modelled the facility with the two-stage piston process. In each of the studies they saw the same problem as above with a higher temperature in L1d than the experiments. However, they saw the L1d value to be a fair margin below the isentropic value but still significantly above the experiments. Doolan states, “It can be seen that the numerical solutions qualitatively capture the one-dimensional transient gas dynamics quite well ... However, the simulations significantly under-predict the amount of heat transfer which occurs during the compression process”. A number of modes of heat transfer which could not be modelled by the code were blamed for the discrepancies. Each was related to the transitional area change in the two-stage piston driver. Stewart attempted to rectify the problem by incorporating extra heat losses at the transition but still saw a significant overprediction in the driver gas temperature. The pressure provided good agreement though it was slightly underestimated, while the length of the slug of driver gas was slightly different. Despite the reasons for the varying slug lengths being discussed no answer was provided for the remaining inconsistent temperatures.

There could be a number of reasons why the temperatures are different in the slug of driver gas between the experiments and the one-dimensional simulations. The heat losses in L1d may not be accurately modelled. The heat transfer coefficient is calculated via the equation $h = \rho C_P |u| St$, assuming that the flow in each cell is part of a fully-developed pipe flow. Here the Stanton number (St) is calculated via empirical relations for turbulent flow in a pipe as given by Holman [91]. The resulting expression, termed the modified Reynolds analogy is, $St = \frac{f}{8} Pr^{2/3}$. These formulas are derived with the inclusion of a number of assumptions. They include that the Prandtl number is 1 and that it is a steady

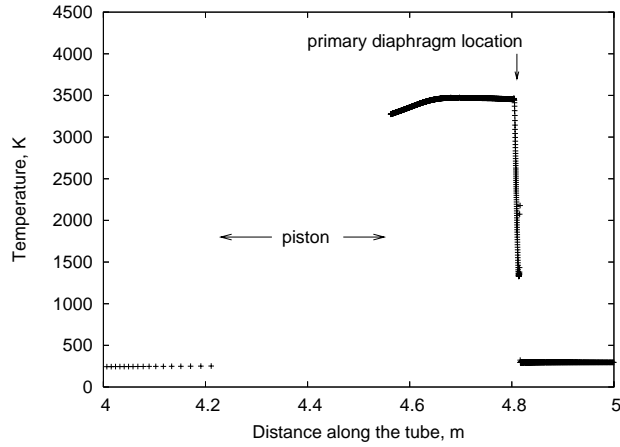


Figure 3.12: Temperature of the slug of gas just before primary diaphragm rupture

incompressible flow. A compressibility correction can be used as proposed by Goddard. The modelling of the compression process of an expansion tube is not in this flow regime as there are large temperature differences. In addition the one-dimensional nature of L1d may pose a problem. To accurately capture the heat transfer, the boundary layer needs to be resolved to provide the property variation adjacent to the wall. This is not possible in L1d. Furthermore, as only one cell is present across the tube, any property in the cell is an average in the radial direction of the entire tube. Thus the large difference between the boundary layer properties and the core flow can increase the values and produce an overestimate of the core flow property. This is supported by the fact that properties such as Pitot pressure and temperature are incorrectly estimated but the static pressure is accurately predicted.

The only known quantities which can be used to estimate the driver gas slug temperature are the shock tube static pressures measured from the experiments. To match the computational and experimental static pressures, the temperature in the driver slug before primary diaphragm rupture was adjusted in L1d and the simulation continued from that point. The geometry that was utilized is shown in Figure 3.13. The pressure in the slug of driver gas was 24 MPa while the length of the slug of driver gas was slightly decreased. It is important that the pressure at the end of the shock tube is similar in the L1d simulation and the experiments as this is what drives the gas down the acceleration tube. The rest of this section presents the final L1d simulations with matched shock tube pressures for each condition that was targeted in this project.

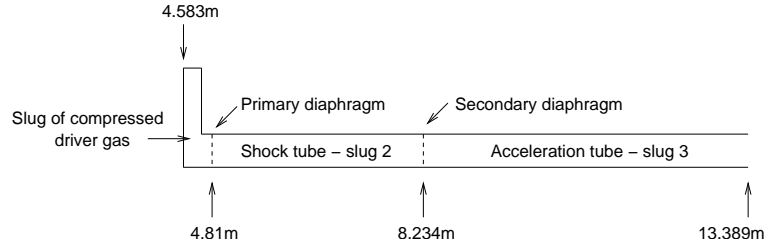


Figure 3.13: Geometry for the final modified one-dimensional simulations

3.4.1 Air Condition 1

The air condition that has been discussed in this chapter will now be referred to as Air Condition 1. The adjusted temperature for the slug of gas was set to equal 2900 K. The start of the slug of driver gas was changed from 4.5655m in the simulation with the compression process to 4.583m as shown in Figure 3.13. This reduced the length of the slug of driver gas. The reason this was done was because both Doolan and Stewart saw an overestimate in the slug length from L1d when compared to experiments. A future project in X2 may be to measure the temperature and length of driver gas in the new configuration to verify the values used here.

The static pressure in the shock tube from the final simulation for Air Condition 1 with the corrected temperature and slug length is graphed in Figure 3.14. Here the jumps in pressure caused by the shock wave in the numerical model and the three shots lie close as they have been matched. After the initial jump in pressure the experimental value remains steady for about 0.2ms before it starts to drop away. This is beneficial as this steady pressure assists in driving the shock wave down the tube. However, the numerical value does not show this and drops away immediately. This may suggest that decreasing the slug length was incorrect and it should, in fact, have been increased. Simulations were performed where the slug length was kept the same as the model with the compression process and some were performed where this length was made longer. Simulations were even performed where instead of a wall being placed on the upstream end of the slug of driver gas, a piston with the same velocity as the model with the compression process was implemented. None of these resulted in a constant level in the static pressure after the shock wave and merely slightly decreased the decay rate and slightly increased the primary shock speed. This constant level was also not seen in the model with the compression process. It was assumed the one-dimensional nature of L1d was unable to capture this.

3.4. FINAL MODIFIED ONE-DIMENSIONAL SIMULATIONS

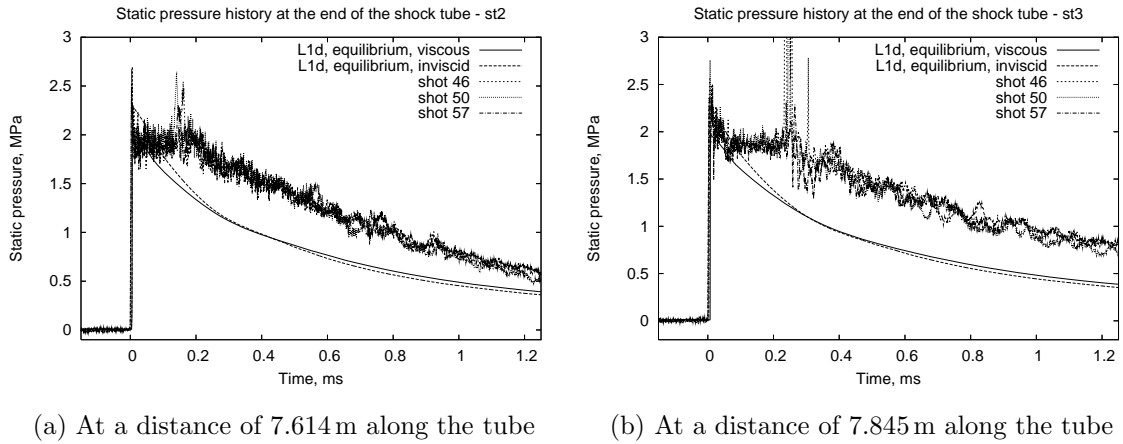


Figure 3.14: Comparison of experimental and numerical static pressure traces in the shock tube for Air Condition 1

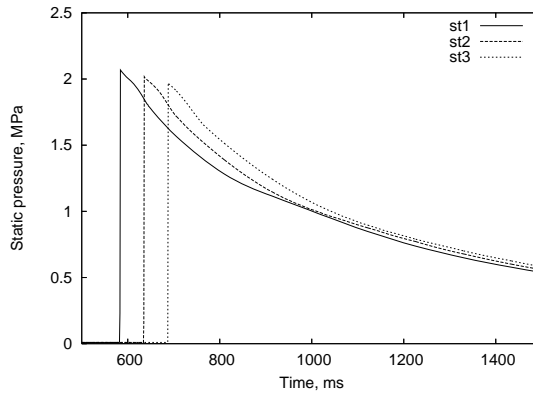


Figure 3.15: Static pressure from L1d towards the end of the shock tube for Air Condition 1

The primary shock speed from the modified simulation was 4.46 km/s which was the same as the experimental value. The static pressure from L1d at the end of the shock tube is shown in Figure 3.15. As in Section 3.3 the new configuration provides a sufficient driver length so that there is no drop in the static pressure jump as the shock moves down the tube.

The results for the core flow properties are shown in Table 3.10 and Figures 3.16. All these properties except for the primary shock speed are taken at the exit to the acceleration tube. These values will be compared to the experiments and axisymmetric simulation in the next chapter. Comparing these graphs to the ones from the simulation with the compression process illustrates that the properties have slightly decreased. Examining the static pressure shows the value has reduced about 6 kPa to 28.5 kPa. This is because the

Table 3.10: Summary of the L1d flow properties for Air Condition 1

Property	L1d viscous	L1d inviscid
Primary shock speed, km/s	4.46	4.76
Secondary shock speed, km/s	7.90	9.65
Static pressure, kPa	28.5	43.0
Pitot pressure, MPa	1.05	2.4
Density, g/m ³	21.5	31.0
Mach number	5.4	7.0
Static temperature, K	4500	4000
Velocity, m/s	7100	9000
Static enthalpy, MJ/kg	9.0	7.9
Total enthalpy, MJ/kg	34.2	48.4
Specific internal energy, MJ/kg	7.5	6.7
Unit Reynolds number, m ⁻¹	1.64×10^6	3.18×10^6
Test time, μ s	43	70

temperature and slug length of the driver gas have been reduced and thus the shock is not as strong. The secondary shock speed came down to 7.9 km/s from 8.53 km/s. This is a bit lower than the 8.5 km/s target speed. Subsequently, another air condition is discussed later which has a shock speed closer to 8.5 km/s. As stated previously, the inviscid simulation produces results that have a large deviation from the viscous simulation. This indicates that inviscid simulations do not accurately model the flow.

Paull and Stalker [56] determined that a speed of sound buffer was required between the expanded driver gas and the shock processed test gas to prevent waves initiated in the driver gas propagating downstream and disturbing the test time. A ratio of $a_3/a_2 < 0.8$ was stated as required to achieve this. For all the conditions in this thesis, the existence of this speed of sound buffer was ensured.

3.4.2 Air Condition 2

Air Condition 2 had exactly the same initial properties as Air Condition 1 except for an acceleration tube fill pressure of 26 Pa instead of 43 Pa. Because tube operation up until the secondary diaphragm was the same, no investigation into the shock tube traces is presented here. The core flow properties are shown in Table 3.11 and Figure 3.17. The

3.4. FINAL MODIFIED ONE-DIMENSIONAL SIMULATIONS

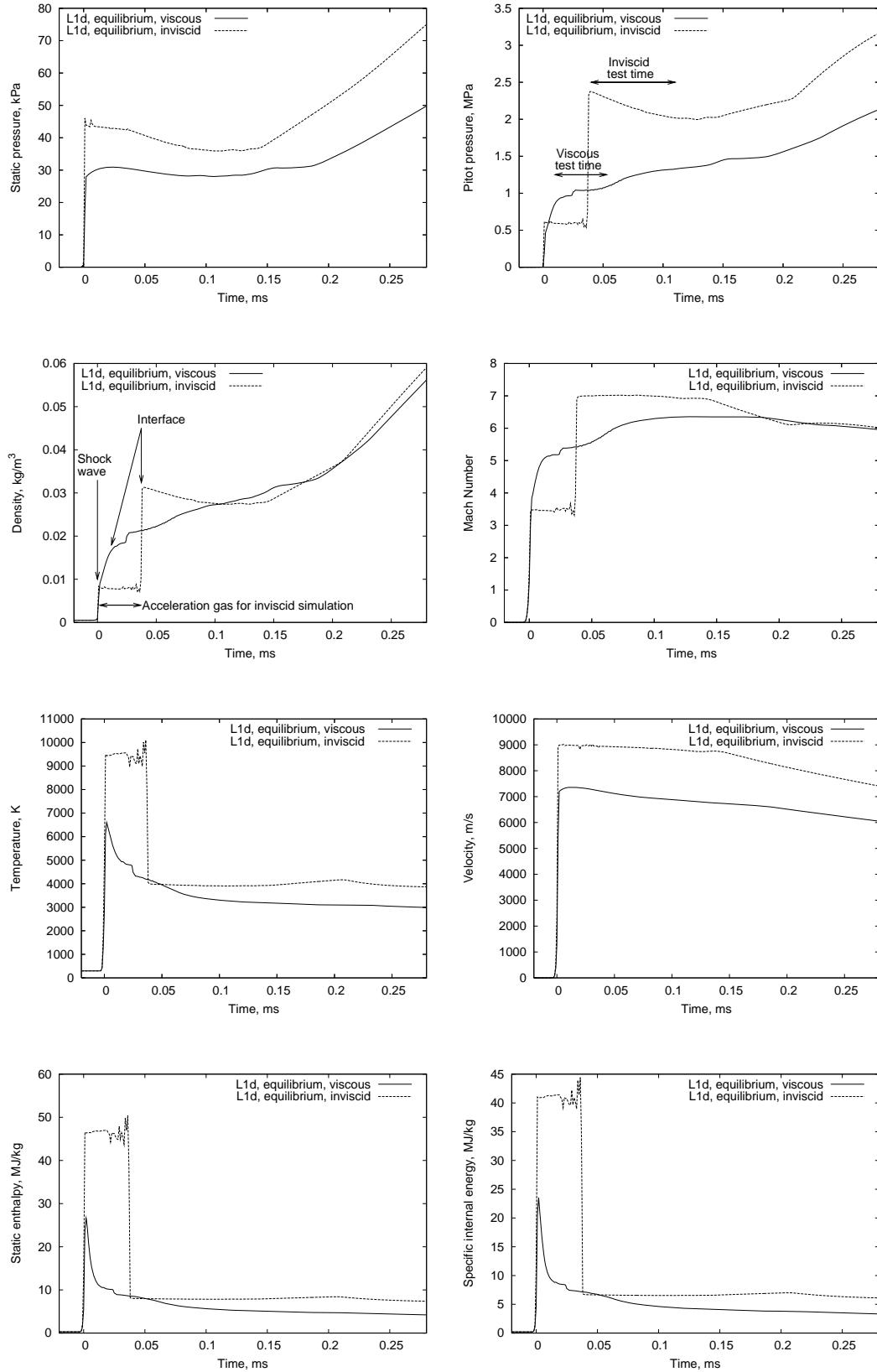


Figure 3.16: Properties from L1d at the end of the acceleration tube for Air Condition 1

Table 3.11: Summary of the L1d flow properties for Air Condition 2

Property	L1d viscous
Primary shock speed, km/s	4.46
Secondary shock speed, km/s	8.31
Static pressure, kPa	21.0
Pitot pressure, kPa	850
Density, g/m ³	14.0
Mach number	5.6
Static temperature, K	4600
Velocity, m/s	7700
Static enthalpy, MJ/kg	9.6
Total enthalpy, MJ/kg	39.2
Specific internal energy, MJ/kg	8.0
Unit Reynolds number, m ⁻¹	1.14×10^6
Test time, μ s	50

secondary shock speed in L1d increased to 8.31 km/s (from 7.90 km/s for Air Condition 1).

3.4.3 Titan Condition

A condition which would be capable of simulating the entry of an aeroshell to Titan, the largest moon of Saturn, was created. Currently there is interest in this with the Cassini-Huygens mission [92, 93]. This spacecraft was launched on October 15th 1997 and reached Saturn on July 1st 2004. It is a joint project between NASA which produced Cassini and the European Space Agency (ESA) which produced Huygens. Saturn was chosen as the destination of this mission because of its rings and many moons. Its biggest moon, Titan, which is the second largest moon in the solar system, is one of only a few with its own atmosphere. It is thought that the atmosphere is similar to what Earth would have been like nearly 4 billion years ago, before life existed here. The aim of Cassini is to examine the planet of Saturn and try to deduced what it was like during its formation and evolution. It also aims to resolve many mysteries relating to its rings and moons. The Huygens probe which landed on Titan on January 14th 2005 aims to discover how the moon and atmosphere were developed. The Huygens probe had a velocity

3.4. FINAL MODIFIED ONE-DIMENSIONAL SIMULATIONS

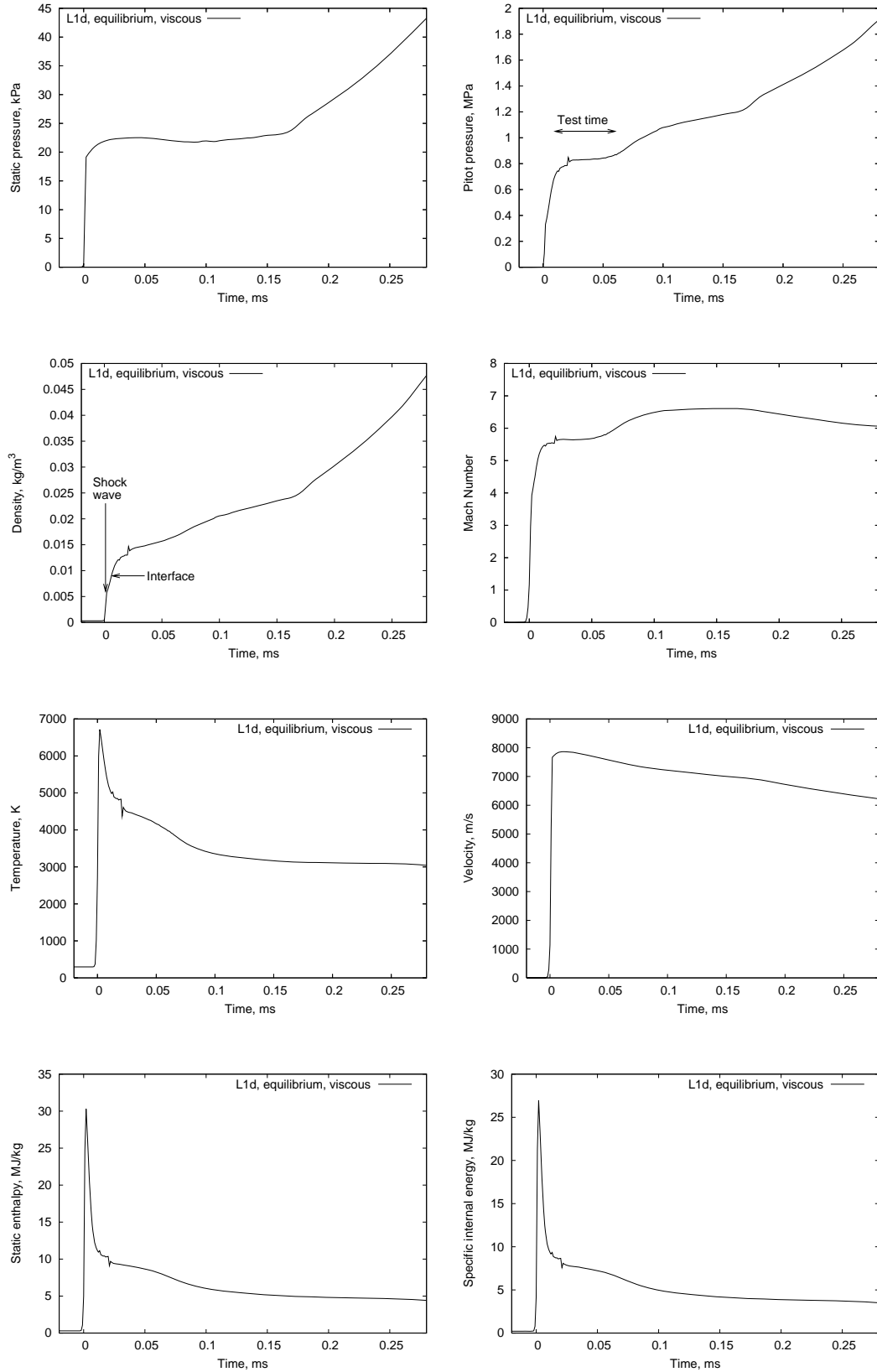


Figure 3.17: Properties from L1d at the end of the acceleration tube for Air Condition 2

of 6 km/s upon entry into Titan's atmosphere and this was decreased to 400 m/s at an altitude of approximately 160 km. The composition of Titan's atmosphere is thought to be 95 % nitrogen plus 5 % methane by volume with small traces of other elements.

In the X2 expansion tube, for the Titan condition, the driver gas was comprised of 57 % helium and 43 % argon by volume at 48 kPa. The shock tube was filled with Titan gas at 3.0 kPa, while the acceleration gas was air at 26 Pa. The addition of argon into the driver gas would alter both the temperature and length of the slug of driver gas before rupture of the primary diaphragm. Similar to the air condition, a simulation was run including the compression process to get an approximation for the slug length and temperature. These values were then altered to match the shock tube pressures. For the final simulation, the start of the slug of gas was set to 4.58 m and the temperature was set to 3300 K. (Refer to Figure 3.13 for the generic geometry arrangement)

The shock tube traces are shown in Figures 3.18 and 3.19. The pressure traces from the CFD do not perfectly match the experiments. The initial jumps caused by the shock wave are equivalent but following this compression waves are evident which are not the same in the numerical and experimental results. The source of the waves can be seen in the x-t diagram in Figure 3.20. As in the air condition, waves are reflected at the area change as they see a larger volume of gas and are pushed downstream. Due to the lower speed of the Titan condition, the reflected waves come through at a much later time and influence the static pressure at the end of the shock tube instead of the beginning. The reason for the discrepancy is again caused by the one-dimensional nature of L1d. This produces a computational primary shock speed which is 5 % lower than the experiments.

The freestream conditions at the end of the acceleration tube are given in Table 3.12 and Figure 3.21. An unrealistically long slug of acceleration gas can be seen in the plots. The reason for this is that the air in the acceleration tube is assumed to be a calorically perfect non-reacting gas. This also results in extremely high temperatures above 14000 K. In the air condition, the acceleration gas was assumed to be an equilibrium chemically reacting gas. The gas model used in this thesis only allows one gas to be in equilibrium while the others must be perfect gases. For this condition, the equilibrium chemically reacting gas was the Titan test gas. The code has since been updated to allow more than one gas in equilibrium.

3.4. FINAL MODIFIED ONE-DIMENSIONAL SIMULATIONS

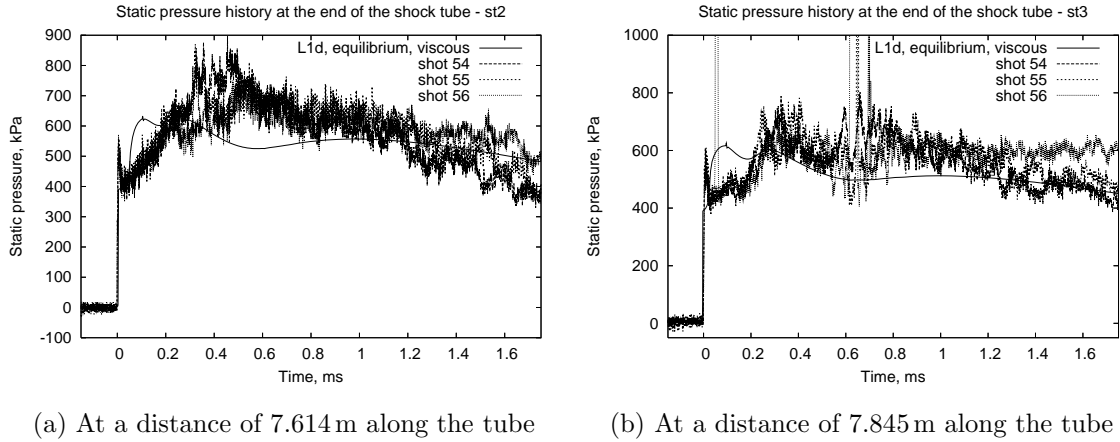


Figure 3.18: Comparison of experimental and numerical static pressure traces in the shock tube for the Titan condition

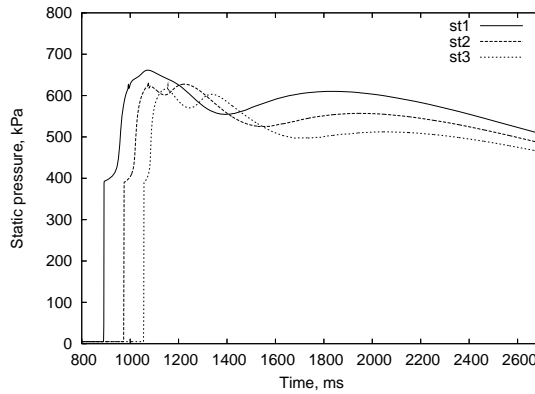


Figure 3.19: Static pressure from L1d towards the end of the shock tube for the Titan condition

3.4.4 Jupiter Condition

There have been previous examinations at the University of Queensland into entry of the Jovian atmosphere [94]. The gas giants at the outer edge of our solar system pose many interesting questions already mentioned with regards to missions to Saturn and Titan. The Galileo mission, which travelled to Jupiter [95, 96], was launched on the 18th October 1989 and ended on the 21st September 2003. Jupiter’s atmosphere is made up of 86 % hydrogen and 14 % helium by volume and the entry speed into the atmosphere for the Galileo spacecraft was 47.4 km/s [97]. As current ground based test facilities cannot reach these speeds, the previous expansion tube experiments substituted helium with neon for the test gas. This provided similarity between the physical processes in the experiments and what was experienced in real life. The same composition was used for the Jovian test

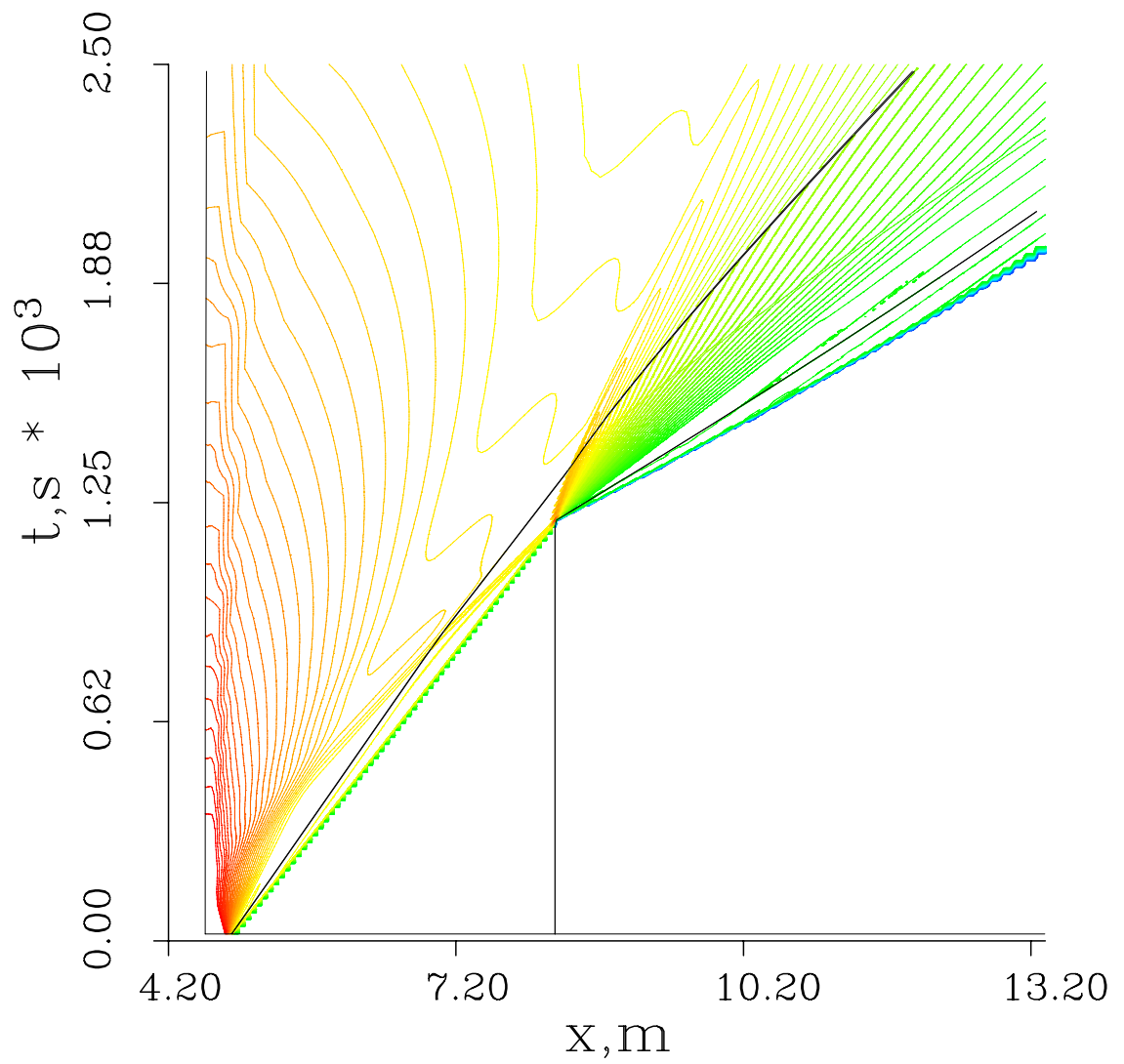


Figure 3.20: An x-t diagram from L1d for the Titan condition

3.4. FINAL MODIFIED ONE-DIMENSIONAL SIMULATIONS

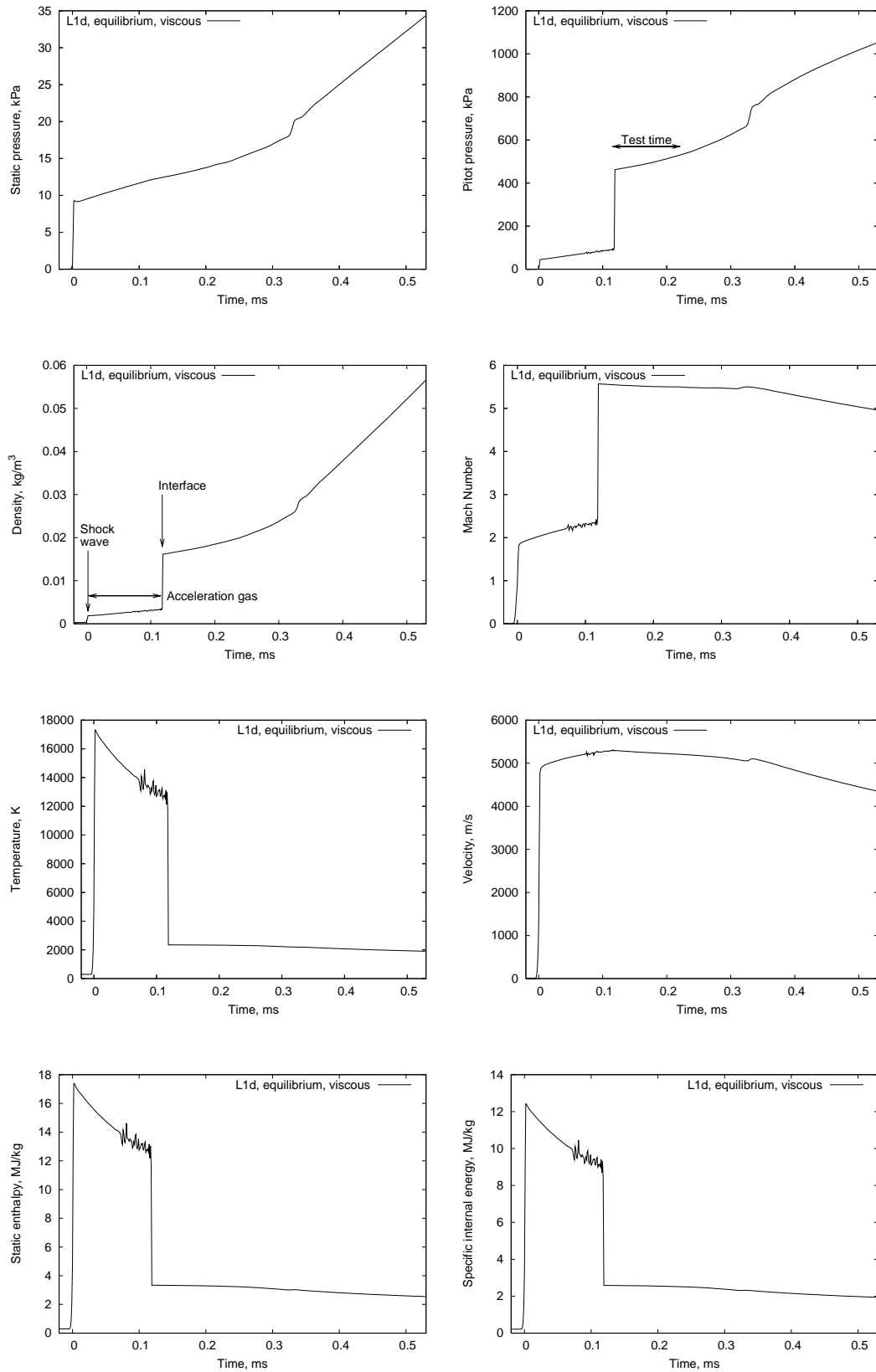


Figure 3.21: Properties from L1d at the end of the acceleration tube for the Titan condition

3.4. FINAL MODIFIED ONE-DIMENSIONAL SIMULATIONS

Table 3.12: Summary of the L1d flow properties for the Titan condition

Property	L1d viscous
Primary shock speed, km/s	2.81
Secondary shock speed, km/s	5.71
Static pressure, kPa	9.2
Pitot pressure, kPa	465
Density, g/m ³	16.1
Mach number	5.6
Static temperature, K	2300
Velocity, m/s	5200
Static enthalpy, MJ/kg	3.32
Total enthalpy, MJ/kg	16.84
Specific internal energy, MJ/kg	2.57
Unit Reynolds number, m ⁻¹	1.1×10^6
Test time, μ s	100

gas in this thesis. The gas was comprised of 15 % hydrogen and 85 % neon by mass.

The initial fill properties for the Jovian condition were a driver gas of 100% helium at 48kPa, Jovian test gas at 3.0 kPa and air in the acceleration tube at 10 Pa. For the L1d simulation the same conditions as in the air case were used for the slug of driver gas before primary diaphragm rupture. Difficulties were encountered in the computational code with the Jupiter condition due to the extremely severe expansion arising from the rupture of the secondary diaphragm. A hold time model is implemented on the diaphragm rupture in the computational model to produce a reflected shock wave and better capture the rupture process. However, the large property gradient across the secondary diaphragm can cause high energy fluxes between cells and result in unrealistically high temperatures. The severity in this instance causes L1d to fail a short time after secondary diaphragm rupture. At the time of the current work, an exact Riemann solver was being investigated by Potter [98] to overcome this problem. In this thesis, the one-dimensional simulation was run with Jovian gas in the shock and acceleration tubes to overcome this problem. The one-dimensional results are displayed in Figure 3.22. The effect of the Jovian gas in the acceleration tube would cause incorrect shock speeds and flow properties.

3.4. FINAL MODIFIED ONE-DIMENSIONAL SIMULATIONS

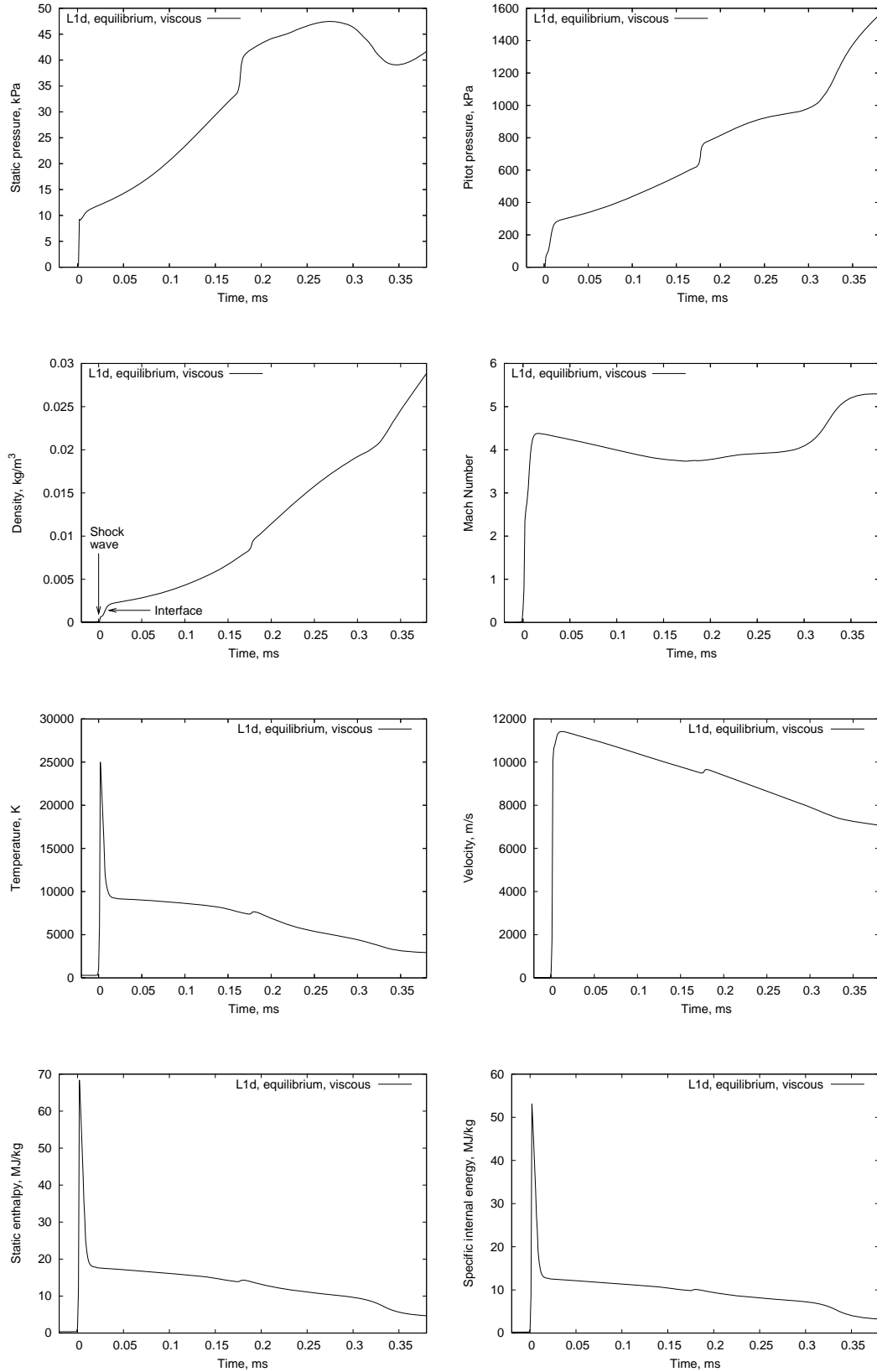


Figure 3.22: Properties from L1d at the end of the acceleration tube for the Jupiter condition

3.5 Axisymmetric Simulations of the Acceleration Tube

The next step in the numerical modelling was to perform axisymmetric simulations of the expansion tube. The overall simulation incorporated a viscous one-dimensional model coupled to an axisymmetric simulation of the acceleration tube. For these hybrid simulations, the viscous L1d was implemented up to the rupture of the secondary diaphragm. A time history was taken at the secondary diaphragm and this was used as a transient uniform inflow boundary condition in the axisymmetric simulation. The code used was the multi-block, two-dimensional compressible flow solver, MB_CNS [99, 100]. This program uses a cell-centred, time-dependant, finite-volume approach with a structured grid to solve the Navier-Stokes equations.

The geometry for these simulations is shown in Figure 3.23. Initially the domain was broken up into 9 blocks which are labelled 0 through to 8 in Figure 3.23. This was later increased to 33 blocks. The grid resolution that was used is discussed in the next section in the grid refinement study. A parallel version of the code that uses a distributed memory approach was implemented. The method of parallelization is known as Message Passing Interface (MPI). In the MPI version of MB_CNS each block is solved on a different processor. Each processor stores data for a single block in local memory but can send and receive information about blocks on other processors. The time a simulation takes to complete can be decreased by a factor proportional to the number of processors used. This factor is less than the number of processors due to overheads such as sending and receiving data. In order to optimize efficiency each block needs to be of similar size. The simulation was run on 33 processors on the Blackhole Linux cluster. Equilibrium chemistry was again provided by look up tables generated from the CEA program. An example of the input file for MB_CNS, called a “sit” file, is given in Appendix C.

The main aim of the CFD in this thesis was to predict the freestream flow conditions produced in the experimental facility. The full set of properties are unknown due to the limited data that can be obtained from experiments. This means that a computational method which consistently provides an accurate representation of the flow is extremely beneficial and helps to analyse what is occurring in the facility as it operates. Recall that the reason experiments are conducted are to validate the computational results.

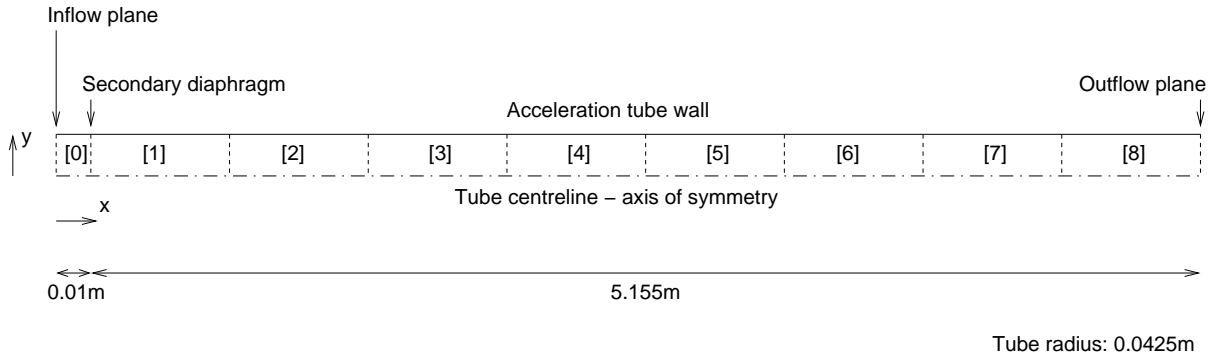


Figure 3.23: Geometry for the MB-CNS simulations

The axisymmetric simulations provide an option that can capture the flow better than the L1d but require a large amount of time and effort. Ideally the computational simulations would be run in three dimensions including all effects such as turbulence and finite-rate chemistry, however, this involves inordinate computing resources. Thus, assumptions are made and the validity of these must be examined and any discrepancies that arise from inadequacies in the model determined. Unfortunately, this can be extremely difficult due to the complex nature of some of the flow phenomena and it is also made harder by measurement errors that arise in the experimental results.

3.5.1 Air Condition 1

The flow properties at the end of the acceleration tube throughout time are shown in Figure 3.24. Two lines are given in each graph with one giving the value on the centreline and one at a distance of 24 mm off the centreline. The second position still remains in the core flow. The properties on the centreline contain oscillations which are not seen at a radial distance of 24 mm. This was due to any slight waves that occur in the flow being amplified at the centreline. Elsewhere in the core flow, off the centerline, any disturbances are not so strongly focused and the trace throughout time is much smoother.

Due to the high unit Reynolds numbers that were encountered, the turbulence model was made active in the simulations. In general, low densities and thus low unit Reynolds numbers are produced in the expansion tubes located at the University of Queensland. Furthermore, the effects of turbulence at the high hypersonic flow speeds can be insignificant when compared to other flow phenomena such as viscous interaction. The boundary layers formed can become extremely thick because of the high temperatures that develop

3.5. AXISYMMETRIC SIMULATIONS OF THE ACCELERATION TUBE

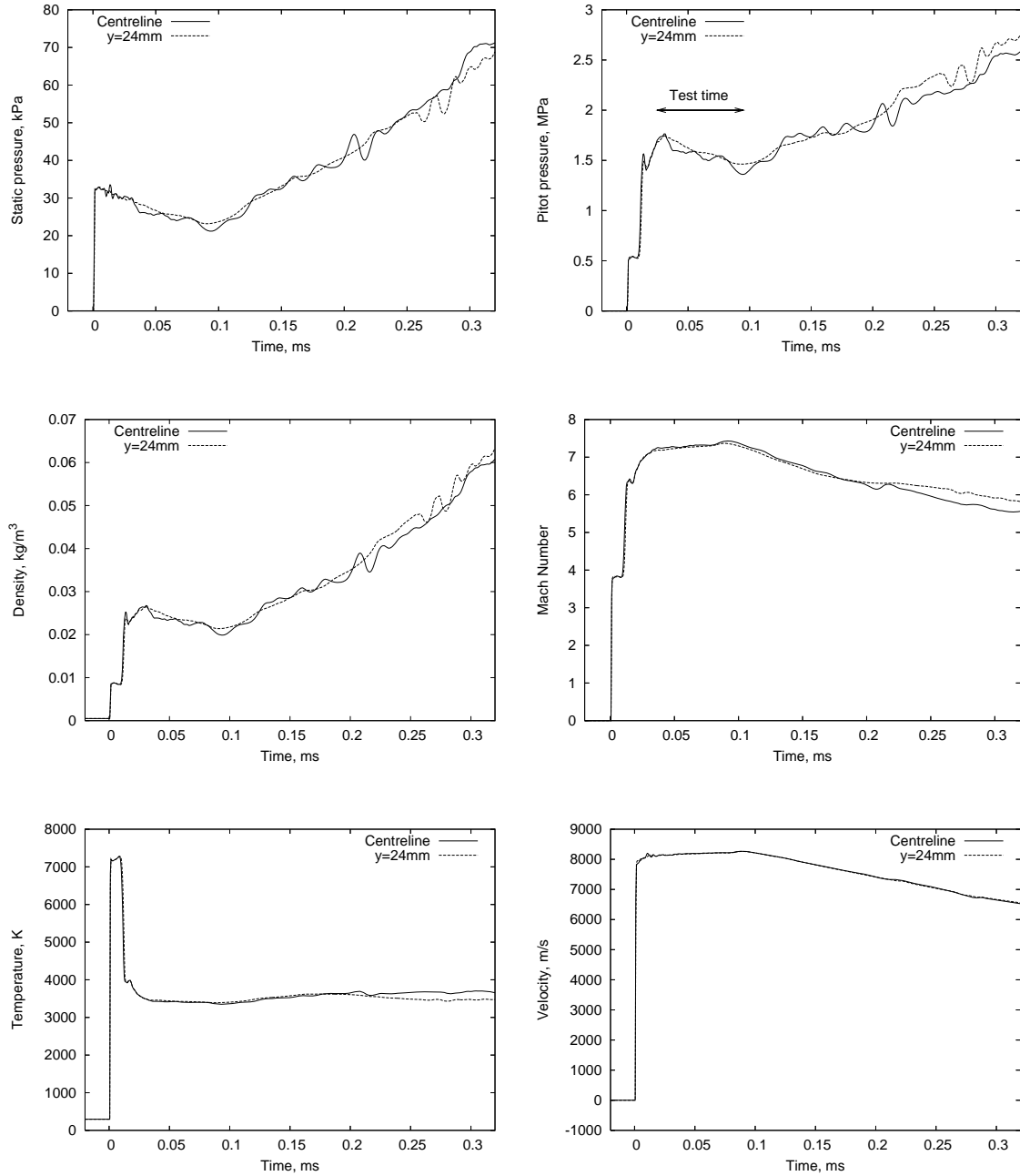


Figure 3.24: Properties from MB_CNS at the end of the acceleration tube for Air Condition 1. For the laminar simulation with equilibrium chemistry.

inside them. However, due to the increased pressure capabilities of the X2 driver, the densities are now an order of magnitude higher than in the old configuration and thus higher Reynolds numbers are generated. The unit Reynolds number at the acceleration tube exit based on the diameter of the tube was over 3×10^6 for the finite-rate simulation. This suggests that the boundary layer would be turbulent and could become influential.

The turbulence model used was the algebraic, Baldwin-Lomax eddy-viscosity model [101]. The freestream flow conditions for the turbulent simulations are shown in Figure 3.36. The Pitot pressure, Mach number and temperature distributions in the radial direction at the end of the acceleration tube are shown in Figures 3.25 and 3.26. Each graph has a number of slices taken at different times. The laminar simulations indicate approximately 75 mm of core flow out of the possible 85 mm diameter tube. This is relatively constant throughout the test gas but tends to slightly decrease later in time. For the turbulent simulation the core flow diameter begins at approximately 80 mm and then decreases to approximately 60 mm throughout the majority of the test time.

Propagation pictures of the flow are given for the laminar and turbulent cases in Figures 3.27 to 3.30 and 3.31 to 3.34 respectively. The sequence of pictures are in intervals of 50 microseconds with the logarithm of density the plotted variable. The starting time for the sequence is the arrival of the shock wave in the acceleration tube. The development of the boundary layer can distinctly be seen in these pictures. In the laminar case, the boundary layer is quite thin, but the growth of the boundary layer causes a gradual decrease in the pressure that can be seen in the pressure history plot in Figure 3.24. Examining the turbulent case at a time of 0.60 ms (Figure 3.33 part(d)), just before the shock wave reaches the exit of the acceleration tube, clearly shows the effects of the addition of turbulence. The thin laminar boundary layer is seen in the gas immediately after the test gas/acceleration gas interface. A transition into the thicker turbulent boundary layer occurs soon after and results in the varying boundary layer thicknesses mentioned above. This increase in boundary layer thickness causes the dip in static pressure that is seen in the history profile in Figure 3.36. This dip was much more pronounced with lower grid resolution as is shown in the grid refinement study. The coarser grid causes the turbulence model to overestimate viscosity which produces an overestimated boundary layer thickness. This causes the velocity to increase and thus the pressure to decrease and hence, results in the dip.

In the propagation pictures for the turbulent simulation (Figures 3.31 to 3.34) disturbances can be seen in the slug of test gas. These disturbances are fed from the boundary layer and cause unsteadiness in the core flow even away from the centreline in the time history plots in Figure 3.36. The perturbations are formed from shear layers in the boundary layer. The shear layers separate, propagate into the flow and cause noise. This was more severe in the coarsest grid because the larger boundary means that the shear layers are more unstable. The effect was not seen at all in the laminar case. Wilson et al. [102] saw similar effects in the HYPULSE expansion tube where the thicker boundary layer causes variations in the test pressure. Noise production by a turbulent boundary layer has been seen regularly in actual flow of impulse facilities [103]. In this numerical study, it was still thought that the overestimation of the viscosity caused excess noise.

For both the laminar and turbulent cases it is difficult to ascertain a value for the test flow pressure because of the dip caused by the boundary growth. This issue is compounded in the turbulent case by the flow disturbances propagating from the boundary layer. A large portion of these issues was thought to be numerical effects. In this thesis, an attempt has been made to be consistent when quoting core flow properties for different conditions and grid resolutions. The property value was typically taken at the end of the acceleration gas and the arrival of the test gas.

Finite-Rate Simulation

The high temperatures experienced in expansion tubes can cause chemical effects to become important. For air above 800 K, the assumption of a calorically perfect non-reacting gas is incorrect. The specific heats can no longer be set constant and thus the ratio of specific heats, γ , usually set to equal 1.4, is also not constant. Due to the excitation of the vibrational energy of the molecules, C_p and C_v depend upon the temperature. The gas must be treated as a chemically reacting gas, as is done throughout the majority of this thesis. Once the gas is determined to be chemically reacting, an assumption of equilibrium, non-equilibrium or frozen flow can then be made. A non-equilibrium process can be defined as one where the vibrational excitation and reactions occur at a rate similar to the characteristic time of the flow. The limiting cases of frozen flow (where the vibrational excitation and reactions occur much slower than the characteristic time) and equilibrium (where the vibrational excitation and reactions occur much quicker than the

3.5. AXISYMMETRIC SIMULATIONS OF THE ACCELERATION TUBE

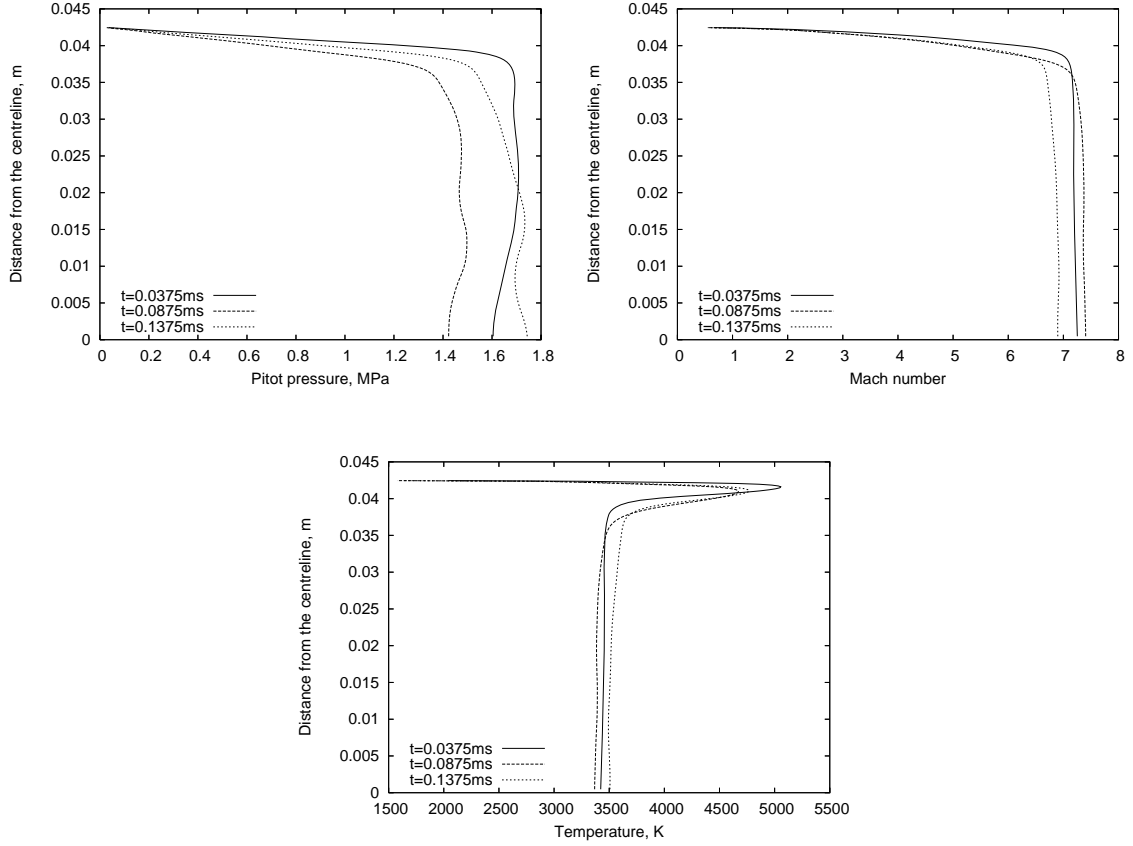


Figure 3.25: Profiles from MB.CNS across the acceleration tube exit for Air Condition 1. For the laminar simulation with equilibrium chemistry.

characteristic time) are much simpler to solve. For equilibrium flow C_p and C_v can be assumed to be purely functions of temperature and pressure. Non-equilibrium flow leads to a more complex situation which takes a large amount of time to solve which is why it is avoided if possible. To determine how much chemical effects influenced the flow in the air conditions of the X2 expansion tube, finite-rate simulations that involved chemically reacting mixtures of perfect gases were conducted.

The amount of dissociation which occurs in the test gas of an expansion tube is governed by the strength of the primary shock wave. The shock processing of the gas increases the temperature and pressure and these values determine the state of the gas. For air at 1 atm, the oxygen dissociation reaction begins at around 2500 K and is complete by around 4000 K. Nitrogen dissociation begins around 4000 K and is complete around 9000 K. Above this, ionization of the atoms occurs. Between 2000 K and 6000 K small

3.5. AXISYMMETRIC SIMULATIONS OF THE ACCELERATION TUBE

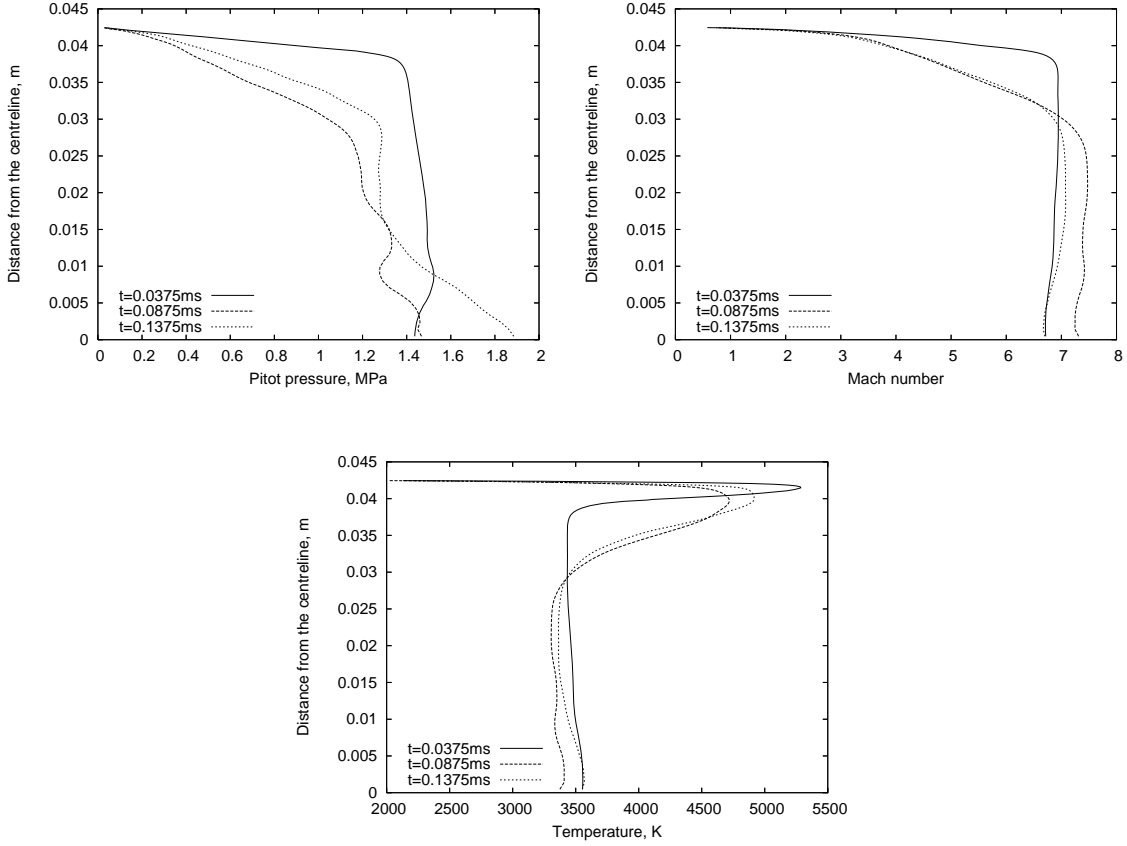
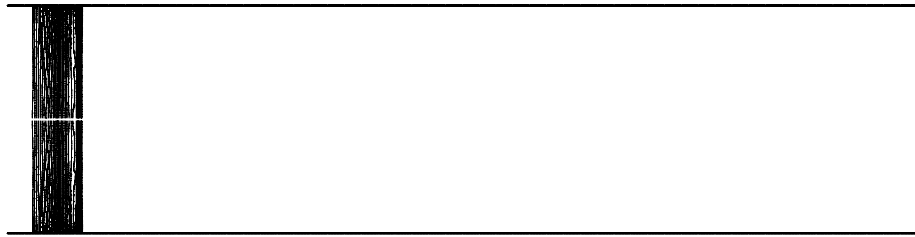


Figure 3.26: Profiles from MB_CNS across the acceleration tube exit for Air Condition 1. For the turbulent simulation with equilibrium chemistry.

amounts of NO form. In expansion tubes, the pressures experienced are higher than atmospheric pressure so the temperatures at which the reactions begin will be higher than these quoted. This corresponds to oxygen beginning to dissociate at primary shock speeds above approximately 2 km/s [16]. Significant dissociation of nitrogen does not occur unless the primary shock speed reaches in excess of 5 km/s. The rupture of the secondary diaphragm also causes a reflected shock wave to propagate back upstream into the test gas which can compound the effects of the primary shock wave. If dissociation does occur, the level of recombination that occurs as the flow travels down the acceleration tube is dictated by the unsteady expansion through which the test gas passes upon rupture of the secondary diaphragm.

There has been previous work on non-equilibrium effects in expansion tubes and the list presented here is not exhaustive. When the idea of expansion tubes was first inves-

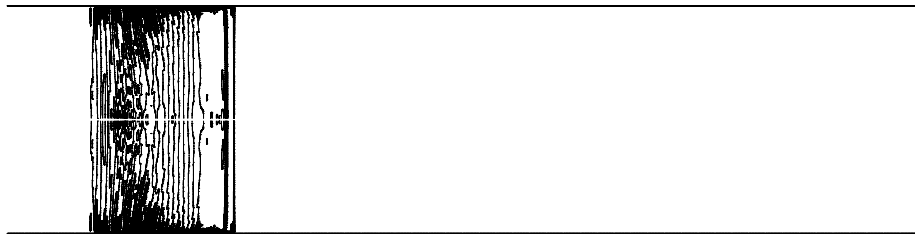
3.5. AXISYMMETRIC SIMULATIONS OF THE ACCELERATION TUBE



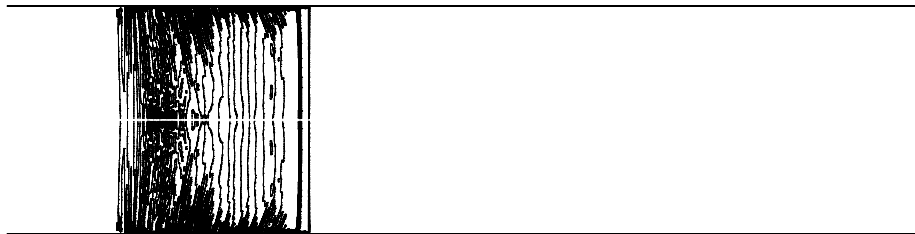
(a) $t=0.05\text{ms}$



(b) $t=0.10\text{ms}$



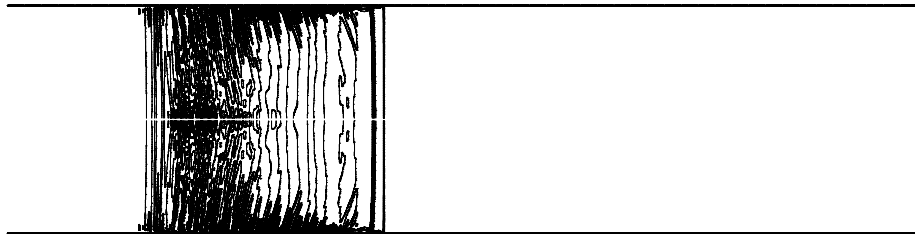
(c) $t=0.15\text{ms}$



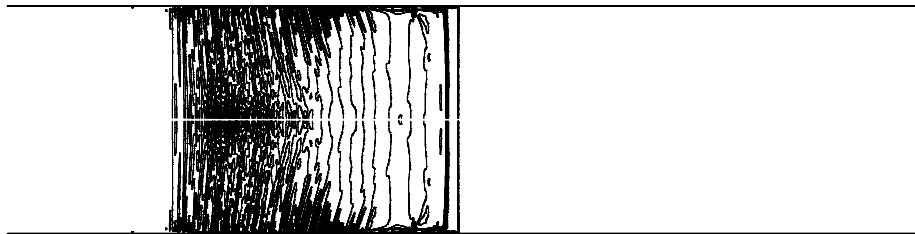
(d) $t=0.20\text{ms}$

Figure 3.27: Propagation of the flow in the acceleration tube for the laminar case: part 1

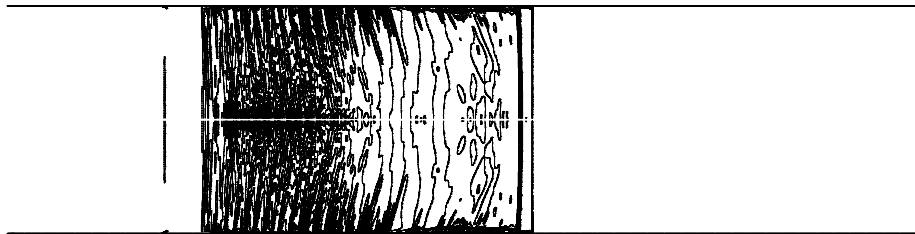
3.5. AXISYMMETRIC SIMULATIONS OF THE ACCELERATION TUBE



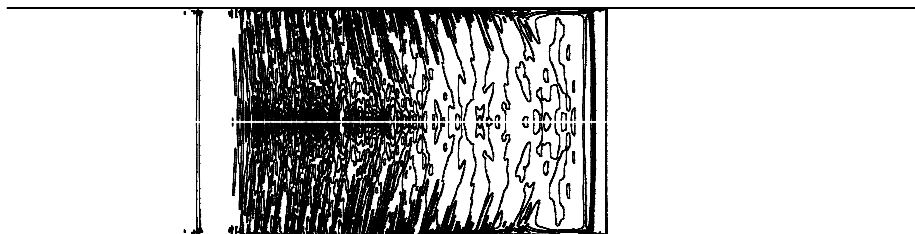
(a) $t=0.25\text{ms}$



(b) $t=0.30\text{ms}$



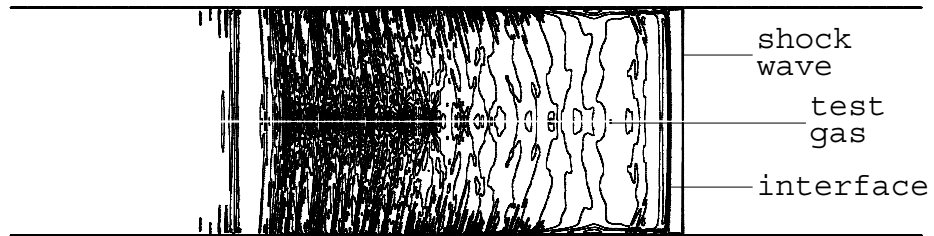
(c) $t=0.35\text{ms}$



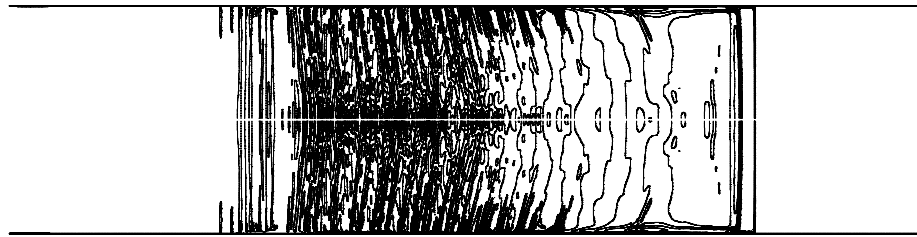
(d) $t=0.40\text{ms}$

Figure 3.28: Propagation of the flow in the acceleration tube for the laminar case: part 2

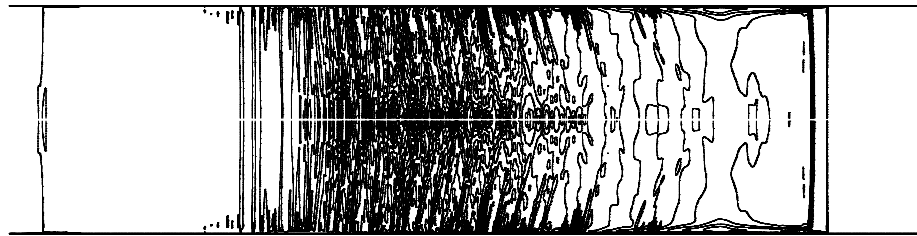
3.5. AXISYMMETRIC SIMULATIONS OF THE ACCELERATION TUBE



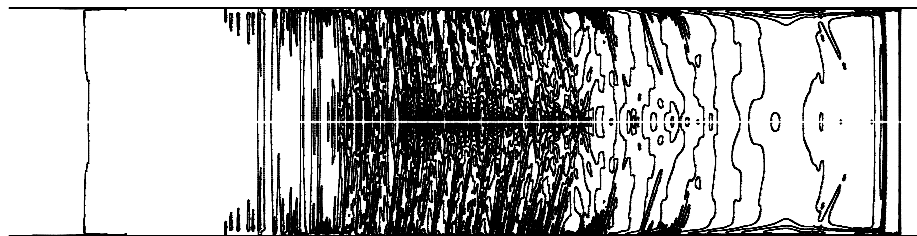
(a) $t=0.45\text{ms}$



(b) $t=0.50\text{ms}$



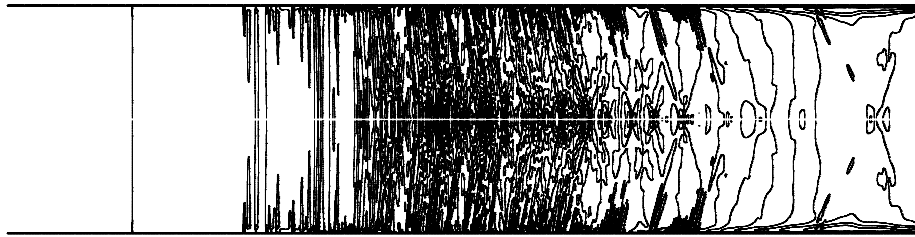
(c) $t=0.55\text{ms}$



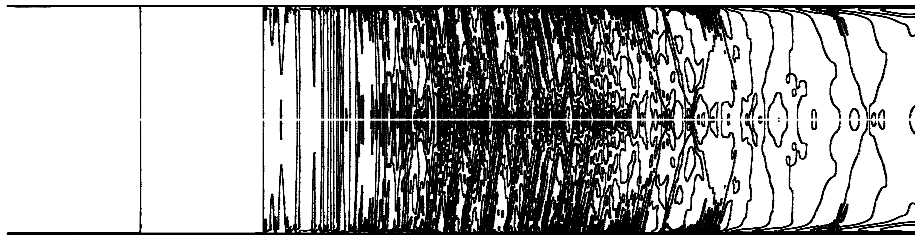
(d) $t=0.60\text{ms}$

Figure 3.29: Propagation of the flow in the acceleration tube for the laminar case: part 3

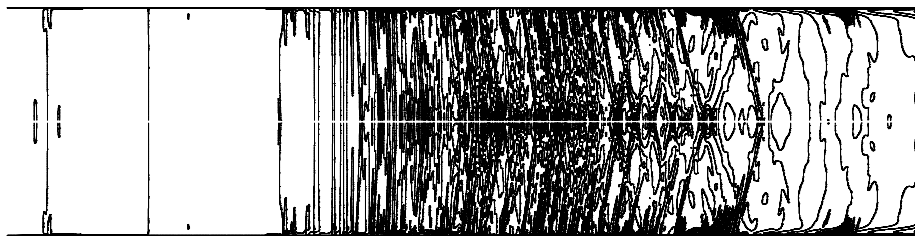
3.5. AXISYMMETRIC SIMULATIONS OF THE ACCELERATION TUBE



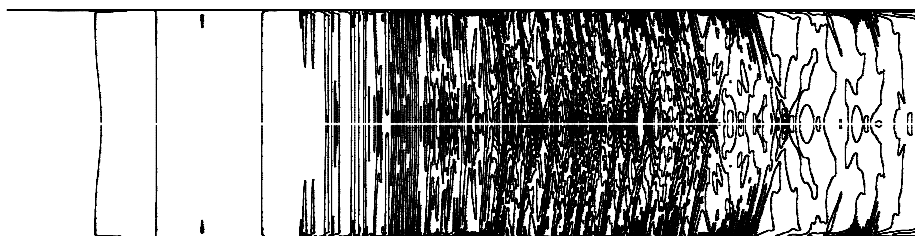
(a) $t=0.65\text{ms}$



(b) $t=0.70\text{ms}$



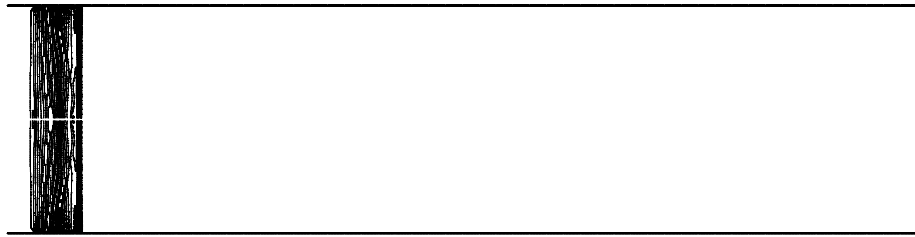
(c) $t=0.75\text{ms}$



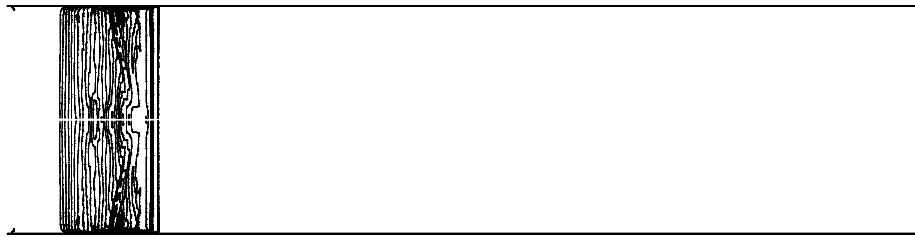
(d) $t=0.80\text{ms}$

Figure 3.30: Propagation of the flow in the acceleration tube for the laminar case: part 4

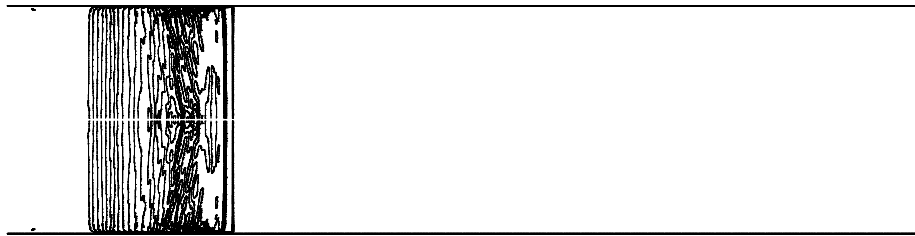
3.5. AXISYMMETRIC SIMULATIONS OF THE ACCELERATION TUBE



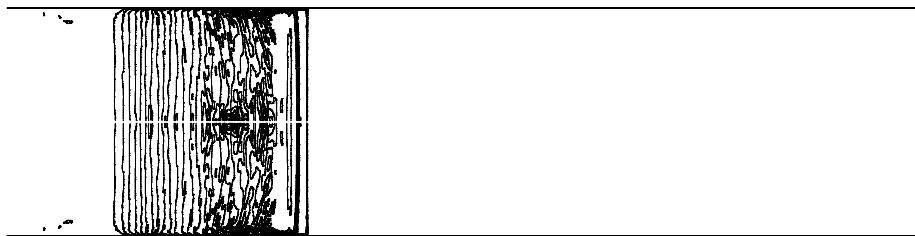
(a) $t=0.05\text{ms}$



(b) $t=0.01\text{ms}$



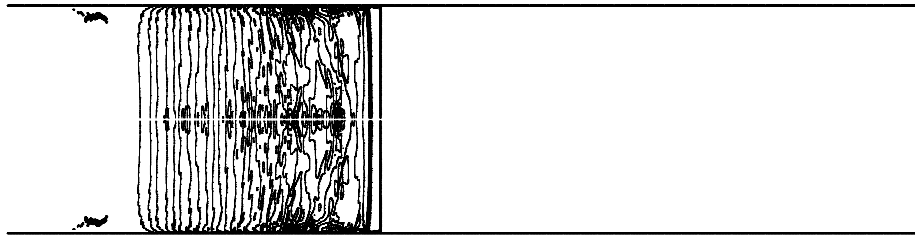
(c) $t=0.15\text{ms}$



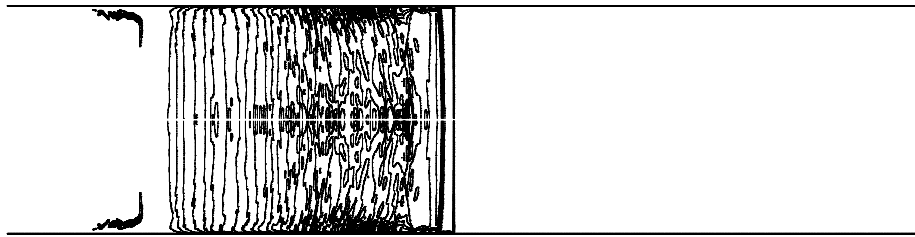
(d) $t=0.20\text{ms}$

Figure 3.31: Propagation of the flow in the acceleration tube for the turbulent case: part 1

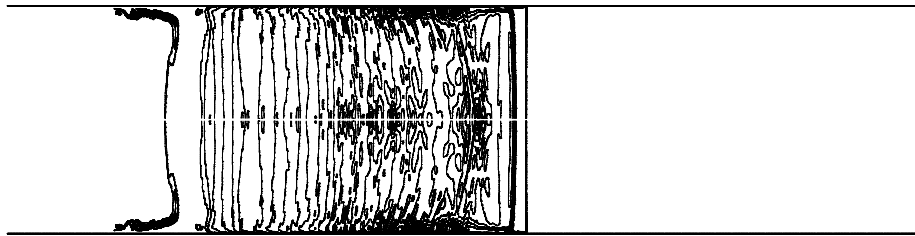
3.5. AXISYMMETRIC SIMULATIONS OF THE ACCELERATION TUBE



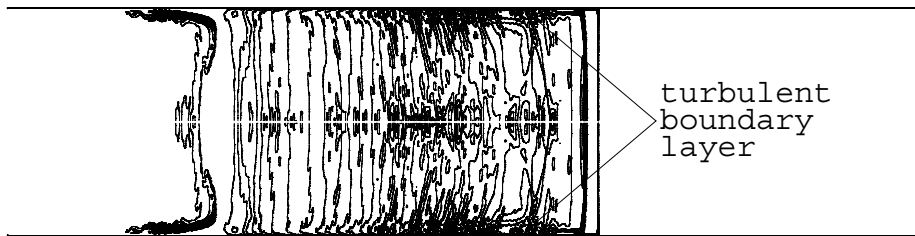
(a) $t=0.25\text{ms}$



(b) $t=0.30\text{ms}$



(c) $t=0.35\text{ms}$



(d) $t=0.40\text{ms}$

Figure 3.32: Propagation of the flow in the acceleration tube for the turbulent case: part 2

3.5. AXISYMMETRIC SIMULATIONS OF THE ACCELERATION TUBE

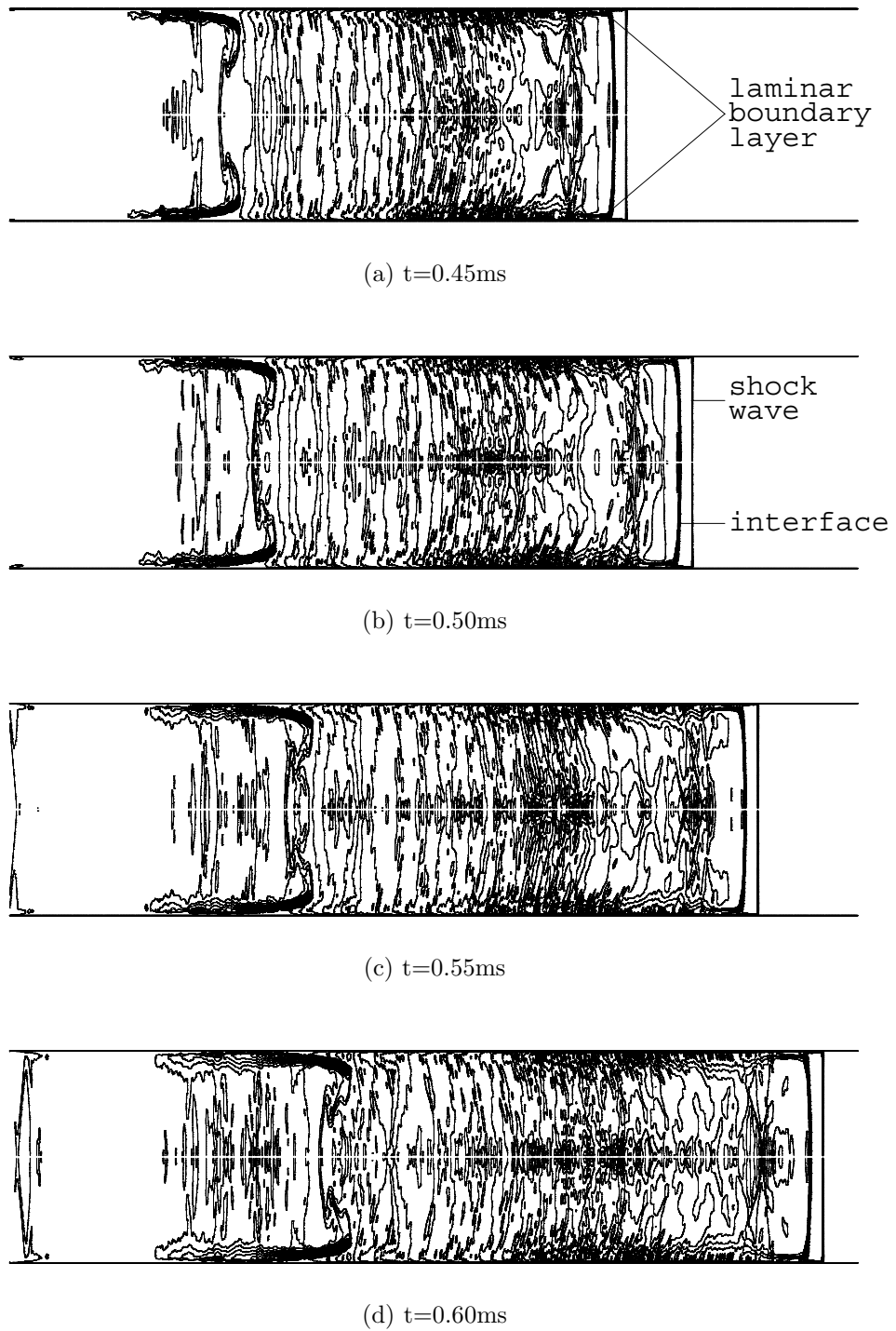
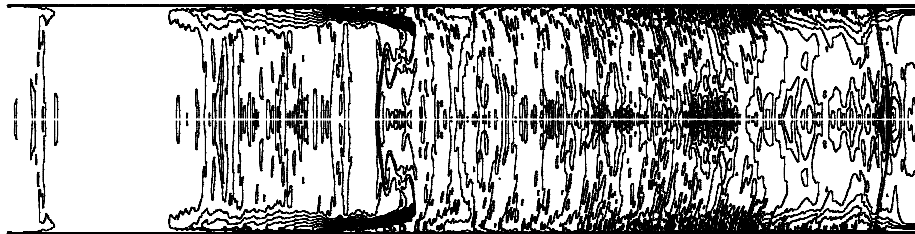
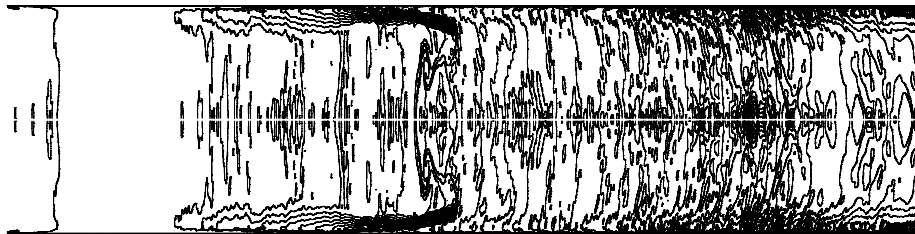


Figure 3.33: Propagation of the flow in the acceleration tube for the turbulent case: part 3

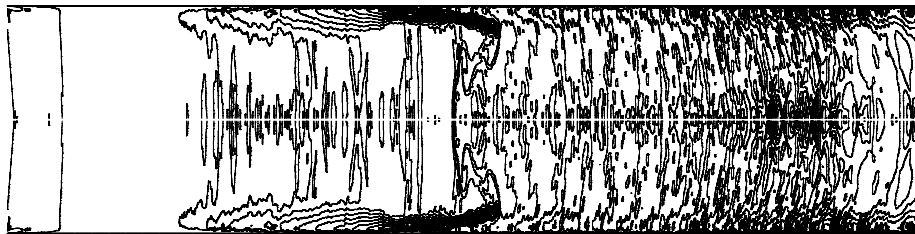
3.5. AXISYMMETRIC SIMULATIONS OF THE ACCELERATION TUBE



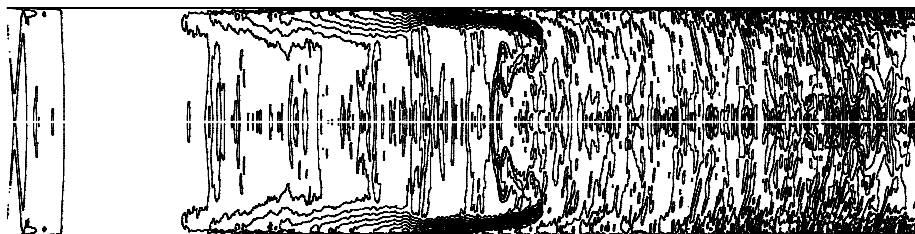
(a) $t=0.65\text{ms}$



(b) $t=0.70\text{ms}$



(c) $t=0.75\text{ms}$



(d) $t=0.80\text{ms}$

Figure 3.34: Propagation of the flow in the acceleration tube for the turbulent case: part 4

tigated in the 1960s, a reasonable amount of work on the area was conducted. One such example was Connor [104] who presented the effects on the flow conditions in the tube produced by chemical and vibrational non-equilibrium. It was said that freestream test temperature was the main property influenced by non-equilibrium, but other properties such as pressure and velocity could also be appreciably influenced.

Wilson [105] performed quasi-one-dimensional simulations of three facilities including the HYPULSE expansion tube. It was found that in this facility large amounts of dissociated species were caused by the reflected shock at the secondary diaphragm and these remained in the test flow due to chemical freezing. Later, Wilson et al. [102, 106] examined two nitrogen conditions in HYPULSE with numerical axisymmetric simulations. One condition had a total enthalpy of 15.2 MJ/kg with a static pressure of 2 kPa. The flow was laminar and characterized by significant chemical non-equilibrium in the acceleration gas. The second condition had a total enthalpy of 10.2 MJ/kg with a much higher static pressure of 38 kPa. One deduction was that the non-equilibrium nature of the accelerator gas could greatly effect the shock speeds. Bakos and Morgan [107] implemented a diaphragm inertia rupture model on the secondary diaphragm as compared to the hold time model used by Wilson [106] and in this thesis. The inertia model resulted in more recombination of the test gas than seen by Wilson.

Sutcliffe [108] used the X1 expansion tube to study four different carbon dioxide conditions. In the investigation it was found that at the two higher enthalpy conditions (flow speeds of 11 and 13 km/s), equilibrium chemistry provided a good match between the numerical and experimental pressures. However, at the two lower enthalpy conditions (flow speeds of 7 and 9 km/s) the flow through the unsteady expansion propagating at the secondary diaphragm was in chemical non-equilibrium. It was concluded that the higher temperatures in the higher enthalpy flows provided more chemical recombination in the expansion.

Stewart analyzed the high-temperature chemistry effects in two air conditions of the old X2 configuration. These simulations were inviscid and completed using the code L1d. The first condition had a flow speed of 6.8 km/s. In the finite-rate calculation, a small amount of nitrogen dissociated in the test gas and then recombined rapidly through the unsteady expansion. This matched fairly well with the dissociation levels from the equilibrium simulation. The oxygen in the test gas did not recombine as quickly in the non-

equilibrium simulation through the unsteady expansion as predicted by the equilibrium simulation. This resulted in a more frozen process and reduced the temperature as well as slightly decreasing the shock speed in the non-equilibrium simulation. The second, higher enthalpy, 9.7 km/s condition saw hardly any recombination of the oxygen in the test gas in the finite-rate simulation. The nitrogen in the test gas from the finite-rate simulation did recombine, but not to the same levels as in the equilibrium simulation. This also resulted in a flow temperature in the finite-rate case of half that from the equilibrium case. It was concluded that the non-equilibrium effects were more influential in the higher enthalpy conditions. It was also stated that finite-rate chemistry should be included to obtain a good value for the final test flow properties and compositions in both conditions. In the author's opinion, though the recombination levels between the equilibrium and finite-rate cases differ by more in the higher enthalpy condition, the influence on the freestream flow properties of the non-equilibrium effects is just as important in the two conditions. Similar percentage differences ($\sim 10\%$) are seen in flow static pressure, Pitot pressure and secondary shock speed for both the conditions and this is not substantial. This small percentage difference can be important though when calculating the free-stream flow properties at the test section. The temperature and density differences between the equilibrium and finite-rate cases are higher (over 50%) in the 9.7 km/s condition, but both conditions constitute a substantial difference.

Due to time and computing constraints the non-equilibrium simulations in this thesis were run assuming only laminar flow on the coarsest mesh. The finite-rate chemistry module implemented in MB_CNS was written by Gollan [109]. The methods used for computing the thermodynamic and transport properties of the multi-species reacting gas are outlined by Gollan [109]. The thermochemical non-equilibrium package in this thesis utilized a 6 species, 17 reaction air model. The forward and backward reaction rate coefficients were computed from a modified Arrhenius expression. The equation constants were obtained from Gupta et al. [110]. The species list, reactions and reaction rates are given in Appendix B.

Finite-rate chemistry was not examined in the shock tube in this thesis. Stewart's results using L1d found that up to the secondary diaphragm there was minimal difference in the flow properties between the equilibrium and finite-rate simulations. This held for both the low enthalpy and high enthalpy conditions that he examined. There would

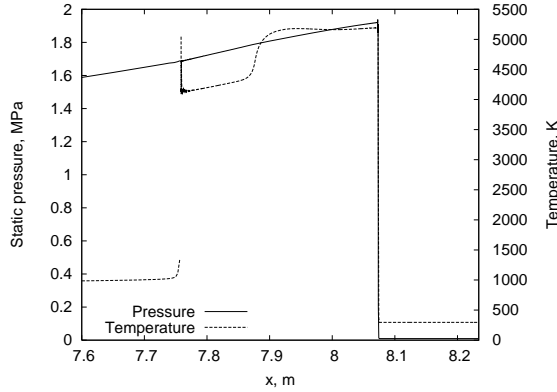


Figure 3.35: Pressure and temperature from L1d along the shock tube

also be little variation between the two chemistry models in the conditions for this thesis up to the secondary diaphragm, so the one-dimensional simulations were only run with equilibrium chemistry. This means that the gas behind the primary shock was assumed to be in equilibrium. The amount which the dissociated gas recombines during the unsteady expansion is more pertinent to whether the operation of the expansion tube can be assumed to be an equilibrium process. One problem that would have existed is that the erroneous temperatures produced by L1d (because of its whole of cross-section averaging) would have given rise to incorrect levels of dissociation predicted by the chemistry model. Little could be done to rectify this problem. The pressure and temperature along the shock tube just before secondary diaphragm rupture is shown in Figure 3.35. The composition of the gas, by mass, in the shock tube at these conditions of 1.88 MPa and 5100 K was 71.8 % N_2 , 0.4 % N, 2.6 % O_2 , 16.7 % O, 7.1 % NO plus other trace components. As expected this signifies the test gas experiences dissociation due to the primary shock wave. This does not include any effects of the rupture of the secondary diaphragm which partially stagnates a region of the test gas.

A comparison of the freestream properties at the end of the acceleration tube between the equilibrium, finite-rate and experimental results is given in the next chapter (pages 118-119). The time history graphs of the computational freestream properties are given in Figure 3.36. Examining the temperature profile in Figure 3.36, the finite-rate case has a large spike after the shock and then decreases to the equilibrium value. This signifies non-equilibrium behaviour in the acceleration gas. A small region of gas behind the shock wave does not immediately reach the equilibrium value as the dissociation reactions take time to

complete. While the reaction occurs the translational energy decreases to allow for some energy to be used to separate the molecules. This causes the decrease in temperature.

The species fractions throughout time at the end of the acceleration tube for both the equilibrium and finite-rate simulations are given in Figure 3.37. The equilibrium simulation includes turbulence which explains the perturbations in the species fractions. The graphs are shifted so that the secondary shock wave arrives at a time of 0 ms. Before this time the levels of species are the same as those for the initial fill gas. In the equilibrium simulation this was 75.52 % N₂ and 23.14 % O₂ obtained from CEA which includes other trace components. For the finite-rate simulation the species were 0.78 % N₂ and 0.22 % O₂ as set by the author. Upon arrival of the shock wave, the dissociation levels jump to the values of those in the shock processed acceleration gas. In both chemistry cases, the oxygen in the acceleration gas is modelled correctly and consists entirely of O due to the high temperature. This is immediately realized behind the shock as shown in the graphs. The finite-rate curve for the nitrogen species does not immediately reach the equilibrium level. This corresponds with the temperature spike and non-equilibrium behaviour discussed above. It demonstrates the inaccuracies of the equilibrium assumption in modelling the acceleration gas.

Following the acceleration gas another jump is seen in these graphs in the species fractions at the accelerator gas/test gas interface. In the test gas the N₂ returns quickly to the equilibrium level for both chemistry cases. In the equilibrium simulations this is a bit lower as more NO is formed due to the higher temperature. The oxygen in the test gas, however, is not in equilibrium. The test flow pressure and temperature from the finite-rate case was 30.66 kPa and 2800 K. For air at these conditions, the equilibrium species fractions would be 73.93 % N₂, 0.0 % N, 19.06 % O₂, 2.27 % O, 3.40 % NO with other trace elements. Though some recombination of the oxygen has occurred through the unsteady expansion and more recombination can be seen as the test gas comes though later in time, the species fraction is different from the equilibrium value. This indicates that the chemistry has an effect on the composition of the test gas in the X2 expansion tube which can not be accurately modelled by the equilibrium assumption. This then influences the flow properties that are predicted by the numerical simulation. In most of the flows generated in expansion tubes and studied at the University of Queensland non-equilibrium flow should be assumed.

3.5. AXISYMMETRIC SIMULATIONS OF THE ACCELERATION TUBE

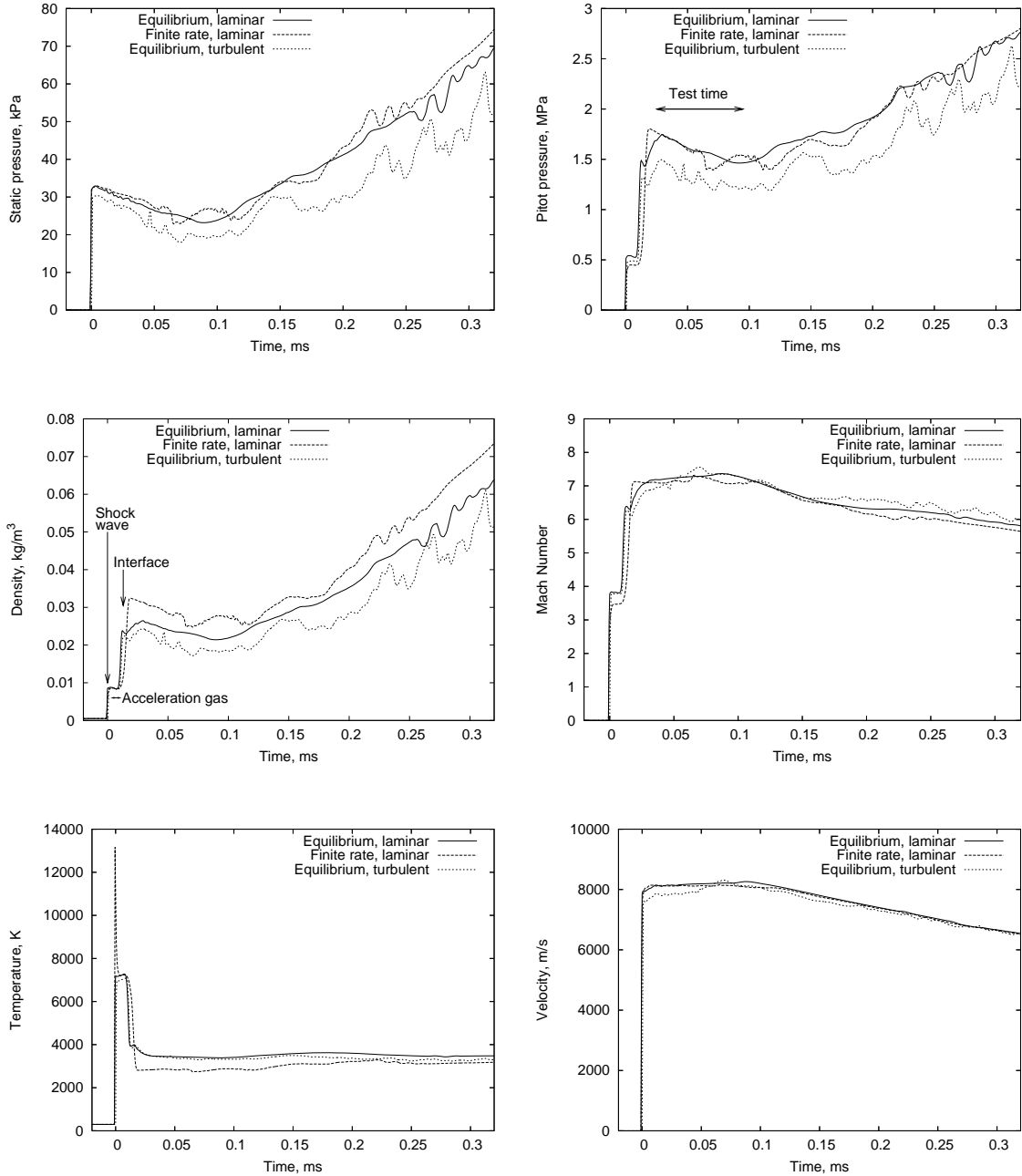


Figure 3.36: Properties from MB_CNS at the end of the acceleration tube for Air Condition 1 comparing the different MB_CNS models. Taken at a radial distance of 24 mm from the centreline.

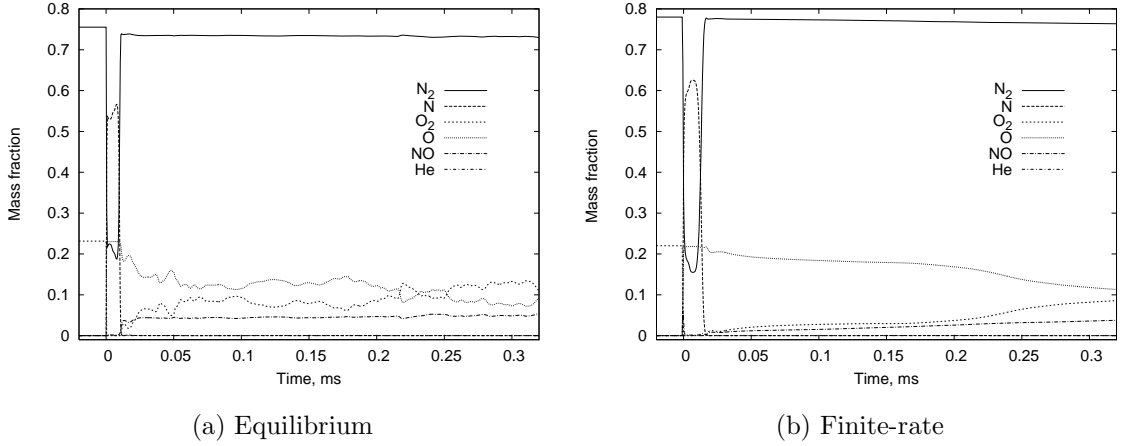


Figure 3.37: Species fractions from MB_CNS at the end of the acceleration tube for Air Condition 1

3.5.2 Air Condition 2

The freestream test properties for Air Condition 2 are plotted in Figures 3.38 to 3.42. Air Condition 1 and Air Condition 2 were very similar, with only the acceleration tube fill pressure varying from 26 Pa to 43 Pa. The effects of the addition of turbulence and finite-rate chemistry which were discussed above will not be restated here. Analogous effects were seen in both the air conditions, which is expected because they have the similar flow enthalpies.

3.5.3 Titan Condition

The axisymmetric simulations conducted for the Titan condition used equilibrium chemistry and the Baldwin-Lomax eddy-viscosity turbulence model. The freestream flow properties at the end of the acceleration tube are graphed in Figures 3.43 and 3.44. As in the one-dimensional Titan simulation, the air in the acceleration tube was assumed to be a calorically perfect gas. This causes the temperature in the acceleration gas to reach an unrealistically high value of 18000 K. From the profiles in the radial direction of the flow, the core diameter is initially 65 mm and then decreases in time. Similar to the air conditions, the boundary layer grows and there is a transition from a laminar to turbulent boundary layer in the test gas. This can be seen in Figure 3.45. However, in this instance it does not produce a decrease in the pressure throughout time. As expected, the lower Reynolds number produces a thicker boundary layer when compared to the air conditions.

3.5. AXISYMMETRIC SIMULATIONS OF THE ACCELERATION TUBE

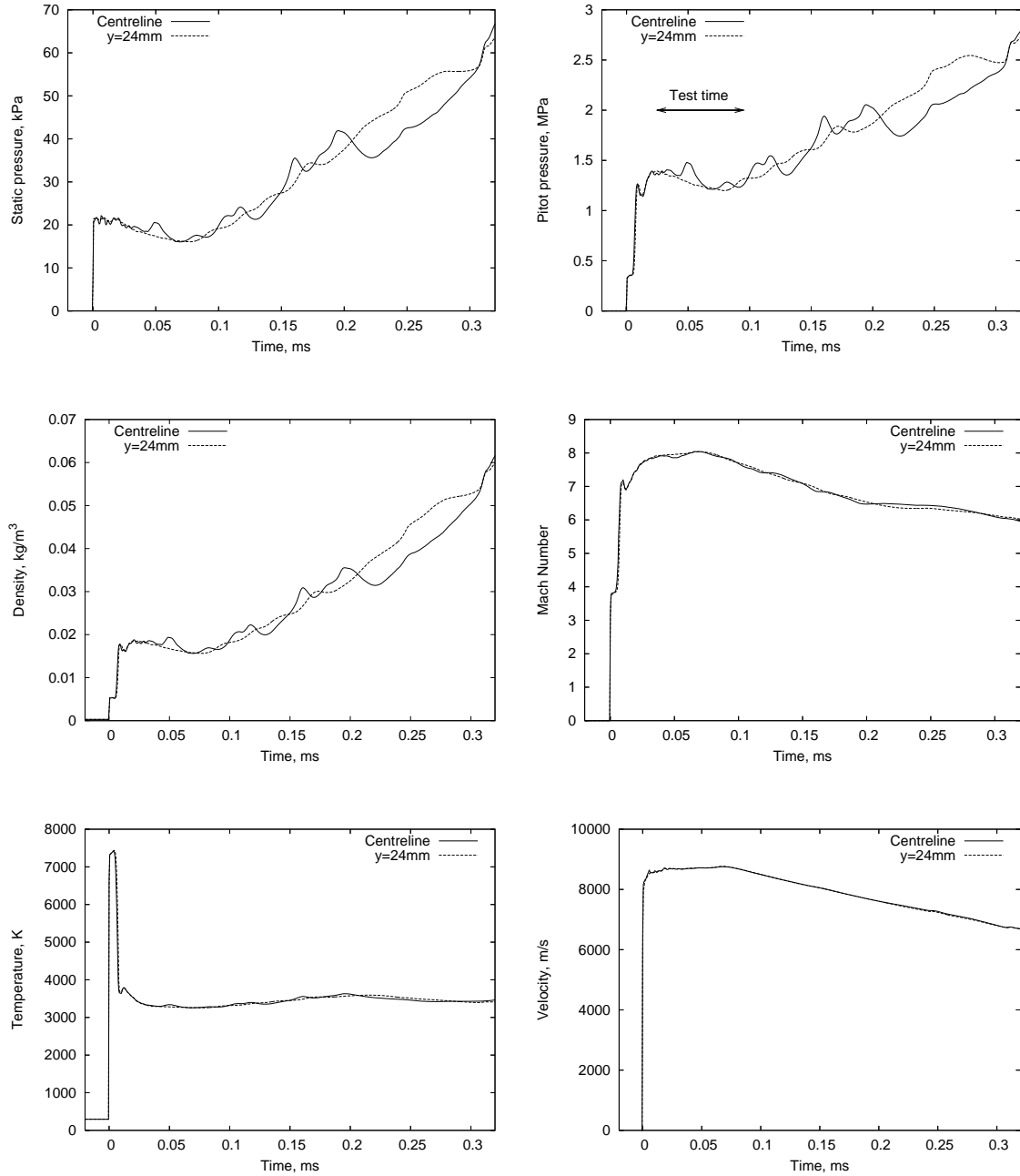


Figure 3.38: Properties from MB_CNS at the end of the acceleration tube for Air Condition 2. For the laminar simulation with equilibrium chemistry.

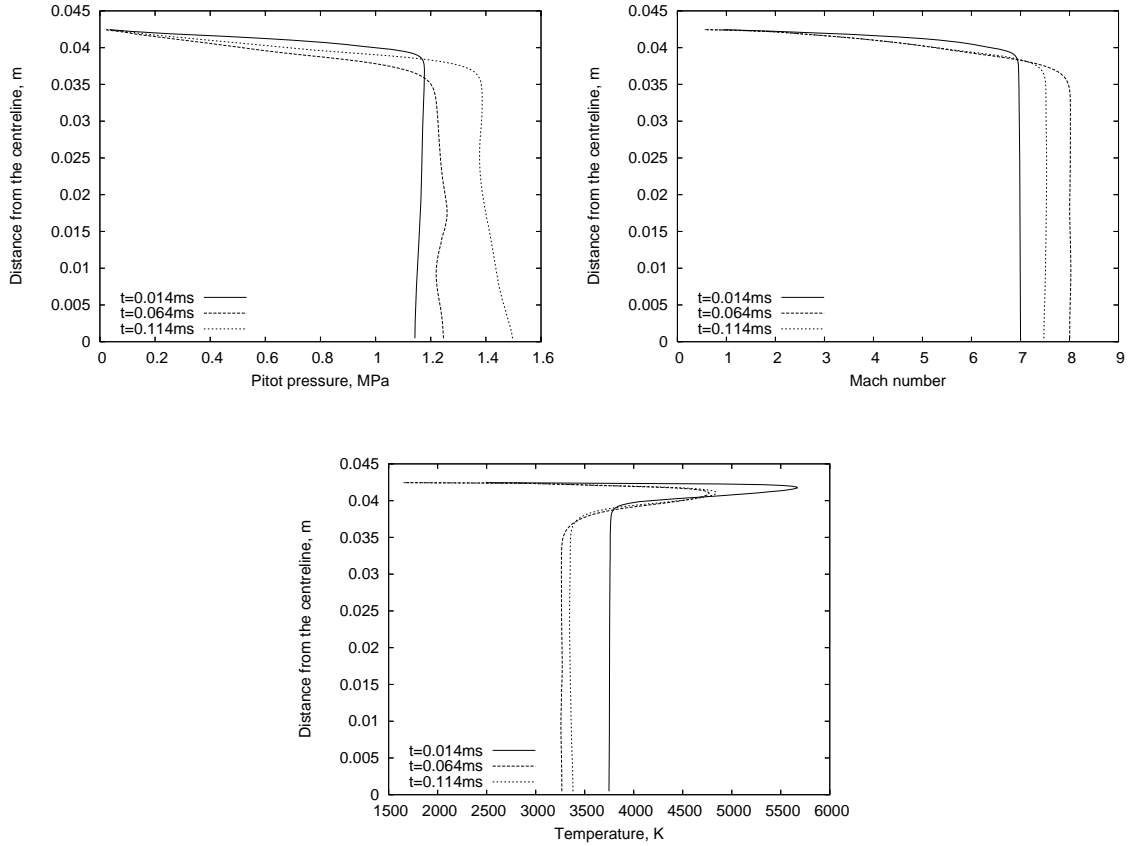


Figure 3.39: Profiles from MB_CNS across the acceleration tube exit for Air Condition 2. For the laminar simulation with equilibrium chemistry.

These numerical results will be compared to the experimental results in Chapter 4 (page 130).

3.5.4 Grid Refinement Study

Laminar Simulations

To ensure that a fully grid independent solution was achieved for the axisymmetric simulations, a grid refinement study was conducted. For the viscous, equilibrium, MB_CNS simulations of Air Condition 1 and Air Condition 2 a number of grid resolutions were used. These meshes increased the number of cells in each direction by a factor of 1.5. For Air Condition 1 an additional mesh was run with the number of cells in the x-direction doubled. The total cells for the varying grids are given in Table 3.13. In the axisymmetric study of X2 by Stewart 16800 cells were used in the acceleration tube. The present study

3.5. AXISYMMETRIC SIMULATIONS OF THE ACCELERATION TUBE

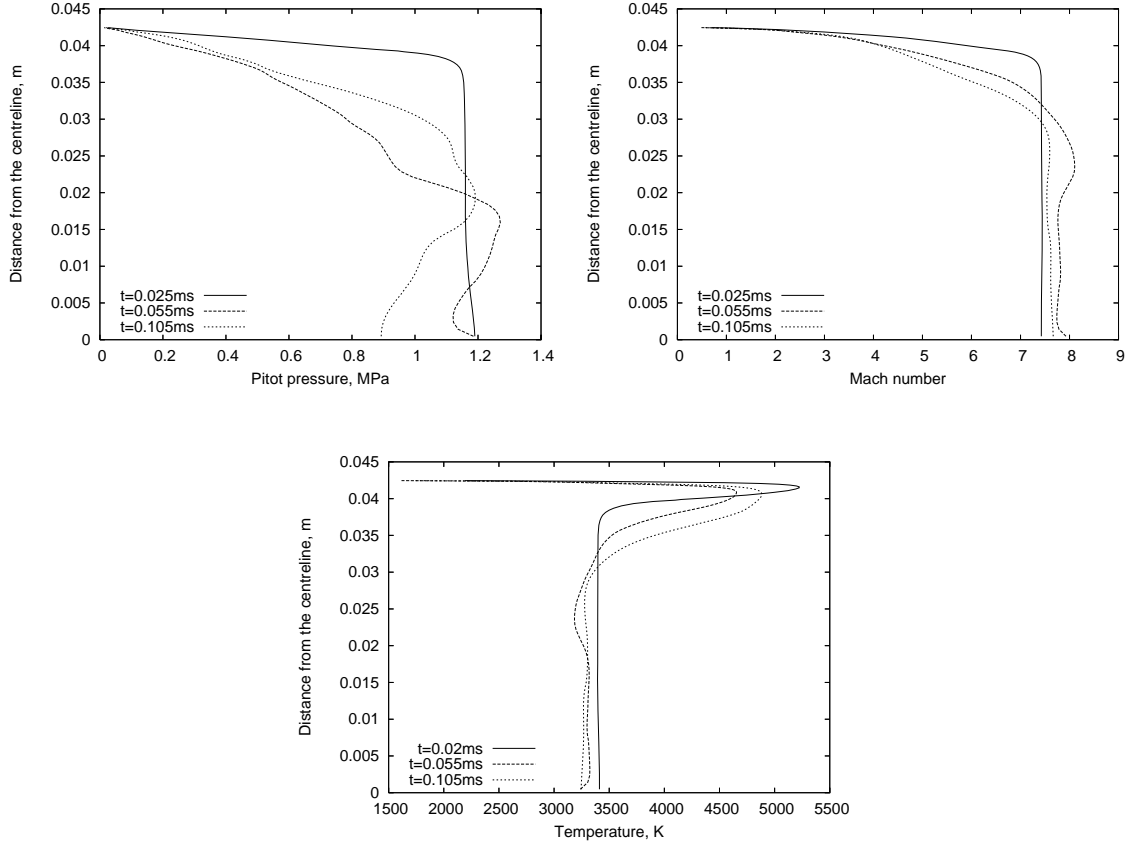


Figure 3.40: Profiles from MB_CNS across the acceleration tube exit for Air Condition 2. For the turbulent simulation with equilibrium chemistry.

Table 3.13: Number of cells used in the acceleration tube for each grid of the axisymmetric simulations

	Number of cells along the tube	Number of cells across the tube
Grid 1	2408	39
Grid 2	3612	58
Grid 3	5426	87
Grid 4	10834	87

uses at least 5.5 times this number of cells in the coarsest grid.

Table 3.14 and Figure 3.46 summarize the core flow properties for the different meshes for Air Condition 1. Table 3.15 and Figure 3.47 summarize these for Air Condition 2. In these figures the properties were taken slightly off the centreline. Predominantly throughout these graphs the properties are not changing with the varying grid. This

3.5. AXISYMMETRIC SIMULATIONS OF THE ACCELERATION TUBE

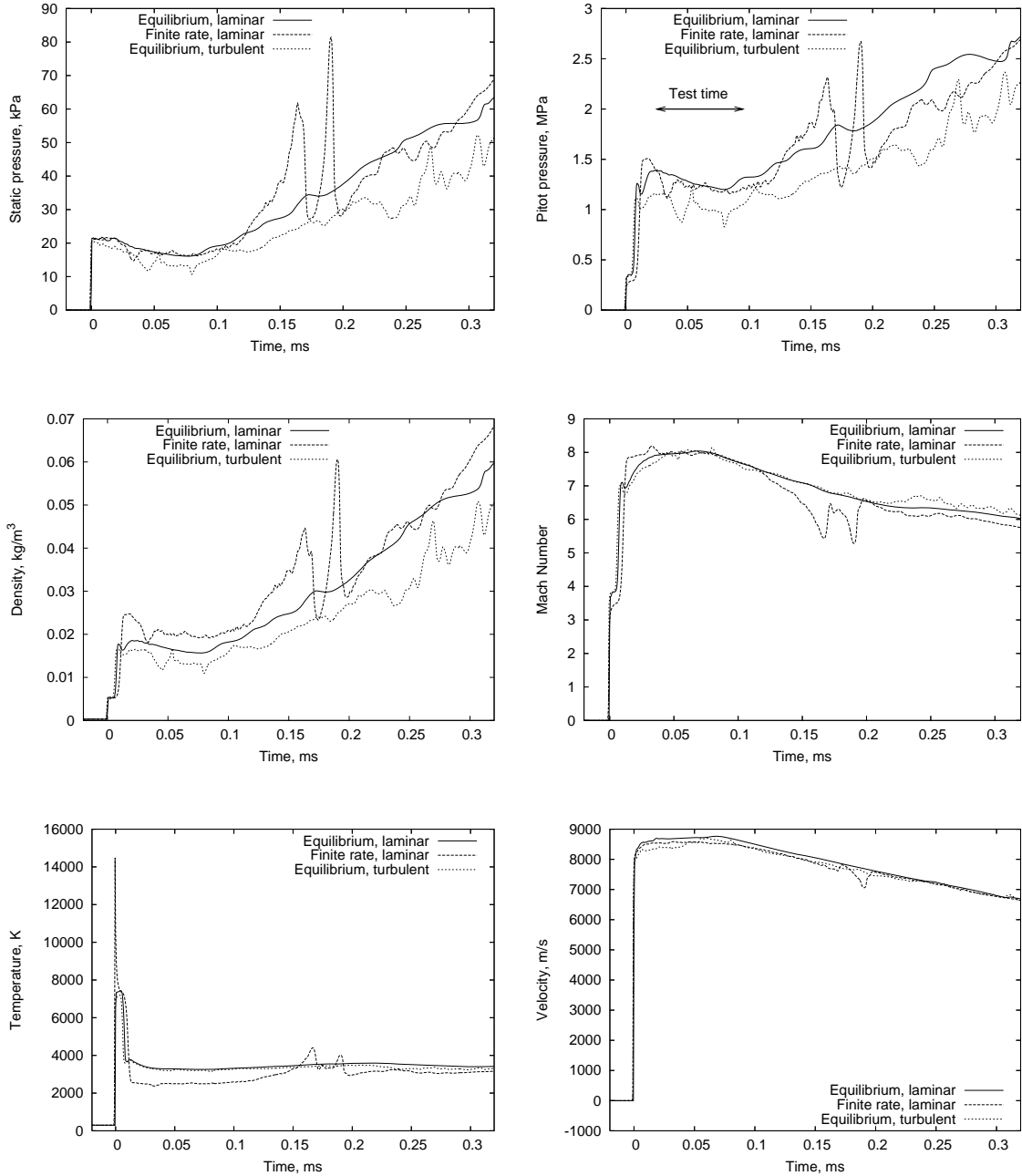


Figure 3.41: Properties from MB_CNS at the end of the acceleration tube for Air Condition 2 comparing the different MB_CNS models. Taken at a radial distance of 24 mm from the centreline.

3.5. AXISYMMETRIC SIMULATIONS OF THE ACCELERATION TUBE

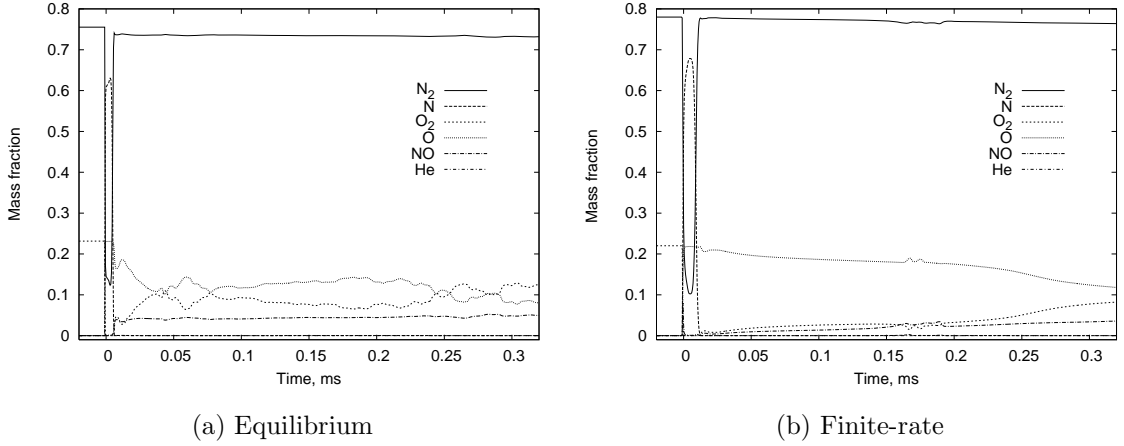


Figure 3.42: Species fractions from MB_CNS at the end of the acceleration tube for Air Condition 2

Table 3.14: Summary of the properties at the acceleration tube exit for the grid refinement study for Air Condition 1

Property	Grid 1	Grid 2	Grid 3	Grid 4
Secondary shock speed, km/s	8.115	8.197	8.241	8.281
Static pressure, kPa	28.31	30.06	29.47	30.28
Pitot pressure, MPa	1.52	1.60	1.65	1.65
Density, g/m ³	24.25	24.42	24.50	24.50
Mach number	7.2	7.3	7.3	7.3
Static temperature, K	3500	3450	3450	3450
Velocity, km/s	8.2	8.2	8.2	8.2
Static enthalpy, MJ/kg	6.33	6.33	6.33	6.33
Total enthalpy, MJ/kg	39.95	39.95	39.95	39.95
Specific internal energy, MJ/kg	5.08	5.08	5.08	5.08
Unit Reynolds number	1.87×10^6	1.87×10^6	1.87×10^6	1.87×10^6

would suggest that the solution is grid independent. Examining the Pitot pressure and density plots a slight decrease is visible later in the test time and is due to the growth of the boundary layer. This tends to disappear as the grid becomes finer which indicates that the boundary layer resolution is not perfect. All the results presented in this chapter and in the next chapter are using grid 3 which has 5426 by 87 cells. The shock speeds were increasing fractionally with increasing grid resolution. The computational shock speeds were calculated by plotting the results from the various grids and then fitting a curve to the values. This is shown in Figure 3.48.

3.5. AXISYMMETRIC SIMULATIONS OF THE ACCELERATION TUBE

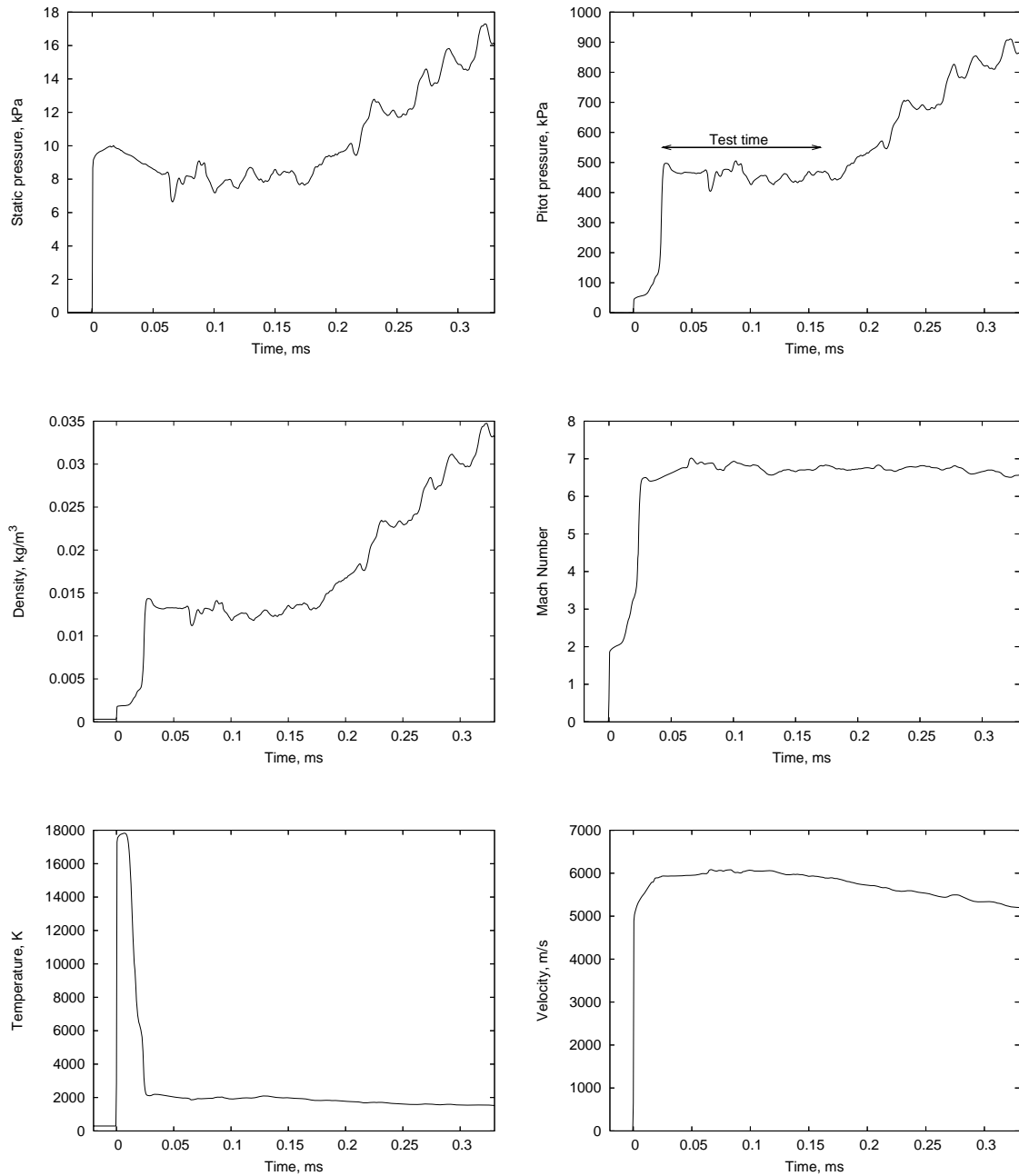


Figure 3.43: Properties from MB_CNS at the end of the acceleration tube for the Titan condition. Taken at a radial distance of 24 mm from the centreline.

3.5. AXISYMMETRIC SIMULATIONS OF THE ACCELERATION TUBE

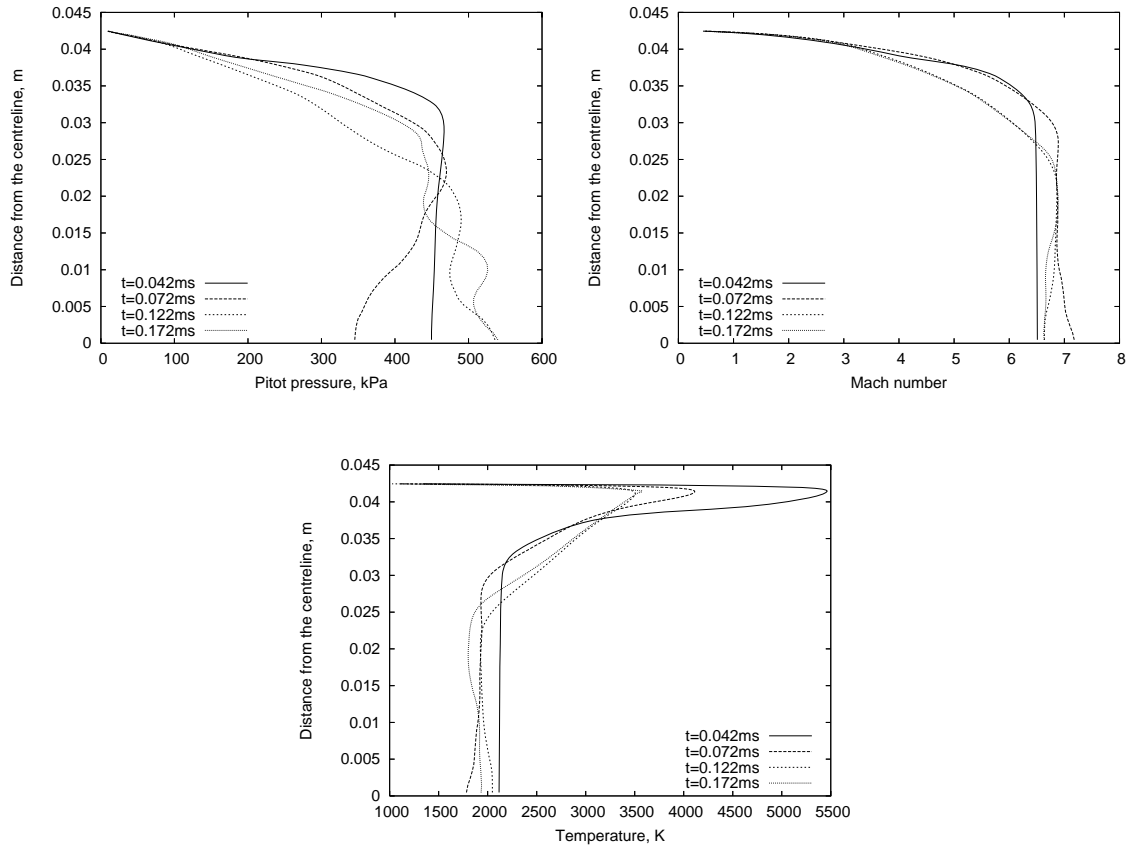


Figure 3.44: Profiles from MB_CNS across the acceleration tube exit for the Titan condition

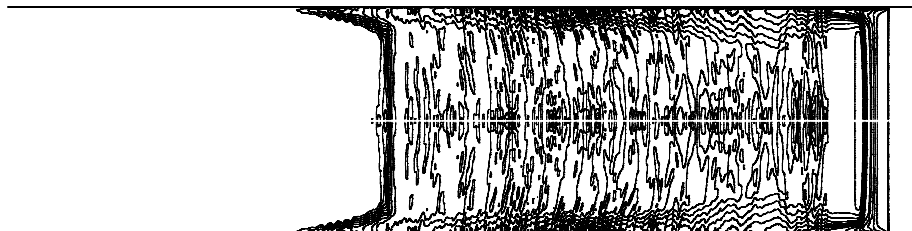


Figure 3.45: Contours of the log of density at $t=0.8\text{ms}$ for the Titan condition. $t=0\text{ms}$ when the shock wave enters the acceleration tube

3.5. AXISYMMETRIC SIMULATIONS OF THE ACCELERATION TUBE

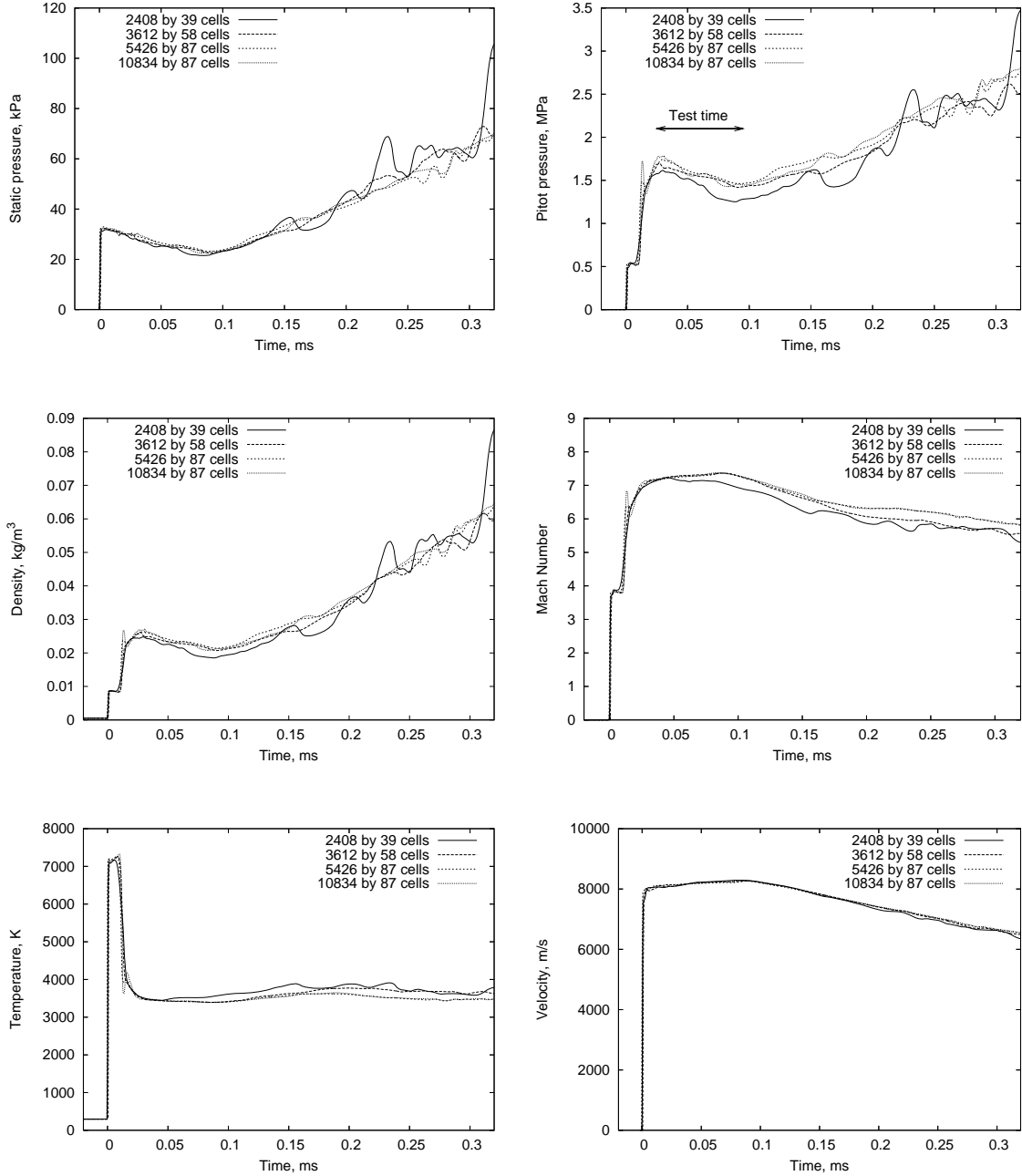


Figure 3.46: Properties from MB_CNS at the end of the acceleration tube for Air Condition 1. Varying grid resolutions for the laminar simulations.

3.5. AXISYMMETRIC SIMULATIONS OF THE ACCELERATION TUBE

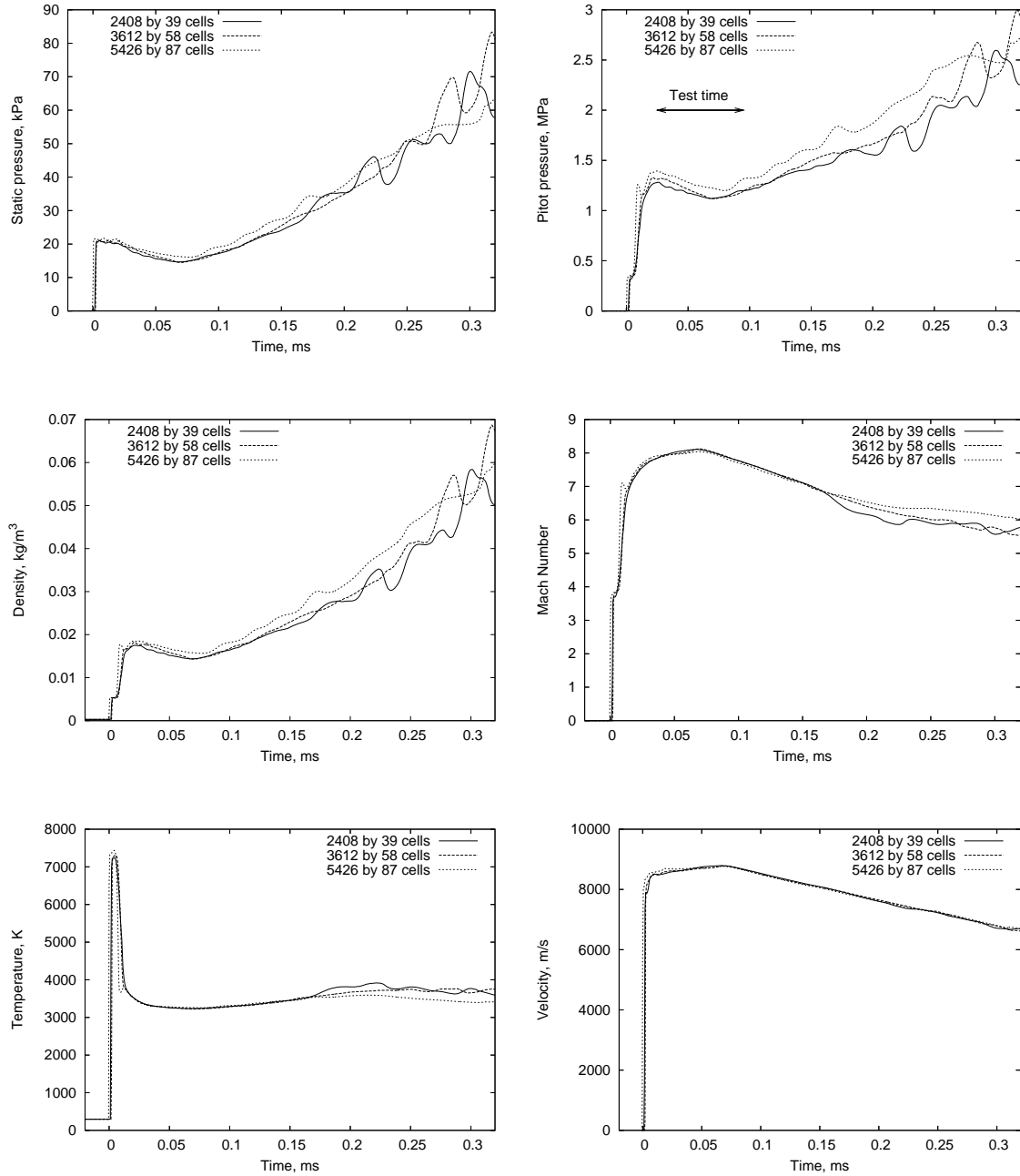


Figure 3.47: Properties from MB_CNS at the end of the acceleration tube for Air Condition 2. Varying grid resolutions for the laminar simulations.

3.5. AXISYMMETRIC SIMULATIONS OF THE ACCELERATION TUBE

Table 3.15: Summary of the properties at the acceleration tube exit for the grid refinement study for Air Condition 2

Property	Grid 1	Grid 2	Grid 3
Secondary shock speed, km/s	8.587	8.632	8.651
Static pressure, kPa	20.19	20.27	20.88
Pitot pressure, MPa	1.17	1.21	1.28
Density, g/m ³	17.0	17.5	17.7
Mach number	7.9	7.9	7.9
Static temperature, K	3300	3300	3300
Velocity, m/s	8700	8700	8700
Static enthalpy, MJ/kg	6.18	6.18	6.18
Total enthalpy, MJ/kg	40.02	40.02	40.02
Specific internal energy, MJ/kg	5.1	5.1	5.1
Unit Reynolds number	1.43×10^6	1.43×10^6	1.43×10^6

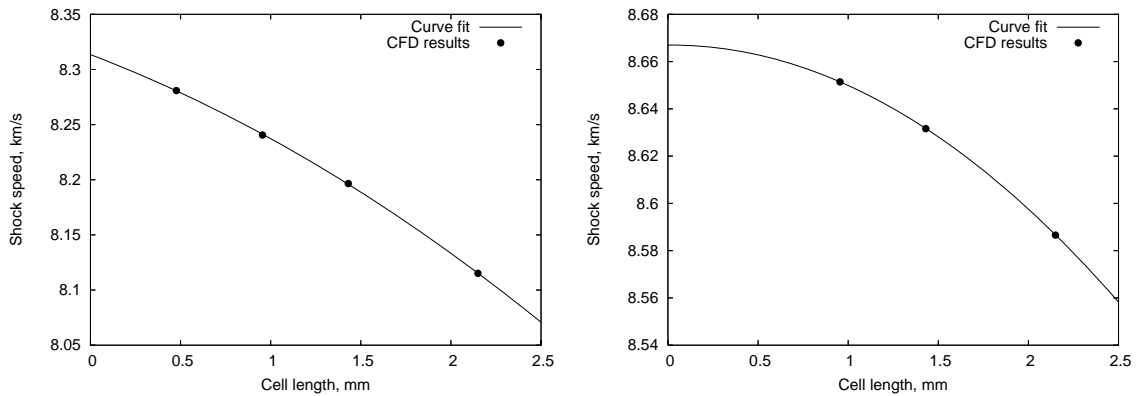


Figure 3.48: Convergence of the shock speeds for different grid resolution for the two air conditions for the laminar simulations.

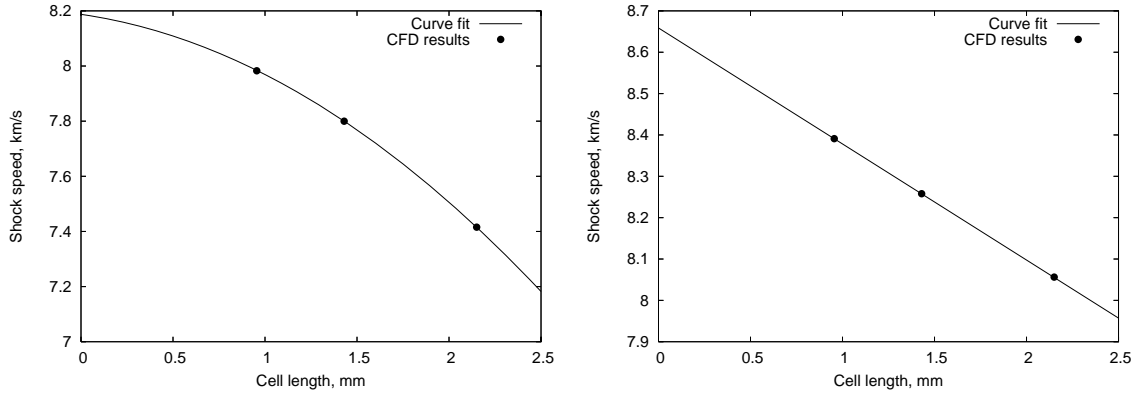


Figure 3.49: Convergence of the shock speeds for different grid resolution for the two air conditions for the turbulent simulations.

Turbulent Simulations

A grid refinement study was also performed for the turbulent simulations of the two air conditions and the Titan condition. As in the laminar case, the shock speeds were calculated by fitting a curve to the obtained results and are shown in Figure 3.49. The final shock speeds were 8.187 km/s and 8.658 km/s for Air Conditions 1 and 2 respectively. The graphs of the properties for the air conditions are shown in Figures 3.50 and 3.51. Examining the figures a pronounced dip in the pressure and density can be seen in the test time. This is significantly stronger than the gradual decrease that was seen in the laminar case. The decrease in pressure and density again corresponds to the boundary layer growth. In the turbulent case the transition from a laminar to turbulent boundary layer dramatically increases the thickness. The coarsest mesh is particularly poor as the turbulence model overestimates the viscosity and thus overestimates the thickness of the boundary layer. Though this is rectified somewhat in the finer mesh the solution would still not be fully grid independent. More cells are necessary to better capture the boundary layer. However, the computational time for a finer mesh would have been too excessive and it was assumed that the finest mesh gave a reasonable estimate of the flow. For the Titan condition in the finest mesh, no dip in the pressure at the end of the acceleration tube was evident but was in the coarser meshes. The finest mesh (grid 3) for the Titan condition better captures the boundary layer than in the air conditions.

3.5. AXISYMMETRIC SIMULATIONS OF THE ACCELERATION TUBE

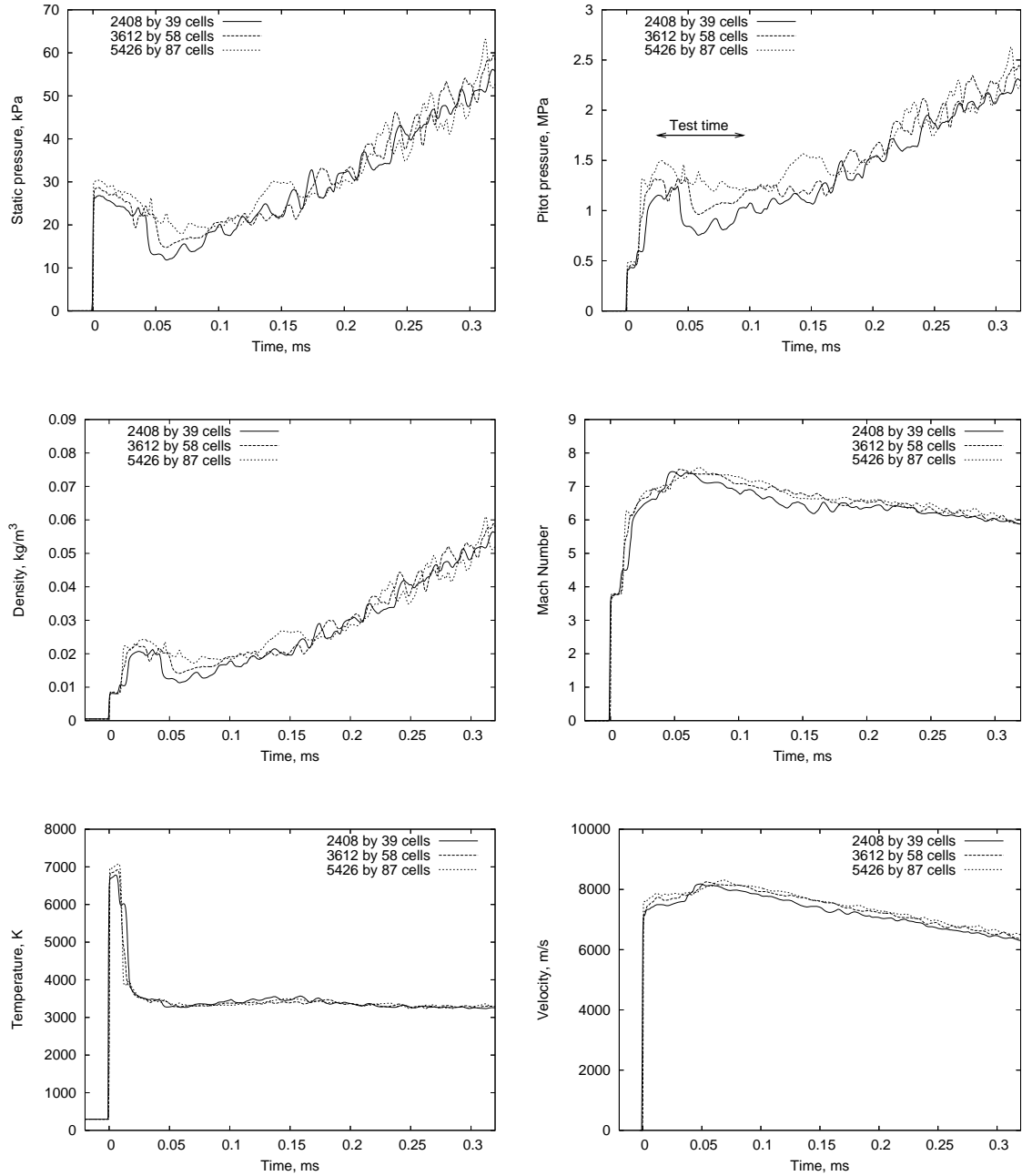


Figure 3.50: Properties from MB_CNS at the end of the acceleration tube for Air Condition 1. Varying grid resolutions for the turbulent simulations.

3.5. AXISYMMETRIC SIMULATIONS OF THE ACCELERATION TUBE

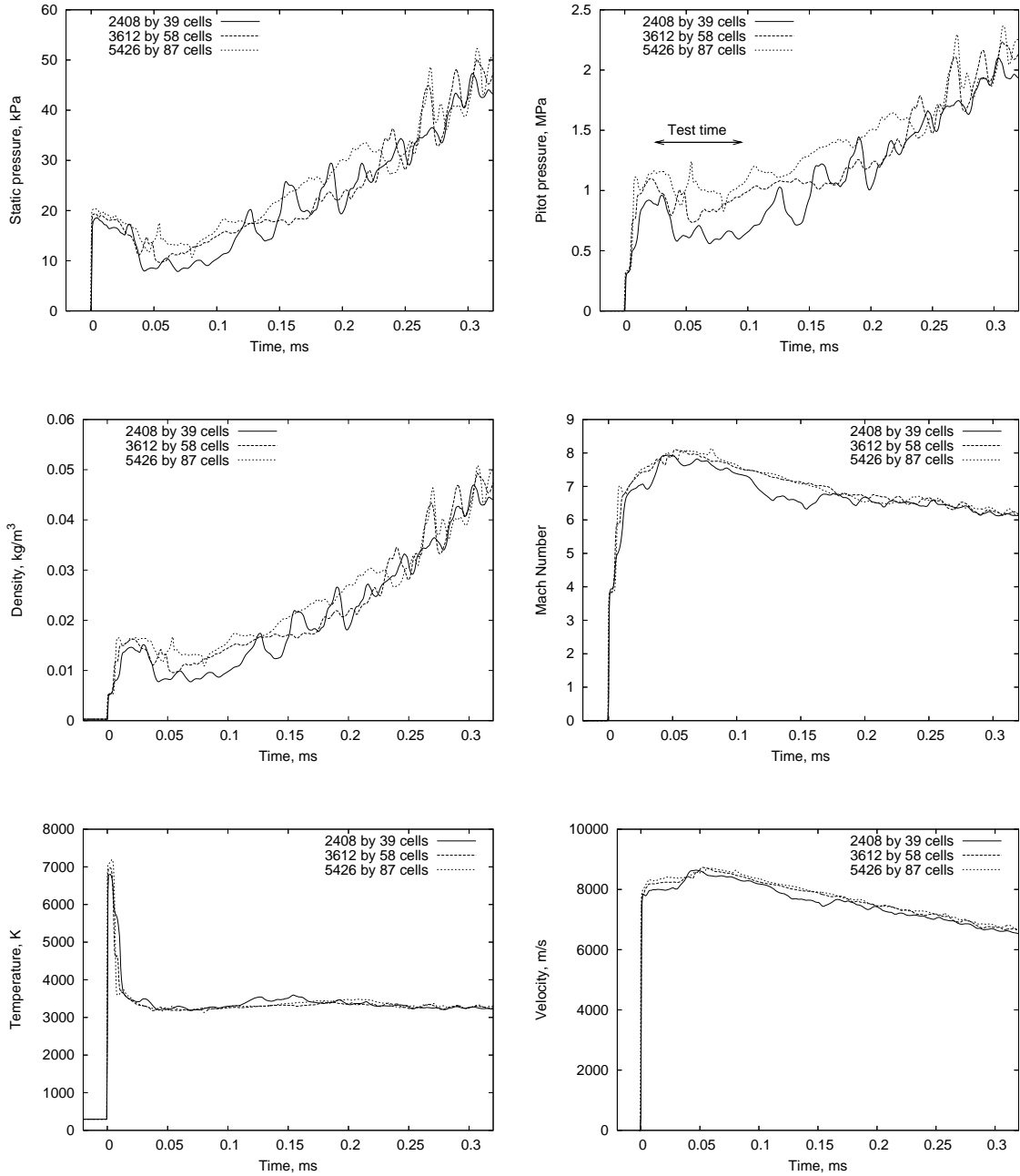


Figure 3.51: Properties from MB_CNS at the end of the acceleration tube for Air Condition 2. Varying grid resolutions for the turbulent simulations.

3.6 Summary

The one-dimensional code, L1d, was used to model the entire X2 expansion tube including the compression process. Parameters such as compression ratio and fill pressures were determined to obtain an initial target condition for the new single-stage, free-piston driver arrangement. The simulations were also used to choose a piston mass as it was not yet fabricated at the time of the work. The target condition used air as the test gas and the desired secondary shock speed was 8.5 km/s.

L1d has previously been used in modelling expansion tube flows but predominantly for two-stage driver configurations. When the current work was undertaken, it was thought that the code would be adequate to model the compression process for the single-stage driver. However, problems were encountered. These were consistent with what was seen in the old two-stage configuration and are due to the code's one-dimensional nature and the heat loss models incorporated in it. The deficiencies result in a temperature that is too high and a length that is incorrect in the slug of compressed driver gas located next to the primary diaphragm before rupture. The incorrect modelling of the compression process in L1d was rectified by rerunning the simulations from the time of the primary diaphragm rupture. The length and temperature of the slug of driver gas were altered so that the shock tube pressure traces at st1, st2 and st3 matched the experimental values. This was done for two air conditions, a Titan condition and a Jovian condition.

The modified air simulations provided excellent agreement between the computational and experimental primary shock speeds. The altering of the conditions in the driver gas slug reduced the freestream test properties at the end of the acceleration tube. Thus a second air condition was examined which had a slightly higher secondary shock speed. In the numerical simulation of the Titan condition the primary shock speed had an error of 5% from the experiments. This was due to reflected waves that were not captured correctly by L1d. The modified Jovian simulation produced a primary shock speed within 1% of the experimental values.

A more detailed description of the test flow was required so axisymmetric simulations of the acceleration tube were conducted. The hybrid simulations use the modified one-dimensional model up to the secondary diaphragm and the axisymmetric code, MB_CNS, in the acceleration tube. The flow from L1d fractionally after the secondary diaphragm is

used as transient uniform inflow into the axisymmetric model. The full hybrid simulations used a large amount of computational effort (on the order of months of CPU hours per calculation) especially when turbulence and finite-rate chemistry were included.

A comparison of equilibrium and finite-rate MB_CNS simulations for the air conditions showed that dissociation of the test gas in the shock tube occurred. Recombination of the gas through the unsteady expansion was not complete and resulted in the oxygen atoms becoming frozen. The laminar and turbulent simulations indicated that a large number of cells was required in the boundary layer to accurately capture it. The transition to a turbulent boundary layer occurred in the test gas. This work showed that modelling the boundary layer correctly and finite-rate chemistry effects should be included in simulations of the expansion tube but how they effect the thermodynamic test properties is discussed in the next chapter. It also looks at how accurately L1d and MB_CNS predict the test flow conditions compared to the experiments.

CHAPTER 4

The New X2 Expansion Tube

Hardware

This chapter begins by examining the new hardware for the single-stage, free-piston driver installed on X2 and the changes that were made in its implementation. It then presents the results from the first series of experiments which were conducted in the modified facility. Initial blanked off tests aimed to ensure that the driver was functioning correctly and attaining the pressures required for rupture of the primary diaphragm. Following this, four conditions were examined in the commissioning of the new facility. Experiments targeted two air test gas conditions, a Titan test gas condition and a Jupiter test gas condition. Each of these were relevant to a past or present aerospace mission and could be used for modelling or the basis of a future project. The experimental results from the four conditions are compared to and used to validate the one-dimensional and axisymmetric simulations from the previous chapter. Any discrepancies between the two methods are examined and features which are important in the computational models are investigated.

4.1 The Old Driver

The T4 shock tunnel and X-series of expansion tubes located at the University of Queensland use free-piston drivers to generate the energy required for producing high speed flow. The X2 expansion tube and the larger X3 expansion tube were both originally designed with a compound piston driver, which compresses the gas in two distinct stages. A schematic of the original X2 expansion tube configuration is shown in Figure 4.1. The

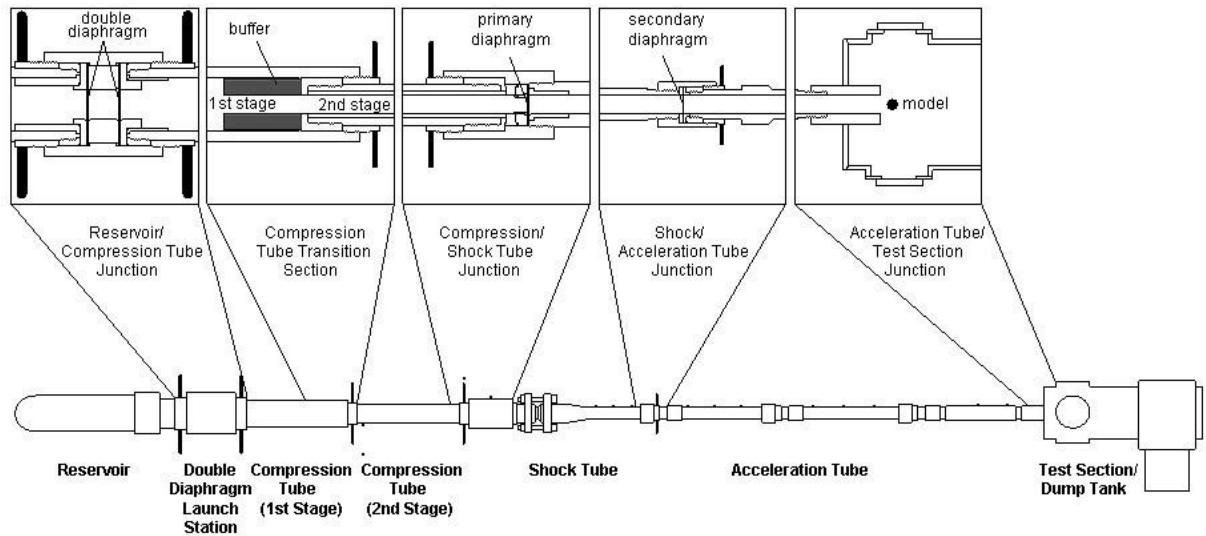


Figure 4.1: Schematic of the old X2 configuration. Taken from [6].

furnishing of X2 with a two-stage piston was solely as a prototype for the larger X3. Doolan [64] gives a comprehensive coverage of the commissioning of X2. Now that X3 is operational, there is no longer a need for the compound piston arrangement on X2. Thus, a new single-stage driver has been installed.

Section 2.2.2 explains the differences between a single-stage and two-stage, free-piston driver. To recapitulate, in a single-stage driver a piston is driven down the compression tube by high pressure reservoir gas. This compresses the driver gas in front of the piston (usually helium, argon or a mixture of both) and when the gas reaches a certain pressure it ruptures a steel diaphragm. In a two-stage piston driver two pistons held together travel down the first stage of the compression tube compressing the driver gas. Upon reaching the second stage of the compression tube, the light primary (or carrier) piston is stopped and the heavy secondary stage piston separates and continues to travel down the compression tube. The advantages of this design are that it reduces the length and size of the facility and decreases the cost. This was the motivation for the use of a compound piston on the two larger facilities at the University of Queensland. Unfortunately, this reduction in cost compromises the performance and ease of operation of the facility.

4.2 The New Driver

A schematic of the new single-stage driver is shown in Figure 4.2. This design has a number of features which are advantageous when compared to the old layout. They are:

- it sustains larger burst pressures across the primary diaphragm
- it has a maximum compression ratio of 60.2 with an initial driver gas volume of 0.224 m^3
- it has a large area ratio of 9 just before the primary diaphragm
- it has a 1.3 m longer shock tube with a new length of 3.424 m

The first two design features listed provide benefits because they produce a stronger shock wave in the shock tube. This means the facility achieves higher shock speeds and pressures. The third attribute assists with driving the shock wave down the shock tube. The old configuration generated an insufficient slug of gas to drive the shock wave and this resulted in primary shock wave attenuation [16]. The area ratio improves this problem as seen in the previous chapter.

Further to above, another advantage is that the piston launching station is now much simpler with the removal of the double diaphragm launcher. Brakes were not installed on the piston. In the old arrangement brakes were required when the the primary diaphragm did not burst. They would stop the secondary piston travelling back up the compression tube and striking the primary piston. In general, the operation of the tube is much easier with only one piston.

The fabrication of the new driver and the associated components was completed in mid to late 2003 and the installation of the new driver was completed in April 2004. The layout of the new X2 configuration is shown in Figure 4.3 and a picture of the new facility in Figure 4.4. The total length of the facility is now 17.3 m. The existing reservoir, shock tube, acceleration tube and dump tank remained the same in the modified arrangement. The new pieces constructed were a piston, a piston launching station, a compression tube, a frame for the compression tube, a new sliding frame for the shock tube, a buffer assembly and two couplings to connect the old shock tube to the new driver section.

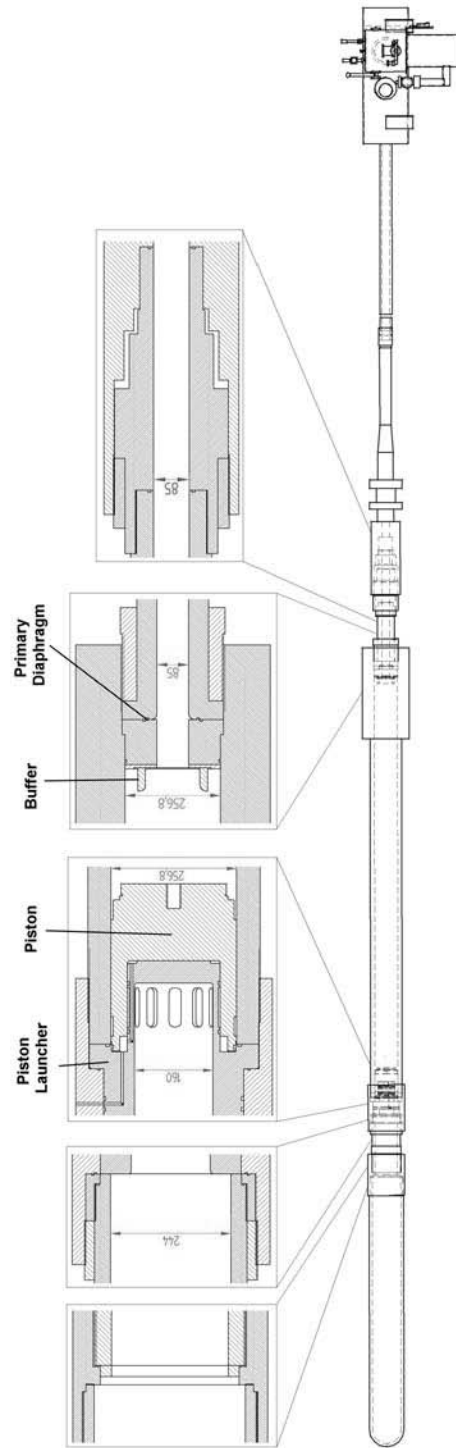


Figure 4.2: Schematic of the new X2 expansion tube

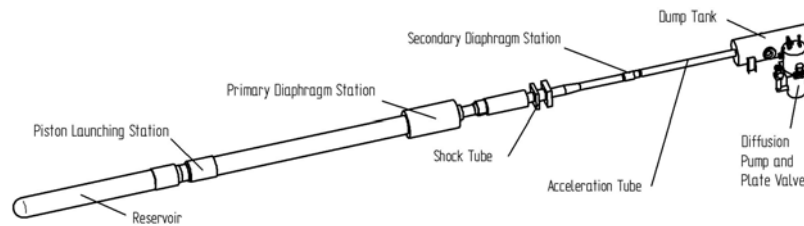


Figure 4.3: Layout of the new X2 expansion tube

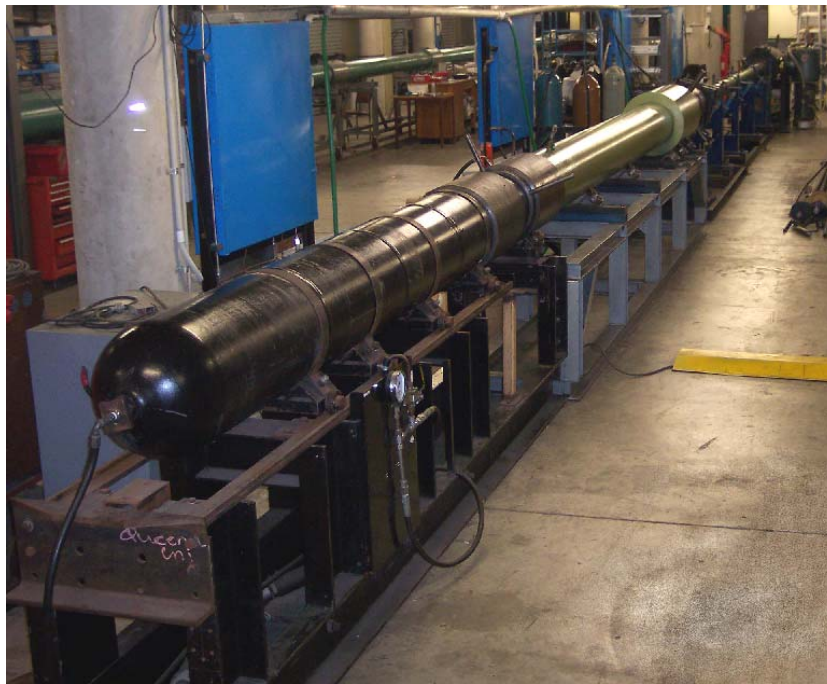


Figure 4.4: The new X2 expansion tube

The new compression tube is 5 m long, weighs 2.7 tonne and has an internal diameter of 256.8 mm. A picture of the section installed on its frame in the new facility is shown in Figure 4.5. At the reservoir end the driver screws into an existing piece and the piston launching station is located here. The downstream end of the driver tube houses the primary diaphragm and buffer assembly. It is attached to the shock tube via two couplings and two capstan nuts.

The new piston launcher for the piston launching station is shown in Figure 4.6. The new piston is shown in Figure 4.7. The total mass of the fully assembled piston is 35 kg, its length is 341 mm and the diameter without the seals and wear rings is 255.8 mm. Two wear rings allow the piston to slide smoothly in the tube while a chevron seal located at the front of the piston prevents leakage of the driver gas. The chevron is similar to



Figure 4.5: The new X2 compression tube

those on the other pistons at the University of Queensland and works by small holes in the brass holder allowing high pressure gas from the front face of the piston into a small cavity between the brass holder and seal. This gas pushes the chevron seal out and provides the force to seal. To conduct an experiment in the tube, the piston is held on the launcher by a vacuum in the small line located in the piston launcher behind the piston. The compression tube is then filled with driver gas. To fire the piston, the vacuum is shut off and high pressure reservoir gas is allowed to flow into the small space behind the piston. This allows the piston to move forward and the reservoir gas can then flow through the slots in the piston launcher.

As mentioned before, two couplings were fabricated to connect the existing shock tube to the new compression tube. They are pictured in Figure 4.8 and a schematic of their layout is shown in Figure 4.9. The downstream end connects to the shock tube and is held permanently in place via a capstan nut. The upstream end slides into the new driver section and is also held in place via a capstan nut. This nut needs to be undone to allow access to the primary diaphragm station. Located in front of this is the buffer assembly comprised of the buffer, buffer locator and buffer plate. The primary diaphragm sits between the buffer locator and the end of the new coupling. The purpose of the rubber buffer is to stop the piston and absorb any remaining energy. Hopefully the velocity of the piston is close to zero upon impact thus reducing the energy absorbed by the buffer and the deformation it sustains. The buffer is the same as the one used on the T4 shock tunnel and at the time of writing required replacing after approximately 20 to 30 shots.

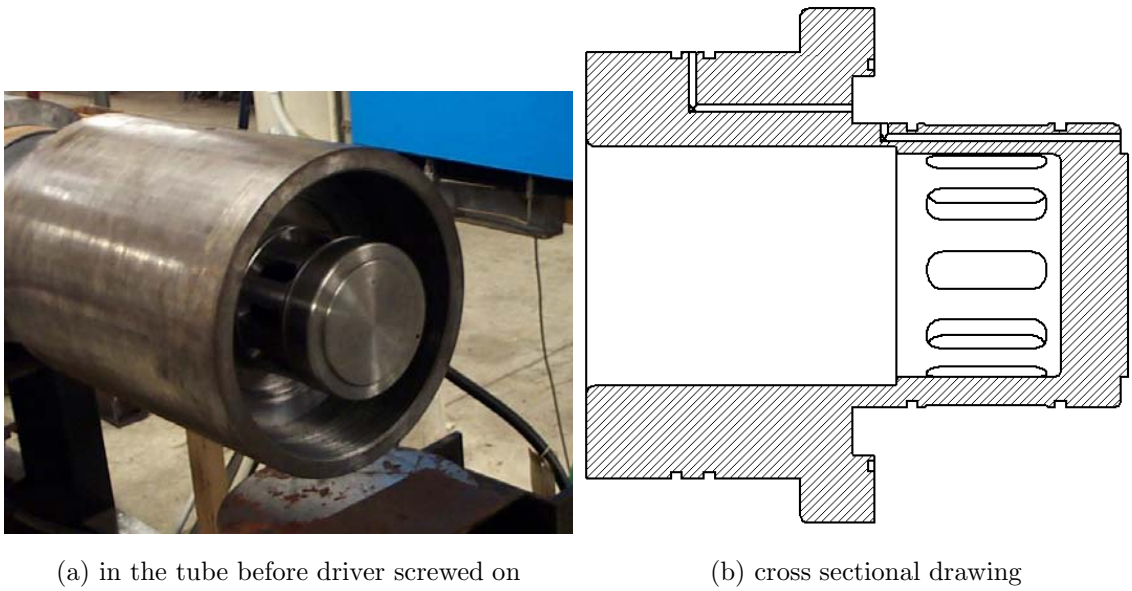


Figure 4.6: The new X2 piston launching station

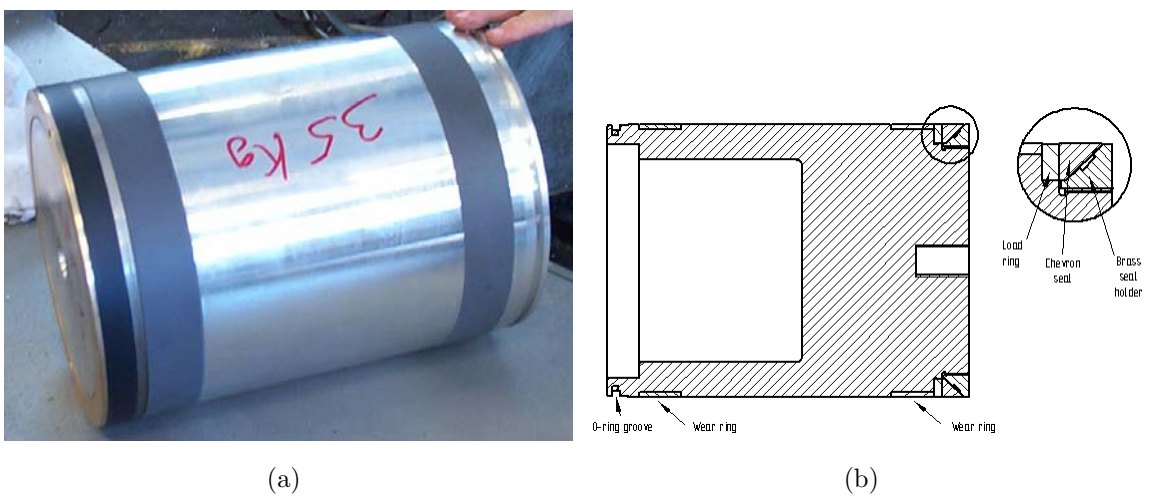


Figure 4.7: The new X2 piston



(a) together



(b) installed in the tube

Figure 4.8: The new X2 couplings

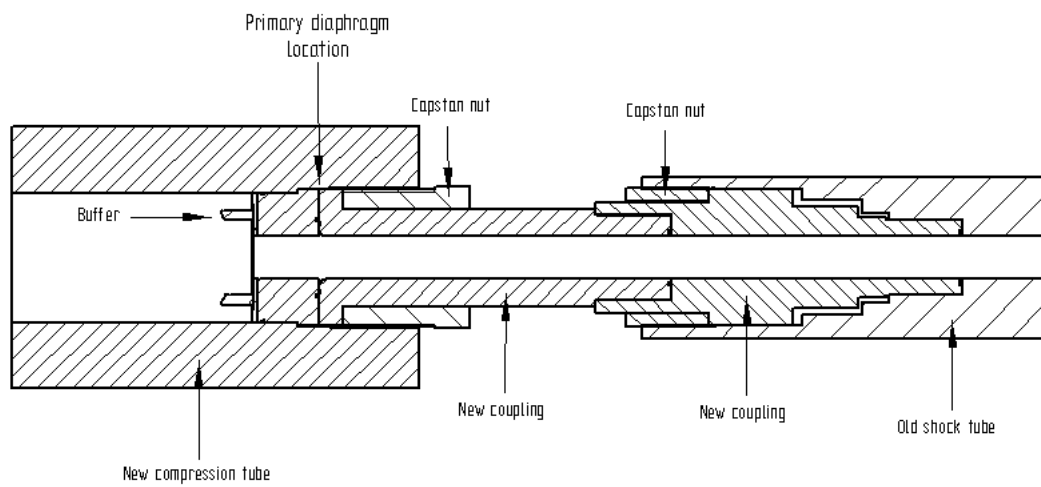


Figure 4.9: Section view of the X2 primary diaphragm station and the new couplings



Figure 4.10: The new X2 buffer assembly

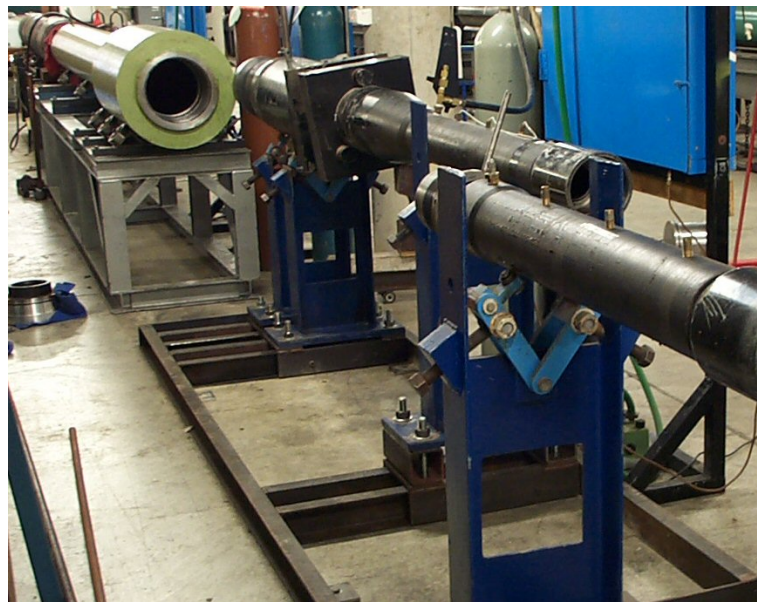


Figure 4.11: The new X2 shock tube frame

A new frame for the X2 shock tube section was fabricated. This frame was comprised of three existing stands placed upon three new rollers. The tube sat upon the stands and the configuration enabled the shock tube to be slid laterally, allowing the piston to be pushed back up the compression tube and relocated on the piston launcher after each shot. The design is shown in Figure 4.11.

4.3 X2 Experimental Results

Four conditions were examined in this thesis and the experimental results from them are presented here. They consisted of two air conditions, a Titan condition and a Jupiter condition and have already been introduced in the numerical modelling section. The two air conditions were similar with the only difference being the acceleration tube fill pressures. All the data presented in this section is without a nozzle attached.

4.3.1 Blanked Off Tests

Preliminary experiments (or shots, as they are referred to) were performed at the beginning of May 2004 to ensure that the new driver was operational and obtaining sufficient burst pressures in the compression tube. For these shots a 30 mm steel primary diaphragm was used so that it would not rupture and the peak barrel pressure in the driver obtained. The steel diaphragm was mounted with three PCB pressure transducers to measure the driver gas pressure. The results from two experiments, shot 6 and shot 7, can be seen in Figure 4.12. Shot 6 had a reservoir fill pressure of 1.35 MPa while for shot 7 it was increased to 1.65 MPa. The solid line in these graphs is the driver pressure from CFD simulations using L1d to model the blanked off tests. There is excellent agreement between the experiment and the numerical models. The only discrepancy that can be discerned is in both shots between the transducer 109B11 SN4884 and the other lines. On shot 7 the numerical data and the other two transducers both gave pressures of 24.5 MPa, while transducer 109B11 SN4884 gave a pressure just above 25 MPa. It was assumed that this was a problem with the transducer reading. Upon re-calibration of the transducer the problem was rectified. With a rupture pressure of approximately 24 MPa required for the first condition to be targeted, it was concluded that the tube was ready for full operation.

4.3.2 Air Conditions

For the first full experiment conducted, shot 8, the same driver fill conditions as the blanked off shot 7 were used while the reservoir fill pressure was increased to 1.7 MPa in order to ensure rupture of the primary diaphragm. However, the diaphragm did not burst. Shot 7 reached a maximum pressure of 24.5 MPa and it was thought that the increase of reservoir fill pressure from 1.65 MPa to 1.7 MPa would certainly produce sufficient

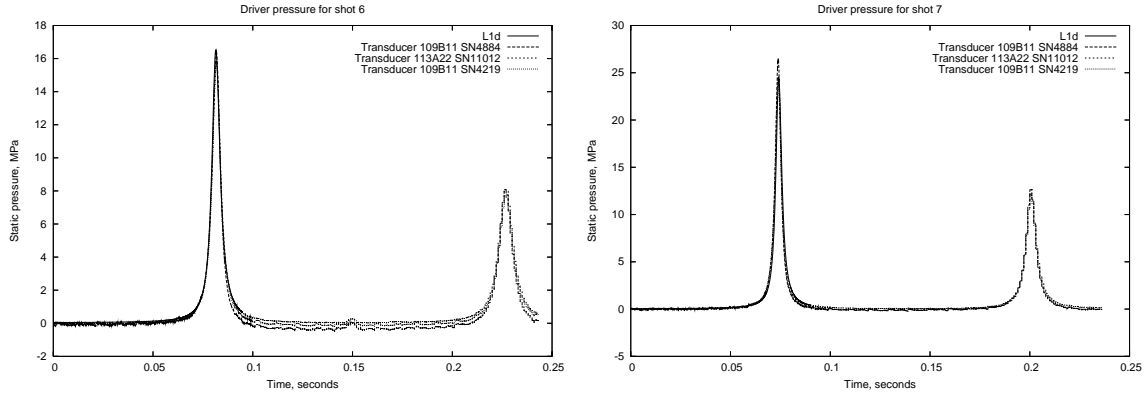


Figure 4.12: Pressure traces in the driver section for the blanked off tests

pressure. The diaphragm, though, was extremely close to rupturing as could be deduced from the amount of deformation it sustained. For the next experiment the reservoir fill pressure was increased to 1.8 MPa and the diaphragm burst. The piston must have hit the buffer with excess energy as the diaphragm was jammed onto the tube. A slight increase in energy must have been required to increase the pressure to fractionally above 24.5 MPa. Following this the reservoir fill pressure for each shot was slightly decreased to a value of 1.75 MPa which is currently used. Ideally a pressure transducer would measure the driver barrel pressure for each shot but the facility was not designed with one. It would be difficult now to move the large driver section to a lathe to install one.

These values of reservoir fill pressures used provide some discrepancies with L1d. In Section 3.2.3 the L1d simulation produced an optimal reservoir fill pressure of 1.56 MPa which is below the 1.75 MPa in the experiments. This difference is due to a number of different reasons. Firstly, in the experiments the small space behind the piston is at a vacuum to hold the piston on the launcher. Upon release of the valve (to allow reservoir gas into this space) the pressure will decrease. This would account for a small percentage (5 %) of the difference between the experimental and computational results. Some of the remaining portion can be explained by the viscous loss coefficients used in the one-dimensional code. The value of 0.5 used at the piston launching station was probably an underestimate. This was calculated by taking the area of the slots as a ratio of the area of the driver tube then adding a bit extra for turbulent effects. In reality there is a contraction into the piston launcher then an expansion out to the driver. There are also going to be extra turbulent losses caused by the slots. The value of 0.5 should be made

larger or another loss factor added. The second loss coefficient at the primary diaphragm station is also incorrect. The value should be 0.5 for an area ratio of 9 not 0.35. This was the author's mistake as the diameter ratio of 3 and not the area ratio was used to calculate this. There was, however, little point rectifying this as there are so many other factors that create differences (and in the end it would only slightly change the conditions in the slug of driver gas before primary diaphragm rupture). These values are corrected for the final simulations as already discussed in Section 3.4. Furthermore, these head loss coefficients are calculated using fluid mechanics for a steady, incompressible flow and the current problem is not in this flow regime. Lastly the coefficient of friction for the seal on the tube wall is only an approximation. The value of 0.4 used could actually be as low as 0.1 or 0.2. A reduction in the coefficient of friction on the piston in L1d would decrease the optimal fill pressure further and this may compensate for some of the effects above.

Even if the issues with the loss coefficients and friction factors was completely resolved, L1d would still not provide exact modelling of the tube. As discussed in Section 3.4, the one-dimensional nature combined with the deficiencies in the heat loss model would give incorrect temperatures. For the X-series of expansion tubes this results in a compression process that has an underestimated pressure and slug lengths that are too long. However, it is still sufficient for modelling up to the secondary diaphragm.

The complete set of gas fill properties for the two air conditions are shown in Tables 4.1 and 4.2. The primary diaphragm was 1.6 mm thick cold rolled steel and the secondary diaphragm was three sheets of approximately 0.015 mm thick polyethylene produce bag. For all the experiments conducted in this thesis, flush mounted transducers were placed along the length of the tube to measure static pressure. A schematic of the layout of the transducers is shown in Figure 4.13 while the distances of the transducers from the primary diaphragm is shown in Table 4.3. For all the experiments without the nozzle, a Pitot rake containing four probes was placed at the exit of the acceleration tube. Their positions are shown in Figure 4.14. Their mounting arrangement was the typical shielded PCB pressure transducer that has been used frequently in the X-series of expansion tubes. A schematic diagram is shown in Figure 4.15.

The shock tube pressures were matched in Chapter 3; the focus of this chapter will be the acceleration tube flow. A summary of the test flow data for the two air conditions is given in Tables 4.4 and 4.5. Here, as well as in the rest of this thesis, the experimental

Table 4.1: Fill conditions for the Air Condition 1 experiments

Reservoir fill pressure	1.75 MPa
Compression tube fill pressure	48 kPa
Shock tube fill pressure	9.6 kPa
Acceleration tube fill pressure	43 Pa
Primary diaphragm burst pressure	24 MPa
Secondary diaphragm burst pressure	Approx. 12 kPa
Driver gas	Helium
Test gas	Air
Acceleration tube gas	Air

Table 4.2: Fill conditions for the Air Condition 2 experiments

Reservoir fill pressure	1.75 MPa
Compression tube fill pressure	48 kPa
Shock tube fill pressure	9.6 kPa
Acceleration tube fill pressure	26 Pa
Primary diaphragm burst pressure	24 MPa
Secondary diaphragm burst pressure	Approx. 12 kPa
Driver gas	Helium
Test gas	Air
Acceleration tube gas	Air

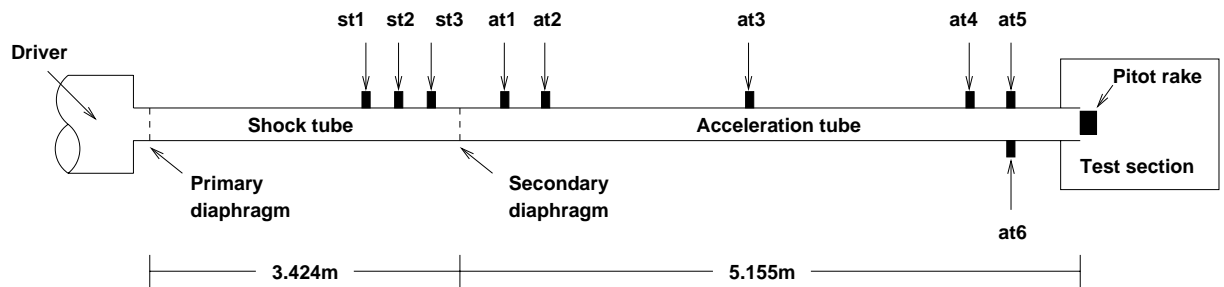


Figure 4.13: Schematic of the pressure transducer locations

Table 4.3: Location of the flush mounted static pressure transducers

Pressure transducer name	Distance from the primary diaphragm (m)
st1	2.572
st2	2.804
st3	3.036
at1	3.955
at2	4.205
at3	6.019
at4	7.865
at5	8.045
at6	8.045

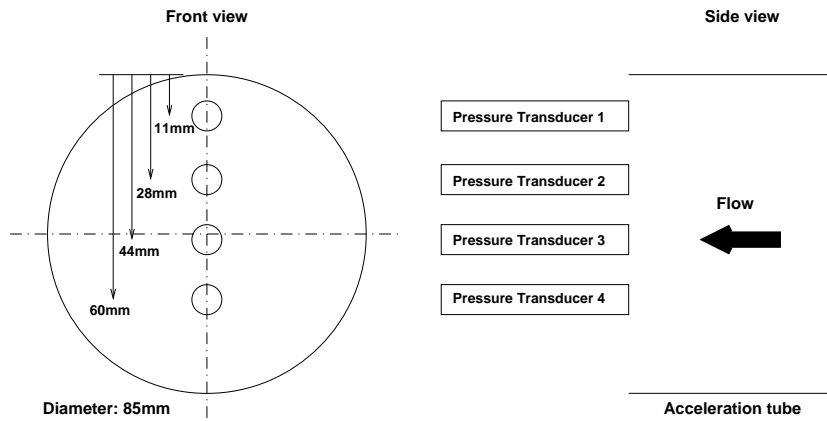


Figure 4.14: Pitot pressure rake at the acceleration tube exit plane

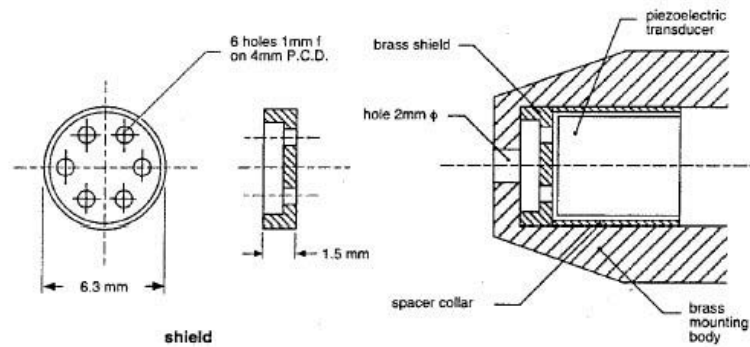


Figure 4.15: Shielded PCB pressure transducer arrangement. Taken from [7].

data is an average from all the shots that were performed. At least four shots were conducted for each condition to ensure repeatability. The shot-to-shot variation for the two air conditions is shown in Table 4.6. These are given as a percentage of the average values presented in Tables 4.4 and 4.5. The variations shown arise from errors in the measurements that are examined in the next paragraph. The primary shock speed was calculated from the static pressure readings at st1 and st3 while the secondary shock speed was calculated from the static pressure readings at at3 and at6. The arrival time of the shock wave can be seen in these graphs. The average shock speed can then be found by dividing the distance between the two transducers by the time it takes the shock wave to travel between the two transducers. The experimental static pressure values at the end of the acceleration tube were averaged over the three transducers at4, at5 and at6. Only the transducer probes that lay in the core flow were used for calculating the average experimental Pitot pressure. These were the transducers 2, 3 and 4 as shown in the Pitot rake in Figure 4.14.

Table 4.4: Summary of the flow properties at the acceleration tube exit for Air Condition 1

Property	L1d	MB_CNS	MB_CNS	MB_CNS	MB_CNS	Experiments
	viscous	viscous, laminar equilibrium	viscous, turbulent equilibrium	viscous, laminar viscous, finite rate	viscous, laminar viscous, finite rate	Experiments
Primary shock speed, km/s	4.46	-	-	-	-	4.46
Secondary shock speed, km/s	7.90	8.313	8.187	8.279	8.14	8.14
Static pressure, kPa	28.5	29.47	27.50	30.66	29.74	29.74
Pitot pressure, MPa	1.05	1.65	1.35	1.65	1.54	1.54
Density, g/m ³	21.5	24.5	22.0	31.5	-	-
Mach number	5.4	7.3	7.3	7.2	-	-
Static temperature, K	4500	3450	3450	2800	-	-
Velocity, km/s	7.1	8.2	7.8	8.2	-	-
Static enthalpy, MJ/kg	9.0	6.33	6.32	6.33	-	-
Total enthalpy, MJ/kg	34.2	39.95	36.74	39.95	-	-
Specific internal energy, MJ/kg	7.5	5.08	5.0	5.3	-	-
Unit Reynolds number	1.64×10^6	1.87×10^6	1.56×10^6	3.28×10^6	-	-
Test time, μ s	45	70	70	70	55	55

Table 4.5: Summary of the flow properties at the acceleration tube exit for Air Condition 2

Property	L1d	MB_CNS	MB_CNS	MB_CNS	Experiments
	viscous	viscous, laminar equilibrium	viscous, turbulent equilibrium	viscous, laminar finite rate	Experiments
Primary shock speed, km/s	4.46	-	-	-	4.46
Secondary shock speed, km/s	8.31	8.667	8.658	8.638	8.61
Static pressure, kPa	21.0	20.88	19.17	20.98	19.14
Pitot pressure, MPa	0.85	1.28	1.10	1.27	1.20
Density, g/m ³	14.0	17.7	16.1	19.9	-
Mach number	5.6	7.9	7.9	8.0	-
Static temperature, K	4600	3300	3250	2500	-
Velocity, km/s	7.7	8.7	8.5	8.5	-
Static enthalpy, MJ/kg	9.6	6.18	6.09	5.75	-
Total enthalpy, MJ/kg	39.2	40.02	42.21	41.88	-
Specific internal energy, MJ/kg	8.0	5.1	4.9	4.8	-
Unit Reynolds number	1.14×10^6	1.43×10^6	1.27×10^6	2.62×10^6	-
Test time, μ s	50	70	70	70	55

Table 4.6: Shot-to-shot variation in the flow properties for the air conditions

Property	Air Condition 1	Air Condition 2
Primary shock speed	1.1 %	1.1 %
Secondary shock speed	0.8 %	0.4 %
Static pressure	24.1 %	18.1 %
Pitot pressure	2.9 %	1.8 %

It is well known that impulse facilities can produce large levels of noise [103]. The expansion tubes at the University of Queensland are no different and have been prone to minor sources of errors which hinder their operation. The problems arise from incorrect acceleration tube fill pressure readings as well as the noisy PCB pressure transducer signals. It is hard to place a quantitative value of the error caused by these problems. In this thesis, the uncertainties in the flow properties have been calculated and then these problems investigated. The uncertainties are defined in the standard way such that the given band produces a range in which the true value is 95 % certain to lie.

The uncertainty in the experimental shock speed came from the measurement of the distance between the transducers as well as the measurement of the time it took for the shock to travel between them. The sampling rate of the data acquisition equipment was set as $1 \mu\text{s}$. This equates to an uncertainty of $\pm 2 \mu\text{s}$ in the calculated time. The uncertainty in the measured distances was $\pm 2 \text{mm}$. This led to an uncertainty of $\pm 1.97 \%$ for the primary shock speed. The uncertainties for the secondary shock speeds were $\pm 0.80 \%$ and $\pm 0.86 \%$ for Air Condition 1 and Air Condition 2 respectively. The reason the transducers at3 and at6 were used to calculate the shock speed was to account for any attenuation that may have occurred as the shock travelled down the tube. Only a slight amount of attenuation was seen down the acceleration tube in both the experimental and computational methods. In the computational method, the shock speeds quoted were also for the latter section of the acceleration tube.

The static pressure along the tube wall and the Pitot pressure in the core flow were measured using PCB pressure transducers. The uncertainty in the calibration of these transducers is specified as $\pm 1 \%$ by the manufacturer. Previous work by Hayne [111] in the X2 expansion tube investigated the effect of the flush mounting of the static pressure

Table 4.7: Noise levels in the experiments for the air conditions

	Air Condition 1	Air Condition 2
Static pressure	$\pm 6\%$	$\pm 7\%$
Pitot pressure	$\pm 13\%$	$\pm 17\%$

transducers. Part of the present thesis involved fabricating new transducer mounts for the entire X2. Despite this work, the alignment of the transducers with the tube wall would not have been perfectly flush. Hayne reported that a transducer which protruded into the flow would have a slightly higher reading than the real pressure due to the compression of the gas over the end of the transducer. It was concluded by Hayne that the uncertainty in the static pressure reading due to the X2 transducer mounting configuration was $\pm 4\%$. This value was also used here for the static pressure uncertainty while a value of $\pm 1\%$ was used for the Pitot pressure uncertainty.

Though the above values were given for the uncertainties in the pressure measurements, the variation levels during the test time were much larger than this. The noise levels from the experiments which were defined as the variation in the signals from the average values is seen in Table 4.7. The percentage of these variations which was actual unsteadiness in the flow and how much was noise caused from outside sources such as measurement techniques is debatable. This has been the focus of numerous studies in expansion tubes [112, 111, 108, 113] but no definitive answer exists despite the large amount of work. Effects such as noise created from unsteadiness in the flow, stress waves through the tube walls, temperature effects on the transducer sensor and noise generated from the transducer mounting arrangement can all be attributed to causing perturbations in the flow properties which do not actually exist in the flow. Real unsteadiness in the flow can result from acoustic waves caused upon rupture of either diaphragm or noise radiated from the boundary layer. The majority of the acoustic noise created by the rupture of the primary diaphragm is trapped in the driver gas by the speed of sound buffer, so is usually unimportant.

An abundance of work in supersonic and hypersonic wind tunnels in general has showed that the noise has an effect on boundary layer transition. More relevant to the current discussion is that acoustic noise radiates from the turbulent boundary layer [103]. Erdos

and Bakos [113] state the best way to develop a quiet shock/expansion tunnel is to avoid a turbulent boundary layer. This, however, is not always possible. Simply stated, noise will exist in expansion tubes but, still to this day, the measurement techniques contribute to the fluctuations which are shown in the test time.

The noise in the experiments in the static and Pitot pressure during the test time make it hard to determine a precise experimental value. The test time in this thesis was defined to end upon arrival of the downstream, tail edge of the unsteady expansion. In this thesis, the best effort was made to estimate a value from the graphs that was most indicative of the level seen in the test time.

The noise in the experimental static pressure traces at the end of the acceleration tube tended to be high frequency oscillations at the natural frequency of the transducer. In reality these oscillations were much larger than those shown in the experimental plots but the data was filtered to remove the majority of the noise. Small traces of the oscillations still remain in the experimental plots. Despite this, the results are predominately steady in the test time while flow features such as the shock wave and unsteady expansion are clearly evident.

The Pitot pressure graphs were considerably noisy with many fluctuations of random nature. Buttsworth and Jacobs [114] studied fluctuations caused by the shielded pressure transducer arrangement. Axisymmetric numerical simulations by Jacobs (private communication) showed that the fluctuations seen in Buttsworth's experiments were caused by the mounting configuration of the transducer. A cavity is situated in the front of the sensor to protect the sensor from debris which can travel down the tube. Waves can form in the cavity which alter the reading of the transducer and create noise that is not in the flow. Another source of noise could be high temperature effects. The PCB pressure transducers used have a temperature range only up to a value of 135 °C. The temperatures in the core flow of the X2 expansion tube are over an order of magnitude large than this. A recent study by Richards [115] showed that applying heat to the PCB transducers can dramatically effect the signal produced. Coatings such as vacuum grease and cellophane could reduce the effects of a thermal load but not completely remove them. In all the shots in this thesis a very light coating of vacuum grease was placed on the sensor then a single layer of plastic bag adhered to this. The evidence presented here supports the argument stated before, that there is noise and unsteadiness in the flow but the mea-

surement techniques exacerbate the noise. Another problem is that the time required to fill the cavity can be large when compared to the scale of the test time. This prompted the use and development of bar gauges by Neely and Morgan [36]. The design was based on that of Mudford et al. [116]. Sutcliffe and Morgan [117] continued the development to reduce noise of the signals produced by the bar gauges. Chiu [112] further developed the gauges so that they were reusable and easier to manufacture. The ideal technique for measuring Pitot pressure in an expansion tube is still not well established.

The fill pressures in the shock and acceleration tube were measured with Varian WV100-2 wide range diaphragm manometers which had platinum alloy Pirani sensors. The manufacturer specifies an error of $\pm 3\%$ or $\pm 0.3\text{ Pa}$ in the measurement. An Edwards Barocel Type 600 vacuum/pressure transducer with a digital display was also used to measure the fill pressures. The error claimed by the manufacturer for this was $\pm 0.15\%$, over the entire measurement range. In the expansion tubes located at the University of Queensland, the measurement of the acceleration tube fill pressures have been a problem in the past. The low values, in the order of a few Pascals, have been hard to measure accurately. The fill pressures with the new driver are an order or magnitude higher but their measurement still presents problems. Doubts may be cast about whether the uncertainty provided by the manufacturers for the gauges is correct across the entire measurement range. Especially at lower pressures, the readings given by the gauges are not accurate and their linearity is questionable. This was evident whenever the gauges were frequently calibrated. For this process, all the gauges were used to measure the same section of tube at pressures ranging from atmospheric down to vacuum. At some pressures the readings on the different gauges varied by as much as 1.5 kPa. It is impossible to determine which gauge is correct or if any are correct unless superior pressure measurement tools are obtained. The effect that the acceleration tube fill pressures had on the flow properties is discussed later in this section.

Experimental and CFD Comparison

The time history graphs of the core flow properties comparing the experimental and numerical methods is shown in Figures 4.16, 4.17, 4.18 and 4.19. The CFD data plotted on these graphs was taken from the turbulent equilibrium simulations run on the finest grid. The test time that is indicated pertains to the value obtained from the experiments.

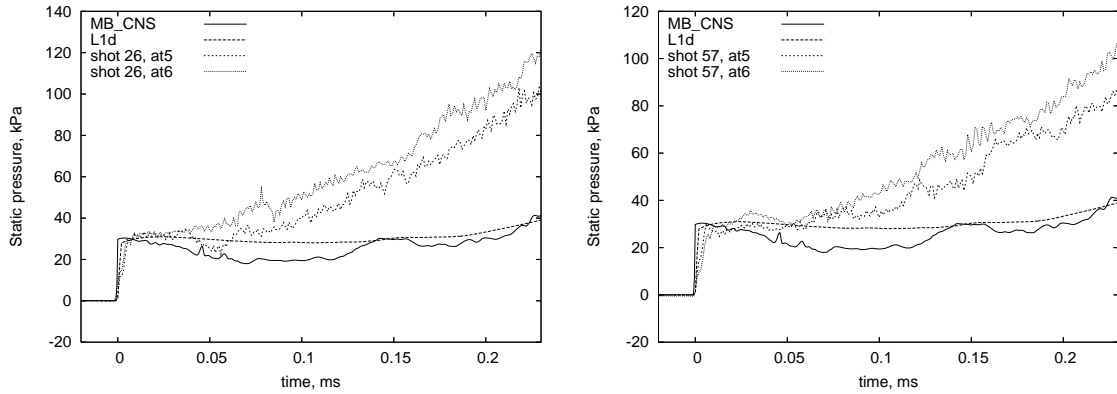


Figure 4.16: Comparison of the experimental and computational static pressures at the acceleration tube exit for Air Condition 1

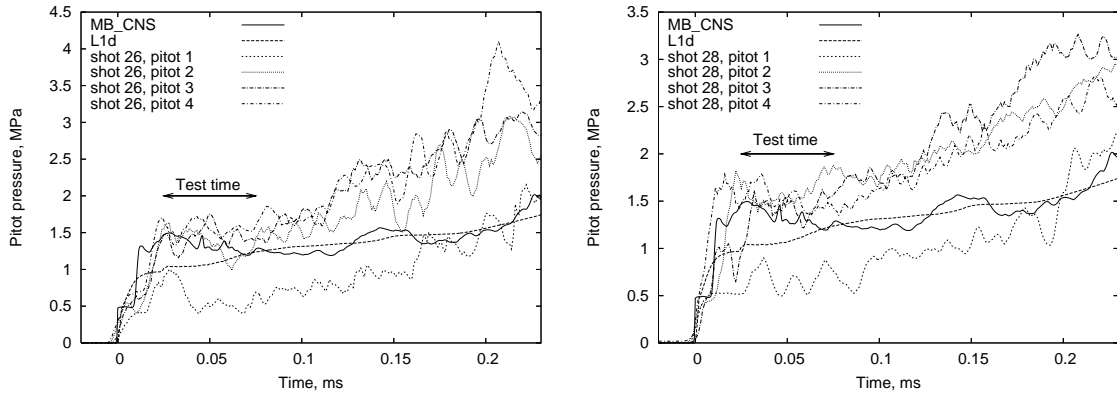


Figure 4.17: Comparison of the experimental and computational Pitot pressures at the acceleration tube exit for Air Condition 1

As in the numerical simulations the test time is terminated by the arrival of the unsteady expansion propagating from the rupture of the secondary diaphragm. Each data line has been shifted so that shock arrival is at a time of 0 ms.

The short falls of the one-dimensional code, L1d, have been discussed previously. The assumption of one-dimensional nature and the methods used for calculating the heat losses lead to incorrect predictions of some of the freestream properties at the acceleration tube exit. For the two air conditions investigated here L1d predicted the secondary shock speeds to within 3% of the experiments and gave good agreement with experimental static pressures. However, it consistently underestimated Pitot pressure by 30% and provided incorrect temperatures. It was also unable to provide more detailed data such as the core flow diameter.

The shock speeds from the various axisymmetric simulations in Air Condition 1 are all

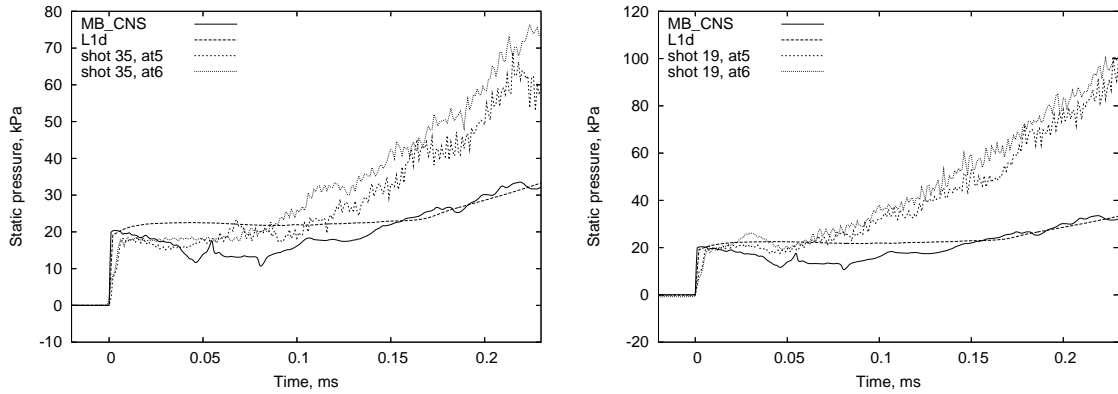


Figure 4.18: Comparison of the experimental and computational static pressures at the acceleration tube exit for Air Condition 2

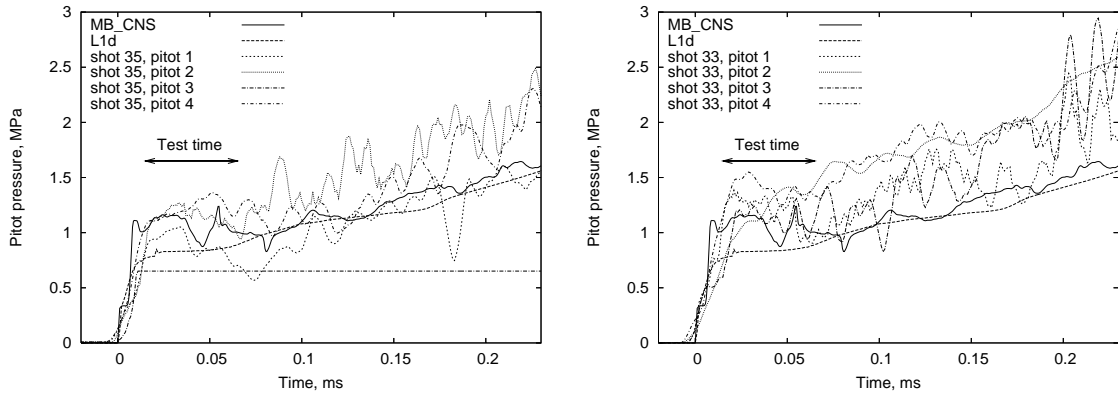


Figure 4.19: Comparison of the experimental and computational Pitot pressures at the acceleration tube exit for Air Condition 2

within 2% of the experimental values, while for Air Condition 2 they were all within 1%. This is within the experimental error for Air Condition 2 but not for Air Condition 1. This seems peculiar as the consistency from shot-to-shot was excellent. The difference can be explained by the acceleration tube fill pressure. The problems with the gauge readings were discussed previously and it is likely that for Air Condition 1 the fill pressure was actually higher than 43 Pa. If this was increased by approximately 5 Pa it would definitely bring the shock speed to within the experimental error of less than 1%. This increase in fill pressure would only have a small effect, within a few percent, on the other flow properties predicted by the numerical simulation.

The addition of turbulence decreased the shock speed by 1.5% in Air Condition 1 and by less than 1% in Air Condition 2. The shock speed was slightly increased when finite-rate chemistry was included. This may not be inherently clear from the tables but the

finite-rate chemistry values were from the coarsest grid. Comparing directly between the laminar, equilibrium simulation and the laminar, finite-rate simulation on Grid 1 shows an increase of approximately 3%. Following the previous trends from the equilibrium simulations, the finite-rate shock speed would increase with a finer mesh. However this would be counterbalanced by the addition of turbulence. The extent of these shifts is unknown and they would not necessarily cancel each other. Unless something unforeseen occurred, the shock speed would still remain within 2 or 3% of the experimental value for Air Condition 1 and less than 1% for Air Condition 2. This excellent agreement shows that the shock speed is not overly sensitive to the effects of turbulence and finite-rate chemistry but was altered by them. The axisymmetric simulations can be used to predict the shock speeds extremely well.

The static pressure from the MB_CNS simulations were within 5-10% of the experimental values. In the computational simulations the pressure levels were the same at locations at4, at5 and at6. A steady decrease in the static pressure was evident during the test time in the axisymmetric simulations but was not seen in the experiments. This has been discussed and is mainly due to numerical effects because the boundary layer was not fully resolved and the code incorrectly calculates viscosity. Besides this numerical disparity and the difficulty in selecting a precise value due to excess noise in the CFD (again due to numerical effects) and noise in the experiments (due to measurement techniques), comparable levels of static pressures can be seen from the different methods. There was only slight variation when turbulence and finite-rate chemistry were added. The addition of these phenomena does not provide any greater accuracy when comparing to the experiments in this thesis. This would be due to the uncertainty and noise in the experiments. The numerical value from a full viscous, turbulent, finite-rate simulation should be closer to the real value in the tube. Again, it must be noted that the finite-rate simulation shown here was on the coarsest grid. Following previous trends, refining the grid would increase the pressure but then, with the addition of turbulence, the pressure would decrease. The fact that the fill pressure in the computational simulation of Air Condition 1 is different to the real fill pressure would not be detrimental to the pressure level. The correct fill pressure would increase the flow static pressure a few percent. Taking into account all these effects, the final numerical static pressure would be within 5-10% of the value that is quoted.

The Pitot pressure levels from the computational methods are all within approximately 10% of the experimental values. The addition of turbulence reduces the Pitot pressure by about 10-15% while the addition of the finite-rate decreases the Pitot pressure by about 5%. Similar trends are seen in the Pitot pressure as to those mentioned with the static pressure. A numerical simulation run on a turbulent, finite-rate, fully grid independent mesh would give a Pitot pressure similar to that quoted for the finite-rate simulation. Though it is not identical to the experiments, it is within the noise and uncertainty. The value compares well enough and this, along with the similar static pressures and shock speeds, confirms that the CFD is capturing the major features of the flow.

In Chapter 3 the core flow properties in the radial direction of the exit of the acceleration tube were plotted. The experimental values compared to the computational values are not plotted here as there were not enough transducers in the experimental Pitot rake to determine the exact size of the core flow. In the Pitot rake the closest probe to the wall was 11 mm away and was always seen to be in the boundary layer in the experiments. The second transducer in the rake was 28 mm from the wall and was always seen to be in the core flow. This meant the core flow diameter had to be greater than 29 mm and smaller than 63 mm. The laminar CFD simulation gave a value of approximately 75 mm for the core flow diameter, while the turbulent simulation gave approximately 60 mm. These values were similar for both Air Condition 1 and Air Condition 2. Despite the lack of a precise comparison, it is apparent that the turbulent simulation was required to capture the boundary layer flow more realistically. The core flow diameter available for testing models would be about 60 mm for these conditions. The lack of turbulence in the laminar model did not drastically effect the core flow properties at the end of the acceleration tube. In future studies in the expansion tube, more transducer probes should be placed in the boundary layer edge region. In the CFD analysis, greater resolution of the boundary layer is required for better capturing of the boundary layer (or a different turbulence model which will do a better job at lower grid resolutions).

In Chapter 3, the assumption of equilibrium chemistry was shown to produce errors in the species mass fractions of the gas at the acceleration tube exit. The finite-rate simulation showed that the oxygen in the test gas dissociates then becomes frozen, while this was not captured by the equilibrium simulation. The ramifications this had on the test flow properties at the end of the acceleration tube, which were measured in the experiments,

was discussed above. To recapitulate, the shock speed, static pressure and Pitot pressure were each increased by a few percent when finite-rate chemistry effects were included. A comparison of the computational simulations shows that the main properties that are effected by the incorrect species mass fractions are density and temperature. Assuming that increasing the grid resolution and the addition of turbulence would follow similar trends to the previously discussed simulations, it would be reasonable to assume that the viscous, laminar, finite-rate values, quoted here, would be within 5-10 % of the real flow properties occurring in the tube. The temperature and density for the equilibrium simulation would be significantly overpredicted, but the other thermodynamics properties are only a few percent different to the finite-rate simulation and would be within 10 % of the properties in the tube. The reason the equilibrium simulation predicted a temperature that was significantly higher than the finite-rate simulation was due to the higher recombination levels. Recombination is an exothermic reaction in which internal energy is converted into the translational, rotational and vibrational modes. The higher recombination level in the equilibrium case means more translational energy and thus a higher temperature.

4.3.3 Titan Condition

Titan is the largest moon of the planet Saturn. The present condition simulated entry into the atmosphere for a Titan aerocapture mission. The fill conditions are displayed in Table 4.8. The test gas was a mixture comprising 95 % nitrogen + 5 % methane by volume which, at the time, was believed to be the composition of the moon's atmosphere.

The shock speeds from the Titan experiments were repeatable with the shot-to-shot variation below 1 %. However, similar to the air conditions the variation in pressure readings was again larger than the uncertainties. Further study into the pressure measurement techniques in expansion tubes is required if the noise (which is believed to not actually exist in the flow) is to be removed.

Table 4.9 and Figures 4.20 and 4.21 provide a comparison between the computational and experimental results. The primary shock speed from the one-dimensional simulation varies by 5 % from the experimental value due to problems with matching reflected waves from the area change. The MB_CNS secondary shock speed varies appreciably from the

Table 4.8: Fill conditions for the Titan experiments

Reservoir fill pressure	1.75 MPa
Compression tube fill pressure	48 kPa
Shock tube fill pressure	5.0 kPa
Acceleration tube fill pressure	26 Pa
Primary diaphragm burst pressure	24 MPa
Secondary diaphragm burst pressure	Approx 8 kPa
Driver gas	57%Helium + 43%Ar by volume
Test gas	Titan gas
Acceleration tube gas	Air

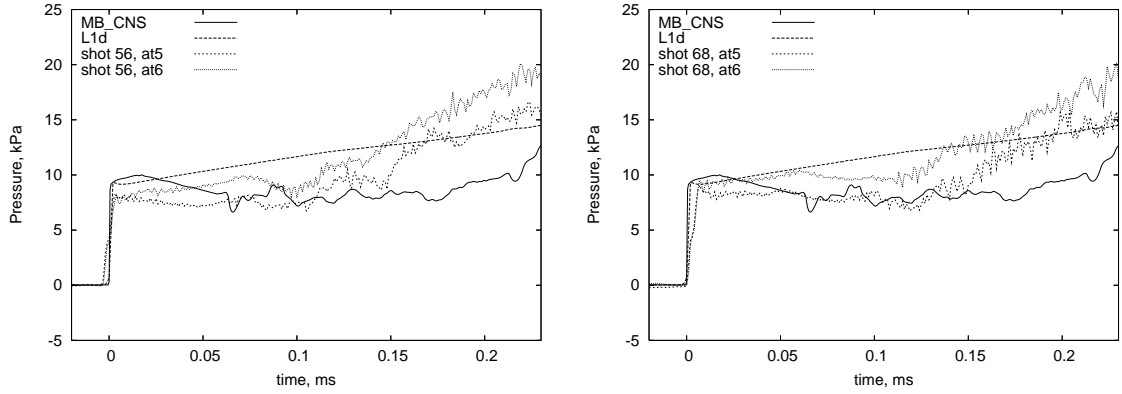
experiments with an error of 10 %. The static and Pitot pressure, though, agree well. The discrepancies may be due to non-equilibrium effects in the test gas. It would be expected at the temperatures that are reached that none of the nitrogen gas would react but that the CH_4 would be significantly dissociated. The code for this has been set up by Gollan and an examination into this is part of other work that is currently being examined. In the air conditions, non-equilibrium effects in the test gas only altered the shock speed by a few percent which may not account for the 10 % seen here. Another contribution may be that the air in the acceleration tube was modelled as a perfect gas. The temperatures that are reached suggest non-equilibrium chemistry could be important in the acceleration gas. The perfect gas assumption would produce a temperature that is too high and thus overestimate viscosity. This would actually underestimate shock speed, which is contrary to what is seen here.

The core flow diameter in the experiments was slightly larger than the air conditions with all four probes in the rake lying in the core flow. This meant the core flow diameter was larger than 63 mm. More pressure transducers in the rake would have been beneficial in obtaining a more accurate measurement of the experimental core flow diameter. The MB_CNS simulation discussed in Chapter 3 gave a core flow diameter of approximately 65 mm at the beginning of the test time then decreased throughout time due to boundary layer growth. This compares fairly well with the experimental value.

The Titan experiments assisted in commissioning the new X2 configuration and gave an estimate of what conditions would be provided. In future studies, more transducers would be required in the Pitot rake to accurately capture the boundary layer size. Due to

Table 4.9: Summary of the flow properties at the acceleration tube exit for the Titan condition

Property	L1d viscous	MB_CNS viscous equilibrium	Experiments
Primary shock speed, km/s	2.81	-	2.95
Secondary shock speed, km/s	5.71	6.088	5.51
Static pressure, kPa	9.2	8.5	8.42
Pitot pressure, kPa	465	470	450
Density, g/m ³	16.1	13.2	-
Mach number	5.6	6.7	-
Static temperature, K	2300	2000	-
Velocity, km/s	5.2	5.95	-
Static enthalpy, MJ/kg	3.32	2.74	-
Total enthalpy, MJ/kg	16.84	20.45	-
Specific internal energy, MJ/kg	2.57	2.1	-
Unit Reynolds number	1.1×10^6	1.5×10^6	-
Test time, μ s	100	50	50

**Figure 4.20:** Comparison of the experimental and computational static pressures at the acceleration tube exit for the Titan condition

the significant levels of noise in the pressure signals, investigation into the measurement techniques would also be required. The computational methods for the Titan condition also require further development which is part of current studies at the University of Queensland. This would more accurately capture the flow that occurs in the tube and would hopefully produce closer results to the experiments.

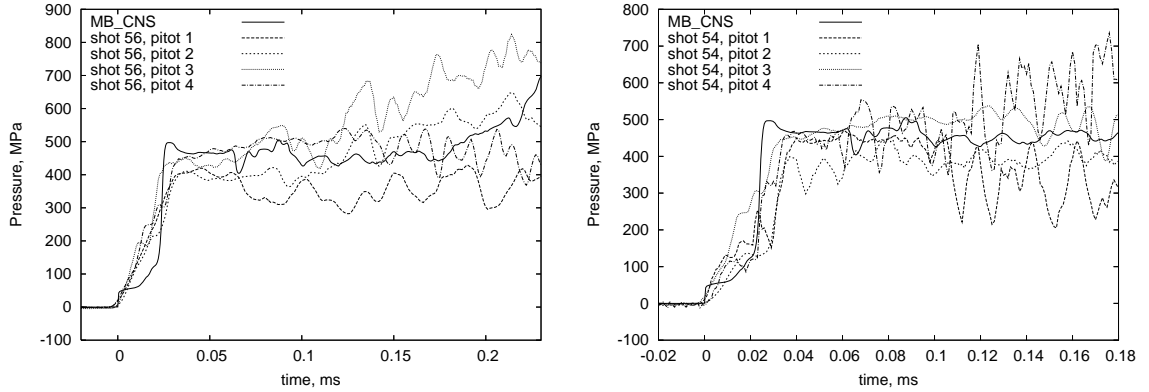


Figure 4.21: Comparison of the experimental and computational Pitot pressures at the acceleration tube exit for the Titan condition

4.3.4 Jupiter Condition

The previous configuration of the X2 expansion tube had test conditions used to simulate entry into the atmosphere of the planet Jupiter. To obtain an estimate of the flow properties which could be achieved for a Jovian condition in the new configuration, three shots were conducted. The fill conditions are shown in Table 4.10. A viscous one-dimensional simulation was run for this condition but no axisymmetric simulation was conducted. Table 4.11 gives a comparison of the computational and experiments results. Like all the other conditions in this thesis, the shot-to-shot variation for the shock speeds was low but the noise levels in the pressure readings was high. Figure 4.22 plots the static and Pitot pressure from one of the shots. Pitot transducer 1 is in the boundary layer, which means the core flow diameter is less than 63 mm.

Deficiencies in the one-dimensional model were discussed in Chapter 3. The flow properties in the numerical simulation changed rapidly throughout the test time which made it difficult to estimate the flow properties. The inaccuracies of the numerical model resulted in large differences from the experiments. The computational model needs to be improved before an accurate approximation of the condition can be used to predict what is occurring in the flow. Nonetheless, these experiments have given an estimate of what conditions are capable for Jovian testing in the new X2 configuration.

Table 4.10: Fill conditions for the Jupiter experiments

Reservoir fill pressure	1.75 MPa
Compression tube fill pressure	48 kPa
Shock tube fill pressure	3.0 kPa
Acceleration tube fill pressure	10 Pa
Primary diaphragm burst pressure	24 MPa
Secondary diaphragm burst pressure	Approx. 8 kPa
Driver gas	Helium
Test gas	Jovian Gas
Acceleration tube gas	Air

Table 4.11: Summary of the flow properties at the acceleration tube exit for the Jupiter condition

Property	L1d viscous	Experiments
Primary shock speed, km/s	5.5	5.46
Secondary shock speed, km/s	12.5	10.5
Static pressure, kPa	12.0	10.02
Pitot pressure, kPa	300	770
Test time, μ s	150	100

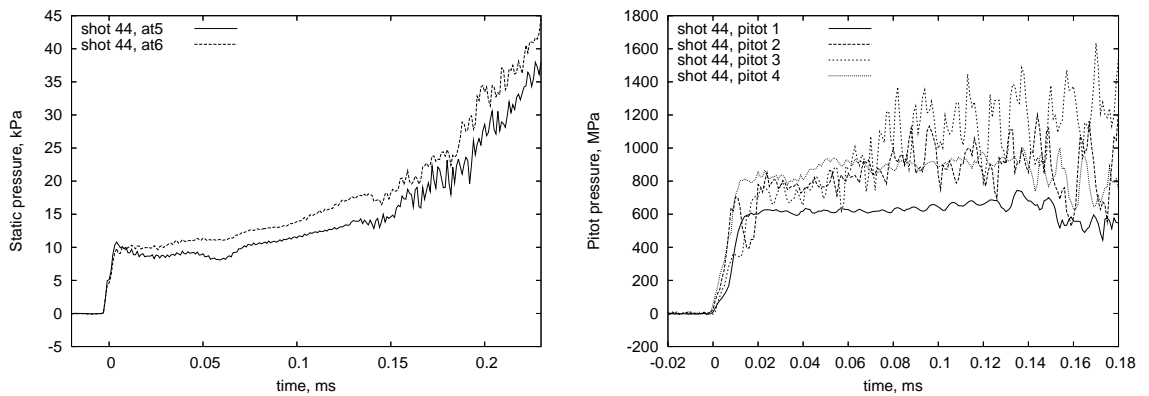
**Figure 4.22:** Static and Pitot pressure at the acceleration tube exit for the Jupiter condition

Table 4.12: Fill conditions for the higher burst pressure experiments

Reservoir fill pressure	2.5 MPa
Compression tube fill pressure	64 kPa
Shock tube fill pressure	9.6 kPa
Acceleration tube fill pressure	43 Pa
Primary diaphragm burst pressure	32 MPa
Secondary diaphragm burst pressure	Approx. 12 kPa
Driver gas	Helium
Test gas	Air
Acceleration tube gas	Air

4.3.5 Higher Burst Pressure

To further test the capabilities of the newly configured X2 expansion tube three shots were conducted with a primary diaphragm burst pressure of 32 MPa. Initially, a series of blanked off tests was conducted to ensure that the rupture pressure of 32 MPa was obtainable. Once this was completed the full experiments were conducted. The fill properties for the condition are shown in Figure 4.12. The compression tube fill pressure was increased to 64 kPa to maintain the compression ratio of 40. The material used for the diaphragm was 2.0 mm hot rolled steel. The free stream flow properties from the experiments were a primary shock speed of 4.86 km/s, secondary shock speed of 8.85 km/s, a static pressure of 36.95 kPa and Pitot pressure of 1.9 MPa. This was an increase in 9% in shock speeds and over 20% in pressure. These extra capabilities further demonstrate the improvements made by the change to a single-stage, free-piston driver. With the driver tube section being rated to over 40 MPa the option exists to again increase the burst pressure, if need be.

4.3.6 Higher Compression Ratio

To determine if a higher compression ratio would increase the shock speed and pressures attained in the tube, three shots were conducted with a compression ratio of 55. The fill properties are shown in Figure 4.13. The results produced were very similar to those with a compression ratio of 40 and showed no distinct advantage in increasing the compression ratio. This was supported by L1d simulations presented in Section 3.2.2. The competing

Table 4.13: Fill conditions for the higher compression ratio experiments

Reservoir fill pressure	1.3 MPa
Compression tube fill pressure	30.1 kPa
Shock tube fill pressure	9.6 kPa
Acceleration tube fill pressure	35 Pa
Primary diaphragm burst pressure	24 MPa
Secondary diaphragm burst pressure	Approx. 12 kPa
Driver gas	Helium
Test gas	Air
Acceleration tube gas	Air

effects of a higher driver gas burst pressure and shorter driver gas slug length result in minimal effect in the flow properties.

4.4 Summary

The upgrade of a new single-stage, free-piston driver to the X2 expansion tube greatly increased the capabilities of the facility. Initial testing in the tube showed that the driver was functioning as desired and capable of producing the necessary rupture pressures. The majority of the work in this thesis involved a primary diaphragm rupture pressure of 24 MPa but some experiments were performed with a rupture pressure of 32 MPa. With the opportunity of increasing the burst pressure to the rated value of 40 MPa comes even greater performance and the prospect of reaching higher enthalpy flows.

For the four conditions that were used in the commissioning program for the new X2 configuration, the shock speeds from the experiments provide good repeatability. The shot-to-shot variation was typically within 1%. The experimental static and Pitot pressure signals contained large levels of noise that were believed to not exist in the actual flow and were produced from the measurement techniques. Oscillations in the static pressure were caused by the natural frequency of the transducer while fluctuations in the Pitot pressure were attributed to the mounting configuration. The noisy signals made it hard to determine an appropriate value for the test flow properties at the end of the expansion tube. A detailed investigation into measurement techniques in expansion tubes is required to rectify the problems.

For the air conditions, the one-dimensional code produced a sufficiently good comparison to the experiments up to the secondary diaphragm. However, the errors in the modelling techniques were exacerbated further downstream and created too many discrepancies in some flow properties such as Pitot pressure and temperature. The one-dimensional code provided a reasonable approximation of the secondary shock speed and static pressure at the acceleration tube exit.

The hybrid MB_CNS simulations provided a much more detailed and accurate depiction of the flow. Ideally, axisymmetric simulations of the acceleration tube would be conducted for all the conditions but this becomes computationally expensive, especially when effects such as finite-rate chemistry and turbulence are included. For the air conditions, all the MB_CNS simulations (regardless of the addition of turbulence and finite-rate chemistry) reasonably predicted the shock speed, static pressure and Pitot pressure from the experiments. The CFD was within 5-10% of the experimental pressures and 1% of the experimental shock speed. A better comparison was unlikely considering the noise in the experimental results and the numerical inaccuracies in the CFD. While the finite-rate, turbulent simulation provided a good representation of the flow, the experimental measurement techniques and numerical simulations both need to be developed further in order to get an extremely precise comparison.

The air conditions were definitely influenced by finite-rate chemistry and turbulence effects. Most of the oxygen in the test gas that was dissociated by the primary shock did not recombine through the unsteady expansion generated by the rupture of the secondary diaphragm. Despite the high-temperature effects the inclusion of finite-rate chemistry was mainly required for correctly estimating temperature and density. The high unit Reynolds numbers meant a turbulence model was needed to accurately capture the boundary layer. The assumption of laminar flow overpredicted the core flow diameter. The addition of turbulence rectified this problem but shear layers in the boundary layer caused unsteadiness in the test time. Further resolution of the grid or a different turbulence model that performed better at lower grid resolutions was required to improve upon this.

The Titan and Jupiter experiments provided estimates of what conditions could be achieved for testing in the X2 expansion tube. Different aspects of the CFD need to be developed further to provide a better comparison to the experiments. In the axisymmetric Titan simulations, the assumption of a perfect gas for the air in the acceleration tube

created unrealistically high temperatures, while the methane in the test gas would have undergone significant dissociation and required the use of finite-rate chemistry. This topic is the purpose of a current study at the University of Queensland. The one-dimensional Jupiter simulations failed due to the extreme severity of the expansion arising from the secondary diaphragm rupture. The implementation of an exact Riemann solver, which was currently being undertaken, would rectify this problem [98].

Most simulations of conditions in the newly configured X2 expansion tube require finite-rate chemistry and turbulence to accurately predict all properties to a high precision. While some short term developments to the codes are required to produce accurate simulations of the tube, the longer term aim of the code development should be a complete axisymmetric simulation of the expansion tube from the primary diaphragm onwards for each condition.

CHAPTER 5

Design of a Hypersonic Nozzle

In Chapter 1 it was stated that a previous study at the University of Queensland [16] examined the addition of a hypersonic nozzle on an expansion tube. Following this, in Chapter 2, an in-depth literature review was presented on expansion tunnels and hypersonic nozzles. In some of these studies it had been stated that an expansion tube nozzle would not only increase the core flow diameter but would also increase the steady time available for testing. Despite these claims, a suitable expansion tube nozzle had not been constructed to demonstrate the hypothesis. Furthermore, no one has ever explained the mechanism behind the test time increase.

This chapter looks at the design and implementation of a contoured hypersonic nozzle for the X2 expansion tube. A technique based on the Parabolized Navier-Stokes (PNS) equations was used to design the nozzle. A series of experiments with the nozzle attached is compared to axisymmetric MB_CNS simulations of the geometry. Finally, the CFD is used to investigate the flow in an attempt to explain what occurs in the nozzle.

5.1 Design Methods

Much work was done on hypersonic nozzle design following the Second World War. Hypersonic nozzles were used extensively on ground based facilities to produce flow conditions capable of testing long range missiles. An extensive history of this work is provided by Lukasiewicz [17]. Both conical and contoured axisymmetric nozzles were designed using the Method Of Characteristics (MOC) proposed by Prandtl and Buseman in 1929 [118]. Traditionally, the nozzle design process involved creating an inviscid wall profile

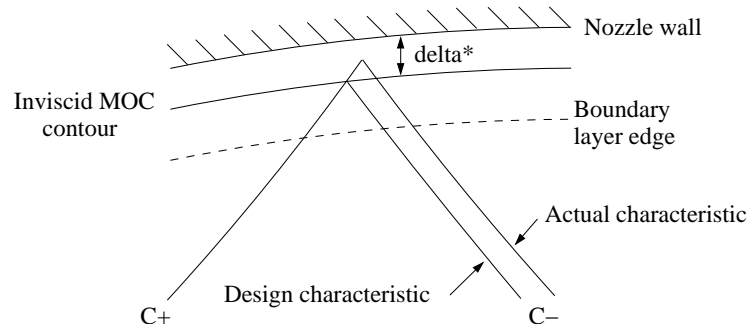


Figure 5.1: Lag between the actual characteristic and the MOC/BL design caused by large boundary layers. Adapted from [8].

that produced the desired uniform flow then correcting the contour to compensate for the Boundary Layer (BL). A separate boundary layer calculation was required to determine the displacement thickness in the technique. Subsequently, it was incorrectly assumed that the core flow and boundary layer were purely independent. At high Mach numbers, when the boundary layer thickness is large compared to the nozzle exit diameter, this assumption causes non-uniform flow. The reason for this can be seen in Figure 5.1. In the classical MOC/BL method described above, the characteristics reflect at the inviscid contour. However, Candler and Perkins [119] have shown that when the boundary layers become thick, the characteristics effectively reflect between the inviscid contour and the wall. This causes lag between the actual and design characteristics. When the flow Mach number reaches 8, the MOC/BL design method does not achieve complete wave cancellation, which results in compression waves that disrupt the flow [8].

An alternative design method was developed in the early 1990s by Korte et al. [120, 121] and later by Keeling [122] and Tolle [123]. This technique incorporates the coupling between the core flow and boundary layer. It is based on the solution of the parabolized Navier-Stokes equations in the nozzle domain. The PNS equations are derived directly from the Navier-Stokes equations by neglecting the diffusion terms in the streamwise direction. The computational effort required to solve these equations is significantly less than the full Navier-Stokes equations because a space-marching solver can be utilized instead of a time-marching solver. Given a set of initial conditions, the flow field in the nozzle can be resolved. The solution and nozzle contour can then be fed into an optimization algorithm which can perturb the nozzle contour. A new solution can then be obtained and the process continued. An objective function can be set and the iterative

routine repeated until a minimum value of the objective function is reached. The computational flow solver in this thesis was developed at the University of Queensland and the code package is called SM_3D⁺. Only basic detail on the program is provided here as it is simply a tool used for the thesis and was not written by the author. In-depth information can be found in the work by Craddock and Jacobs [124, 125]. The code was written in the C programming language and the optimization algorithm utilized is the Nelder-Mead simplex optimization technique [126].

5.2 Current Nozzle Design

In an expansion tube nozzle the flow is already hypersonic when entering the nozzle as opposed to the subsonic or supersonic inflow in a typical converging-diverging nozzle. This means that the contour is purely diverging and there is no throat section. There is the possibility of a skimmer type nozzle where not all the incoming flow is captured. This is discussed in this section along with the other design choice of a conical or contoured nozzle profile.

5.2.1 Skimmer vs Full Capture Nozzles

At high hypersonic speeds, like those experienced in the acceleration tube of an expansion tunnel, the boundary layers grow rapidly and can be extremely thick. This creates a highly non-uniform inflow into the nozzle which in turn can produce non-uniform flow at the exit. A skimmer (or scoop) type nozzle has an inlet diameter smaller than the exit diameter of the acceleration tube. This removes the boundary layer and provides a more uniform inflow to the nozzle. The drawback of this design is that it can cause shocks emanating from the leading edge of the nozzle which disrupt the flow. Also, for a given nozzle exit diameter, a skimmer nozzle requires a larger area ratio when compared to a full capture nozzle and this produces lower total pressures or a smaller cross-section.

The design for the X2 expansion tube nozzle was a full capture inlet. Non-uniform inflow effects were taken into account in the design. The non-uniform profile at the exit of the acceleration tube was obtained from the axisymmetric MB_CNS simulations discussed in Chapter 3. This was used as the inflow boundary condition to the nozzle.

Problems with highly non-uniform inflow, such as that seen by Chue et al. [127], were not encountered in this work.

5.2.2 Conical vs Contoured Nozzles

Contoured nozzles have wall shapes that rely on wave cancellation to provide uniform exit flow. At non-design operating conditions non-uniformities can develop making them only suitable for a small operating regime or even a single condition. Conical nozzles are less susceptible to non-uniformities developing at off design conditions, but the flow at the exit is both diverging and expanding. The current design was a contoured nozzle. These types of nozzles expand the flow by a gradual increase in the wall profile. Any waves that are formed by the expansion are cancelled by the flow straightening portion at the end of the nozzle. It was reasoned that if the nozzle did not work at non-design operating conditions other nozzles could be designed if necessary. However, most conditions in the X-series of expansion tubes produce flow with an acceleration tube exit Mach number close to 7, which is one of the main design parameters.

5.2.3 Method Of Characteristics (MOC)

A preliminary design for the nozzle contour used the classical method of characteristics design. The profile obtained was used as the first guess for the technique using the PNS equations. Details describing the fundamentals of the method of characteristics can be found in most compressible flow texts such as Liepmann and Roshko [128]. For this work, the code was an Interactive implementation of the method of characteristics called IMOC [129, 130]. The program solves the flow field in a two-dimensional, inviscid and irrotational flow. The only specifications required are the inflow Mach number and the desired outflow Mach number.

No restrictions were placed on the length of the nozzle. Other design parameters such as the area ratio were kept fairly modest. The nozzle was required to increase the flow diameter from 85 mm to at least 185 mm. In IMOC the Mach number was set to increase from 7.3 to 10 through the expansion. The main purpose of the nozzle was to increase the diameter of the core flow, so a large increase in velocity was not necessary. The contour co-ordinates for the IMOC design are shown in Table 5.1 and these were used as the initial

Table 5.1: Nozzle co-ordinates from IMOC

x(m)	y(m)	x(m)	y(m)
0.0	0.0425	0.396339	0.064488
0.02347	0.043275	0.485922	0.07005
0.048777	0.044259	0.586846	0.076006
0.084543	0.045893	0.7015	0.082115
0.129626	0.048223	0.834357	0.087935
0.183443	0.051269	0.992243	0.09272
0.245741	0.055024	1.17933	0.095768
0.316571	0.059451	1.39849	0.096963

profile in SM_3D⁺.

5.2.4 Optimized Design Profile

For this project, the front interface of SM_3D⁺ [124, 125] was converted into the Python programming language by Peter Jacobs. In the original version of the code, a parameter file was created which contained data such as the grid resolution, inflow conditions and computational domain. However, certain configuration macros and the gas model had to be manually set in the source code. In addition to this the geometry and optimization parameters had to be hard coded for some problems. These options which were embedded into the code would necessitate recompiling for each specific problem. Once the code was compiled, a pre-processor could be run to generate an initial solution and then the main space marching program could be implemented. In the new revised version, the Nelder-Mead optimization algorithm was rewritten in Python. The parameter file was now written as a Python script and this controlled all the necessary options. The code no longer required recompiling and hard coding. Features such as the objective function and how the profile was perturbed between iterations were set in the Python parameter file. The execution of the parameter file ran the pre-processor then the main space marching code and any necessary post processing. The input file for the final optimized design is shown in Appendix D.

The nozzle contour was defined by a Bezier polynomial with ten control points. The code worked by perturbing the location of these nodes for the Bezier polynomial. The

contour co-ordinates were obtained from the Bezier nodes for each new iteration of the algorithm. The optimized nozzle profile was found as the shape which gave the lowest value of the objective function. The first contour point was set at the axial distance of 0 m and radial distance of 0.0425 m. This corresponded with the exit of the acceleration tube. The final contour point was set at an axial distance of 1.4 m. This seemed a suitable length as it was close to what was given by the IMOC solution.

The target parameters for the nozzle design were a core flow exit Mach number of 10 and a flow exit angle of 0° . The objectives for the Nelder-Mead technique were set as a variation in these two values of 0.01. When the algorithm reached these goals the simulation was stopped. These objectives were set to very high standards similar to that done by Craddock [124]. This helped to improve the convergence of the optimization algorithm. The technique did not actually reach these values due to their strict nature in which case the simulation stopped when it could get no closer. Initially, the criteria for the objective function was set as an equally weighted percentage of both the variation of the Mach number and flow angle in the core flow of the nozzle exit. The function is seen in equations 5.1, 5.2 and 5.3. In these equations N is the number of cells in the core flow while ϕ_θ and ϕ_M are the weighting parameters for the flow angle and Mach number respectively. The edge of the core flow was defined as when the gradient of the Mach number across the tube was greater than 3 degrees.

$$\text{Objective function} = \left(\frac{f_\theta + f_M}{N} \right)^2 \quad (5.1)$$

$$f_\theta = \frac{1}{N} \frac{\sum_{j=1}^N (\theta - \theta_{design})}{\phi_\theta^2} \quad (5.2)$$

$$f_M = \frac{1}{N} \frac{\sum_{j=1}^N (M - M_{design})}{\phi_M^2} \quad (5.3)$$

When designing the nozzle, a problem was encountered with the criteria for the objective function. The optimization algorithm continually produced a hump in the beginning of the profile as shown in Figure 5.2. This generated extremely straight flow at the exit to

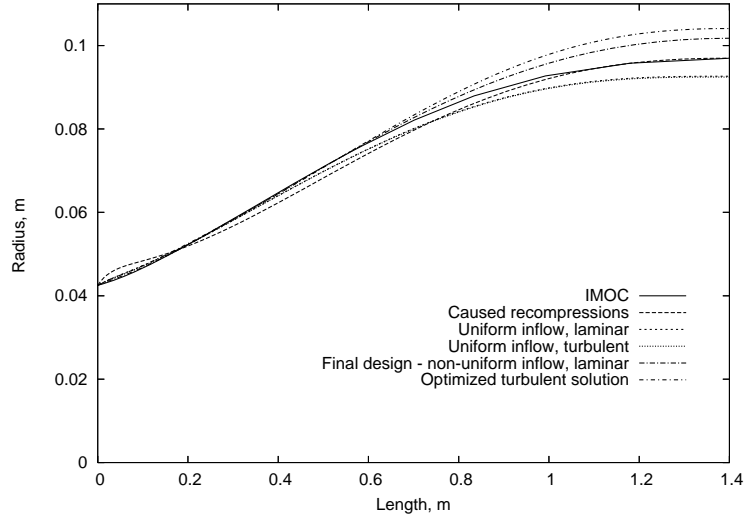


Figure 5.2: Profiles of various nozzle designs

the nozzle as required but caused large recompressions along the centreline of the nozzle. To overcome this, the objective function was corrected to incorporate the Mach number distribution along the centreline. A penalty was imposed if the Mach number along the centreline decreased as the flow moved downstream. The weighting for the function defining the flow angle variation was also increased by a factor of 10. This was done as the actual Mach number at the exit was not significant as long as it was uniform across the core flow. It was more important to the design that the flow was straight at the exit.

The computational domain initially consisted of forty cells across the nozzle plane clustered with a stretching parameter of 1.05 towards the wall. To test the new Python interface, the simulation was run assuming a laminar boundary layer and a uniform inflow. The inflow conditions were set as a Mach number of 7.3, a temperature of 3500 K and a pressure of 30.0 kPa. The comparison between the IMOC profile and uniform inflow, laminar SM_{3D}⁺ profile is shown in Figure 5.2. At the start, the IMOC contour expands less rapidly but then increases to a steeper rise at about 0.2 m along the nozzle. Due to this more rounded curve, the IMOC contour has to correct further in the flow straightening portion of the nozzle. The SM_{3D}⁺ and IMOC contours should have been very similar. The difference may have been due to turbulent boundary layer effects. The simulation was completed again including turbulence and the profile was the same, as shown in Figure 5.2. Another possible explanation was the Bezier curve was not infinitely flexible and may have a family of shapes not quite close to the necessary streamline shape for fully

corrected flow.

Proceeding with this work, viscous terms and a non-uniform inflow were added to the simulation. The inflow profile came from the hybrid axisymmetric simulations of the acceleration tube. The final SM_3D⁺ design took 94 hours of CPU time on a single processor of the Blackhole cluster. The properties at the exit plane of the nozzle from SM_3D⁺ are shown in Figure 5.3. The Mach number is fractionally off 10 as the objective function was weighted more towards the other parameters. The air in the nozzle was assumed to be a perfect gas. This incorrect chemistry model would result in temperatures that were much higher than would occur in reality and subsequently do not match the MB_CNS results presented later in this chapter. The static pressure of 2.7 kPa compares reasonably with the experimental value of 3.1 kPa and 2.9 kPa from the finite-rate CFD. The important flow property from SM_3D⁺ is the flow angle, which is less than 0.02 in the core flow. This is on the limit of what can actually be measured currently in test facilities. To better model the flow in the nozzle in SM_3D⁺, finite-rate chemistry effects could have been included. However, this would have taken an extremely large amount of time to solve.

A comparison of the final design contour and the IMOC contour is shown in Figure 5.2. The final optimized design profile compensates for the boundary layer growth that was not incorporated in the method of characteristics. Besides this, little difference existed between the contours. The Mach number distribution along the centreline in Figure 5.4 shows that no recompression was present with the refined objective function.

The final optimized design of the nozzle was performed in SM_3D⁺ with the assumption of laminar flow. This produced a large core flow diameter of 150 mm as shown in Figure 5.3. This number seemed to be an overestimate when compared to the experimental and axisymmetric MB_CNS simulations that are presented later in this chapter. After the nozzle was designed and installed, SM_3D was rerun for the designed profile with the inclusion of turbulence. The core flow diameter was then reduced to 100 mm which compared well with the experimental and MB_CNS values. This further supports the requirement for including turbulence in order to achieve the correct boundary layer size when modelling the X2 expansion tube. To determine how much the contour would be altered from the final design the nozzle was redesigned including turbulence. The simulation took over 146 hours to run on a single processor of the Blackhole cluster. As

Table 5.2: Bezier points for the optimized turbulent profile

x(m)	y(m)	x(m)	y(m)
0.0	0.0425	0.403471	0.058292
0.034483	0.044861	0.590938	0.076543
0.085036	0.046159	0.825679	0.100123
0.158080	0.047400	1.100956	0.104087
0.261443	0.060497	1.4	0.104087

shown in Figure 5.2, the optimized turbulent design further compensates for the larger boundary layer and expands more towards the exit. A possibility exists to re-machine the nozzle to the optimized turbulent profile thus producing a larger core flow. The Bezier co-ordinates for the design are presented in Table 5.2. These points, used in conjunction with the Python scripts presented in Appendix D, gives the nozzle contour co-ordinates plotted in Figure 5.2.

To ensure that the grid resolution was sufficient, the mesh was refined from 40 cells to 80 cells and then 160 cells in the cross stream direction of the nozzle. These simulations were only conducted with uniform inflow and for a laminar boundary layer. The Mach number and flow angle at the nozzle exit are plotted in Figure 5.5 for the two denser meshes. Little difference existed between the plots demonstrating that the solution was grid independent.

5.3 Manufacture and Installation

The construction and installation of the X2 expansion tube nozzle was completed in August 2005. The nozzle was comprised of 3 separate sections which were bolted together. Technical design drawings for the nozzle and the nozzle frame are presented in Appendix E. The nozzle was fabricated from mild steel grade 1045. The Numerically Controlled (NC) lathe located at the University of Queensland was used to produce the contoured profile of the nozzle. The number of points specified on the machine for each section was 421, 426 and 418. A sample of these final design co-ordinates used for the nozzle machining is given in Table 5.3. The full co-ordinates can be obtained from the Bezier control points in Table 5.4 and the Python scripts in Appendix D. The nozzle frame

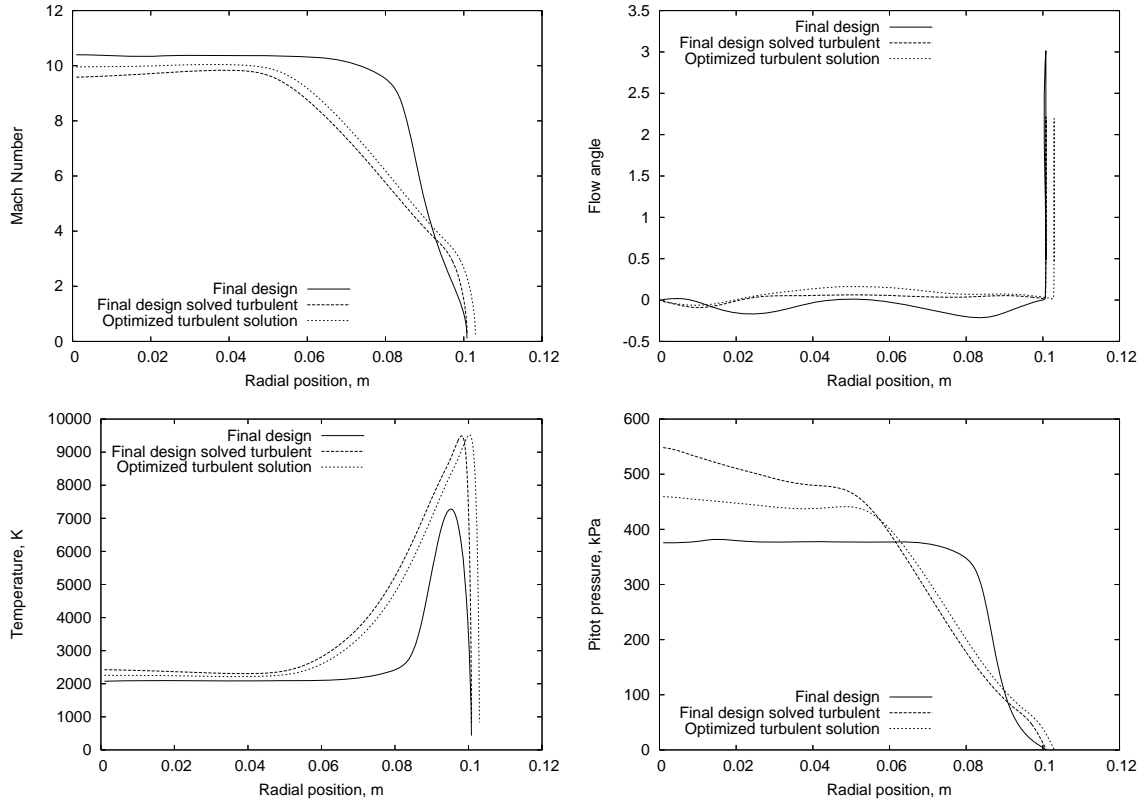


Figure 5.3: Properties from SM_{3D}⁺ at the nozzle exit

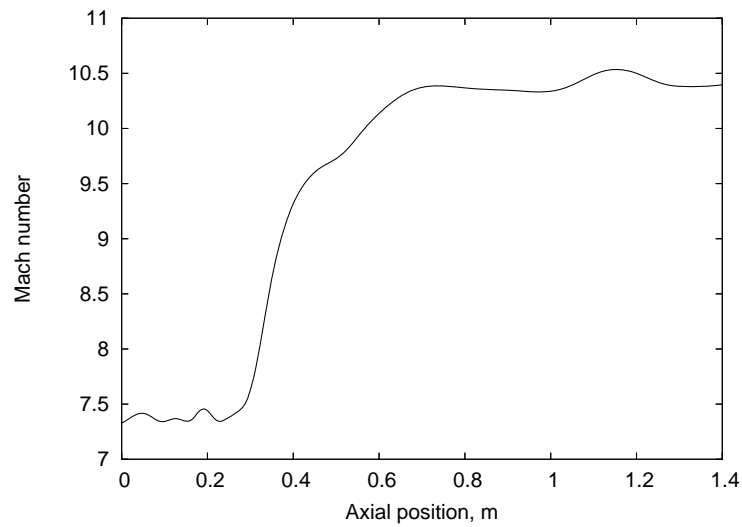


Figure 5.4: Mach number from SM_{3D}⁺ along the centreline of the nozzle

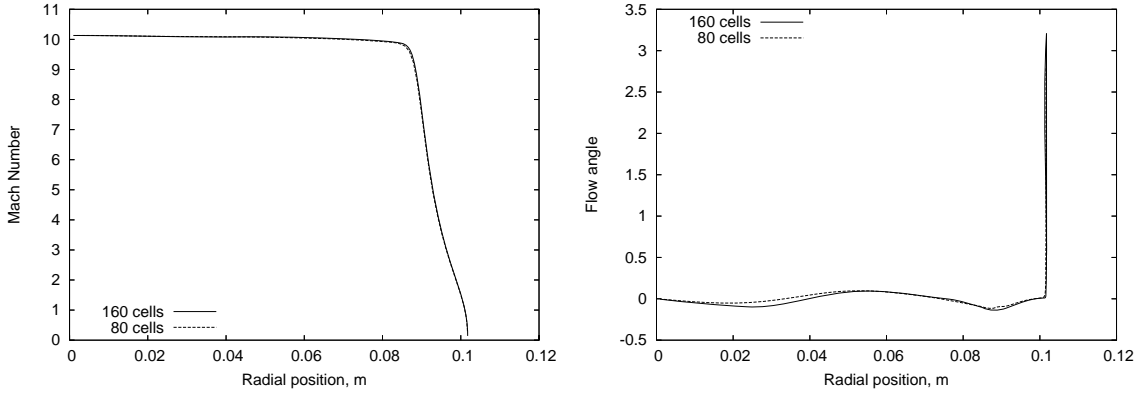


Figure 5.5: Mach number and flow angle from SM_{3D}⁺ across the nozzle exit plane

Table 5.3: Sample of the nozzle co-ordinates for the final design

x(m)	y(m)	x(m)	y(m)
0.0	0.0425	0.419119	0.066033
0.023422	0.043480	0.520628	0.072266
0.052994	0.044748	0.635471	0.078971
0.089767	0.046478	0.763763	0.085705
0.134836	0.048842	0.905261	0.091856
0.189295	0.051939	1.059306	0.096749
0.254202	0.055822	1.224769	0.099827
0.330529	0.060521	1.4	0.100840

and the other associated pieces were constructed in house at the Mechanical Engineering Department at the University of Queensland. The existing dump tank front cover was modified to allow the larger diameter nozzle to slide in and out. A connection plate was built so that experiments could be performed when the nozzle was not required.

Figure 5.6 to Figure 5.11 are pictures of the manufactured nozzle. It was connected to the acceleration tube by a capstan nut similar to the other section breaks on X2. An existing 315 mm section was unscrewed at the end of the acceleration tube then a connecting nut placed on the acceleration tube. The capstan sitting on the first section of the nozzle was then screwed into the nut. The contoured section of the nozzle was 1.4 m long with the total length of the nozzle being 1.626 m. A 226 mm straight section of diameter 85 mm was placed before the profiled wall to compensate for the short section removed from the acceleration tube. The nozzle diameter increased from 85.0 mm to 201.8 mm

Table 5.4: Bezier points for the final design

x(m)	y(m)	x(m)	y(m)
0.0	0.0425	0.403471	0.059879
0.034483	0.043906	0.590938	0.080346
0.085036	0.046412	0.825679	0.094781
0.158080	0.047054	1.100956	0.100840
0.261443	0.060095	1.4	0.100840



Figure 5.6: Section 1 of the nozzle before painting



Figure 5.7: Section 2 of the nozzle before painting

producing an area ratio of 5.64. The total weight of the nozzle was approximately 200 kg.

5.3. MANUFACTURE AND INSTALLATION



Figure 5.8: Section 3 of the nozzle before painting



Figure 5.9: The 3 sections of the nozzle

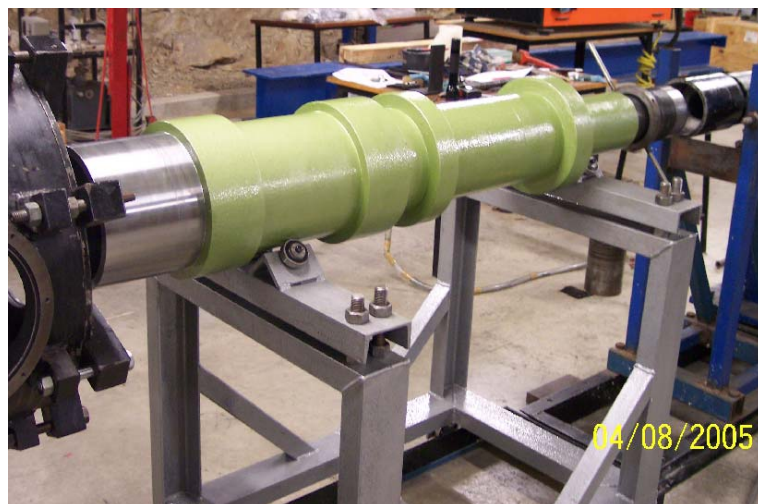


Figure 5.10: The installed nozzle and frame - view 1

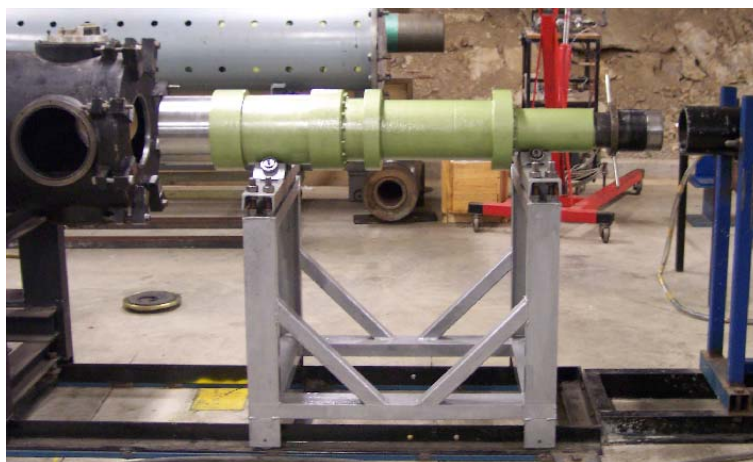


Figure 5.11: The installed nozzle and frame - view 2

5.4 Comparison of Nozzle Simulations and Experiments

5.4.1 Experiments with the Nozzle Attached

The static pressure transducers along the tube, for the experiments conducted with the nozzle attached, remained in the same locations as the previous experiments. In addition to the three shock tube and six acceleration tube transducers, two extra transducers were placed at the exit of the nozzle. The Pitot pressure rake which was situated at the nozzle exit was expanded from four transducers to nine. The rake from the X3 tube was utilized with a new support stand constructed to allow it to be mounted in the X2 dump tank. The spacing of the transducers in the flow is shown in Figure 5.12. Five shots were conducted for each of the air conditions, while four shots were conducted for the Titan Condition.

Similar levels of pressure fluctuations in the test time were seen in the nozzle experiments to those in Chapter 4. Again, the amount that was due to actual unsteadiness in the flow was debatable. While some noise was expected to exist in the flow, excess fluctuations were thought to be caused by the measurement techniques. Temperature effects, oscillations at the natural frequency of the transducer, stress waves through the tube wall and waves caused by the shielding arrangement in the Pitot probes all would have produced variations in the pressure readings. This was previously discussed in detail in Section 4.3.2.

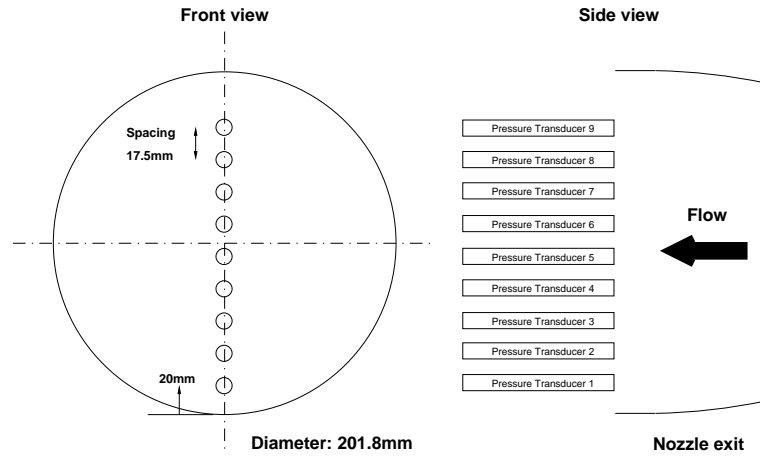


Figure 5.12: Pitot pressure rake at the nozzle exit plane

5.4.2 Axisymmetric Simulations

Similar simulations to those presented in Section 3.5 were conducted to compare to the experiments with the nozzle attached. As before, the main aim of the CFD was to obtain the thermodynamic flow properties at the nozzle exit. The knowledge of these conditions would be extremely beneficial when studying the scaled models tested in the facility. The advantage of the CFD is that it gave a much more detailed description of the flow, while the experiments were needed to validate the CFD.

As in the acceleration tube simulations, the plausibility of laminar and equilibrium flows in the numerical methods was investigated. Finite-rate chemistry was again incorporated on the coarsest mesh. For Air Condition 1, the finite-rate simulation took over 81 hours to run on 42 processors which equated to 142 days of CPU time. This included modelling both the flow in the acceleration tube and the nozzle. On the finer grids, the simulations would have taken nearly 2 weeks and 40 days respectively to run on 42 processors. This equates to 500 days of CPU time for Grid 2 and nearly 5 years of CPU time for Grid 3. This amount of computing time on the current facilities was too large especially when considering the amount that had already been utilized. For Air Condition 2 the finite-rate simulation took even longer at over 103 hours to run.

The axisymmetric simulation geometry was comprised of 42 blocks. These were the same 33 blocks which were used for modelling the acceleration tube plus an extra 9 blocks comprising the nozzle region. The number of cells used in the nozzle mesh are given in Section 5.4.2 Grid Refinement Study, while the number of cells in the acceleration tube

Table 5.5: Number of cells for each grid of the axisymmetric nozzle simulations

	Number of cells along the nozzle	Number of cells across the nozzle
Grid 1	867	39
Grid 2	1300	58
Grid 3	1950	87

corresponds to those given in Section 3.5.4.

Grid Refinement Study

A grid refinement study was conducted for the axisymmetric simulations with the nozzle attached. Only the results for the grid refinement study of the two air conditions are presented here. The number of cells in the 1.4 m length of the nozzle are shown in Table 5.5. The freestream properties just off the centreline at the nozzle exit are shown in Figures 5.13 to 5.16. In both the laminar and turbulent cases, the velocity, Mach number and temperature remained constant over the various grids. However, the pressures and densities changed between meshes which indicated that the solution was not totally grid independent. The constraint was again computing resources. Air Condition 1 on Grid 3 for the laminar, equilibrium case took 41 hours to complete on 42 processors. Air Condition 2 on Grid 3 for the laminar, equilibrium case took 61 hours on 42 processors. These two simulations by themselves reflect a huge amount of computer processor time. The large number of one-dimensional and axisymmetric simulations which were conducted in this thesis represent a large amount of computational time and effort. At the present time it is not feasible to continue refining the grid, especially when this was only for the equilibrium case. To compensate for this, the slight variation in pressure and density which would occur at a finer grid was taken into account in the discussion of the results.

5.4.3 Air Condition 1

A summary of the freestream flow data at the nozzle exit for Air Condition 1 is presented in Table 5.6. Due to the variation of the properties in the test time, bounds were placed on the pressure values in the table. The computational value which best indicated the result was selected and then a range which indicated the property variation in the test

5.4. COMPARISON OF NOZZLE SIMULATIONS AND EXPERIMENTS

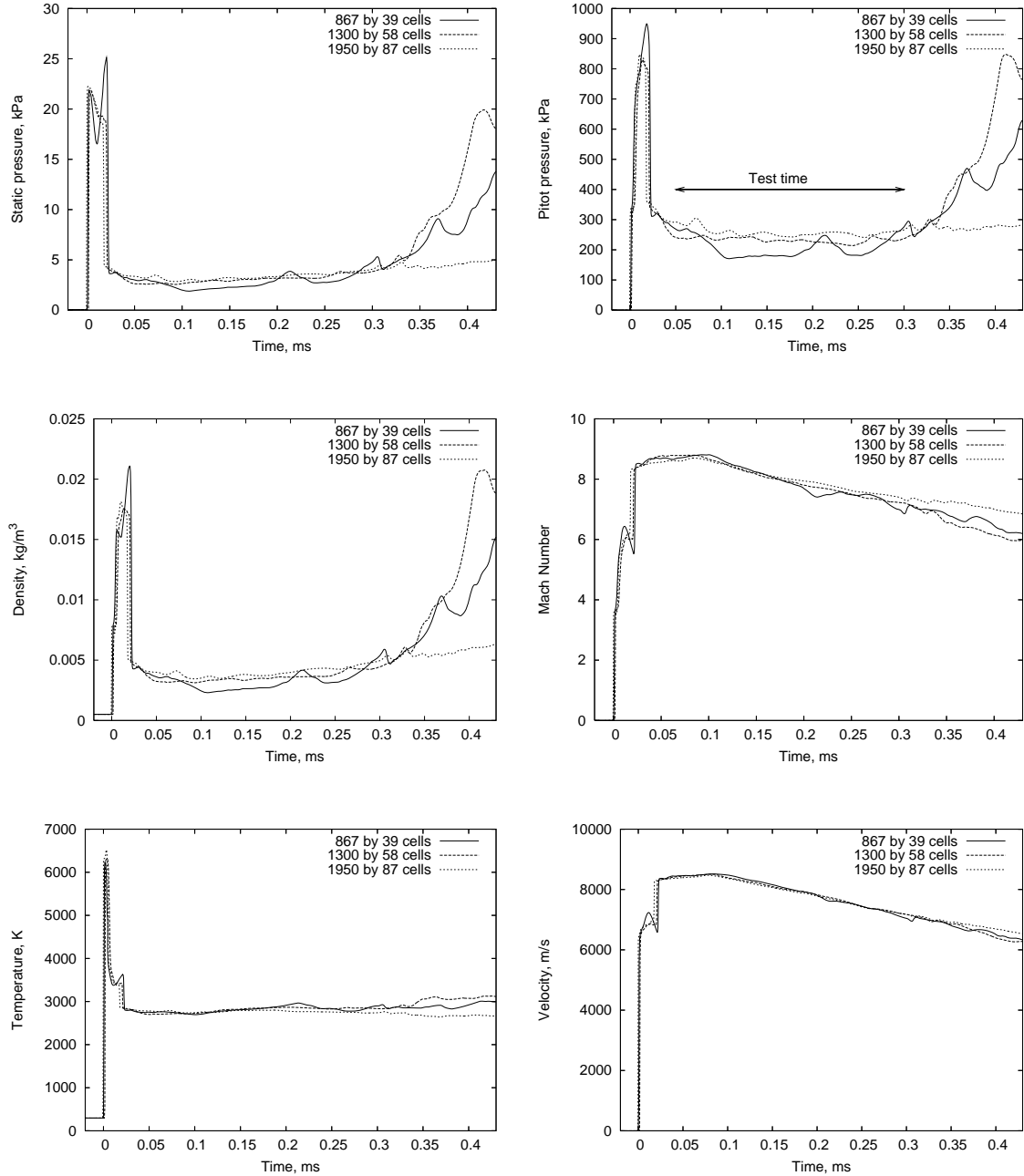


Figure 5.13: Properties from MB_CNS at the nozzle exit for Air Condition 1. Varying grid resolutions for the laminar simulations.

5.4. COMPARISON OF NOZZLE SIMULATIONS AND EXPERIMENTS

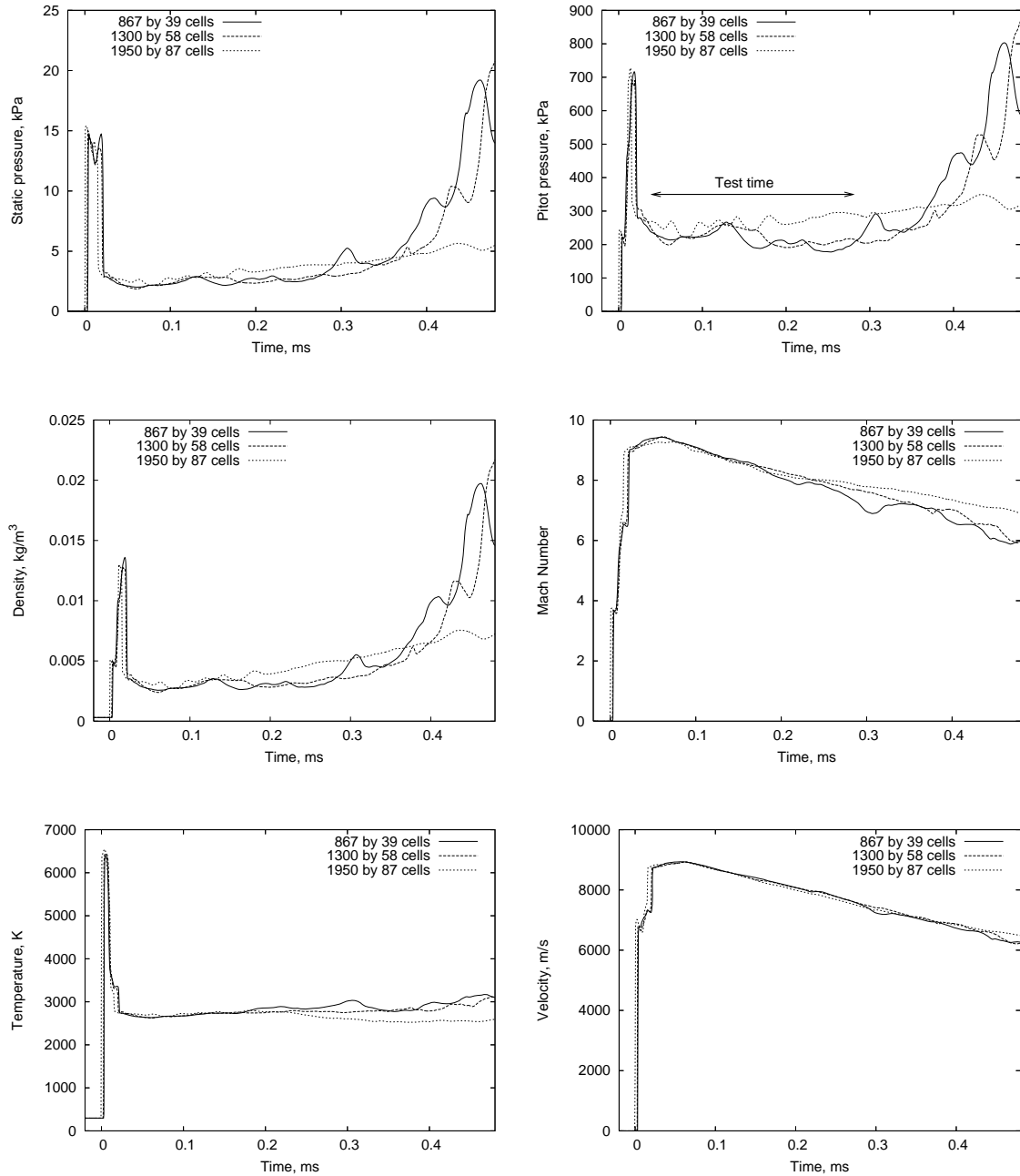


Figure 5.14: Properties from MB_CNS at the nozzle exit for Air Condition 2. Varying grid resolutions for the laminar simulations.

5.4. COMPARISON OF NOZZLE SIMULATIONS AND EXPERIMENTS

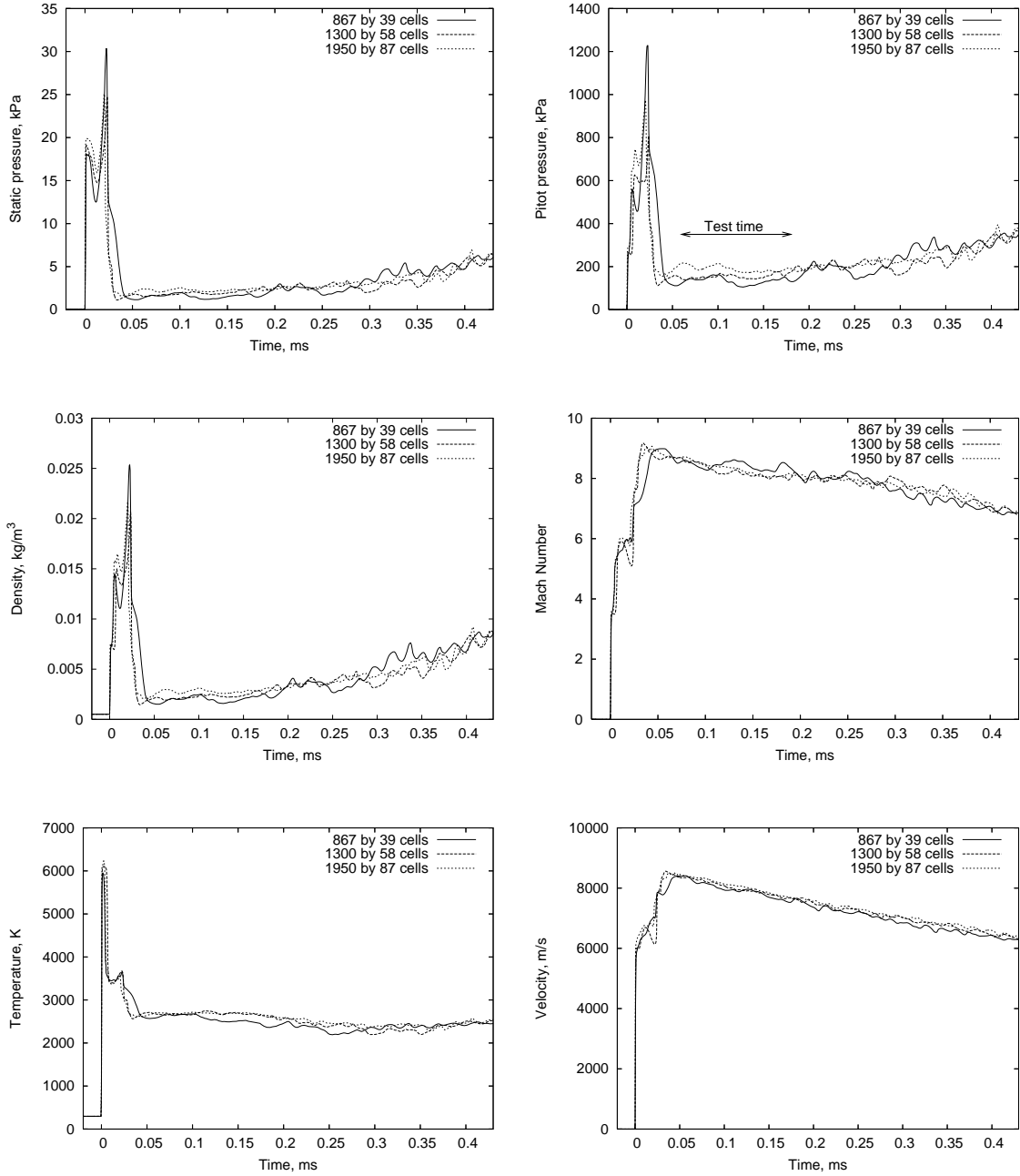


Figure 5.15: Properties from MB_CNS at the nozzle exit for Air Condition 1. Varying grid resolutions for the turbulent simulations.

5.4. COMPARISON OF NOZZLE SIMULATIONS AND EXPERIMENTS

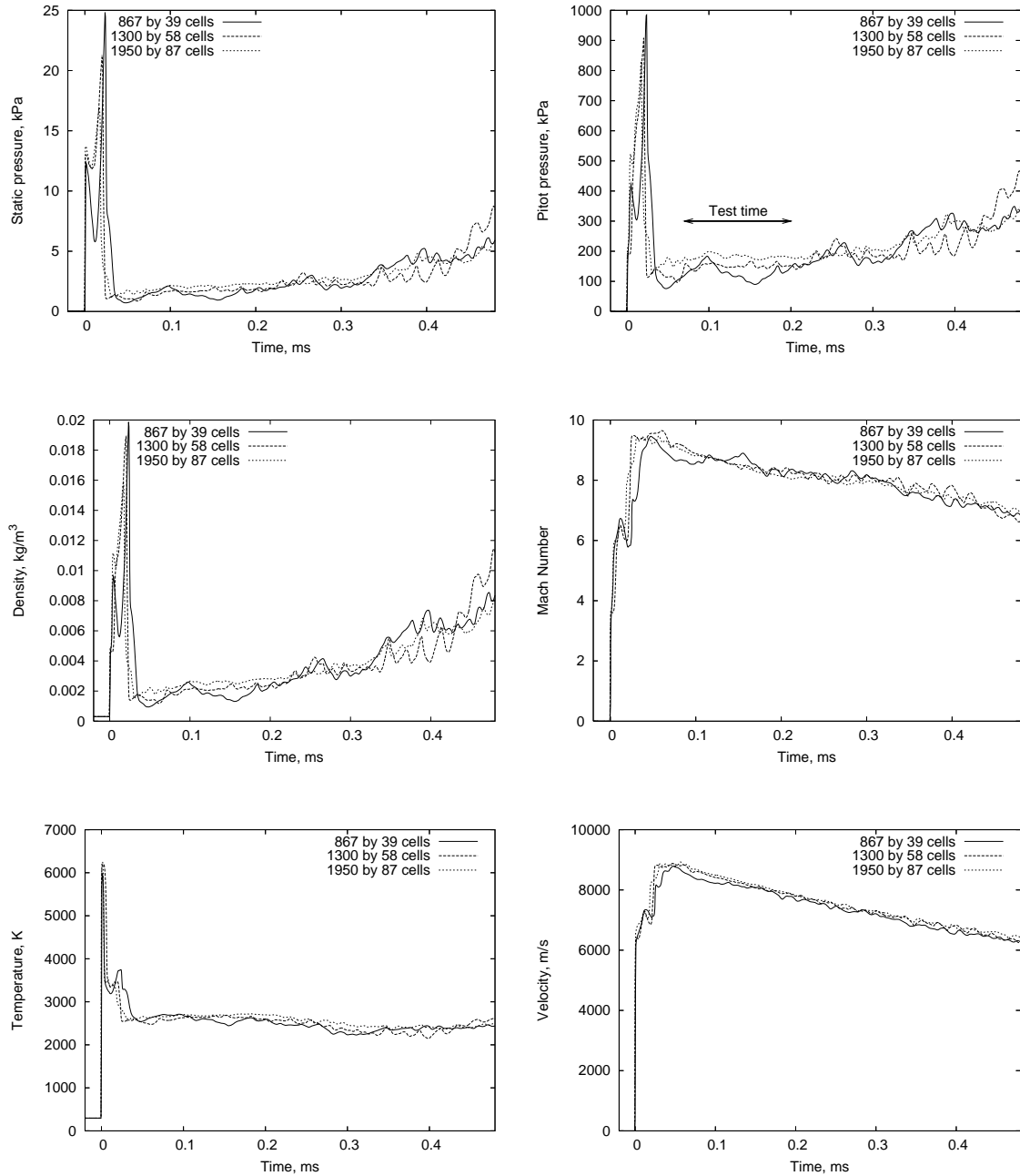


Figure 5.16: Properties from MB_CNS at the nozzle exit for Air Condition 2. Varying grid resolutions for the turbulent simulations.

time was placed around it. The experimental Pitot pressure value was an average from all the transducers in the core flow from all the shots. The static pressure was approximated analogously. The flow properties for the three different MB_CNS cases are plotted in Figure 5.17. In this figure the test time is indicative of that from the turbulent, equilibrium simulation. The static pressure, Pitot pressure and test time for a sample of the experiments for Air Condition 1 are shown in Figures 5.18 and 5.19.

The static and Pitot pressures from the MB_CNS simulations compare reasonably with the experiments. It must be taken into account that the grid for the equilibrium CFD simulations needs to be refined further, which means the pressure values would be slightly higher than those given. Also, the finite-rate simulation was conducted on the coarsest grid with the assumption of a laminar boundary layer. Following previous trends, increasing the grid resolution to a much finer grid would significantly increase the pressure while the addition of turbulence would decrease the pressure. Roughly predicted, the results for a fully grid independent finite-rate and turbulent model would give a Pitot pressure of 300 kPa and a static pressure of 3.0 kPa. This equates to an error of 15 % in Pitot pressure and 5 % in static pressure. This included some large assumptions. It remains uncertain by how much the addition of turbulence and finite-rate chemistry varies the properties at the nozzle exit. At times, the pressures in the test time varied by over 30 %. When modelling the acceleration tube, the pressures did not vary by such substantial magnitudes and the comparison was not so hard to infer. The comparison in the nozzle was also not aided by the amplitude of the noise in the computational simulations.

The time history of the species fractions at the nozzle exit are shown in Figure 5.20. In the acceleration gas, more of the nitrogen has recombined than from the end of the acceleration tube. The nitrogen in the test gas remains in equilibrium. It is shown in these graphs that the equilibrium simulation predicts that the majority of the oxygen in the test gas recombines by the time it reaches the nozzle exit. This is incorrect and it remains frozen as shown in the finite-rate case. This has much more of an effect on the properties at the nozzle exit than what was shown at the end of the acceleration tube. As expected, finite-rate chemistry was required to model the flow correctly in the nozzle.

It is shown in Table 5.6 that the temperature from the equilibrium simulation was much higher than predicted by the finite-rate simulation. Recombination is an exothermic reaction and thus the excess recombination that is predicted causes an overestimate of

temperature. This in course has an impact on the density and Mach number. In the finite-rate MB_CNS simulation the Mach number was expanded from 7.2 to 9.6 in the nozzle. The original design in SM_3D⁺ was based upon a Mach number expansion from 7.3 to 10.2 which is sufficiently accurate when compared to the MB_CNS. The difference which occurs would be due to the perfect gas assumption in SM_3D⁺. The equilibrium MB_CNS predicted a Mach number increase from 7.3 to 8.6-8.7, which indicates that the finite-rate simulation is definitely required to accurately predict this. It is interesting to note that even though in the equilibrium acceleration tube simulation, the temperature was wrong, the Mach number was very similar to the finite-rate simulation.

From the time history graphs of the Pitot pressure measurements, an increase in the test time that was available at the acceleration tube exit is evident. A test time of at least $150\ \mu\text{s}$ is present in all the computational work. The test time may appear to be much larger in the equilibrium cases but later in time the boundary layer becomes extremely large and eliminates the majority of the core flow. The u-a wave comes through later in time in the equilibrium simulations due to the incorrect temperature. The overestimated temperature leads to a high speed of sound which results in a slower u-a wave. The experiments had a test time of $110\ \mu\text{s}$ which was an increase from the $55\ \mu\text{s}$ at the acceleration tube exit. The two methods do not match perfectly and the axisymmetric model may not capture the flow exactly, but they both demonstrate the same essential effects. The difference between the two methods can be attributed to the modelling of the boundary layer. As is explained in Section 5.5 the test time increase is due to the boundary layer growth in the acceleration tube. The incorrect reconstruction of the boundary layer in the CFD work, which is discussed in the next paragraph, results in longer times of steady pressure. The main point which can be taken from this is that, undoubtedly, the test time from both methods increases.

The Pitot pressure, Mach number and temperature distributions, at various periods in the test time, in the radial direction at the nozzle exit, are shown in Figures 5.21 to 5.23. The graph of Pitot pressure includes the comparison with the experimental values. The experiments displayed a slight curvature in pressure across the core flow. This may have been exacerbated by the laminar design of the nozzle. The high Mach number of the flow resulted in very large boundary layers. Both Pitot transducer 1 and Pitot transducer 2 lay in the boundary layer in the experiments. This meant the experiments indicated

approximately 100 mm of core flow diameter. The high Reynolds number caused the laminar simulations to incorrectly represent the boundary layer and the core flow diameter was dramatically overestimated. The turbulent simulations gave a much better depiction of the flow. Towards the edge of the boundary layer, a large hump developed in the computational plots which appeared to not occur in the experimental plots. This hump indicated that the flow towards the boundary layer was not fully expanded. However, the graph is deceiving due to the single time taken for the experimental pressure readings at Pitot transducers 1 and 2. This was at a time of approximately 0.05 ms. Examining the time history plots in Figure 5.19, both the transducers values near the wall increased in time. Taking values at various instances which correspond to the times from the CFD plots in Figure 5.21, there was good agreement between the experimental and CFD values. In the numerical work the pressure rise in the boundary layer is slightly steeper. This suggests that a few more cells were required to more accurately capture the boundary layer. The comparison here was adequate and the computational work demonstrates the features that are occurring in the real flow. The core flow diameter agreed fairly well with the turbulent SM_3D⁺ simulations. The quality and size of the flow produced across the nozzle was sufficient for testing models.

Contour plots of the log of density in the nozzle for the turbulent, equilibrium simulation are shown in Figures 5.24 to 5.27. The times given are those pertaining to the time from the rupture of the secondary diaphragm. The shock structure that forms when the secondary shock enters the nozzle can be seen in these plots along with the growth of the boundary layer. The disturbances in the acceleration tube flow that were caused by the turbulent boundary layer fed into the nozzle flow. To compound this, shear layers in the nozzle boundary layer generated more disturbances. The disturbances were again assumed to be slightly overestimated by the numerical model due to the overestimation of turbulent viscosity. Even with this effect the wave reflection in the nozzle seemed to dissipate the unsteadiness and very little fluctuation resulted in the properties during the test time. The flow was much cleaner in the equilibrium simulations at the nozzle exit than at the acceleration tube exit.

Table 5.6: Summary of the flow properties at the nozzle exit for Air Condition 1

Property	MB_CNS	MB_CNS	MB_CNS	Experiments
	viscous, laminar equilibrium	viscous, turbulent equilibrium	viscous, laminar finite-rate	
Static pressure, kPa	3.0 + 0.7 - 0.2	2.3 + 0.7 - 0.3	3.0 + 0.7 - 0.2	3.1 ± 0.4
Pitot pressure, kPa	260 ± 10	190 + 30 - 0	300 + 30 - 10	263 ± 40
Density, g/m ³	3.7	2.7	5.3	-
Mach number	8.6	8.7	9.6	-
Static temperature, K	2760	2700	1650	-
Velocity, km/s	8.35	8.35	8.23	-
Static enthalpy, MJ/kg	4.16	3.96	4.46	-
Total enthalpy, MJ/kg	39.02	38.83	38.32	-
Specific internal energy, MJ/kg	3.3	3.15	3.91	-
Unit Reynolds number	3.48 × 10 ⁵	2.28 × 10 ⁵		-
Test time, μs	250	150	150	110

5.4.4 Air Condition 2

Air Condition 2 was slightly off the design condition of the hypersonic nozzle. The flow inlet Mach number as predicted by the finite-rate MB_CNS simulation was 8.0 which was increased to 12.0 at the nozzle exit. Similar to before, the equilibrium simulation predicts incorrect Mach numbers due to temperature effects. The same graphics that were illustrated for Air Condition 1 are presented here for Air Condition 2. Table 5.7 gives a summary of the results while Figure 5.28 depicts the time history graphs. Figure 5.29 gives the species fractions throughout time at the nozzle exit and Figures 5.30 and 5.31 present a sample of the experimental results. Figures 5.32 to 5.34 give the Pitot pressure, Mach number and temperature profiles at the nozzle exit. The flow phenomena experienced in this condition was analogous to Air Condition 1 and the all effects stated above will not be restated here. The characteristics of the flow can be inferred from the tables and figures presented.

The contoured nature of the nozzle makes it susceptible to shock formation at non-design conditions. Despite the higher Mach number, it was clearly evident that no compression waves were formed in the nozzle. A core flow diameter of approximately 100 mm developed with a test time of 110 μ s. From the profiles across the nozzle exit no curvature of the flow existed as was seen in Air Condition 1. Though this condition was not significantly different to the intended design, it demonstrates the nozzle is capable of producing usable flow in other conditions.

5.4. COMPARISON OF NOZZLE SIMULATIONS AND EXPERIMENTS

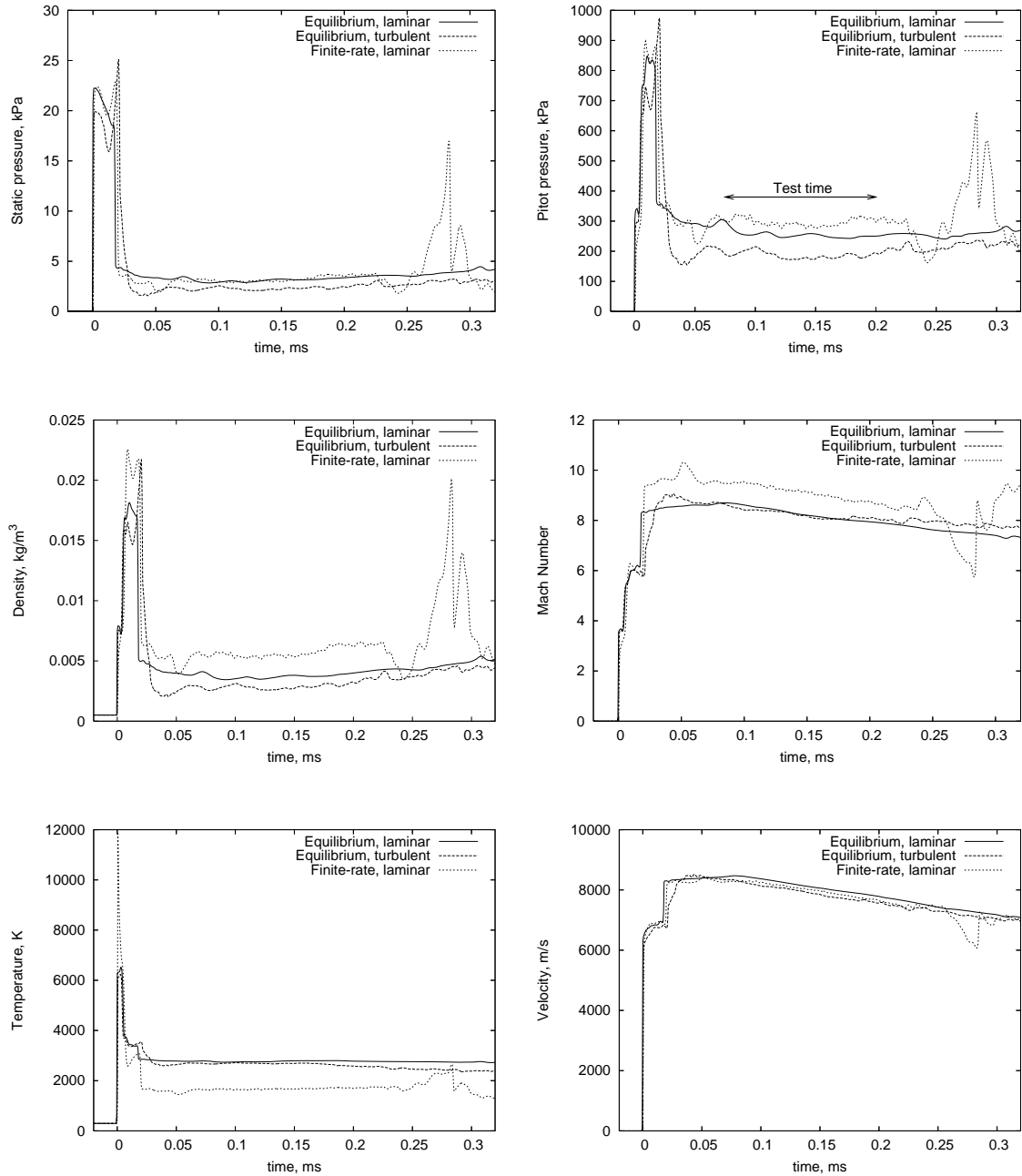


Figure 5.17: Properties from MB-CNS at the nozzle exit for Air Condition 1 comparing the different MB-CNS models.

5.4. COMPARISON OF NOZZLE SIMULATIONS AND EXPERIMENTS

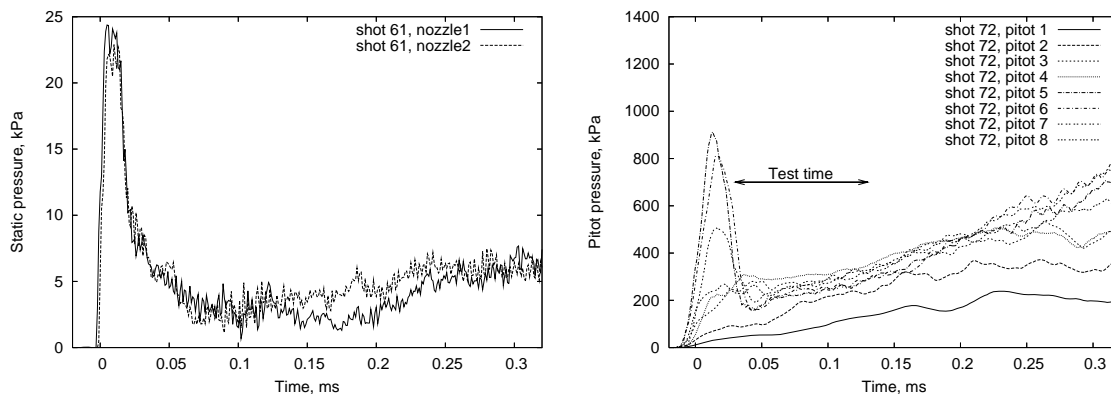


Figure 5.18: Static and Pitot pressures from the experiments at the nozzle exit for Air Condition 1

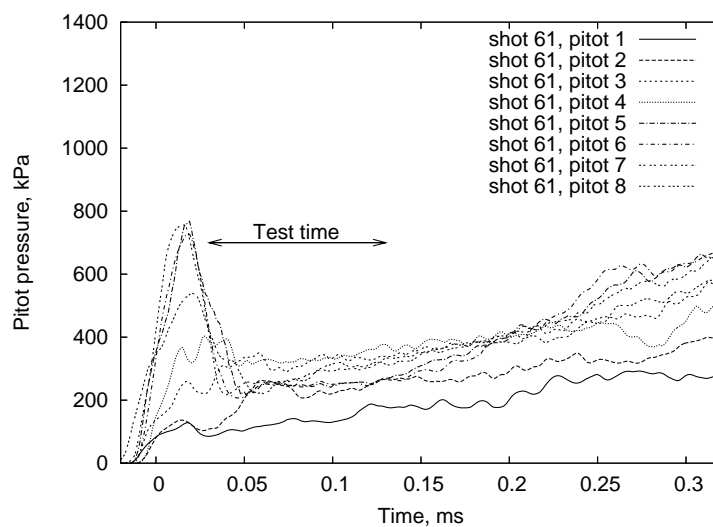


Figure 5.19: Pitot pressures from the experiments at the nozzle exit for Air Condition 1

5.4. COMPARISON OF NOZZLE SIMULATIONS AND EXPERIMENTS

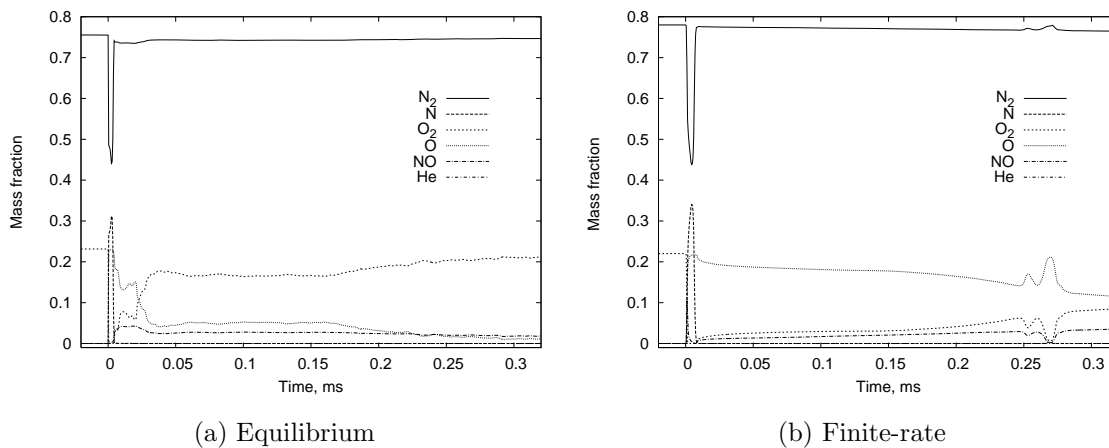


Figure 5.20: Species fractions from MB_CNS at the nozzle exit for Air Condition 1

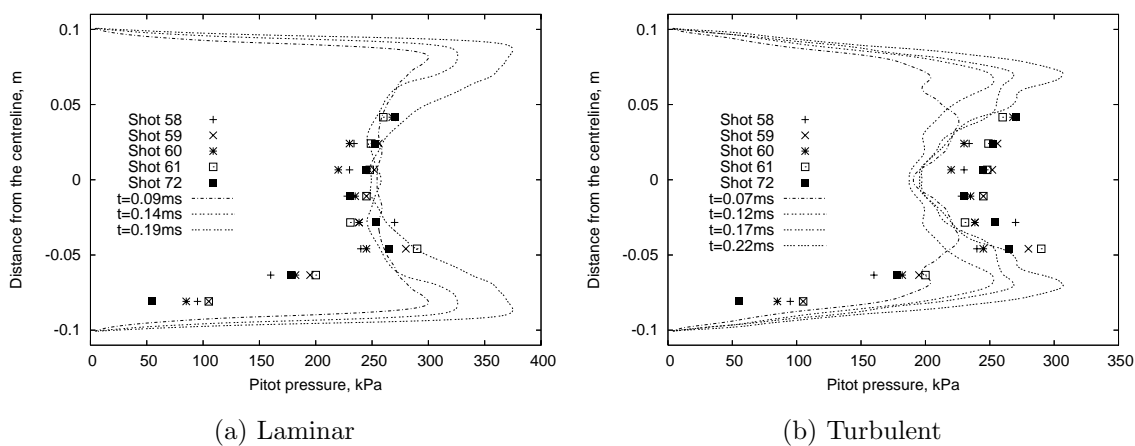


Figure 5.21: Comparison of the experimental and computational Pitot pressure profiles at the nozzle exit for Air Condition 1

5.4. COMPARISON OF NOZZLE SIMULATIONS AND EXPERIMENTS

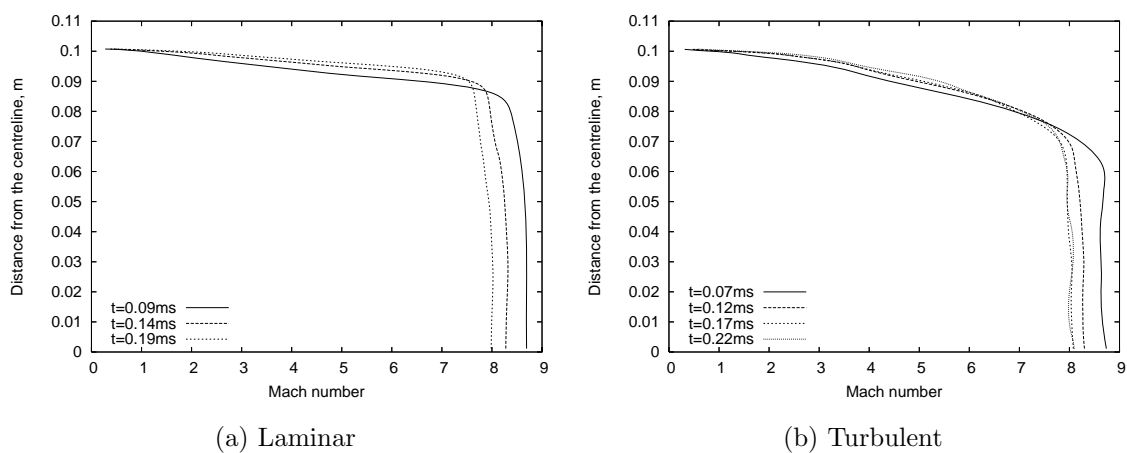


Figure 5.22: Mach number profiles from MB.CNS across the nozzle exit for Air Condition 1

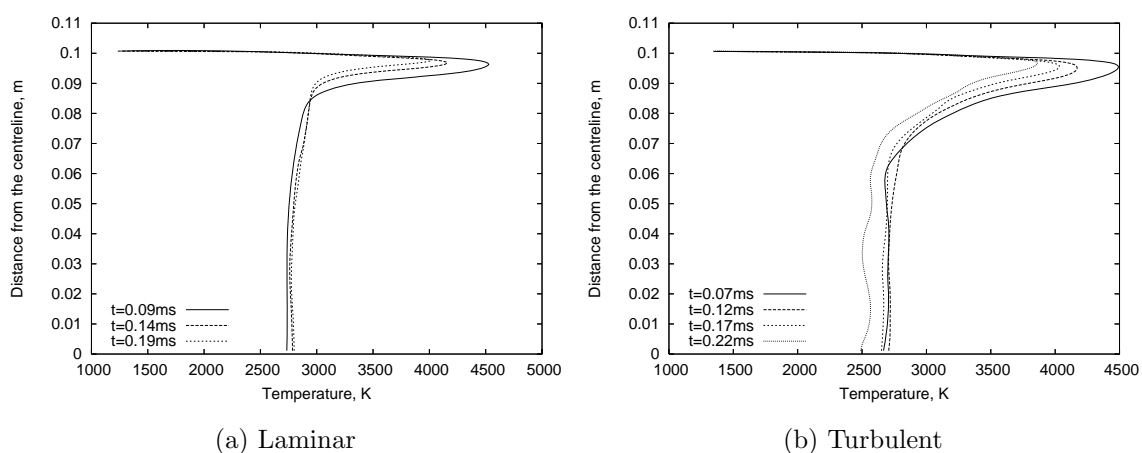
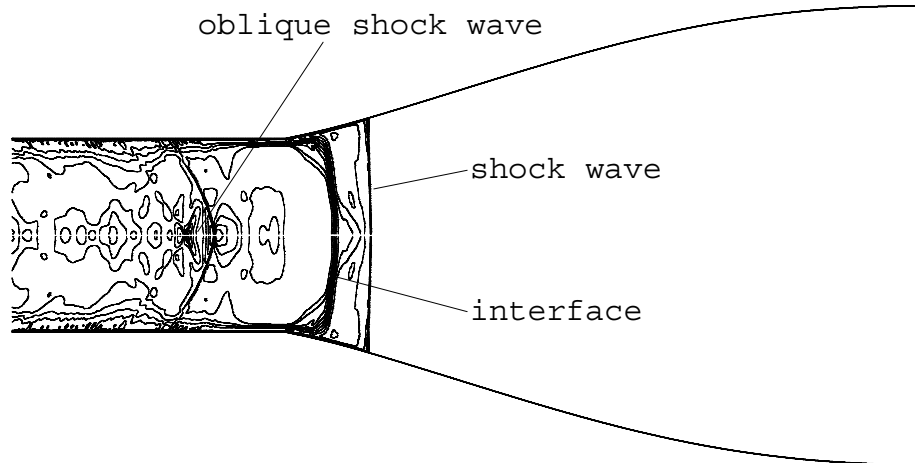
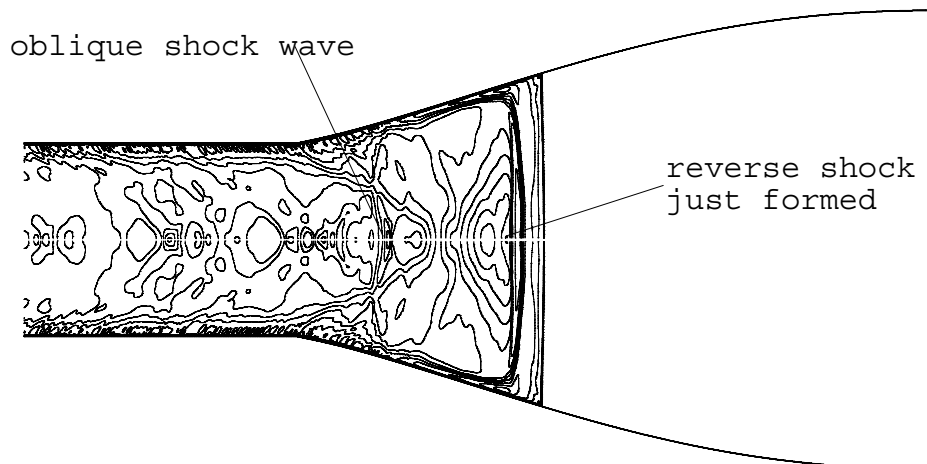


Figure 5.23: Temperature profiles from MB.CNS across the nozzle exit for Air Condition 1

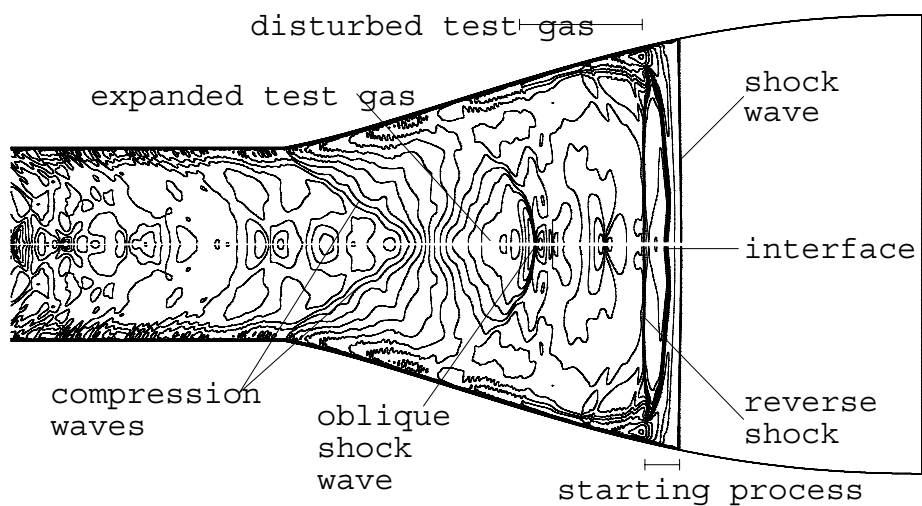


(a) $t=0.65\text{ms}$

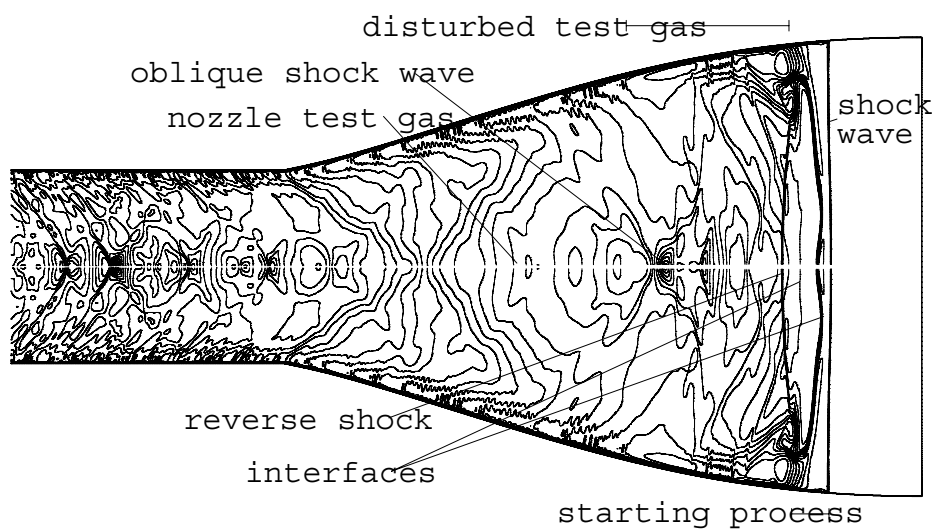


(b) $t=0.70\text{ms}$

Figure 5.24: Propagation of the flow in the nozzle for the turbulent case: part 1

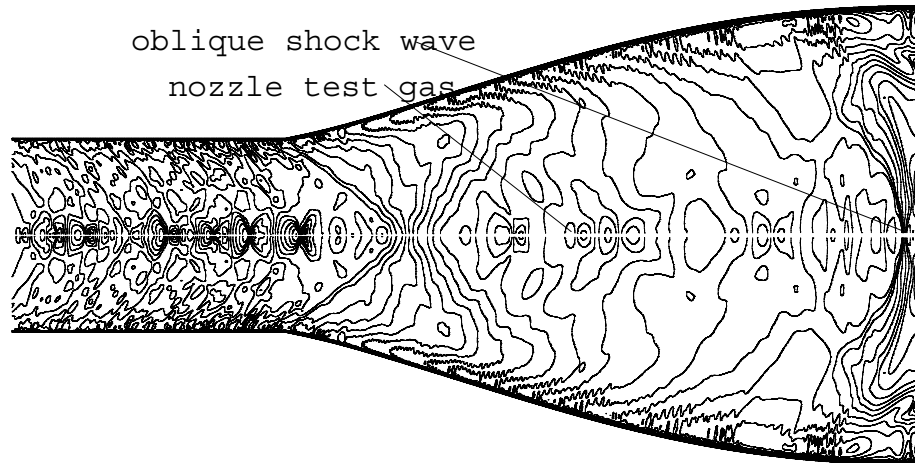


(a) $t=0.75\text{ms}$

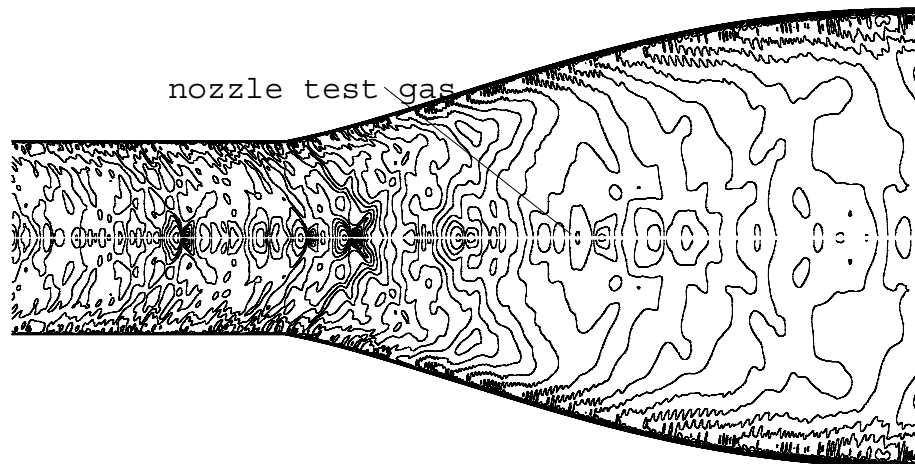


(b) $t=0.80\text{ms}$

Figure 5.25: Propagation of the flow in the nozzle for the turbulent case: part 2

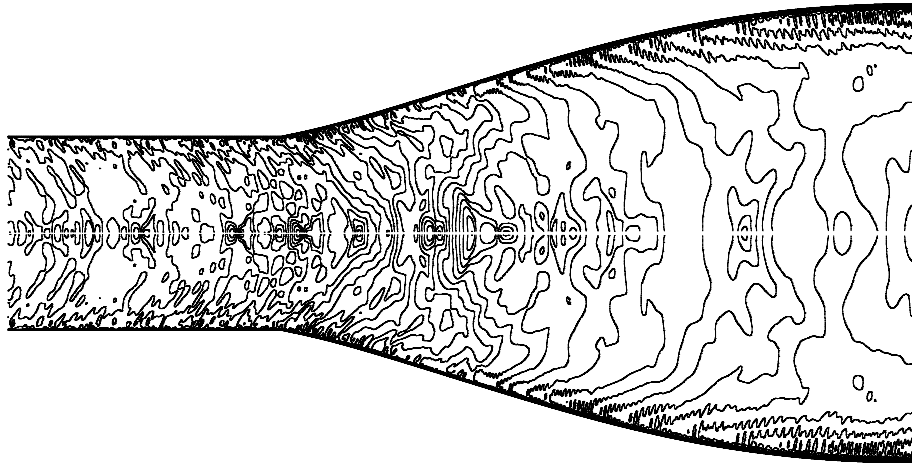


(a) $t=0.85\text{ms}$

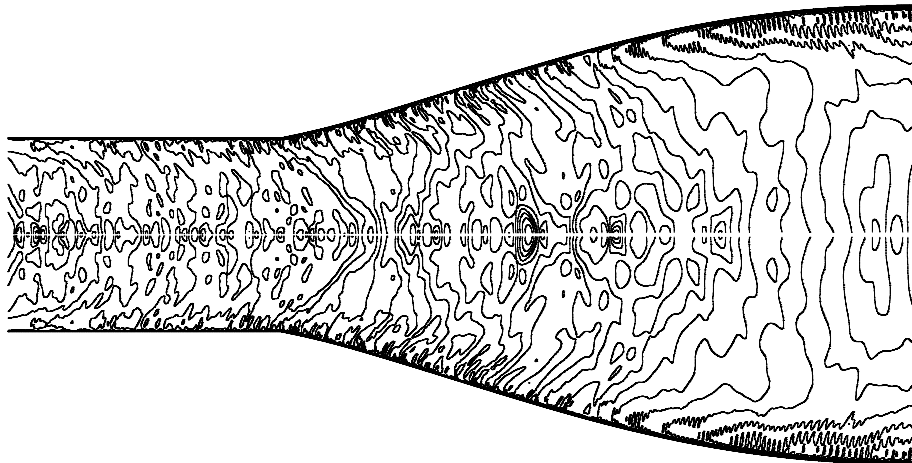


(b) $t=0.90\text{ms}$

Figure 5.26: Propagation of the flow in the nozzle for the turbulent case: part 3



(a) $t=0.95\text{ms}$



(b) $t=1.00\text{ms}$

Figure 5.27: Propagation of the flow in the nozzle for the turbulent case: part 4

Table 5.7: Summary of the flow properties at the nozzle exit for Air Condition 2

Property	MB_CNS		MB_CNS		Experiments
	viscous, laminar equilibrium	viscous, laminar equilibrium	viscous, turbulent equilibrium	viscous, laminar finite rate	
Static pressure, kPa	2.5 + 1.0 - 0.3	2.1 + 0.1 - 0.6	1.0 + 0.7 - 0.2		1.5 ± 0.5
Pitot pressure, kPa	270 + 10 - 40	180 + 20 - 10	160 ± 20		215 ± 30
Density, g/m ³	3.0	2.5	2.2		-
Mach number	9.05	9.3	12.0		-
Static temperature, K	2700	2690	1200		-
Velocity, km/s	8.83	8.8	8.7		-
Static enthalpy, MJ/kg	4.03	4.04	4.00		-
Total enthalpy, MJ/kg	42.97	42.76	41.85		-
Specific internal energy, MJ/kg	3.20	3.20	3.55		-
Unit Reynolds number	3.00 × 10 ⁵	2.55 × 10 ⁵			-
Test time, μ s	200	150	150		110

5.4.5 Titan Condition

The Titan condition had a significantly slower secondary shock speed, of 5.51 km/s, compared to the design condition for the hypersonic nozzle. Despite this, the inflow Mach number of 6.7 from the MB_CNS simulation was similar to the design Mach number of 7.3. Table 5.8 presents a comparison of the CFD and experimental properties. Figures 5.35 and 5.36 give the time history graphs of the properties at the acceleration tube exit. The properties from the two methods did not compare well and this was probably due to deficiencies in the numerical model. The air in the acceleration gas was modelled as a perfect gas which would have resulted in significantly higher temperatures than those that actually existed in the flow. The equilibrium assumption in the Titan test gas would have also produced errors. The methane would have been dissociated, creating non-equilibrium effects. These problems need to be investigated in order for the CFD to provide a better estimates. This work is part of other studies at the University of Queensland.

The MB_CNS simulation indicated only a slight increase in the test time with the nozzle attached. The accuracy of this is questionable, especially considering the differences between the experimental and numerical pressures. The experiments indicated a test time of $100\mu\text{s}$, a significant increase from the $50\mu\text{s}$ at the acceleration tube exit. The experiments showed a gradual decrease in the Pitot pressure in the test time of shot 73, but this was not evident in shot 70 or the other shots.

Figures 5.37 and 5.38 give the flow properties across the nozzle exit for the experiments and the equilibrium, turbulent simulation. The CFD shows a core flow diameter of approximately 90 mm which compares well with the experiments. Also, the boundary layer was reasonably well predicted. However, the core flow diameter pressure changes considerably throughout the test time which is due to numerical effects. The experiment values remain constant throughout time and the flow is extremely constant across the tube.

The results indicated that the Titan condition with the nozzle attached would have been very suitable for testing. Though the CFD and experiments did not provide great agreement, it was assumed that the incorrect assumptions in the modelling caused errors in the numerical results. It was demonstrated that the experiments gave a sufficient core flow diameter and ample test time which could be used for testing of a model.

5.4. COMPARISON OF NOZZLE SIMULATIONS AND EXPERIMENTS

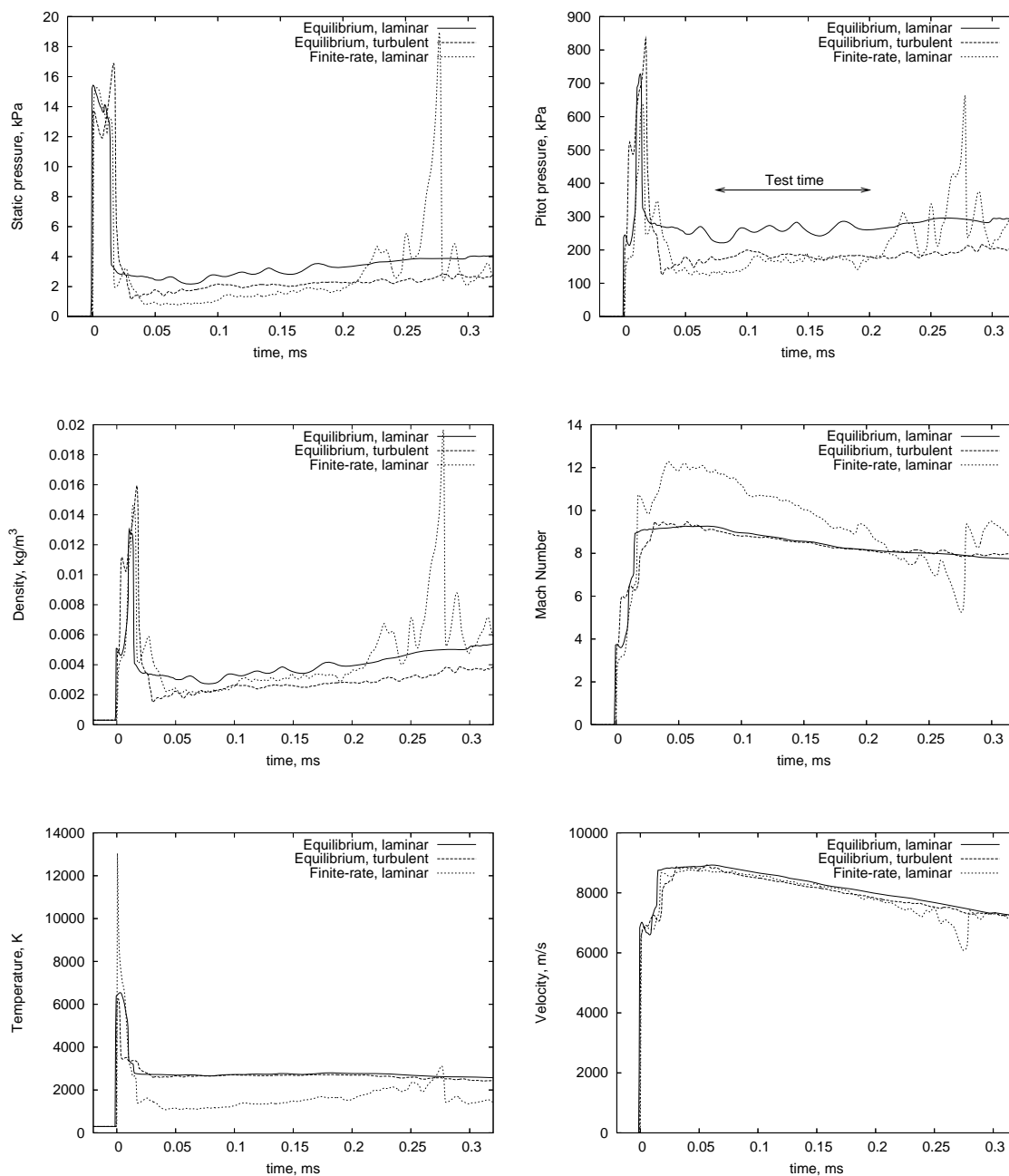


Figure 5.28: Properties from MB-CNS at the nozzle exit for Air Condition 2 comparing the different MB-CNS models.

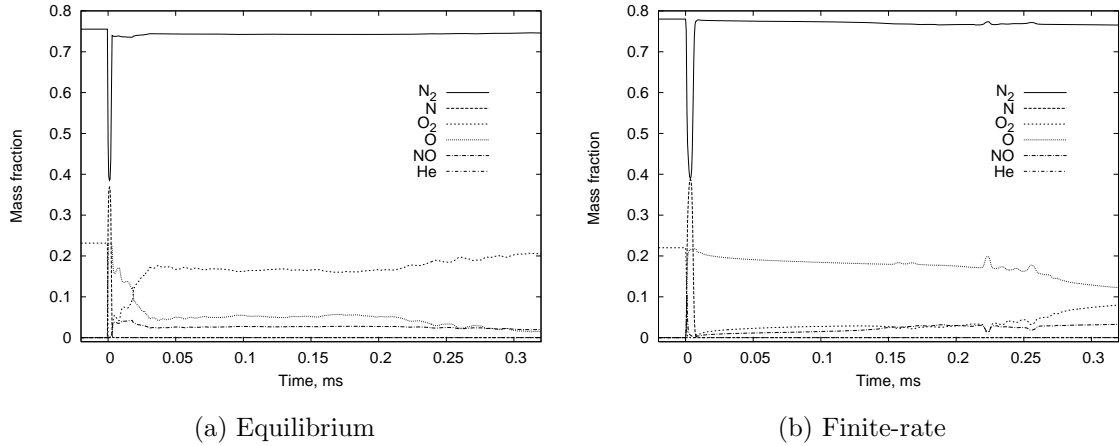


Figure 5.29: Species fractions from MB_CNS at the nozzle exit for Air Condition 2

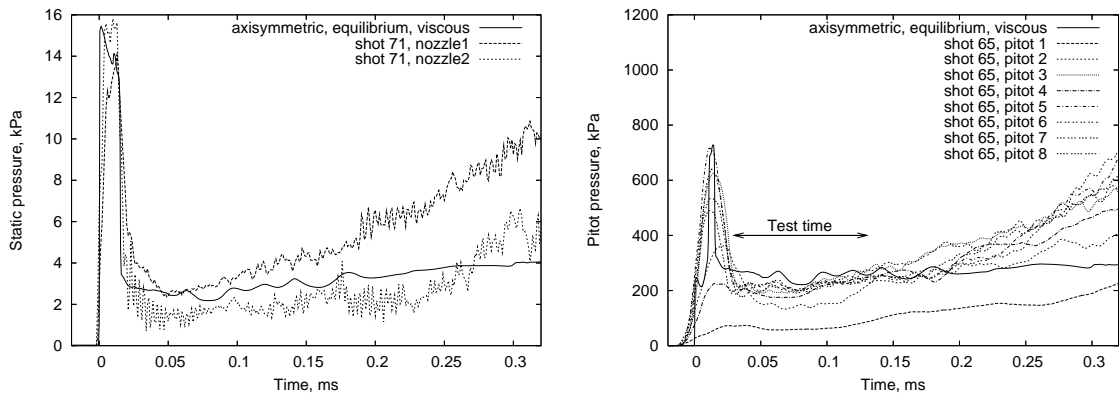


Figure 5.30: Static and Pitot pressures from the experiments at the nozzle exit for Air Condition 2

5.5 Examination of the Hypersonic Nozzle

To recapitulate, the new single-stage driver for X2 was discussed in Chapter 4 along with the CFD and experiments which were conducted for this arrangement. From this work, an inflow condition was obtained to design a contoured hypersonic nozzle. Once the nozzle was installed, more experiments and CFD were conducted on the new configuration. Though the comparison between the flow properties at the nozzle exit was not perfect, it was shown that an increase in both the test time and core flow diameter resulted from the implementation of the nozzle. This occurred at the three conditions which were examined including two conditions off the original design. This section investigates the nozzle phenomena and presents the reasoning behind why it is thought the test time

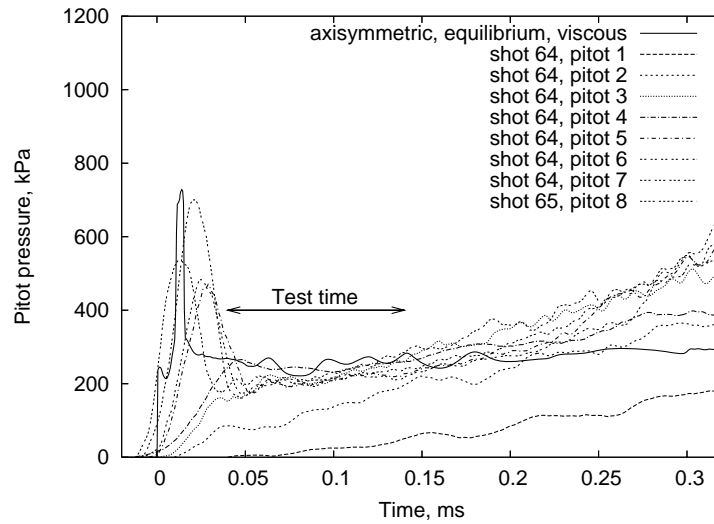


Figure 5.31: Pitot pressures from the experiments at the nozzle exit for Air Condition 2

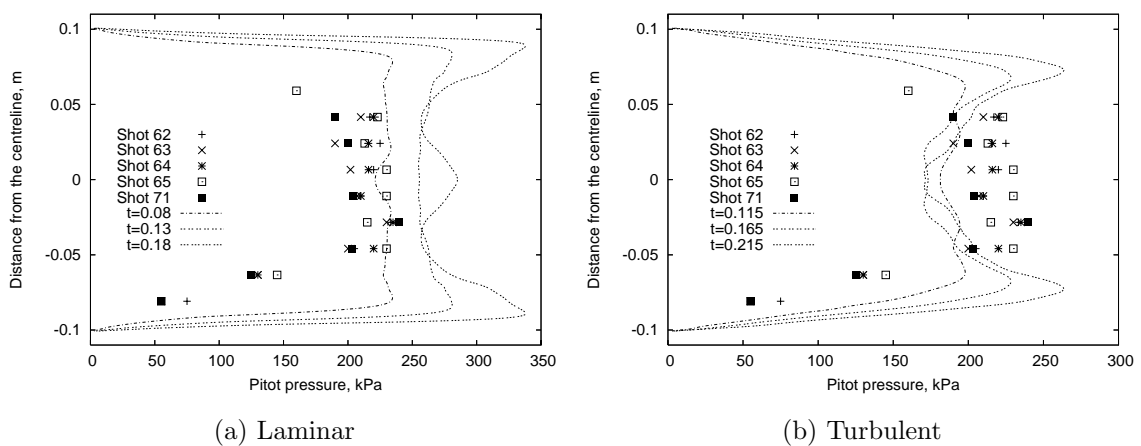


Figure 5.32: Comparison of the experimental and computational Pitot pressure profiles at the nozzle exit for Air Condition 2

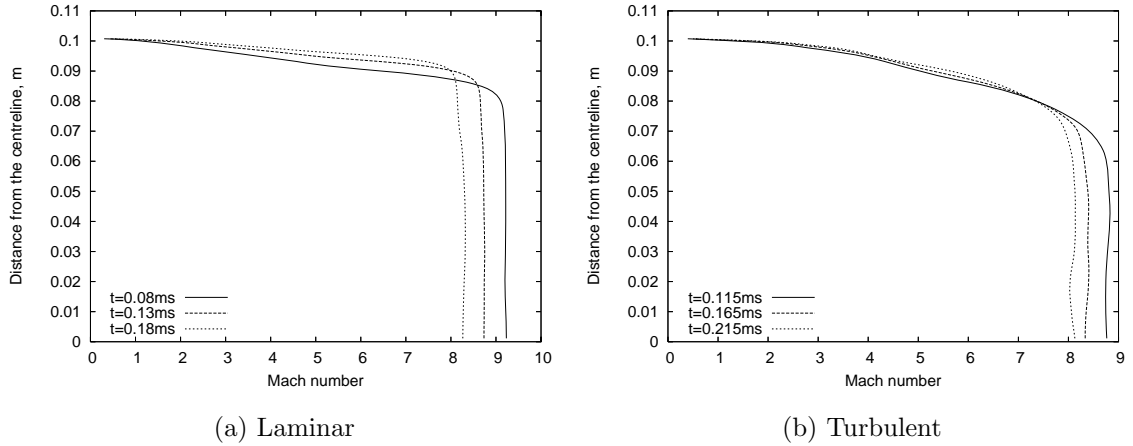


Figure 5.33: Mach number profiles from MB_CNS across the nozzle exit for Air Condition 2

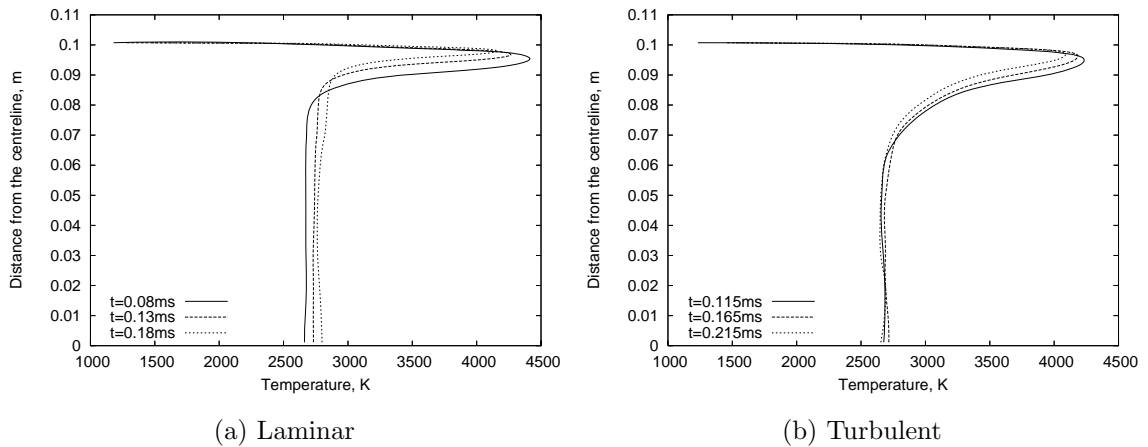


Figure 5.34: Temperature profiles from MB_CNS across the nozzle exit for Air Condition 2

increased.

The main purpose of a supersonic/hypersonic nozzle is generally to increase the speed of the flow. In this investigation the primary aim was more towards increasing the core flow diameter and test time. The increase in velocity was still an important aspect. With a contoured nozzle, due to the wave cancelling nature, it can be susceptible to shocks forming at non-design conditions. These waves would be visible in the flow and would disrupt the test time and render it unusable. This did not occur and suitable flow was generated for all the conditions. Though different conditions were tested in the nozzle, none with Mach numbers considerably different from the original design were tried. The Mach number from the finite-rate simulation of Air Condition 1 increased from 7.2 at

5.5. EXAMINATION OF THE HYPERSONIC NOZZLE

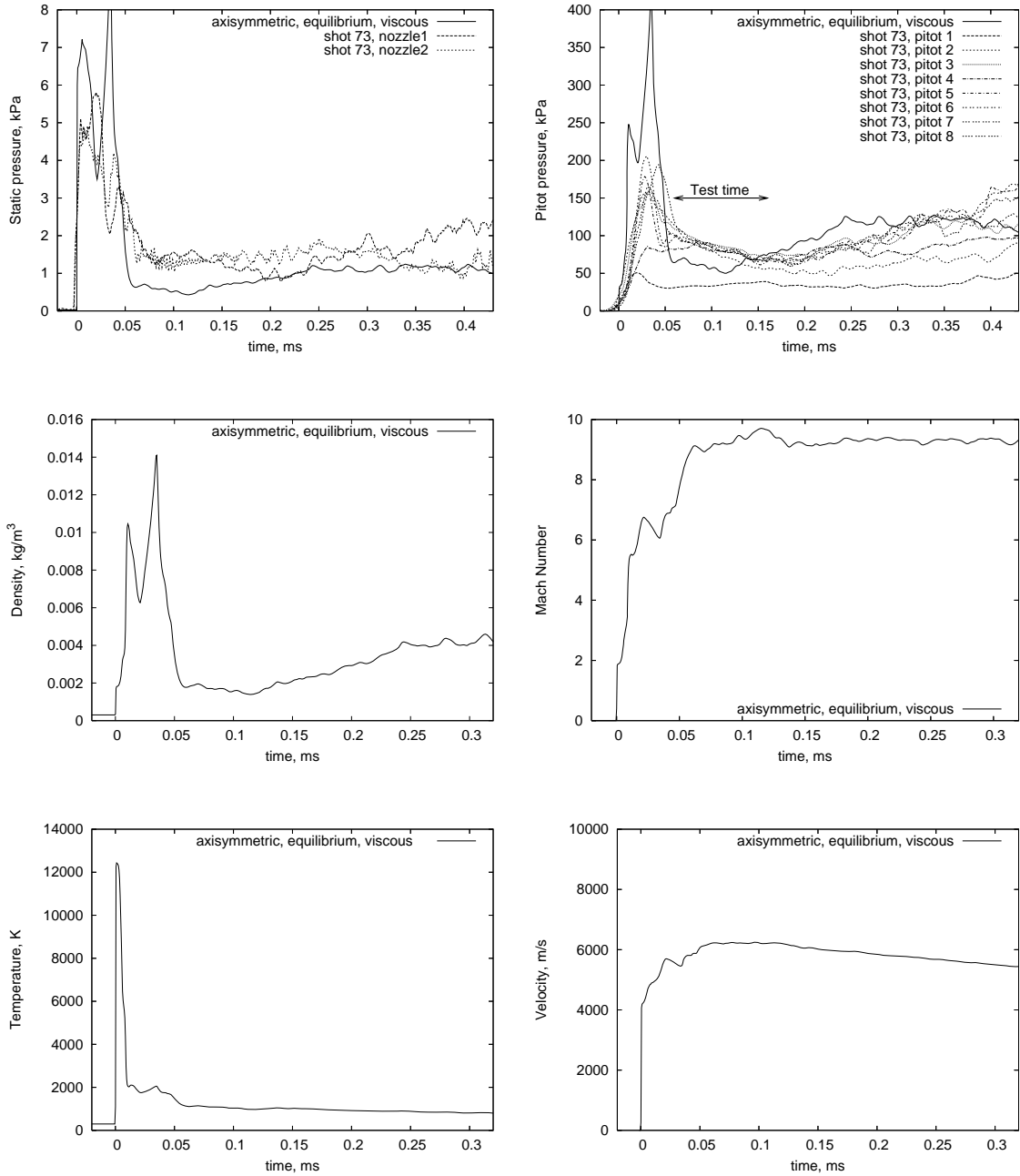


Figure 5.35: Properties at the nozzle exit for the Titan condition with a comparison of the experimental and computational pressures

Table 5.8: Summary of the flow properties at the nozzle exit for the Titan condition

Property	MB_CNS viscous, turbulent equilibrium	Experiments
Static pressure, kPa	0.6-0.8	1.40
Pitot pressure, kPa	60-70	82.8
Density, g/m ³	1.6-2.0	-
Mach number	9.2	-
Static temperature, K	1000	-
Velocity, km/s	6.0	-
Static enthalpy, MJ/kg	1.47	-
Total enthalpy, MJ/kg	19.47	-
Specific internal energy, MJ/kg	1.0	-
Test time, μ s	60	100

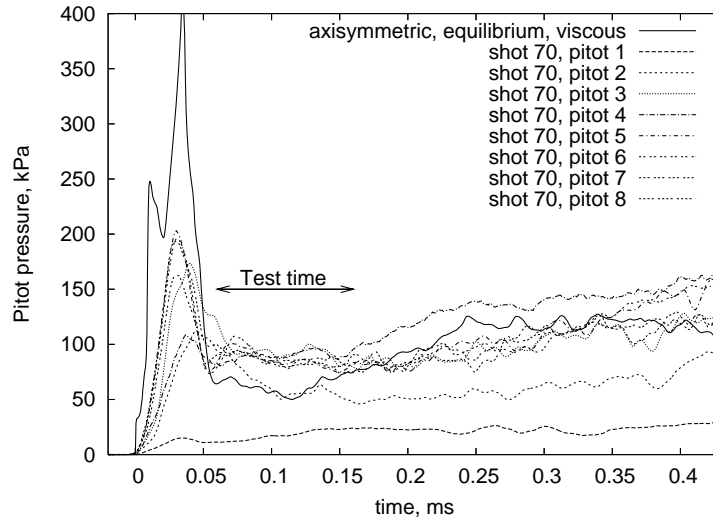


Figure 5.36: Comparison of the experimental and computational Pitot pressures at the nozzle exit for the Titan condition

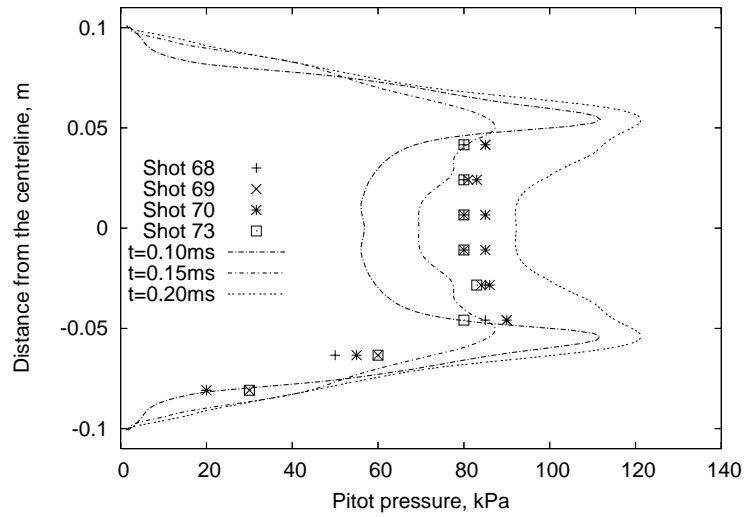


Figure 5.37: Comparison of the experimental and computational Pitot pressure profiles at the nozzle exit for the Titan condition

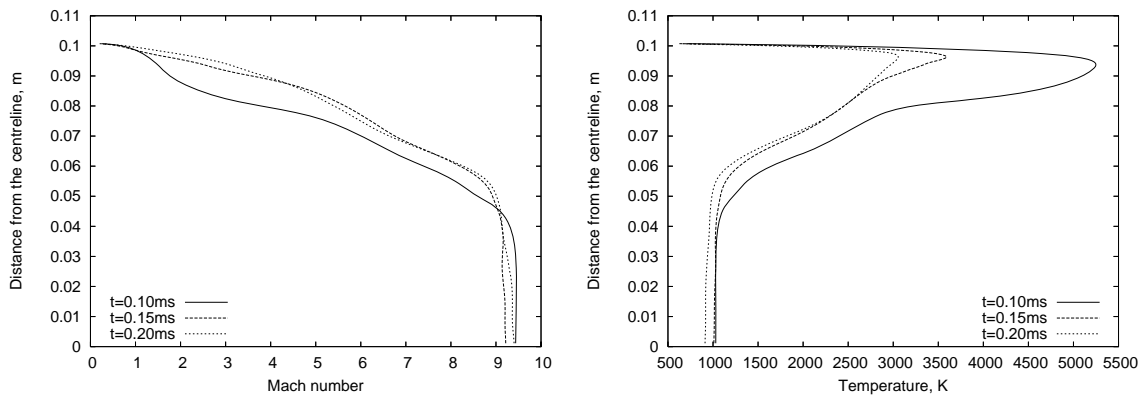


Figure 5.38: Profiles from MB-CNS across the nozzle exit for the Titan condition

the nozzle inlet to 9.6 at the nozzle exit. This was comparable to the 7.3 and 10.2 that were stated in the SM_3D⁺ design work. The two non-design conditions, Air Condition 2 and the Titan condition, increased the Mach number from 8.0 to 12.0 and 6.7 to 9.2 respectively. The inflow operating regime of the nozzle was thus at least between Mach 6.7 and 8. Much larger inflow Mach numbers are to be tested in other studies at the University of Queensland. It is expected that the nozzle would not produce clean test flow with an inflow Mach number considerably above 8.

The purpose of this study was to support the claim that both the core flow diameter and steady time available for testing increased in an expansion tube with the addition of a hypersonic nozzle. The experiments showed that the air conditions increased the test time from 55 μ s to 110 μ s. The core flow diameter increased from 60 mm to 100 mm which would have been greater if the nozzle had been designed assuming a turbulent boundary layer. The Titan experiments showed an increase in the test time from 50 μ s to 100 μ s and the core flow diameter from 65 mm to 90 mm. Though the CFD did not give these same results it demonstrated similar trends. The test time for the air conditions increased from 70 μ s to 150 μ s and the core flow diameter for the turbulent simulations increased from 60 mm to 100 mm. The CFD work showed that the nozzle was doing what was claimed and the experimental results confirmed this.

The x-t diagrams in Figures 5.39 and 5.40 illustrate the wave interaction in the acceleration tube and nozzle from the equilibrium, turbulent simulation of Air Condition 1. The wave interaction is extremely complex. Examining Figure 5.40 reveals the starting process of the nozzle. This can also be seen in the contour plots in Figure 5.24. The shock wave slows down as it enters the initial diverging section of the nozzle due to the increasing area ratio. The interface also slows down, but not to the same extent as the shock wave. Thus the interface catches up to the shock and by the time they reach the nozzle exit they are very close together. As these waves slow down, expanded gas collects at the back of them. A reverse shock is formed which moves upstream relative to the fluid but is pushed downstream by the high speed of the flow. This reverse shock gets stronger as time goes by. Between the interface and the reverse shock another interface forms which is clearly evident in the time history plots in Figure 5.42. The arrival of the u-a wave or tail of the unsteady expansion is what causes the end of the steady pressure at the acceleration tube exit. The speed of sound decreases through the nozzle so u-a

wave actually gets faster as it progresses further down the nozzle.

The flow structure which establishes as part of the nozzle starting process is supposed to consume part of the test gas that exists at the acceleration tube exit [131, 132]. This is the case as is seen in the x-t diagram of Figure 5.40, but it does not have a major effect. The increase in speed of the u-a wave is more influential in reducing the time. The combination of these two phenomena imply that the test time should decrease. Furthermore, the majority of the test gas from the acceleration tube exit gets disturbed by an oblique wave which is formed in the acceleration tube and then amplified in the start of the nozzle. This wave is curved across the nozzle as seen in the contour plots and by the time it reaches the nozzle exit becomes damped considerably. However, this gas is not assumed part of the test gas at the nozzle exit and gets flushed out at around 0.27 ms on the Pitot pressure time history plots. The test time at the nozzle exit actually occurs after this. The pressure at this time should be increasing as the unsteady expansion comes through. This indicates that there is some other compensating effect which makes the gas later in time have steady properties.

A plausible explanation for the test gas at the nozzle exit beginning at the downstream end of the unsteady expansion is due to the boundary layer growth in the acceleration tube. The boundary layer at the acceleration tube exit becomes larger in time. This is confirmed by Figure 5.43 which plots the Pitot pressure and Mach number across the acceleration tube exit at various times. The times noted here are referenced to the rupture of the secondary diaphragm. The shock wave reaches the acceleration tube exit at 0.613 ms. These plots are thus after the acceleration tube test time and this flow is what is used as the nozzle test time. The increasing acceleration tube boundary layer causes the core flow to see a varying area ratio through the nozzle. The gas later in time is expanded more. This compensates for the property variation caused by the unsteady expansion wave. It is not just the pressure which is steady in time at the nozzle exit but also temperature, density and velocity. There is no reason why this flow cannot be used for the testing of models. Even if the mechanism proposed here for the increase in steady test time is incorrect it ultimately does not matter. What is important is that the compensating effect always appears to occur in the nozzle and the flow is suitable for testing models.

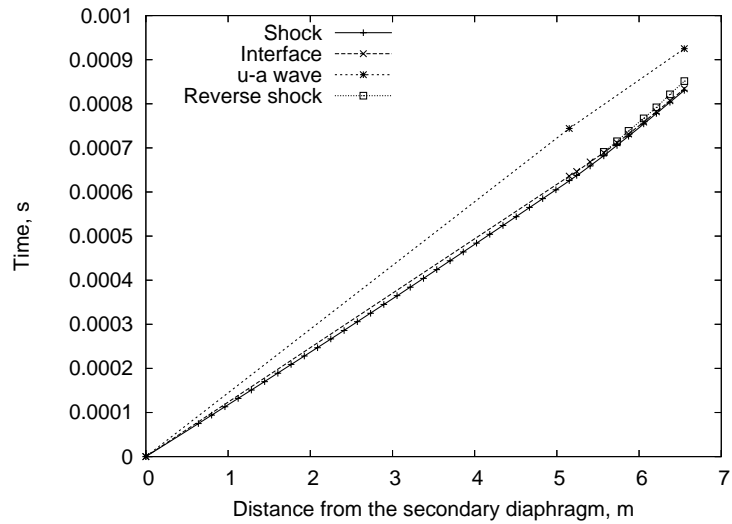


Figure 5.39: An x-t diagram constructed from the equilibrium, turbulent simulation of Air Condition 1

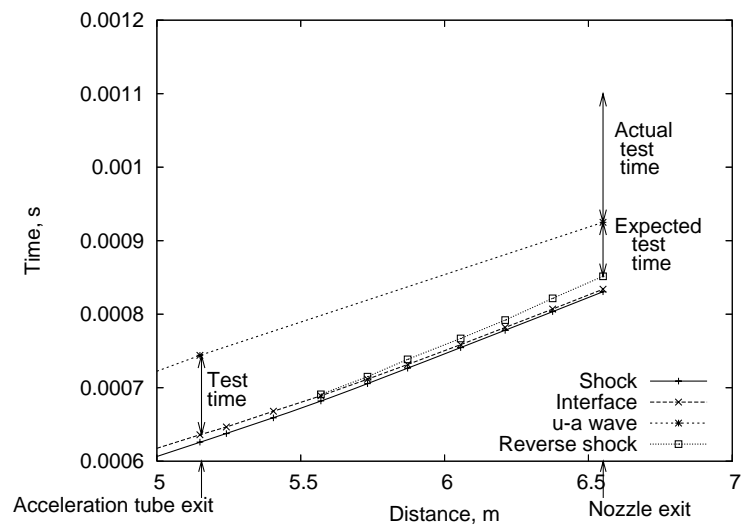


Figure 5.40: A x-t diagram in the nozzle constructed from the equilibrium, turbulent simulation of Air Condition 1

5.5. EXAMINATION OF THE HYPERSONIC NOZZLE

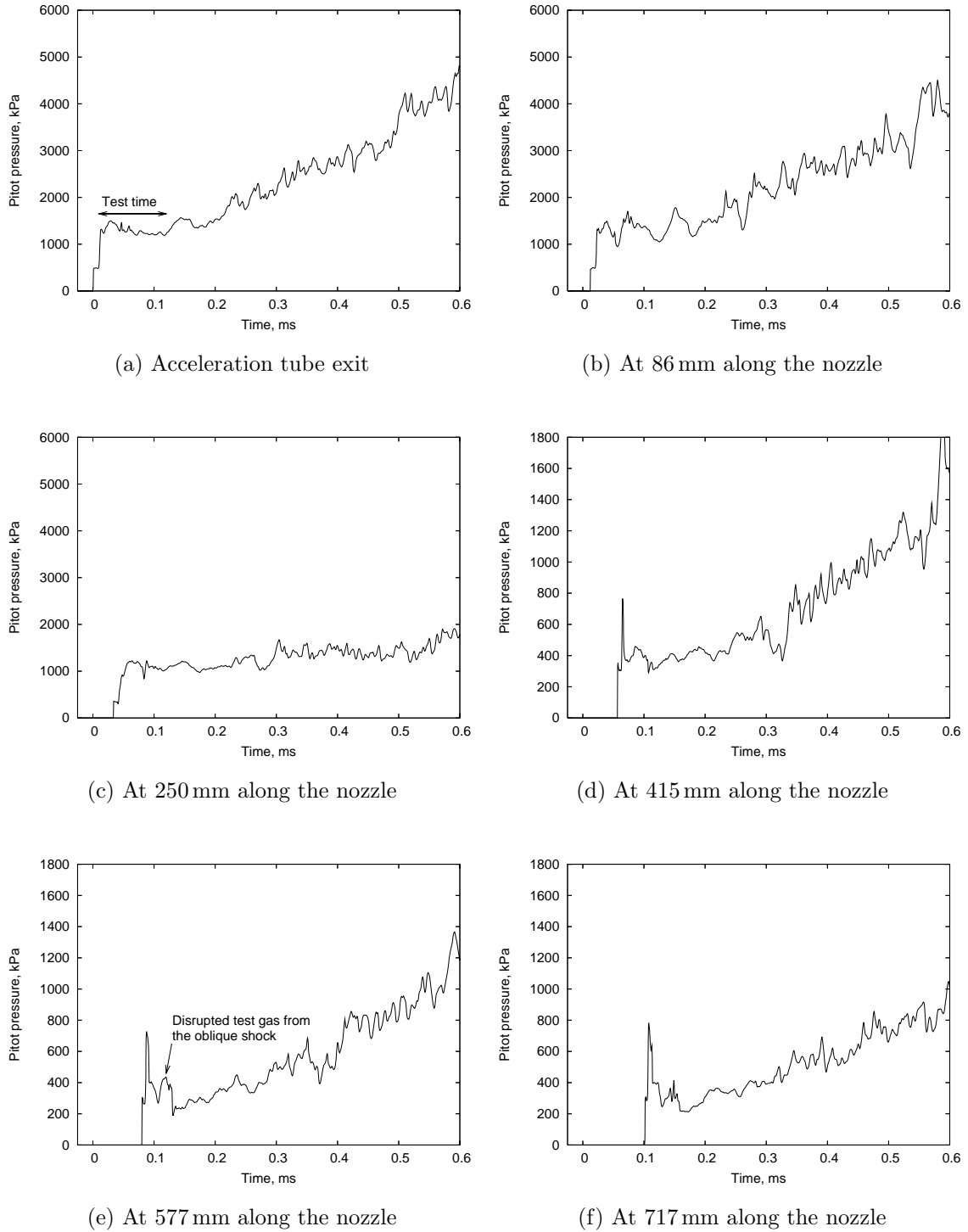


Figure 5.41: Pitot pressure time history along the nozzle for Air Condition 1: part 1

5.5. EXAMINATION OF THE HYPERSONONIC NOZZLE

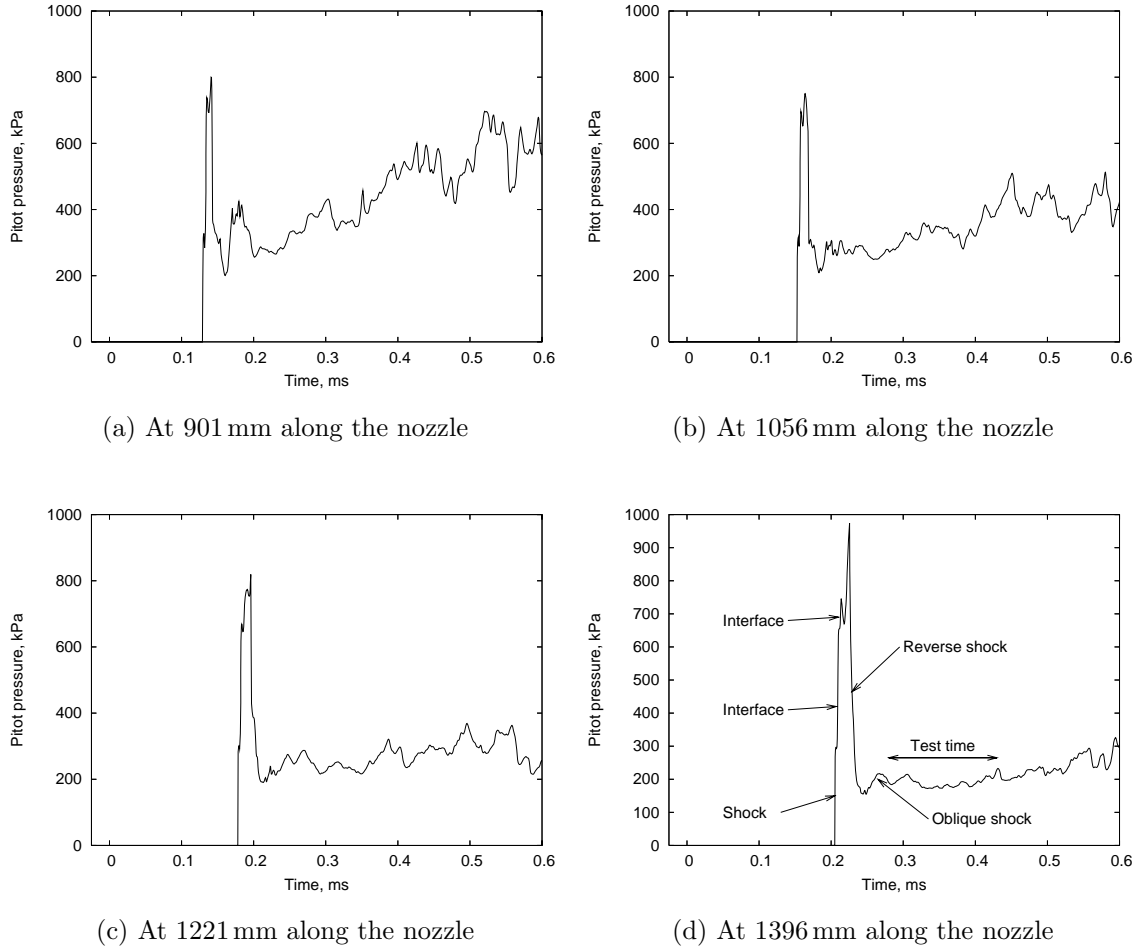


Figure 5.42: Pitot pressure time history along the nozzle for Air Condition 1: part 2

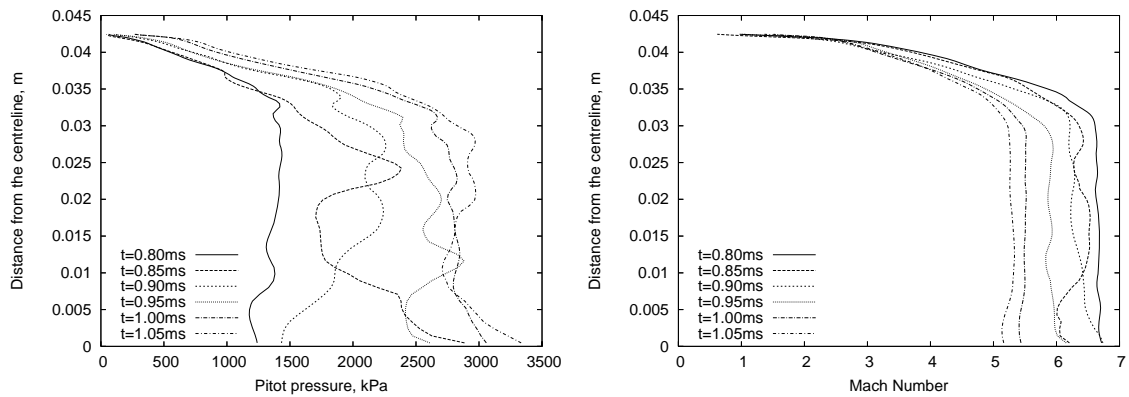


Figure 5.43: The boundary layer growth at the acceleration tube exit

5.6 Summary

A full capture, contoured, shock-free hypersonic nozzle was designed for the X2 expansion tube. Traditional axisymmetric nozzle design is done using the method of characteristics. This method produces an inviscid wall profile which is then corrected to compensate for the boundary layer. This approach incorrectly assumes that the core flow and boundary layer are not coupled, which can cause non-uniform flow at high Mach numbers. An alternative method utilizes the parabolized Navier-Stokes coupled to a Nelder-Mead simplex optimization algorithm. In this thesis, a code previously developed at the University of Queensland called SM_3D⁺ was used for the design. The length of the nozzle was 1.4 m, while the flow was expanded from a diameter of 85 mm to 201.8 mm. In SM_3D⁺ the Mach number increased from 7.3 to 10.2. The nozzle was designed assuming a laminar boundary layer. After manufacture and installation, the nozzle profile was redone assuming a turbulent boundary layer. A future project could be to remachine the nozzle with the improved design. This would hopefully give a slightly larger core diameter and straighter flow.

Experiments with the nozzle installed were conducted at three different conditions. These were the same air conditions and the Titan test gas condition which were examined before the nozzle was attached. Despite contoured nozzles being susceptible to shock formation at off design conditions, all three conditions produced suitable flow for the testing of models. The inflow Mach number into the nozzle for the three conditions was close to the design value of 7.3. It would be expected that at higher Mach number inflow the profiled contour of the nozzle could result in shocks which would destroy any test flow. The testing of this will be part of future work at the University of Queensland. The air conditions produced 110 μ s of test time with a core flow diameter of 100 mm. Both these values nearly doubled from the acceleration tube exit where they were 55 μ s and 60 mm respectively. The Titan condition produced a flow with a test time of 100 μ s and a core flow diameter of 90 mm. These also increased from 50 μ s and 65 mm when there was no nozzle. This experimental work confirmed the claim that a hypersonic expansion tube nozzle would not only increase the core flow diameter but also increase the steady time time.

The axisymmetric, MB_CNS air models of the acceleration tube provided little varia-

tion in the flow pressures and shock speeds between the equilibrium and finite-rate cases. This did occur when modelling the nozzle. The finite-rate chemistry showed that the oxygen in the test gas was frozen in both the acceleration tube and nozzle. The equilibrium simulations were unable to capture the chemistry properly and this resulted in incorrect temperatures and species fractions. This led to a large variation in the estimates for the thermodynamic flow properties in the nozzle flow. While a turbulent, viscous non-equilibrium simulation is preferred when modelling the X2 expansion tube, it becomes even more important when trying to accurately predict the flow properties at the nozzle exit.

Even though the axisymmetric simulations did not perfectly compare with the experimental results, similar effects were seen in the nozzle in both methods. The core flow diameter and steady time available for testing increased. This counter-intuitive result was seen in all the experiments and all the computational work for every condition. The starting process in the hypersonic nozzle should theoretically decrease the test time. The shock speed slows down as it enters the initial diverging section of the nozzle while the u-a wave speeds up due to the decrease in the speed of sound. The reason this has no effect is the actual test time at the nozzle exit occurs after the unsteady expansion arrives. All the flow prior to this is disrupted by the nozzle flow phenomena. The reason for the increase in test time at the nozzle exit is due to the growth of the boundary layer in the acceleration tube. As the unsteady expansion exits the acceleration tube the boundary layer grows in time. This results in the nozzle flow seeing a varying area ratio which counteracts the change in properties through the unsteady expansion. All of the relevant thermodynamic properties such as pressure, temperature, density and velocity remain steady at the nozzle exit and thus the flow is suitable for the testing of models.

CHAPTER 6

Conclusions and Recommendations

This thesis was concerned with developing the X2 expansion tube at the University of Queensland and implementing modelling techniques capable of predicting the flow produced in it. The broad aim of this work was to continue increasing the capabilities of ground based testing facilities in the high flow speed regime. This final chapter provides a summary of what was done to achieve this and presents the findings of the work. It also provides recommendations on further work that should be conducted.

6.1 The Modified X2 Expansion Tube

A new single-stage, free-piston driver was installed and commissioned on the X2 expansion tube. This increased the performance when compared to the old two-stage configuration. The design features which were advantageous included larger primary diaphragm burst pressures, a larger area ratio of 9 at the primary diaphragm, an increase in shock tube length of 1.3m and an increased driver gas volume. These features can be attributed to the stronger shock waves which were produced and thus subsequent high shock speeds and flow pressures. In addition to this, the new driver configuration was simpler to operate.

The components of the new driver arrangement were fabricated by late 2003 and their installation was finished in April 2004. Initial commissioning tests ensured that the free-piston driver reached adequate rupture pressure. The tests involved placing a thick steel blank, which was mounted with three pressure transducers, at the primary diaphragm location. The piston was released as in a normal experiment and the pressure in the slug

of driver gas was measured. The experiments showed that the driver was functioning correctly and the measured pressures compared well to one-dimensional simulations.

Four conditions in X2 were investigated in this thesis. The experiments aimed to determine what flow properties the new facility was capable of producing for the testing of models. The first condition was a 8 km/s air condition and was based on Robert Palmer's Condition 7 in the old configuration. The single-stage driver was able to give much larger freestream flow densities due to the increased performance. The other conditions examined were an air condition with a slightly faster secondary shock speed, a 5.5 km/s Titan condition and a 10.5 km/s Jupiter condition.

Each condition which was examined produced adequate flow for testing. The shock speeds were consistently repeatable, typically varying by no more than 1 % from shot-to-shot. The pressure reading variations were much larger than this. Impulse facilities have been well known for producing large levels of noise. The amount of unsteadiness which actually exists in the flow and the portion which is contributed by the measurement techniques used in the expansion tubes is uncertain in this work. For example, large fluctuations in the static pressure existed due to oscillations at the natural frequency of the PCB transducer. Temperature effects and the shielded arrangement of the Pitot probes caused noise and this has been verified by previous investigations. For these reasons it was thought that a considerable percentage of the measured unsteadiness was due to measurement techniques. If more accurate comparisons between experiment and numerical work are to be achieved in the future, these problems need to be addressed. Also, superior pressure gauges for measuring the low range fill values used in the shock and acceleration tubes would be advantageous.

Experiments with the same fill properties as Air Condition 1 but with a thicker diaphragm were conducted. The 2 mm steel diaphragm increased the rupture pressure from 24 MPa to 32 MPa. The results indicated an increase in secondary shock speed of 9 % and in pressure of over 20 %. The increased capability of X2 provides a wide range of testing conditions. The possibility of increasing the rupture pressure to the rated 40 MPa further demonstrates the benefits of the new single-stage driver. Experiments with a compression ratio of 55 instead of the original 40 showed little benefit and were not considered as basis for future work.

A full capture, contoured nozzle was designed, constructed and installed at the end of the X2 acceleration tube. Experiments with the nozzle attached were conducted for the two air conditions and the Titan condition. It was discovered that the experiments showed an increase in both the core flow diameter and steady test time. This supported the previous claim pertaining to the hypersonic expansion tube nozzle. The flow at the nozzle exit of all three conditions was suitable for testing, despite the general tendency for profiled nozzles to be susceptible to shock formation at off design conditions. More testing would be required to determine if the nozzle could be used at inflow Mach numbers above 8.

6.2 Expansion Tube Modelling

Aerodynamic data is essential for the design of flight vehicles. A combination of computational and experimental methods is required to accurately predict the flow conditions that an aeroshell model would encounter. Experiments cannot provide a full set of flow properties and thus, a numerical study can provide a superior depiction of the flow phenomena. However, CFD requires experimental validation because numerical errors can create inaccurate results. In addition to this, simplifying assumptions which are made to reduce the computational resources required, can render the results as physically invalid.

The numerical modelling began with one-dimensional simulations of the entire new X2 expansion tube arrangement. The first condition examined was the 8 km/s air condition. The simulations generated a temperature which was too high in the slug of driver gas before rupture of the primary diaphragm. This problem had been seen before in the one-dimensional code but had been attributed to the old two-stage driver configuration. The main reasons for the incorrect modelling were the calculation of the heat losses and the one-dimensional nature of the code. The heat transfer coefficients in L1d were calculated via the modified Reynolds analogy for a fully developed pipe flow. This assumes the Prandtl number is 1 and the flow is steady and incompressible. To rectify this, modified simulations were conducted where only the tube from the time of primary diaphragm rupture onwards was modelled. The conditions of the slug of gas of driver gas were set such that the shock tube pressure matched between the experiments and CFD. When this was done the primary shock speed compared extremely well with the experiments. If

this method continues to be used for modelling the X-series of expansion tubes, it may be beneficial to measure the temperature and length of the slug of driver gas in the tube to compare to the values used in the modified simulations.

L1d models for the three other conditions were conducted. Both the Titan and Jupiter models had a few problems. In each case the air in the acceleration tube was modelled as a calorically perfect gas. This resulted in unrealistically high values of temperature. At the time of the work, L1d could only have one gas in equilibrium which was the test gas. The code has since been updated to rectify this. The severity of the expansion in the Jupiter condition caused high energy fluxes between cells and L1d failed. An exact Riemann solver was being examined by Potter [98] to overcome this.

L1d and other one-dimensional codes have been extensively used in the past to obtain the flow properties at the exit of an expansion tube. It was seen in this thesis that, due to the one-dimensional nature of the code utilized here, the temperature and Pitot pressure could be wrong by over 30 %. It also failed to provide detailed description of the flow such as the core flow diameter. L1d can be used as a relatively quick means to obtain an initial approximation of the static pressure and shock speed of a condition. Issues in the code such as the heat loss models could be addressed but the one-dimensional nature of the code would still exist. At the current time the best option is to model downstream of the primary diaphragm with L1d and then use the time history from this as transient uniform inflow into an axisymmetric simulation of the acceleration tube.

Limited research has been done on axisymmetric simulations of expansion tubes due to the enormous amount of computing power and resources required. The finite-rate simulation of both the acceleration tube and nozzle for Air Condition 1 took over 81 hours to run on 42 processors. That equated to 142 days of CPU time and that was only for the coarsest grid without the addition of turbulence. On the finest grid the simulation would have taken well over a month to complete. The equilibrium, turbulent simulation took 41 hours on 42 processors for the finest grid which is still a lot of computing resources.

Good agreement was seen between the experimental and CFD flow properties for the air conditions at the acceleration tube exit. The addition of turbulence and finite-rate chemistry in the numerical simulations varied the pressure and shock speeds marginally. The difference in the pressure between the CFD and experiments was 10 %, while the

shock speeds were generally within 1%. To accurately capture the boundary layer, a turbulence model was required. The high unit Reynolds number of over 3×10^6 indicated that the boundary layers would be turbulent. The effects of finite-rate chemistry were also evident in the simulations. The equilibrium assumption incorrectly calculated the species fractions. The oxygen in the test gas did not have time to recombine through the unsteady expansion in the acceleration tube. This was not captured by the equilibrium simulation. The inability to predict the freezing of the oxygen lead to incorrect temperatures. The exothermic nature of the recombination reaction means that the overestimated recombination levels lead to excessive temperatures. The numerical models of the nozzle saw a lot of variation in the pressure as well as the other thermodynamic properties when turbulence and finite-rate chemistry were added. A finite-rate simulation was only run on the coarsest grid with a laminar boundary layer. Following previous trends, the properties for a fully grid independent, turbulent, finite-rate simulation were predicted. The results were within 15% of the experimental Pitot pressure and 5% of the static pressure. The equilibrium simulation predicted that the oxygen in the test gas would continue to recombine in the nozzle and be close to fully recombined by the nozzle exit. In reality, the oxygen remained frozen and this was seen in the finite-rate chemistry simulation.

The axisymmetric Titan simulation still requires further work. The air in the acceleration tube was modelled as a calorically perfect gas giving unrealistically high temperatures. The methane in the Titan gas would have also be dissociated which would necessitate the use of finite-rate chemistry. This investigation is part of another (continuing) study at the University of Queensland. Despite this, the simulation predicted the secondary shock speed to within 10% and the pressures to within 5% of the experiments.

The numerical work in this thesis has helped to develop the modelling techniques for expansion tubes. This is an ongoing process and the main requirement for further advancement is larger computer resources. The ideal situation would be to run an axisymmetric MB_CNS model from the primary diaphragm onwards. At the current time this is unrealistic. Hopefully in the near future this can be achieved. The only code development required would be some minor changes to the current diaphragm models in MB_CNS. At the present time, the hybrid simulations are sufficient in providing a detailed description of the flow while giving estimates of the flow properties. The comparison of the flow properties was made difficult by fluctuations in the numerical simulations and

excess noise in the experimental results. In the future, if more accurate comparisons are to be obtained, larger computers are required to run the simulations on finer grids and the noise caused by the measurement techniques in the experiments needs to be reduced.

6.3 Hypersonic Nozzles for Expansion Tubes

Expansion tubes are limited in the size of the models they can test by the diameter of the acceleration tube. The addition of a contoured, steady expansion nozzle at the exit of the acceleration tube could greatly increase the model size. A previous study by Stewart had claimed that a hypersonic nozzle would not only increase the core flow diameter but also the test time. A nozzle was designed for the X2 expansion tube and then tested in order to validate the claim.

The classical nozzle design of the method of characteristics can produce non-uniform flow at high Mach numbers due to the coupled nature of the core flow and boundary layer. An alternative approach is to solve the parabolized Navier-Stokes equations in the nozzle domain. By using a Nelder-Mead simplex optimization algorithm to repeatedly perturb the nozzle contour, a profile which gives the optimal specified design parameters can be found. The code used in this thesis was SM_3D⁺. Initially, the nozzle was designed assuming a laminar boundary layer. After manufacture and installation the contour was recalculated to incorporate turbulence. It would be recommended that at some stage the nozzle profile be re-machined to the turbulent boundary layer design. This would provide a slightly larger core flow diameter.

The nozzle was a full capture design, which meant the nozzle inlet diameter was the same size as the acceleration tube exit. The nozzle had a length of 1.4 m while the flow was expanded to a diameter 201.8 mm, with an area ratio of 5.6. The design parameters set in the optimization algorithm were a exit flow angle of 0° and a Mach number of 10.0. This was weighted more towards the flow angle. These were unrealistically high tolerances for the design parameters and merely aimed to improve convergence of the optimization algorithm. The final SM_3D⁺ design gave a flow angle of less than 0.02 across the exit plane while the Mach number increased from 7.3 to 10.2.

Though there were some discrepancies between the experiments and when the nozzle flow was solved with the axisymmetric code, similar nozzle effects were found in both

cases. The CFD indicated that the addition of the nozzle would approximately double the test time, while the core flow diameter would also increase. The same benefits occurred in all three conditions that were tested. The experiments verified these results. The thermodynamic properties of pressure, density, velocity and temperature were all steady in the test period, which shows that the flow was suitable for testing. Due to the high Mach numbers of the flow, the boundary layers were extremely large, thus reducing the core flow diameter to about half of size of the exit.

The reasoning behind the phenomena was thought to be due to boundary layer growth in the acceleration tube. Theoretically, the test time should decrease due to the starting process of the nozzle. The shock wave and interface slow down as they enter the initial diverging section of the nozzle. The u-a wave, which signals the end of the test time, speeds up due to the decrease in the speed of sound. This does occur in the nozzle. Furthermore, the majority of the theoretical test time is disrupted by an oblique wave that is formed in the acceleration tube and amplified in the nozzle. The actual test time at the nozzle exit occurs after the unsteady expansion arrives. The pressure should be increasing but as the unsteady expansion exits the acceleration tube the boundary layer thickness grows as time progresses. This results in the nozzle flow seeing a varying area ratio which counteracts the change in properties caused by the unsteady expansion. These two effects appear to compensate each other, which is fortuitous.

The previous study by Stewart focused on converting the manufactured components of the RHYFL shock tunnel into an expansion tube. It was proved here that if the RHYFL-X expansion tube was to come to fruition and a nozzle was attached it would increase both the test time and core flow diameter. This would make the facility a great proposition for ground based testing. The success of the current work has prompted a new single-stage driver and contoured nozzle to be installed on the larger X3 expansion tube. These changes should greatly increase the capabilities for ground based testing at the University of Queensland.

Bibliography

- [1] J.W. Hicks and G. Trippensee. NASA hypersonic X-plane flight development of technologies and capabilities for the 21st century access to space. In *AGARD Future Aerospace Technology in Service to the Alliance*, Paris, France, April 1997.
- [2] W.R.B. Morrison and R.J. Stalker. Exporting hypervelocity technology. In *Fifth National Space Engineering Symposium*, pages 14–19, Canberra, Australia, November–December 1989.
- [3] B.S. Stewart, R.G. Morgan, P.A. Jacobs, K.J. Austin, and D.M. Jenkins. Establishment of test conditions in the RHYFL-X facility. In *37th AIAA/ASME/SAE/ASEE Joint Propulsion Conference and Exhibition*, July 2001. AIAA Paper 2001-3678.
- [4] R. G. Morgan. A review of the use of expansion tubes for creating superorbital flows. In *35th Aerospace Sciences Meeting*, January 1997. AIAA Paper 97-0279.
- [5] C.G. Miller III and J.J. Jones. Development and performance of the NASA Langley Research Center expansion tube/tunnel, a hypersonic-hypervelocity real-gas facility. In *Shock Tubes and Waves: 14th International Symposium on Shock Tubes and Waves*, Sydney, Australia, August 1983.
- [6] T. Eichmann. An experimental investigation of shock shapes and shock stand-offs in super-orbital facilities. Master’s thesis, Department of Physics, University of Queensland, 2003.
- [7] A.J. Neely, R.J. Stalker, and A. Paull. High enthalpy, hypervelocity flows of air and argon in an expansion tubes. *The Aeronautical Journal*, 95(946):175–186, June/July 1991.

- [8] J. Benton, J. Perkins, and A. Edwards. Limitations of the method of characteristics when applied to axisymmetric hypersonic nozzle design. In *28th Aerospace Sciences Meeting*, Reno, Nevada, January 1990. AIAA Paper 90-0192.
- [9] J.D. Anderson. *Introduction to Flight*. McGraw-Hill, New York, third edition, 1989.
- [10] C.R. McClinton, V.L. Rausch, L.T. Nguyen, and J.R. Sitz. Preliminary X-43 flight test results. In *55th International Astronautical Congress*, Vancouver, Canada, October 2004.
- [11] N.E. Hass, M.K. Smart, and A. Paull. Flight data analysis of HyShot 2. In *13th AIAA/CIRA International Space Planes and Hypersonic Systems and Technologies Conference*, Capua, Italy, May 2005. AIAA Paper 2005-3354.
- [12] J. Allday. *Apollo in Perspective: Spaceflight Then and Now*. Institute of Physics Publishing, 2000.
- [13] P.D. Wooster, W.K. Hofstetter, and E.F. Crawley. Crew exploration vehicle destination for human lunar exploration: the lunar surface. In *AIAA Space 2005 Conference and Exposition*, August-September 2005. AIAA Paper 2005-6626.
- [14] P. Hurdle and A. Rolland. RHYFL - a tool for attaining hypersonic flight. *Threshold: An Engineering Journal of Power Technology*, (6):42–55, Spring 1990.
- [15] W. Chinitz, J.I. Erdos, O. Rizkalla, G.Y. Anderson, and D.M. Bushnell. Facility opportunities and associated stream chemistry considerations for hypersonic air-breathing propulsion. *AIAA Journal of Propulsion and Power*, 10(1):6–17, January-February 1994.
- [16] B.S. Stewart. *Predicted scramjet testing capabilities of the proposed RHYFL-X expansion tube*. PhD thesis, Department of Mechanical Engineering, University of Queensland, 2004.
- [17] J. Lukasiewicz. *Experimental Methods of Hypersonics*. Marcel Dekker, Inc., 1972.
- [18] F.K. Lu and D.E. Marren, editors. *Advanced hypersonic test facilities*. American Institute of Aeronautics and Astronautics, Inc., 2002.

- [19] M.P. Vieille. Sur les discontinuités produites par la détente brusque de gaz comprimés. *Comptes Rendus de L'Académie des Sciences*, 129:1228–1230, 1899. English translation located in Shock Tubes: Proceedings of the Seventh International Shock Tube Symposium.
- [20] A. Hertzberg. Shock tube research, past, present and future: a critical survey. In *Shock Tubes: Proceedings of the Seventh International Shock Tube Symposium*, pages 3–10, University of Toronto, Canada, June 1969.
- [21] A. Hertzberg. A shock tube method of generating hypersonic flows. *Journal of the Aeronautical Sciences*, 18:803–804, 1951.
- [22] A. Hertzberg, W.E. Smith, H.S. Glick, and W. Squire. Modifications of the shock tube for the generation of hypersonic flow. Technical Note 55-14, Arnold Engineering Development Center, March 1955.
- [23] R.J. Goozée. *Simulation of a complete shock tunnel using parallel computer codes*. PhD thesis, Department of Mechanical Engineering, University of Queensland, 2003.
- [24] P.B. Coates and A.G. Gaydon. A simple shock tube with detonating driver gas. *Proceedings of the Royal Society of London*, 283(1392):18–32, 1965.
- [25] M. Habermann, H. Olivier, and H. Grönig. Operation of a high performance detonation driver in upstream propagation mode for a hypersonic shock tunnel. In *22nd International Symposium on Shock Waves*, pages 447–452, 1999.
- [26] F.K. Lu, D.R. Wilson, R.J. Bakos, and J.I. Erdos. Recent advances in detonation techniques for high-enthalpy facilities. *AIAA Journal*, 38(9):1676–1684, September 2000.
- [27] F.K. Lu and D.R. Wilson. Detonation driver for enhancing shock tube performance. *Shock Waves*, 12(6):457–468, 2003.
- [28] R. J. Stalker. The free-piston shock tube. *The Aeronautical Quarterly*, 17:351–370, 1966.
- [29] R.J. Stalker. Development of a hypervelocity wind tunnel. *The Aeronautical Journal*, 76:374–384, 1972.

- [30] R.J. Stalker and H.G. Hornung. Two developments with free piston drivers. In *Proceedings of the Seventh International Shock Tube Symposium*, pages 242–258, Toronto, Canada, June 1969.
- [31] R.G. Morgan. Development of X3, a superorbital expansion tube. In *38th Aerospace Sciences Meeting and Exhibit*, Reno, Nevada, January 2000. AIAA Paper 2000-0558.
- [32] C.J. Doolan and R.G. Morgan. A two-stage free-piston driver for expansion tubes. In *34th Aerospace Sciences Meeting and Exhibit*, Reno, Nevada, January 1996. AIAA Paper 96-0854.
- [33] B.D. Henshall. The use of multiple diaphragms in shock tubes. Technical Report Current Paper Number 291, A.R.C., 1956.
- [34] R. G. Morgan and R. J. Stalker. Double diaphragm driven free piston expansion tube. In *18th International Symposium on Shock Waves*, pages 1031–1038, Sendai, Japan, July 1991.
- [35] A.J. Neely and R.G. Morgan. Flow measurements and calibration of a superorbital expansion tube. In *11th Australasian Fluid Mechanics Conference*, University of Tasmania, Hobart, Australia, December 1992.
- [36] A.J. Neely and R.G. Morgan. The superorbital expansion tube concept, experiment and analysis. *The Aeronautical Journal*, 98(973):97–105, March 1994.
- [37] M. Kendall, R. Morgan, and P. Petrie-Repar. A study of free-piston double-diaphragm drivers for expansion tubes. In *35th Aerospace Sciences Meeting and Exhibit*, Reno, Nevada, January 1997. AIAA Paper 97-0985.
- [38] R.L. Trimpi. A preliminary theoretical study of the expansion tube, a new device for producing high-enthalpy short-duration hypersonic gas flows. Technical Report R-133, NASA, 1962.
- [39] E.L. Resler and D.E. Bloxsom. Very high number flows by unsteady flow principles. Limited distribution monograph, Cornell University Graduate School of Aeronautical Engineering, January 1952.

- [40] H. Bernstein. A double-diaphragm shock tube to produce transient high Mach number flows. *Journal of the Aeronautical Sciences*, 20:790–791, November 1953.
- [41] J.J. Jones. Some performance characteristics of the LRC $3\frac{3}{4}$ -inch pilot expansion tube using an unheated hydrogen driver. In *Fourth Hypervelocity Techniques Symposium*, pages 7–26, Arnold Air Force Station, Tennessee, November 1965.
- [42] J.J. Givens, W.A. Page, and R.M. Reynolds. Evaluation of flow properties in a combustion-driven expansion tube operating at 7.5 km/sec. In *Fourth Hypervelocity Techniques Symposium*, pages 27–48, Arnold Air Force Station, Tennessee, November 1965.
- [43] J.H. Spurk. Design, operation, and preliminary results of the BRL expansion tube. In *Fourth Hypervelocity Techniques Symposium*, pages 111–143, Arnold Air Force Station, Tennessee, November 1965.
- [44] J.J. Jones and J.A. Moore. Exploratory study of performance of the Langley pilot model expansion tube with a hydrogen driver. Technical Note D-3421, NASA Langley Research Center, May 1966.
- [45] J.A. Moore. Description and initial operating performance of the Langley 6-inch expansion tube using heated helium driver gas. Technical Memorandum X-3240, NASA Langley Research Center, September 1975.
- [46] C.G. Miller. Flow properties in expansion tube with helium, argon, air, and CO₂. *AIAA Journal*, 12(4):564–566, April 1974.
- [47] C.G. Miller III. Shock shapes on blunt bodies in hypersonic-hypervelocity helium, air, and CO₂ flows, and calibration results in Langley 6-inch expansion tube. Technical Note D-7800, NASA Langley Research Center, February 1975.
- [48] C.G. Miller and J.A. Moore. Shock shapes of blunt bodies in hypersonic helium, air, and CO₂ flows. *AIAA Journal*, 12(3):411–413, March 1974.
- [49] C.G. Miller and J.A. Moore. Flow-establishment times for blunt bodies in an expansion tube. *AIAA Journal*, 13(12):1676–1678, December 1975.

- [50] C.G. Miller III. Operational experience in the Langley expansion tube with various test gases. Technical Memorandum 78367, NASA Langley Research Center, December 1977.
- [51] C.G. Miller III. Operational experience in the Langley expansion tube with various test gases. *AIAA Journal*, 16(3):195–196, March 1978.
- [52] J.L. Shinn and C.G. Miller III. Experimental perfect-gas study of expansion-tube flow characteristics. Technical Paper 1317, NASA, December 1978.
- [53] I.A. Stringer. "TQ" free piston expansion tube - design and operation. Technical Report Report 4/89, Department of Mechanical Engineering, University of Queensland, 1989.
- [54] A. Paull, R. J. Stalker, and I. Stringer. Experiments on an expansion tube with a free-piston driver. In *AIAA 15th Aerodynamic Testing Conference*, pages 173–178, San Diego, CA, May 1988. AIAA Paper 88-2018.
- [55] C.M. Gourlay. Expansion tube test time predictions. Technical Report Report 8/88, Department of Mechanical Engineering, University of Queensland, 1988.
- [56] A. Paull and R.J. Stalker. Test flow disturbances in an expansion tube. *Journal of Fluid Mechanics*, 245:493–521, 1992.
- [57] P.A. Jacobs. Single-block navier-stokes integrator. Interim Report 18, Institute for Computer Applications in Science and Engineering, NASA Langley Research Centre, July 1991.
- [58] J. Tamagno, R. Bakos, M. Pulsonetti, and J. Erdos. Hypervelocity real gas capabilities of GASL's expansion tube (HYPULSE) facility. In *AIAA 16th Aerodynamic Ground Testing Conference*, Seattle, Washington, June 1990. AIAA 90-1390.
- [59] J.I. Erdos. Capabilities of a free piston driven expansion tube/tunnel. Paper Number 237, GASL, April 1991.
- [60] J. Erdos, J. Calleja, and J. Tamagno. Increase in the hypervelocity test envelope of the HYPULSE shock-expansion tube. In *AIAA 18th Ground Testing Conference*, June 1994. AIAA paper 94-2524.

- [61] R.J. Bakos, J.F. Calleja, J.I. Erdos, , M.A. Sussman, and G.J. Wilson. An experimental and computational study leading to new test capabilities for the HYPULSE facility with a detonation driver. In *19th AIAA Advanced Measurement and Ground Testing Conference*, New Orleans, LA, June 1996. AIAA Paper 96-2193.
- [62] A.J. Neely and R.J. Stalker. Hypervelocity flows of argon produced in a free piston driven expansion tube. In *18th International Symposium on Shock Waves*, pages 997–1004, Sendai, Japan, 1991.
- [63] A.J. Neely. *Experimental and analytical study of a pilot superorbital expansion tube for aerothermodynamic testing to 13 kms⁻¹ in air*. PhD thesis, Department of Mechanical Engineering, University of Queensland, August 1995.
- [64] C.J. Doolan. *A two-stage free-piston driver for hypervelocity expansion tubes*. PhD thesis, Department of Mechanical Engineering, University of Queensland, 1997.
- [65] C.J. Doolan and R.G. Morgan. A two-stage free-piston driver. *Shock Waves*, 9(4):239–248, August 1999.
- [66] R.A. Palmer. *Measurement of heat transfer in superorbital flows*. PhD thesis, Department of Mechanical Engineering, University of Queensland, 1999.
- [67] C. J. Doolan and R.G. Morgan. Hypervelocity simulation in a new large scale expansion facility. In *18th AIAA Aerospace Ground Testing Conference*, Colorado Springs, Colorado, June 1994. AIAA Paper 94-2492.
- [68] R.G. Morgan. Superorbital expansion tubes. In *21st International Symposium on Shock Waves*, Great Keppel Island, Australia, July 1997.
- [69] M.M. Abdel-Jawad, D.J. Mee, R.G. Morgan, P.A. Jacobs, and J.A. Philpot. Transient force measurements at superorbital speeds. In *23rd International Symposium on Shock Waves*, Fort Worth, Texas, July 2001.
- [70] A. Sasoh, Y. Ohnishi, K. Koremoto, and K. Takayama. Operation and performance of a free-piston-driven expansion tube. In *37th AIAA Aerospace Sciences Meeting and Exhibit*, Reno, Nevada, January 1999. AIAA Paper 99-0825.

- [71] J. Kawaguchi, K. Hitoshi, A. Fujiwara, and T. Uesugi. MUSES-C, its launch and early orbit operations. In *Proceedings of the 5th IAA International Conference on Low-Cost Planetary Missions*, Noordwijk, Netherlands, September 2003.
- [72] R.L. Trimpi and L.B. Callis Jr. A perfect-gas analysis of the expansion tunnel, a modification to the expansion tube. Technical Report R-233, NASA Langley Research Center, 1965.
- [73] L.B. Callis Jr. A theoretical study of the effect on expansion-tube performance of area changes at primary and secondary diaphragm stations. Technical Note D-3303, NASA, March 1966.
- [74] L.B. Callis Jr. An analysis of supersonic flow phenomena in conical nozzles by a method of characteristics. Technical Note D-3550, NASA, August 1966.
- [75] R.L. Trimpi. A theoretical investigation of simulation in expansion tubes and tunnels. Technical Report R-243, NASA Langley Research Center, 1966.
- [76] G.D. Norfleet, J.J. Lacey Jr., and J.D. Whitfield. Results of an experimental investigation of the performance of an expansion tube. In *Fourth Hypervelocity Techniques Symposium*, pages 49–110, Arnold Air Force Station, Tennessee, November 1965.
- [77] G.D. Norfleet and F.C. Loper. A theoretical real-gas analysis of the expansion tunnel. Technical Report 66-71, Arnold Engineering Development Center, June 1966.
- [78] C.G. Miller III. Operational experience in the Langley expansion tube with various gases and preliminary results in the expansion tunnel. In *AIAA 9th Aerodynamic Testing Conference*, Arlington, Texas, June 1976.
- [79] I.A. Leyva. Study of the addition of a divergent nozzle to an expansion tube for increasing test time. In *18th AIAA Aerospace Ground Testing Conference*, June 1994. AIAA Paper 94-2533.
- [80] R.J. Bakos, J.F. Calleja, J.I. Erdos, A.H. Auslender, M.A. Sussman, and G.J. Wilson. Design, calibration and analysis of a tunnel mode of operation for the HY-

- PULSE facility. In *19th AIAA Advanced Measurement and Ground Testing Conference*, June 1996. AIAA Paper 96-2194.
- [81] O. Sudnitsin. Design and testing of expansion tube with area change. Master's thesis, Department of Mechanical Engineering, University of Queensland, 2000.
- [82] R.S.M. Chue, R.J. Bakos, C.-Y. Tsai, and A. Betti. The design of an expansion tunnel nozzle in HYPULSE. In *23rd International Symposium on Shock Waves*, pages 356–366, Fort Worth, Texas, July 2001.
- [83] M.S. Holden, T.P. Wadhams, and G.V. Candler. Experimental studies in the LENS shock tunnel and expansion tunnel to examine real-gas effects in hypervelocity flows. In *42nd AIAA Aerospace Sciences Meeting and Exhibit*, Reno, Nevada, January 2004. AIAA Paper 2004-916.
- [84] I. Nompelis, G.V. Candler, T.P. Wadhams, and M.S. Holden. Numerical simulation of high-enthalpy experiments in the LENS-X expansion tube facility. In *42nd AIAA Aerospace Sciences Meeting and Exhibit*, Reno, Nevada, January 2004. AIAA Paper 2004-1000.
- [85] P.A. Jacobs, T.B. Silvester, R.G. Morgan, M.P. Scott, R.G. Gollan, and T.J. McIntyre. Superorbital expansion tube operation: estimates of flow condition via numerical simulation. In *43rd AIAA Aerospace Sciences Meeting*, Reno, Nevada, January 2005. AIAA Paper 2005-694.
- [86] I. McIntyre, T.J. and Lourel, T.N. Eichmann, R.G. Morgan, P.A. Jacobs, and A.I. Bishop. Experimental expansion tube study of the flow over a toroidal ballute. *AIAA Journal of Spacecraft and Rockets*, 41(5):716–725, September-October 2004.
- [87] P.A. Jacobs. L1d: A computer program for the simulation of transient-flow facilities. Technical Report Report 1/99, Department of Mechanical Engineering, University of Queensland, 1999.
- [88] P.A. Jacobs. Shock tube modelling with L1d. Technical Report Report 13/98, Department of Mechanical Engineering, University of Queensland, 1998.

- [89] S. Gordon and B.J. McBride. Computer program for calculation of complex chemical equilibrium compositions and applications: I analysis. Reference Publication 1311, NASA, 1994.
- [90] R.W. Fox and A.T. McDonald. *Introduction to Fluid Mechanics*. John Wiley and Sons, Inc., fifth edition, 1998.
- [91] J.P. Holman. *Heat Transfer*. McGraw-Hill, New York, fifth edition, 1981.
- [92] NASA. NASA - Cassini-Huygens: Close Encounter with Saturn, http://www.nasa.gov/mission_pages/cassini/main/index.html. [Accessed 1st June 2005].
- [93] ESA. ESA - Cassini-Huygens, <http://www.esa.int/SPECIALS/Cassini-Huygens/>. [Accessed 1st June 2005].
- [94] C.E. Higgins. *Aerothermodynamics of the gas giants*. PhD thesis, Department of Mechanical Engineering, University of Queensland, 2004.
- [95] NASA. NASA's Solar System Exploration: Galileo Legacy Site, <http://galileo.jpl.nasa.gov/>. [Accessed 30th September 2005].
- [96] NASA. Galileo Project: Jupiter, <http://www2.jpl.nasa.gov/galileo/jupiter/jupiter.html>. [Accessed 30th September 2005].
- [97] F.S Milos. Galileo probe heat shield ablation experiment. *AIAA Journal of Spacecraft and Rockets*, 34(6):705–713, 1997.
- [98] D. Potter. Superorbital flows of a jovian test gas in an expansion tube. Undergraduate thesis, Division of Mechanical Engineering, University of Queensland, October 2005.
- [99] P.A. Jacobs. MB_CNS: A computer program for the simulation of transient compressible flows. Technical Report Report 10/96, Department of Mechanical Engineering, University of Queensland, 1996.
- [100] P.A. Jacobs. MB_CNS: A computer program for the simulation of transient, compressible flows; 1998 update. Technical Report Report 7/98, Department of Mechanical Engineering, University of Queensland, 1998.

- [101] B. Baldwin and H. Lomax. Thin-layer approximation and algebraic model for separated turbulent flows. In *16th AIAA Aerospace Sciences Meeting*, January 1978. AIAA Paper 78-257.
- [102] G.J. Wilson, M.A. Sussman, and R.J. Bakos. Numerical simulation of the flow in the HYPULSE expansion tube. Technical Memorandum 110357, NASA Ames Research Center, June 1995.
- [103] S.P. Schneider. Effects of high-speed tunnel noise on laminar-turbulent transition. *AIAA Journal of Spacecraft and Rockets*, 38(3):323–333, May-June 2001.
- [104] L.N. Connor Jr. Calculation of the centred one-dimensional unsteady expansion of a reacting gas mixture subject to vibrational and chemical nonequilibrium. Technical Note D-3851, NASA, February 1967.
- [105] G. Wilson. Time-dependent quasi-one-dimensional simulations of high enthalpy pulse facilities. In *AIAA Fourth International Aerospace Planes Conference*, Orlando, Florida, December 1992. AIAA Paper 92-5096.
- [106] G. Wilson. Numerical simulation of high enthalpy pulse facilities. In *Proceedings of the 20th International Symposium on Shock Waves*, July 1995.
- [107] R.J. Bakos and R.G. Morgan. Chemical recombination in an expansion tube. *AIAA Journal*, 32(6), 1994.
- [108] M.A. Sutcliffe. *The use of an expansion tube to generate carbon dioxide flows applicable to Martian atmosphere entry simulation*. PhD thesis, Department of Mechanical Engineering, University of Queensland, 2000.
- [109] R.J. Gollan. Yet another finite-rate chemistry module for compressible flow codes. Technical Report Report 9/2003, Department of Mechanical Engineering, University of Queensland, July 2003.
- [110] R.N. Gupta, J.M. Yos, R.A. Thompson, and Lee K.-P. A review of reaction rates and thermodynamic and transport properties for an 11-species air model for chemical and thermal nonequilibrium calculations to 30 000K. Reference Publication 1232, NASA, 1990.

- [111] M. Hayne. *Hypervelocity Flow Over Rearward-Facing Steps*. PhD thesis, Department of Mechanical Engineering, University of Queensland, 2004.
- [112] S. H.-H. Chiu. *Using an expansion tube to generate rarefied hypervelocity gas flows*. PhD thesis, Department of Mechanical Engineering, University of Queensland, 2005.
- [113] J.I. Erdos and R. Bakos. Prospects for a quiet hypervelocity shock-expansion tunnel. In *18th AIAA Aerospace Ground Testing Conference*, Colorado Springs, Colorado, June 1994. AIAA Paper 94-2500.
- [114] D.R. Buttsworth and P.A. Jacobs. Measurement of fluctuations in a Mach 4 shock tunnel nozzle flow. In *7th Australasian Heat and Mass Transfer Conference*, James Cook University, Townsville, July 2000.
- [115] J. Richards. Analysis of experimental data of the X3 expansion tube. Undergraduate thesis, Division of Mechanical Engineering, University of Queensland, October 2004.
- [116] N.R. Mudford, R.J. Stalker, and I. Shields. Hypersonic nozzles for high enthalpy nonequilibrium flow. *Aeronautical Quarterly*, 31:113–131, 1980.
- [117] M.A. Sutcliffe and R.G. Morgan. The measurement of Pitot pressure in high enthalpy expansion tubes. *Measurement Science and Technology*, 12:327–334, 2001.
- [118] J. D. Anderson. *Modern Compressible Flow: with Historical Perspective*. McGraw-Hill, New York, second edition, 1990.
- [119] G. Candler and J Perkins. Effects of vibrational nonequilibrium on axisymmetric hypersonic nozzle design. In *29th Aerospace Sciences Meeting*, Reno, Nevada, 1991. AIAA Paper 91-0297.
- [120] J.J. Korte, A. Kumar, D.J. Singh, and B. Grossman. Least squares/ parabolized Navier-Stokes procedure for optimizing hypersonic wind tunnel nozzles. In *AIAA/SAE/ASME 27th Joint Propulsion Conference*, Sacramento, California, June 1991. AIAA Paper 91-2273.
- [121] J.J. Korte, A. Kumar, D.J. Singh, and J.A. White. CAN-DO CFD-based Aerodynamic Nozzle Design and Optimization program for supersonic/hypersonic wind

- tunnels. In *AIAA 17th Aerospace Ground Testing Conference*, Nashville, Tennessee, July 1992. AIAA Paper 92-4009.
- [122] S.L. Keeling. A strategy for the optimal design of nozzle contours. In *AIAA 28th Thermophysics Conference*, Orlando, Florida, July 1993. AIAA Paper 93-2720.
- [123] R. Tolle. A new optimum design code for hypersonic nozzles, utilizing response surface methodology. In *35th Aerospace Sciences Meeting and Exhibit*, Reno, Nevada, January 1997. AIAA Paper 97-0519.
- [124] C.S. Craddock. *Computational optimization of scramjets and shock tunnel nozzles*. PhD thesis, Department of Mechanical Engineering, University of Queensland, 1999.
- [125] C.S. Craddock and P.A. Jacobs. A space-marching compressible flow solver with chemistry and optimization SM_3D^{PLUS}. Technical Report Report 6/98, Department of Mechanical Engineering, University of Queensland, 1998.
- [126] J.A. Nelder and R. Mead. A simplex method for function minimization. *Computer Journal*, 7:308–312, 1965.
- [127] R.S.M. Chue, R.J. Bakos, C.-Y. Tsai, and A. Betti. Design of a shock-free expansion tunnel nozzle in HYPULSE. *Shock Waves*, 13(4):261–270, 2003.
- [128] H.W. Liepmann and A. Roshko, editors. *Elements of gas dynamics*. John Wiley and Sons, Inc., 1957.
- [129] P.A. Jacobs and C.M. Gourlay. An interactive method-of-characteristics program for gas-dynamic calculations. *International Journal of Applied Engineering Education*, 7(3):242–250, 1991.
- [130] P.A. Jacobs. IMOC: Interactive method-of-characteristics for two-dimensional supersonic flow. Technical Report Report 3/00, Department of Mechanical Engineering, University of Queensland, 2000.
- [131] C.E. Smith. The starting process in a hypersonic nozzle. *Journal of Fluid Mechanics*, 24(4):625–642, 1966.

- [132] H.O. Amann. Experimental study of the starting process in a reflection nozzle. *The Physics of Fluids*, 12(5):150–153, 1969.

APPENDIX A

L1d Input Files

Listed in this appendix are two L1d input files for Air Condition 1. The files for the other simulations which were run were similar with only the initial thermodynamic conditions and gases different. The input files listed are:

- **A.1 - air_condition_1.Lp:** for the full simulation including the compression process as discussed in Chapter 3, Section 3.3.
- **A.2 - modified_air_condition_1.Lp:** for the simulation with the modified temperature and length of driver gas.

A.1 air_condition_1.Lp

```

#lid-3.0 air condition including the compression process
0 96 0      test_case, gas_index, fr_chem
4 1 2      nslug, npiston, ndiaphragm
8.5e-2 25000000  max_time, max_step
1.0e-9 0.25      dt_init, CFL
2 2 0 0      Xorder, Torder, k
2          n_dt_plot
0.0 0.5e-3 4.0e-4  t_change, dt_plot, dt_his
7.2e-2 0.02e-3 1.0e-6  t_change, dt_plot, dt_his
10         hn_loc
7.381      n, nseg
7.614      xb[0], Diamb[0], linear[0]
7.845      xb[1], Diamb[1], linear[1]
8.24       xb[2], Diamb[2], linear[2]
8.765      xb[3], Diamb[3], linear[3]
9.015      xb[4], Diamb[4], linear[4]
10.829     xb[5], Diamb[5], linear[5]
12.675     xb[6], Diamb[6], linear[6]
12.855     xb[7], Diamb[7], linear[7]
13.385     xb[8], Diamb[8], linear[8]
           xb[9], Diamb[9], linear[9]
           nkl
           -0.36 0.15 0.5  xbeginK[0], xendK[0], Kvalue[0]

4.6 4.8 0.35      xbeginK[1], xendK[1], Kvalue[1]
296.0 0          T_nominal, nT

piston [0] is the x2 piston
12
35.0 0.2568 0.341  mass, diam, length
P_restrain, is_restrain
x_buffer, hit_buffer
with_brakes, brakes_on
left_slug_id, left_slug_end_id
right_slug_id, right_slug_end_id
x0, v0

is_burst, P_burst, hold_period, blend_delay, blend_dx
left_slug_id, left_slug_end_id, dx
right_slug_id, right_slug_end_id, dx

is_burst, P_burst, hold_period, blend_delay, blend_dx
left_slug_id, left_slug_end_id, dx
right_slug_id, right_slug_end_id, dx

slug [0]: compressed air to push the piston
300 0 0 0.0      nmx, to_end_1, to_end_2, strength
600 0 0 0.0      nxmax, adaptive, dxmin, dxmax
1 0              viscous_effects, adiabatic
V 0.0           left boundary: wall with zero velocity
P 0             right boundary: piston
1             hn_cell
1             hx_cell
-3.89 0.0 1.56e6 0 296.0  initial: x1, x2, p, u, T
1.0 0.0 0.0 0.0 0.0  species mass fraction
slug [1]: compressed helium driver gas
550 0 1 1.05     nmx, to_end_1, to_end_2, strength
1200 0 0 0.0    nxmax, adaptive, dxmin, dxmax
1 0             viscous_effects, adiabatic
P 0            left boundary: piston
SD 2 L 0       right boundary: slug 2 diaphragm 0
1             hn_cell

```

```

1          hx_cell          7.614
0.341 4.81 48.0e3 0.0 296.0  initial: x1, x2, p, u, T
0.0 0.0 1.0 0.0 0.0  species mass fraction
slug [2]: air test gas in the shock tube
1500 1 1 1.02
3000 0 0.0 0.0
1 0
SD 1 R 0
SD 3 L 1
1          hn_cell
1          hx_cell          7.845
4.81 8.234 9.6e3 0.0 296.0  initial: x1, x2, p, u, T
1.0 0.0 0.0 0.0 0.0  species mass fraction
slug [3]: air in the acceleration tube
600 1 0 1.02
1200 1 0.015 0.045
1 0
SD 2 R 1
F          secondary diaphragm [0]
1          hn_cell          8.24
8.234 13.389 43.0 0.0 296.0  initial: x1, x2, p, u, T
1.0 0.0 0.0 0.0 0.0  species mass fraction
1.0 0.0 0.0 0.0 0.0
1          hx_cell          8.765
9.015
10.829
12.675
12.855
13.385
tube definition follows:
1000 3
4.583 0.2568 0
4.6 0.2568 0
4.7 0.085 0
13.389 0.085 0
1
4.6 4.8 0.5
296.0 0
secondary diaphragm [0]
0 12.0e3 5.0e-6 0.0 0.0
1 R 0.0
2 L 0.0
slug [0]: compressed helium driver gas
75 0 1 1.05
1200 0 0 0.0
1 0
V 0.0
left boundary: wall with zero velocity
right boundary: slug 1
1          hn_cell          1500 1 1 1.02
1          hx_cell          3000 0 0.0 0.0
4.583 4.81 24.0e6 0.0 2900.0  initial: x1, x2, p, u, T
0.0 0.0 1.0 0.0 0.0  species mass fraction
slug [1]: air test gas in the shock tube
1500 1 1 1.02
3000 0 0.0 0.0
1 0
viscous_effects, adiabatic
left boundary: slug 1 diaphragm 0
right boundary: slug 3 diaphragm 1
#Lid-3.0 air condition 1 with corrected slug length and temperature
0 96 0
test_case, gas_index, fr_chem
3 0 1
nslug, npiston, ndiaphragm
2.0e-3 25000000
max_time, max_step
1.0e-9 0.25
dt_init, CFL
2 2 0
Xorder, Torder, k
1          n_dt_plot
0.0 0.02e-3 1.0e-6
t_change, dt_plot, dt_his
10
hn_loc
7.381
n, nseg
xb[0], Diamb[0], linear[0]
xb[1], Diamb[1], linear[1]
xb[2], Diamb[2], linear[2]
xb[3], Diamb[3], linear[3]
nkl
xbegink[1], xendk[1], Kvalue[1]
T_nominal, nT
is_burst, P_burst, hold_period, blend_delay, blend_dx
left_slug_id, left_slug_end_id, dx
right_slug_id, right_slug_end_id, dx
slug [0]: compressed helium driver gas
nnx, to_end_1, to_end_2, strength
nxmax, adaptive, dxmin, dxmax
viscous_effects, adiabatic
left boundary: wall with zero velocity
right boundary: slug 1
hn_cell
hx_cell
initial: x1, x2, p, u, T
species mass fraction
slug [1]: air test gas in the shock tube
nnx, to_end_1, to_end_2, strength
nxmax, adaptive, dxmin, dxmax
viscous_effects, adiabatic

```

A.2 modified_air_condition_1.Lp

```

S 0          left boundary: slug 0
SD 2 L 0    right boundary: slug 2 diaphragm 0
1           hm_cell
1           hx_cell
4.81 8.234 9.60e3 0.0 296.0  initial: x1, x2, p, u, T
1.0 0.0 0.0 0.0 0.0          species mass fraction
slug [2]: air in the acceleration tube
600 1 0 1.02                mnx, to_end_1, to_end_2, strength
1200 1 0.015 0.045          nxmax, adaptive, dxmin, dxmax
1 0                          viscous_effects, adiabatic
SD 1 R 0    left boundary: slug 1 diaphragm 0
F           right boundary: free boundary at the end of the tube
1           hm_cell
1           hx_cell
8.234 13.389 43.0 0.0 296.0  initial: x1, x2, p, u, T
1.0 0.0 0.0 0.0 0.0          species mass fraction

```

APPENDIX B

Finite-Rate Chemistry Input File

The input file for the finite-rate chemistry package is given below. The reactions and their respective reaction rates for the 6 species, 17 reaction air model is shown within.

B.1 air_he.chm

```

# air_he.chm

# Reference:
# Gupta, R.N., Yos, J.M., Thompson, R.A. and Lee, K-P. (1990).
# A Review of Reaction Rates and Thermodynamic and Transport
# Properties for an 11-species Air Model for Chemical and
# Thermal Nonequilibrium Calculations to 30 000K.
# NASA RP-1232
#
# 06-Sept-2003
# Updated:
# 31-May-2004
# 02-Jun-04 He last to match Lid LUT bits (PJ)
# Version 3.0
# 15-Oct-04

SPECIES
N2 N O2 O NO He

END

REACTIONS qss cms 0.5
N2 + N2 <=> 2 N + N2 1.92e17 -0.5 1.131e5
REV/ 1.09e16 -0.5 0.0 /
N2 + N <=> 2 N + N 4.15e22 -1.5 1.131e5
REV/ 2.32e21 -1.5 0.0 /
N2 + O2 <=> 2 N + O2 1.92e17 -0.5 1.131e5
REV/ 1.09e16 -0.5 0.0 /
N2 + O <=> 2 N + O 1.92e17 -0.5 1.131e5
REV/ 1.09e16 -0.5 0.0 /
N2 + NO <=> 2 N + NO 1.92e17 -0.5 1.131e5
REV/ 1.09e16 -0.5 0.0 /
O2 + O <=> 2 O + O 3.61e18 -1.0 5.94e4
REV/ 3.01e15 -0.5 0.0 /
O2 + N <=> 2 O + N 3.61e18 -1.0 5.94e4
REV/ 3.01e15 -0.5 0.0 /
O2 + O2 <=> 2 O + O2 3.61e18 -1.0 5.94e4
REV/ 3.01e15 -0.5 0.0 /
O2 + N2 <=> 2 O + N2 3.61e18 -1.0 5.94e4
REV/ 3.01e15 -0.5 0.0 /
NO + N <=> N + O + N 3.97e20 -1.5 7.56e4
REV/ 1.01e20 -1.5 0.0 /
NO + O2 <=> N + O + O2 3.97e20 -1.5 7.56e4
REV/ 1.01e20 -1.5 0.0 /
NO + O <=> N + O + O 3.97e20 -1.5 7.56e4
REV/ 1.01e20 -1.5 0.0 /
NO + NO <=> N + O + NO 3.97e20 -1.5 7.56e4
REV/ 1.01e20 -1.5 0.0 /
NO + O <=> O2 + N 3.18e9 1.0 1.97e4
REV/ 9.63e11 0.5 3.6e3 /
N2 + O <=> NO + N 6.75e13 0.0 3.75e4
REV/ 1.5e13 0.0 0.0 /

END

```

APPENDIX C

MB_CNS Input File

This appendix has a sample input file for the axisymmetric code, MB_CNS. The input files for the code are termed sit files. This sit file was from the equilibrium, turbulent simulation of Air Condition 1 including the nozzle. The mesh for the simulation was grid 3 which contained 5426 by 87 cells in the acceleration tube and 1950 by 87 cells in the nozzle. The computational domain was comprised of 42 blocks with 33 in the acceleration tube and 9 in the nozzle.

C.1 x2_air_condition_1_with _nozzle_grid_3.sit

```

# X2 Expansion tube with nozzle attached for air condition 1

# set ::debug_level 1

# Define cross-section of shock tube in the (x,y)-plane.
# Tube 1 is the driven tube.
# Tube 4 is the driver tube.
# Dimensions are in metres.
set L1 5.155
set L4 0.01
set x0 0.0
set diameter 0.085
set r [expr $diameter / 2.0]

# Accelerator tube and nozzle initial condition.
set p10 43.0; # Pascals
set T10 296.0; # Kelvin
set u10 0.0;

# Shock tube initial condition
set p1 9.6e3;
set T1 $T10
set u1 0.0

set Twall $T10

# Number of blocks in each tube.
# We can set these to greater than 1 to run in parallel.
set N1 32
set N4 1
set dx1 [expr $L1 / $N1]
set dx4 [expr $L4 / $N4]

# Overall discretisation
set beta 1.05
set mx1 169
set mx4 18
set nx33 150
set nx34 225
set nx35 225
set nx36 225
set nx37 225
set nx38 225
set nx39 225
set nx40 225
set nx41 225
set nny 87

# Gas and flow properties
GAS_TYPE LUT_MIX
GAS_STATE state_1_gas $p1 $u1 0.0 $T1 1.0 0.0 0.0 0.0 0.0
GAS_STATE state_10_gas $p10 $u10 0.0 $T10 1.0 0.0 0.0 0.0 0.0

puts "Driven tube: start at the diaphragm (x0) and work downstream."
set x $x0
MODE z1a_0 $x 0.0
MODE z1r_0 $x $r
LINE v1_0 z1a_0 z1r_0
set west v1_0
POLYLINE $west 1 + $west
DISCRETISE $west $nny 0 1 $beta

for { set i 1 } { $i <= $N1 } { incr i } {
    set blockName driven$i
    puts "begin driven block: $blockName"

    # Names of nodes at west side
    set w0 z1a_[expr $i - 1]; # Node on the axis
    set w1 z1r_[expr $i - 1]; # Node on the tube wall

```

```

# Nodes at east side
set x [expr $x0 + $i * $dx1]
set e0 z1a_$i
set e1 z1r_$i
puts "corner nodes: $w0 $w1 $e0 $e1"
NODE $e0 $x 0.0
NODE $e1 $x $r

# Names of lines (and polylines)
set west v1_[expr $i - 1]; # vertical line
set east v1_$i; # vertical line
set north h1r_$i; # horizontal line - wall
set south h1a_$i; # horizontal line - axis
puts "line segments: $north $east $south $west"

# The three new lines around this block
LINE $east $e0 $e1
LINE $south $w0 $e0
LINE $north $w1 $e1

# Since there is only one segment per polyline, reuse names.
POLYLINE $north 1 + $north
POLYLINE $east 1 + $east
POLYLINE $south 1 + $south

DISCRETISE $north $nmx1 0 0 0.0
DISCRETISE $east $nny 0 1 $beta
DISCRETISE $south $nmx1 0 0 0.0

BOUNDARY_SPEC $north FIXED_T $twall

BLOCK $blockName + $north + $east + $south + $west
FILL_BLOCK $blockName state_10_gas
puts "finished block: $blockName"
}

puts "Driver tube: start at the diaphragm (x0) and work upstream."
set x $x0
NODE z4a_0 $x 0.0
NODE z4r_0 $x $r
LINE v4_0 z4a_0 z4r_0
set east v4_0
POLYLINE $east 1 + $east
DISCRETISE $east $nny 0 1 $beta

for { set i 1 } { $i <= $N4 } { incr i } {
    set blockName driver$i
    puts "begin driver block: $blockName"

    # Names of nodes at east side
    set e0 z4a_[expr $i - 1]
    set e1 z4r_[expr $i - 1]

    # Nodes at west side
    set x [expr $x0 - $i * $dx4]
    set w0 z4a_$i
    set w1 z4r_$i
    puts "corner nodes: $w0 $w1 $e0 $e1"
    NODE $w0 $x 0.0
    NODE $w1 $x $r

    # Names of lines
    set west v4_$i
    set east v4_[expr $i - 1]
    set north h4r_$i
    set south h4a_$i
    puts "line segments: $north $east $south $west"

    # The three new lines around this block
    LINE $west $w0 $w1
    LINE $south $w0 $e0
}

```

```

LINE $north $w1 $e1
# Since there is only one segment per polyline, reuse names.
POLYLINE $north 1 + $north
POLYLINE $south 1 + $south
POLYLINE $west 1 + $west

DISCRETISE $north $nx4 0 0 0.0
DISCRETISE $south $nx4 0 0 0.0
DISCRETISE $west $ny 0 1 $beta

BOUNDARY_SPEC $north FIXED_T $Twall
if { $i == $N4 } {
BOUNDARY_SPEC $west transient_uni
}

BLOCK $blockName + $north + $east + $south + $west
FILL_BLOCK $blockName state_1_gas
puts "finished block: $blockName"
}

puts "Lets get going on the nozzle"
# Dont need a and u
NODE b 5.17842422508 0.04348029365
NODE c 5.20799371126 0.04474811195
NODE d 5.24476653803 0.04647826885
NODE e 5.28983559172 0.04884240235
NODE f 5.34429516716 0.05193948765
NODE g 5.40920168497 0.05582184378
NODE h 5.48552900640 0.06052100210
NODE i 5.53179775374 0.06339967096
NODE j 5.57411899523 0.06603327563
NODE k 5.61917728825 0.06882149948
NODE l 5.67562814681 0.07226583305
NODE m 5.73597235269 0.07585133454
NODE n 5.79047127691 0.07897054120
NODE o 5.83511156873 0.08142052787
NODE p 5.87494723589 0.08351425964
NODE q 5.87494723589 0.0
NODE r 5.73597235269 0.0
NODE s 5.57411899523 0.0
NODE t 5.40920168497 0.0
NODE u 5.24476653803 0.0
NODE v 5.91876343870 0.08570479474
NODE w 5.99640731082 0.08926495630
NODE x 6.06026141414 0.09185600161
NODE y 6.09763203161 0.09322262887
NODE z 6.15435212895 0.09507846909
NODE aa 6.21430630685 0.09674933719
NODE ab 6.27263205935 0.09808771144
NODE ac 6.32232164541 0.09900786684
NODE ad 6.37976894639 0.09982682012
NODE ae 6.44182990505 0.10042977650
NODE af 6.50506772048 0.10076251031
NODE ag 6.55500000000 0.10083969668
NODE ah 6.55500000000 0.0
NODE ai 6.37976894639 0.0
NODE aj 6.21430630685 0.0
NODE ak 6.06026141414 0.0
SPLINE z1r_32d 3 z1r_32 b c d
SPLINE dg 3 d e f g
SPLINE gj 3 g h i j
SPLINE jm 3 j k l m
SPLINE mp 3 m n o p
SPLINE py 3 p w x y
SPLINE yab 3 y z aa ab
SPLINE abae 3 ab ac ad ae
SPLINE aeah 3 ae af ag ah
LINE qp q p
LINE rm r m
LINE sj s j
LINE tg t g

```

```

LINE ud u d
LINE z1a_32u z1a_32 u
LINE ut u t
LINE ts t s
LINE sr s r
LINE rq r q
LINE aly al y
LINE akab ak ab
LINE ajae aj ae
LINE aiah ai ah
LINE qal q al
LINE alak al ak
LINE akaj ak aj
LINE ajai aj ai
LINE aiah ai ah
LINE ajae aj ae
LINE akab ak ab
LINE aly al y

# dont need va or z1a_32zir_32
POLYLINE r33 1 + z1r_32d
POLYLINE e33 1 + z1a_32u
POLYLINE e33w34 1 + ud
POLYLINE r34 1 + dg
POLYLINE e34 1 + ut
POLYLINE e34w35 1 + tg
POLYLINE r35 1 + gj
POLYLINE e35 1 + ts
POLYLINE e35w36 1 + sj
POLYLINE r36 1 + jm
POLYLINE e36 1 + sr
POLYLINE e36w37 1 + rm
POLYLINE r37 1 + mp
POLYLINE e37 1 + rq
POLYLINE e37w38 1 + qp
POLYLINE r38 1 + py

POLYLINE s38 1 + qal
POLYLINE e38w39 1 + aly
POLYLINE n39 1 + yab
POLYLINE s39 1 + alak
POLYLINE e39w40 1 + akab
POLYLINE n40 1 + abae
POLYLINE s40 1 + akaj
POLYLINE e40w41 1 + ajae
POLYLINE n41 1 + aeah
POLYLINE s41 1 + ajai
POLYLINE e41 1 + aiah

DISCRETISE n33 $nnx33 0 0 0.0
DISCRETISE s33 $nnx33 0 0 0.0
DISCRETISE n34 $nnx34 0 0 0.0
DISCRETISE s34 $nnx34 0 0 0.0
DISCRETISE n35 $nnx35 0 0 0.0
DISCRETISE s35 $nnx35 0 0 0.0
DISCRETISE n36 $nnx36 0 0 0.0
DISCRETISE s36 $nnx36 0 0 0.0
DISCRETISE n37 $nnx37 0 0 0.0
DISCRETISE s37 $nnx37 0 0 0.0
DISCRETISE n38 $nnx38 0 0 0.0
DISCRETISE s38 $nnx38 0 0 0.0
DISCRETISE n39 $nnx39 0 0 0.0
DISCRETISE s39 $nnx39 0 0 0.0
DISCRETISE n40 $nnx40 0 0 0.0
DISCRETISE s40 $nnx40 0 0 0.0
DISCRETISE n41 $nnx41 0 0 0.0
DISCRETISE s41 $nnx41 0 0 0.0
DISCRETISE e33w34 $nny 0 1 $beta
DISCRETISE e34w35 $nny 0 1 $beta
DISCRETISE e35w36 $nny 0 1 $beta
DISCRETISE e36w37 $nny 0 1 $beta
DISCRETISE e37w38 $nny 0 1 $beta
DISCRETISE e38w39 $nny 0 1 $beta

```

```

DISCRETISE e39w40 $mny 0 1 $beta
DISCRETISE e40w41 $mny 0 1 $beta
DISCRETISE e41 $mny 0 1 $beta

BOUNDARY_SPEC n33 FIXED_I $Twall
BOUNDARY_SPEC n34 FIXED_I $Twall
BOUNDARY_SPEC n35 FIXED_I $Twall
BOUNDARY_SPEC n36 FIXED_I $Twall
BOUNDARY_SPEC n37 FIXED_I $Twall
BOUNDARY_SPEC n38 FIXED_I $Twall
BOUNDARY_SPEC n39 FIXED_I $Twall
BOUNDARY_SPEC n40 FIXED_I $Twall
BOUNDARY_SPEC n41 FIXED_I $Twall
BOUNDARY_SPEC e41 SUP_OUT

BLOCK block33 + n33 + e33w34 + s33 + v1_32
BLOCK block34 + n34 + e34w35 + s34 + e33w34
BLOCK block35 + n35 + e35w36 + s35 + e34w35
BLOCK block36 + n36 + e36w37 + s36 + e35w36
BLOCK block37 + n37 + e37w38 + s37 + e36w37
BLOCK block38 + n38 + e38w39 + s38 + e37w38
BLOCK block39 + n39 + e39w40 + s39 + e38w39
BLOCK block40 + n40 + e40w41 + s40 + e39w40
BLOCK block41 + n41 + e41 + s41 + e40w41

FILL_BLOCK block33 state_10_gas
FILL_BLOCK block34 state_10_gas
FILL_BLOCK block35 state_10_gas
FILL_BLOCK block36 state_10_gas
FILL_BLOCK block37 state_10_gas
FILL_BLOCK block38 state_10_gas
FILL_BLOCK block39 state_10_gas
FILL_BLOCK block40 state_10_gas
FILL_BLOCK block41 state_10_gas

CONNECT_BLOCKS driver1 east driven1 west
# centreline and further out near the end of each block
}

for { set i 2 } { $i <= $N1 } { incr i } {
    set im1 [expr $i - 1]
    CONNECT_BLOCKS driven$im1 east driven$i west
}

for { set i 2 } { $i <= $N4 } { incr i } {
    set im1 [expr $i - 1]
    CONNECT_BLOCKS driver$im1 west driver$i east
}

for { set i 34 } { $i <= 41 } { incr i } {
    set j [expr $i - 1]
    CONNECT_BLOCKS block$j east block$i west
}

CONNECT_BLOCKS driven$N1 east block33 west

puts "Set simulation control parameters."
TITLE X2 Expansion Tube Nozzle
CASE_ID 0
FLUX_CALC adaptive
VISCOUS
TURBULENT driver1
for { set i 1 } { $i <= 32 } { incr i } {
    TURBULENT driven$i
}

for { set i 33 } { $i <= 41 } { incr i } {
    TURBULENT block$i
}

AXISYMMETRIC
MAX_TIME 1.3e-3
MAX_STEP 900000
TIME_STEP 5.0e-10
DT_PLOT 5.0e-5
DT_HISTORY 5.0e-7
for { set i 4 } { $i <= $N1 } {incr i} {
}

```

```

HISTORY_CELL driven$i [expr $nrx1 - 5] 6;
HISTORY_CELL driven$i [expr $nrx1 - 5] [expr $ny / 4];
HISTORY_CELL driven$i [expr $nrx1 - 5] $ny;
}

HISTORY_CELL block33 [expr $nrx33 - 5] 6;
HISTORY_CELL block33 [expr $nrx33 - 5] [expr $ny / 4];
HISTORY_CELL block33 [expr $nrx33 - 5] $ny;
HISTORY_CELL block34 [expr $nrx34 - 5] 6;
HISTORY_CELL block34 [expr $nrx34 - 5] [expr $ny / 4];
HISTORY_CELL block34 [expr $nrx34 - 5] $ny;
HISTORY_CELL block35 [expr $nrx35 - 5] 6;
HISTORY_CELL block35 [expr $nrx35 - 5] [expr $ny / 4];
HISTORY_CELL block35 [expr $nrx35 - 5] $ny;
HISTORY_CELL block36 [expr $nrx36 - 5] 6;
HISTORY_CELL block36 [expr $nrx36 - 5] [expr $ny / 4];
HISTORY_CELL block36 [expr $nrx36 - 5] $ny;
HISTORY_CELL block37 [expr $nrx37 - 5] 6;
HISTORY_CELL block37 [expr $nrx37 - 5] [expr $ny / 4];
HISTORY_CELL block37 [expr $nrx37 - 5] $ny;
HISTORY_CELL block38 [expr $nrx38 - 5] 6;
HISTORY_CELL block38 [expr $nrx38 - 5] [expr $ny / 4];
HISTORY_CELL block38 [expr $nrx38 - 5] $ny;
HISTORY_CELL block39 [expr $nrx39 - 5] 6;
HISTORY_CELL block39 [expr $nrx39 - 5] [expr $ny / 4];
HISTORY_CELL block39 [expr $nrx39 - 5] $ny;
HISTORY_CELL block40 [expr $nrx40 - 5] 6;
HISTORY_CELL block40 [expr $nrx40 - 5] [expr $ny / 4];
HISTORY_CELL block40 [expr $nrx40 - 5] $ny;
HISTORY_CELL block41 [expr $nrx41 - 5] 6;
HISTORY_CELL block41 [expr $nrx41 - 5] [expr $ny / 4];
HISTORY_CELL block41 [expr $nrx41 - 5] $ny;
puts "Name the output files and build them."
BEZIER_FILE x2_nozzle.bez
PARAM_FILE x2_nozzle.p
MPOST_FILE x2_nozzle.mpost
MPOST_SCALES 0.25 1.0
BUILD
EXIT

```

APPENDIX D

SM_3D⁺ Input File

This appendix contains the python script “x2_nozzle_laminar_with_non_uniform_inflow.py” for the SM_3D⁺ code which was used for the hypersonic nozzle design. The simulation accounted for non-uniform inflow into the nozzle and utilized the objective function which compensated for the recompression which could form along the axis of the nozzle. Following this are three python scripts which can be used in conjunction with the bezier control points to produce the nozzle contour. The script “wall_definition.py” when run, will print out the nozzle co-ordinates to three text files, corresponding to each section of the nozzle. This script calls the two other files “roberts.py” and “bezier.py” when executed.

D.1 x2_nozzle_laminar_with_ non_uniform_inflow.py

```

#!/usr/bin/env python
##
## \ingroup geom
##
## \brief Use the sm_3d code in single-solution mode to do lots of
## what-if simulations of a nozzle.
##
## \author PA Jacobs
##
## The nelmin optimizer supervises the calculations,
## with the goal of generating a good quality flow.
##
## \version 21-Mar-05 first attempt, inviscid design on Mach number only
## 22-Mar-05 inviscid design including both Mach number and angle
##
## Sincd altered by Peebs for his X2 nozzle

import os
from math import sqrt
from Numeric import array, arange
from wall_definition import bezier_nodes_for_wall
from bezier import bezier3D_eval

def prepare_input_file(jobName, opt_parameters):
    """Prepares the .par file from a template and the supplied values.

    opt_parameters is the list of optimization parameters.
    See below to find their interpretation.
    """
    template = """The parameter file for ideal-gas design of X2 M10 contour.
0 case_id - generic case
0.4 300 0.0001 CFL, max_t_steps, closing tolerance

2 3 0.9 Xorder, i_suppress, p_safety
0.0 0.0001 1.0 10000 Xi_0, dXi, X_max, max_x_steps 2000,
0.005 dXi_plot
1 slice_ident
160 2 nny, nuz
0 10 smooth_grid, smooth_iter
5 3 3 3 bc_N, E, S, W
296.0 296.0 296.0 296.0 Twall_N, E, S, W
<rho> <ux> 0.0 0.0 <e> free stream rho, ux, uy, uz, e
0 1 1 use_B_spline, bezier_box, 2d format
"""
    # Inflow properties
    M = 7.15 # Mach number
    T = 4000.0 # degrees K
    p = 30.0e3 # Pascals
    g = 1.4 # ratio of specific heats
    Rgas = 287.0 # gas constant J/(kg.K)
    Cv = Rgas / (g - 1.0)
    rho = p / (Rgas * T)
    e = Cv * T
    a = sqrt(g * Rgas * T)
    ux = M * a
    template = template.replace("<rho>", ("%12.4e" % rho))
    template = template.replace("<ux>", ("%12.4e" % ux))
    template = template.replace("<e>", ("%12.4e" % e))
    #
    # Wall profile
    x_list, y_list = bezier_nodes_for_wall(opt_parameters)
    n_nodes = len(x_list)
    template += ("%d\n" % n_nodes)
    for i in range(n_nodes):
        template += ("%12.4e %12.4e A %d\n%12.4e %12.4e B %d\n" % \
            (x_list[i], 0.0, i, x_list[i], y_list[i], i))
    f = open(jobName+".par", "wt")
    f.write(template)
    f.close()

```

```

current directory.
The TECPLOT format of the first few lines is...

TITLE = "Solution data from x2_nozzle "
VARIABLES = "y" , "rho" , "p" , "M" , "T" , "Ang(deg)"
ZONE T="Variable iy, ix = 200, iz = 1" , I=40, F=POINT
3.757928e-03 0.0329487 18621.4 8.79282 1969.21 -0.930024
1.123198e-02 0.0231717 11191.2 9.55019 1682.83 -1.3846
"""
if verbose: print "Extracting profile...."
fi, fo = os.popen2("sm_prof.x")
fi.write(jobName +
"""
201 160 2
1 200 0 1
0 1 0
1 0 0 1 1 0 1
""")
resultFlag = fi.close()
if resultFlag:
    print "Some problem with sm_prof:", resultFlag
prof_stdout = fo.read()
if verbose:
    print prof_stdout
fo.close()
#
# How pick up the profile data.
f = open(jobName + ".plt", "r")
content = f.readlines()
values = []
for line in content[3:]:
    numbers = [float(word) for word in line.split()]
    values.append(numbers)
va = array(values)
y = va[:,0]

return

def run_sm_prep(jobName, verbose=0):
    """Runs the inflow profile preparation program"""
    if verbose:
        print "Prepare inflow data."
    fi, fo = os.popen2("sm_prep.x")
    fi.write(jobName + "\n")
    resultFlag = fi.close()
    if resultFlag:
        print "Some problem with sm_prep:", resultFlag
    prep_stdout = fo.read()
    if verbose:
        print prep_stdout
    fo.close()
    return

def run_sm_3d_simulation(jobName, verbose=0):
    """Runs the sm_3d simulation program"""
    if verbose:
        print "Run simulation..."
    fi, fo = os.popen2("sm_3d.x")
    fi.write(jobName + "\n")
    resultFlag = fi.close()
    if resultFlag:
        print "Some problem with sm_3d:", resultFlag
    simulation_stdout = fo.read()
    if verbose:
        print simulation_stdout
    fo.close()
    return

def extract_profile_data(jobName, verbose=0):
    """Runs the postprocessing program.

    This should result in a .pit file being written into the

```

```

rho = va[:,1]
p = va[:,2]
M = va[:,3]
T = va[:,4]
theta = va[:,5]
return y, rho, p, M, T, theta

def extract_mach(jobName, verbose=0):
    """Runs the postprocessing program.

    This should result in a .plt file being written into the
    current directory.

    """
    if verbose: print "Extracting profile...."
    fi, fo = os.popen2("sm_prof.x")
    fi.write(jobName +

    """
    201 160 2
    1
    0 0 0 1
    1 1 0
    0 0 0 0 1 0 0 0
    """)
    resultFlag = fi.close()
    if resultFlag:
        print "Some problem with sm_prof:", resultFlag
    prof_stdout = fo.read()
    if verbose:
        print prof_stdout
    fo.close()
    #
    # Now pick up the profile data.
    f = open(jobName + ".plt", "r")
    content = f.readlines()
    values = []
    for line in content[3:]:
        numbers = [float(word) for word in line.split()]
        values.append(numbers)
    va = array(values)
    x = va[:,0]
    y = va[:,1]
    M = va[:,2]
    return x, y, M

def objective_function(parameter_list, verbose=0):
    """Runs the simulation with current guess for parameters and
    returns an error indicator"""
    #
    if verbose: print "Begin objective function..."
    print "p_list=", [("%13.5e" % p) for p in parameter_list]
    jobName = "x2_nozzle"
    prepare_input_file(jobName, parameter_list)
    #
    run_sm_prep(jobName, verbose)
    run_sm_3d_simulation(jobName, verbose)
    if verbose: print "End Sim Job"
    y, rho, p, M, T, theta = extract_profile_data(jobName, verbose)
    # print "y=", y, "M=", M
    #
    # Construct the objective function estimate from
    # (a) the deviation of mach number from the design value
    # (b) the deviation of flow angle from zero
    # across the exit plane.
    # For inviscid design, include the whole profile.
    # For viscous design, include only that part in the core flow.
    N = len(y)
    #
    avg_M = sum(M) / N
    M_design = 10.0 # desired Mach number
    dM_design = 0.01 # desired deviation limit
    theta_design = 0
    dtheta_design = 0.01
    sum_dev_M = 0

```

```

sum_dev_t = 0
for j in range(1,N):
    if abs((M[j-1]-M[j])/(y[j-1]-y[j])) < 20 and y > 0.06:
        temp1 = M[j-1] - M_design
        temp2 = theta[j-1] - theta_design
    else:
        temp1 = 0
        temp2 = 0
        sum_dev_M = sum_dev_M + temp1*temp1
        sum_dev_t = sum_dev_t + temp2*temp2
    f_M = 1.0/N * sum_dev_M / (dM_design**2)
    f_theta = 10.0/N * sum_dev_t / (dtheta_design**2)
#
x_current, y_current, M_current = extract_mach(jobName, verbose)
extra = 0
number = len(x_current)
for k in range (1, number):
    if M_current[k] < M_current[k-1]:
        extra = extra + ((M_current[k-1] - M_current[k])*1e4)**2
    f_obj = (f_M + f_theta)**2 + extra/1.5
#
print "f_obj= %13.5e" % f_obj
sys.stdout.flush()
return f_obj

import nelmin
import sys

if __name__ == '__main__':
    # We are running a stand-alone script, so get on with some work.
    if len(sys.argv) == 1 or (len(sys.argv) > 1 and sys.argv[1] == '-help'):
        print "Usage: design_x2_nozzle.py [-opt|-single|-help]"
        sys.exit()

    print "Begin"
    param = [0.044143622293801157, 0.045749214570684697, 0.047391380958099125,
0.059227502662833199, 0.058663178812094117, 0.080883480315167414,
0.095318527711046125, 0.10176105116843867]
    if sys.argv[1] == '-opt':
        dparam = [0.002,] * len(param) # nominal perturbations
        popt, fpopt, conv_flag, nfe, nres = \
            nelmin.minimize(objective_function, param, dparam, 1.0e-6, 100)
        print "optimised parameters=", popt
        print "objective=", fpopt
        print "convergence-flag=", conv_flag
        print "number-of-fn-evaluations=", nfe
        print "number-of-restarts=", nres
    elif sys.argv[1] == '-single':
        objective_function(param, 1)
    else:
        print "Unknown command option:", sys.argv[1]
        print "Done"

```

D.2 wall_definition.py

```

#!/usr/bin/env python
##
## \file wall_definition.py
## \ingroup geom
##
## \brief Define a nozzle wall in terms of nodes of a Bezier polynomial.
##
## \author PA Jacobs
##
## \version 21-Mar-05 first attempt, X2 nozzle
##
## Since alter by Peebs. This was the program I used to output the contour in
the format for the guys in the Mech Eng workshop. Afterwards I manually added
a few points to the start (about 5mm worth) so that the tool would keep going
past the edge of the nozzle. I then had to flipped them upside down (as I had
them order from start to end instead of end to start).

```

```

from Numeric import array, arange
from roberts import distribute_points_1
from bezier import bezier3D_eval

def bezier_nodes_for_wall(parameter_list):
    """Generates the coordinates for the nodes defining the wall."""
    y_inlet = 0.0425 # inner radius of X2 acceleration tube
    n_nodes = 1 + len(parameter_list) + 1
    xmax = 1.4 # metres
    beta = 1.05 # clustering parameter (see Roberts stretching function)
    x = distribute_points_1(0.0, xmax, n_nodes-1, 1, 0, beta)
    y = array([y_inlet,]*n_nodes)
    for i in range(1,n_nodes):
        iparam = i - 1
        if iparam < len(parameter_list):
            y[i] = parameter_list[iparam]
        else:
            # the last y-node is at the same height as the
            # second-last y-node to get a zero-slope exit.
            y[i] = parameter_list[-1]
    return x, y

#-----
if __name__ == '__main__':
    p_list = [0.043905961068708386, 0.046412063542271995, 0.04705386857951985,
              0.060095483668831662, 0.059878522081421651, 0.080346210364914392,
              0.094781316949121036, 0.10083969668316217]
    x, y = bezier_nodes_for_wall(p_list)
    f = open("section1.txt", "wt")
    f.write("X85.000 Z-500.000;\n")
    g = open("section2.txt", "wt")
    g.write("X114.062 Z-551.000;\n")
    h = open("section3.txt", "wt")
    h.write("X177.098 Z-575.000;\n")
    # For 1000 control points get the contour for the first section

for t in arange(0.0,1.001,0.001):
    xp, yp, zp = bezier3D_eval(t, Bx=x, By=y)
    axial_distance = xp * 1000
    diameter = yp * 1000 * 2
    if axial_distance < 274.0:
        axial_distance = 274.0-axial_distance
        axial_distance = ("%6.3f" % axial_distance)
        diameter = ("%6.3f" % diameter)
        f.write("X" + diameter + " Z-" + axial_distance + ";\n")
    # For 1225 control points get the contour for the second section
    for t in arange(0.0,1.001,0.0008163265306):
        xp, yp, zp = bezier3D_eval(t, Bx=x, By=y)
        axial_distance = xp * 1000
        diameter = yp * 1000 * 2
        if axial_distance > 274.0 and axial_distance < 825.0:
            axial_distance = 825.0-axial_distance
            axial_distance = ("%6.3f" % axial_distance)
            diameter = ("%6.3f" % diameter)
            g.write("X"+ diameter + " Z-" + axial_distance + ";\n")
    # For 1750 control points get the contour for the final section
    for t in arange(0.0,1.001,0.000571428571):
        xp, yp, zp = bezier3D_eval(t, Bx=x, By=y)
        axial_distance = xp * 1000
        diameter = yp * 1000 * 2
        if axial_distance > 825.0 and axial_distance <= 1400.0:
            axial_distance = 1400.0-axial_distance
            axial_distance = ("%6.3f" % axial_distance)
            diameter = ("%6.3f" % diameter)
            h.write("X" + diameter + " Z-" + axial_distance + ";\n")
        f.write("X114.062" + " " + "Z- 0.000" + ";\n")
        g.write("X177.098" + " " + "Z- 0.000" + ";\n")
    f.close()
    g.close()
    h.close()

```

D.3 roberts.py

```

#!/bin/env python
## \file roberts.py
## \ingroup mm
##
## \brief Node distribution and coordinate stretching functions.
##
## These functions should behave the same as the C code functions.
##
## \author PA Jacobs
##
## \version 1.0: 22-Mar-2005

from Numeric import arange, power

def roberts(eta, alpha, beta):
    """
    Computes the stretched coordinate in the range [0.0..1.0]
    using the boundary-layer-like transformation devised by Roberts.

    eta : unstretched coordinate, 0 <= eta <= 1.0
    beta : stretching factor (more stretching as beta --> 1.0)
    alpha : location of stretching
            alpha = 0.5 : clustering of nodes at both extremes of eta
            alpha = 0.0 : nodes will be clustered near eta=1.0

    Works for both scalars and arrays.
    """
    lmbda = (beta + 1.0) / (beta - 1.0)
    # Note that power is a ufunc from Numeric
    lmbda = power(lmbda, ((eta - alpha)/(1.0 - alpha)))
    etabar = (beta + 2.0 * alpha) * lmbda - beta + 2.0 * alpha
    etabar = etabar / ((2.0 * alpha + 1.0) * (1.0 + lmbda))
    return etabar

def distribute_points_1(t1, t2, n, end1, end2, beta):
    """
    Generate a set of points nonuniformly distributed from t1 to t2.

    t1 : parameter value 1
    t2 : parameter value 2
    n : number of intervals (the number of points is n+1)
    end1 : =0 points are not clustered to end 1
           : =1 points ARE clustered to end 1
    end2 : =0 points are not clustered to end 2
           : =1 points ARE clustered to end 2
    beta : grid stretching parameter
           : 1 < beta < +inf : points are clustered
           : The closer to 1, the more the clustering.
           : beta < 1 : no clustering

    Returns t[0:n] an array of distributed values.
    """
    # Decide on stretching parameters for Robert's transform.
    alpha = 0.5;
    reverse = 0;
    cluster = 1;
    if (end1 == 0 and end2 == 0) or beta < 1.0:
        cluster = 0
    if end1 == 1 and end2 == 1:
        alpha = 0.5
    if end1 == 1 and end2 == 0:
        reverse = 1
    alpha = 0.0
    if end1 == 0 and end2 == 1:
        reverse = 0
    alpha = 0.0
    # Compute the grid points as an array.
    # The intermediate parameter is uniformly distributed.
    del_eta = 1.0 / n
    i = arange(n+1)

```

```

eta = del_eta * i;
# Cluster the points.
if cluster:
    if reverse: eta = 1.0 - eta;
    etabar = roberts(eta, alpha, beta);
    if reverse: etabar = 1.0 - etabar;
else:
    etabar = eta;
# Compute the parameter value within the given end-points.
x = (1.0 - etabar) * t1 + etabar * t2;
return x
#-----
if __name__ == "__main__":
    print "Begin roberts demo..."
    a = 0.5
    b = 1.1
    print "Scalar use..."
    for eta in arange(0.0, 1.0, 0.1):
        print "eta=", eta, "roberts=", roberts(eta, a, b)
    print "Vector use..."
    eta = arange(0.0, 1.0, 0.1)
    print "eta=", eta, "roberts=", roberts(eta, a, b)
    print "Distribute points..."
    print "x=", distribute_points_1(0.0, 1.0, 5, 1, 0, 1.1)
    print "x=", distribute_points_1(0.0, 1.0, 5, 0, 1, 1.1)
    print "x=", distribute_points_1(0.0, 1.0, 5, 1, 1, 1.1)
    print "x=", distribute_points_1(0.0, 1.0, 5, 0, 0, 1.1)
    print "Done."

## \ingroup: geom
"""
Bezier polynomial functions like those in bezier.c.
P.J. May, June 2004.
Reference:
Fujio Yamaguchi
Curves and Surfaces in Computer Aided Geometric Design
Springer-Verlag 1988
"""
from copy import copy

def bezier_eval(t, B):
    """
    Evaluate the Bezier polynomial at parametric location 0<t<1.
    For an n-th order curve, we expect n+1 points.
    The de Casteljau algorithm is used for simplicity.
    """
    assert len(B) > 1
    assert t > -0.1 and t < 1.01
    n = len(B) - 1 # order of the polynomial
    Q = copy(B) # work array
    # Now, generate one new level at a time;
    # over-writing the work array at each level.
    for k in range(n):
        for i in range(n-k):
            Q[i] = (1.0 - t) * Q[i] + t * Q[i+1]
    return Q[0]

```

D.4 bezier.py

```

#!/usr/bin/env python
## \file: bezier.py

```

```

def bezier3D_eval(t, Bx, By=[], Bz=[]):
    """
    Evaluate the Bezier polynomial for 1, 2 or 3D space.
    """
    assert len(Bx) > 1
    n = len(Bx) - 1 # order of the polynomial
    if not By: By = [0.0] * (n+1)
    if not Bz: Bz = [0.0] * (n+1)
    assert len(By) == n+1
    assert len(Bz) == n+1
    return (bezier_eval(t,Bx), bezier_eval(t,By), bezier_eval(t,Bz))

def bezier_add_one_point(B):
    """
    Adds one control point and returns the new list of control points.

    The algorithm in Section 5.1.8 on page 208 of Yamaguchi is used.
    This effectively increases the order of the polynomial by one.
    """
    n = len(B) - 1
    assert n >= 1
    Q = [B[0], ] # First point is a special case
    for i in range(1,n+1):
        Qnew = (i * B[i-1] + (n + 1 - i) * B[i]) / (n + 1.0)
        Q.append(Qnew)
    Q.append(B[n]) # Last point is also a special case
    return Q

```

```

# -----
if __name__ == '__main__':
    print "Bezier demo begin..."
    print bezier3D_eval(0.66667, [0.0, 2.0, 4.0, 6.0],
        [-2.0, 1.0, 4.0, 7.0])
    print "Done."

```

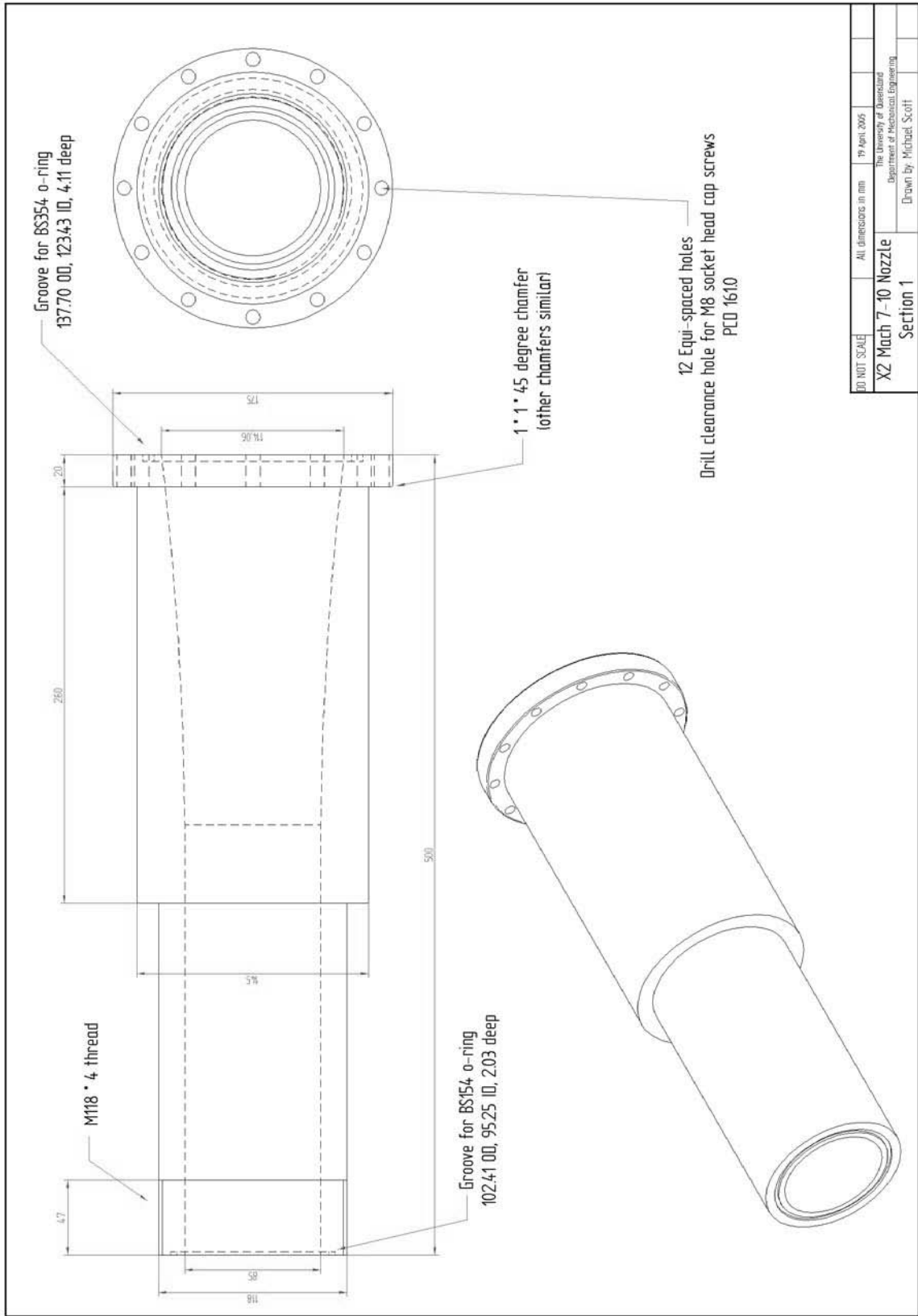
APPENDIX E

Technical Drawings

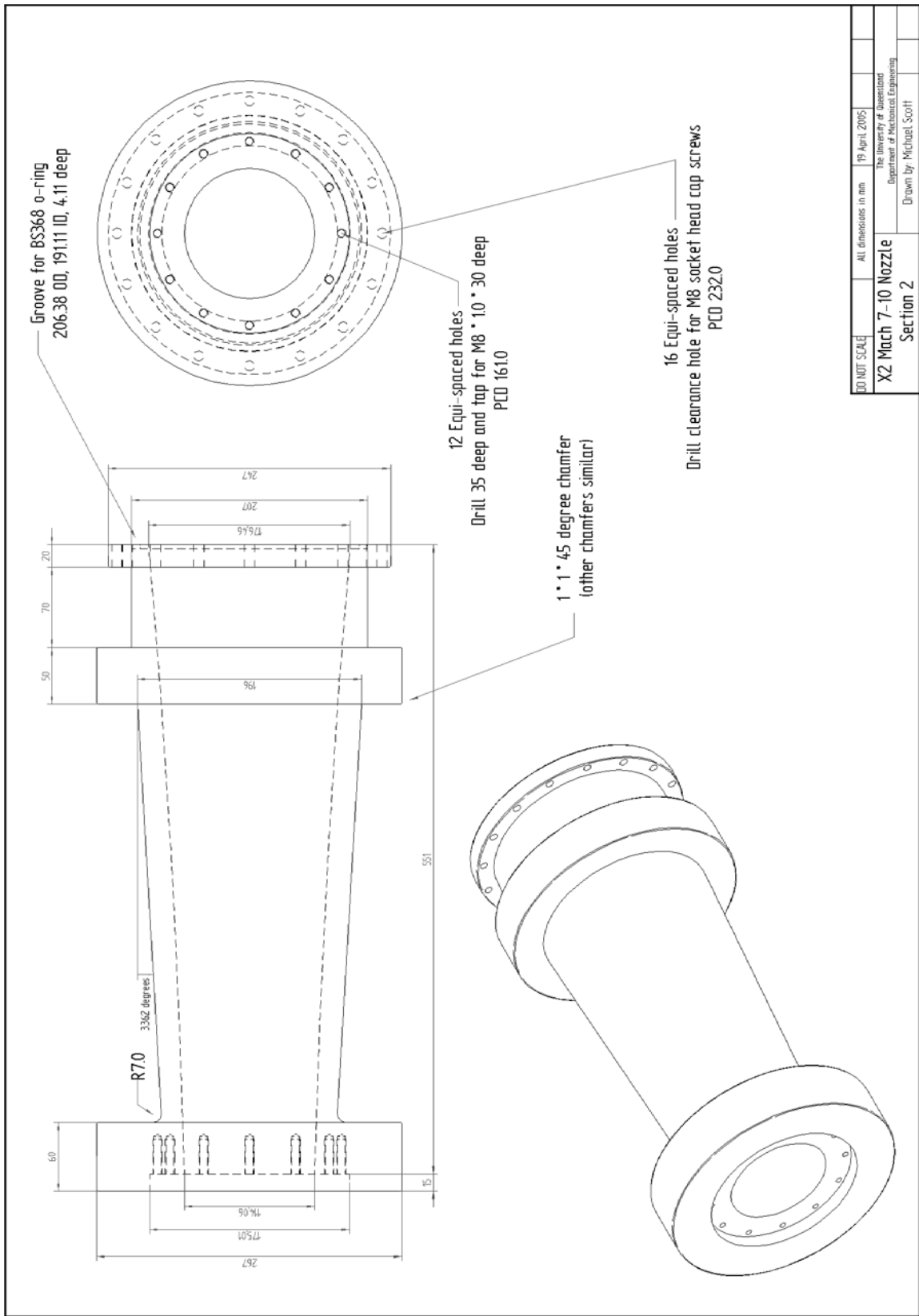
Presented in this appendix are the technical drawings that were used in the design of the hypersonic nozzle. A list of the drawings is provided below.

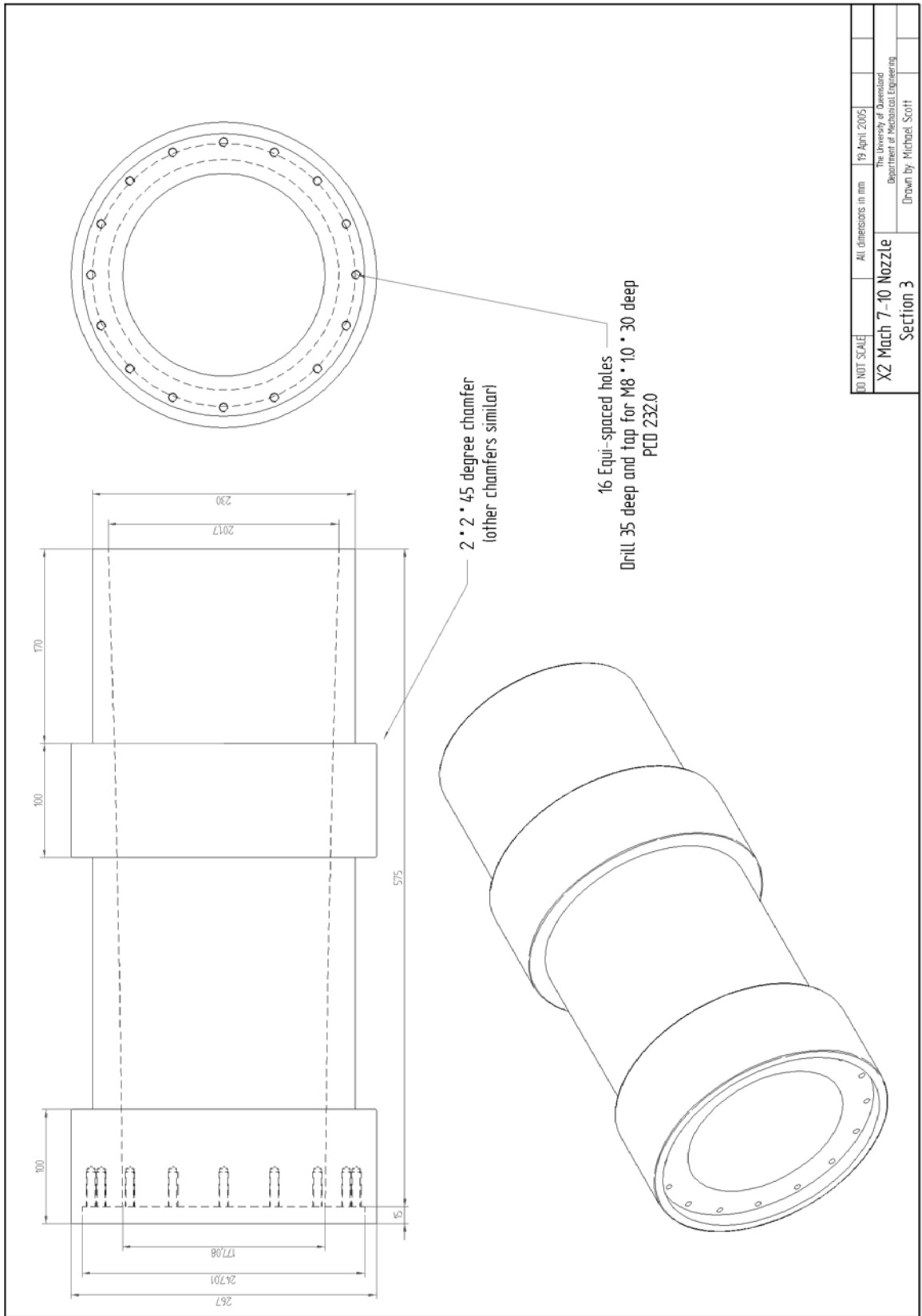
Table E.1: List of technical drawings

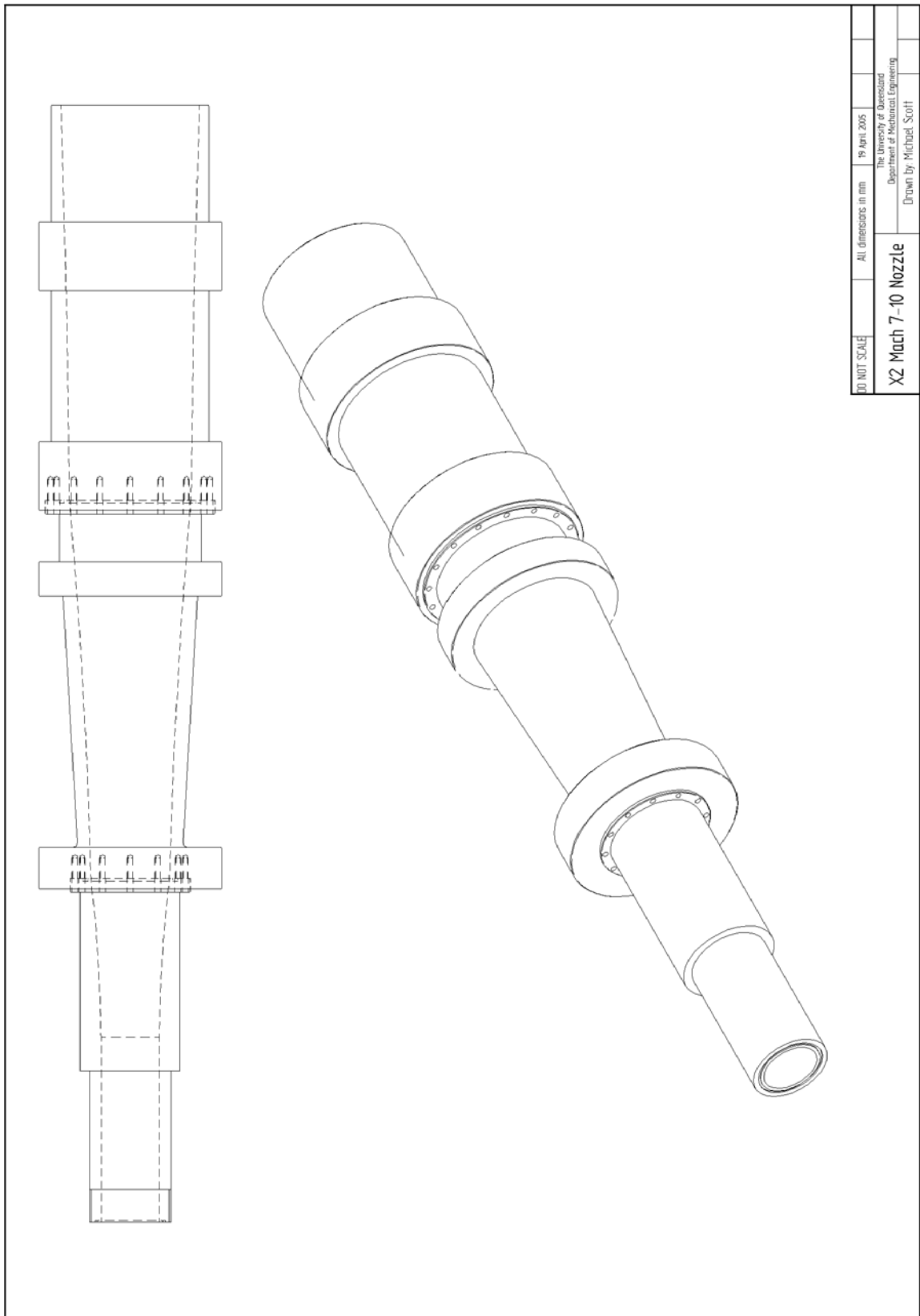
Drawing number	Component
1	Section 1 of the hypersonic nozzle
2	Section 2 of the hypersonic nozzle
3	Section 3 of the hypersonic nozzle
4	The complete hypersonic nozzle
5	The nozzle frame with dimensions
6	The nozzle frame layout
7	The support roller for the nozzle frame
8	The small support roller #1 for the nozzle frame
9	The small support roller #2 for the nozzle frame



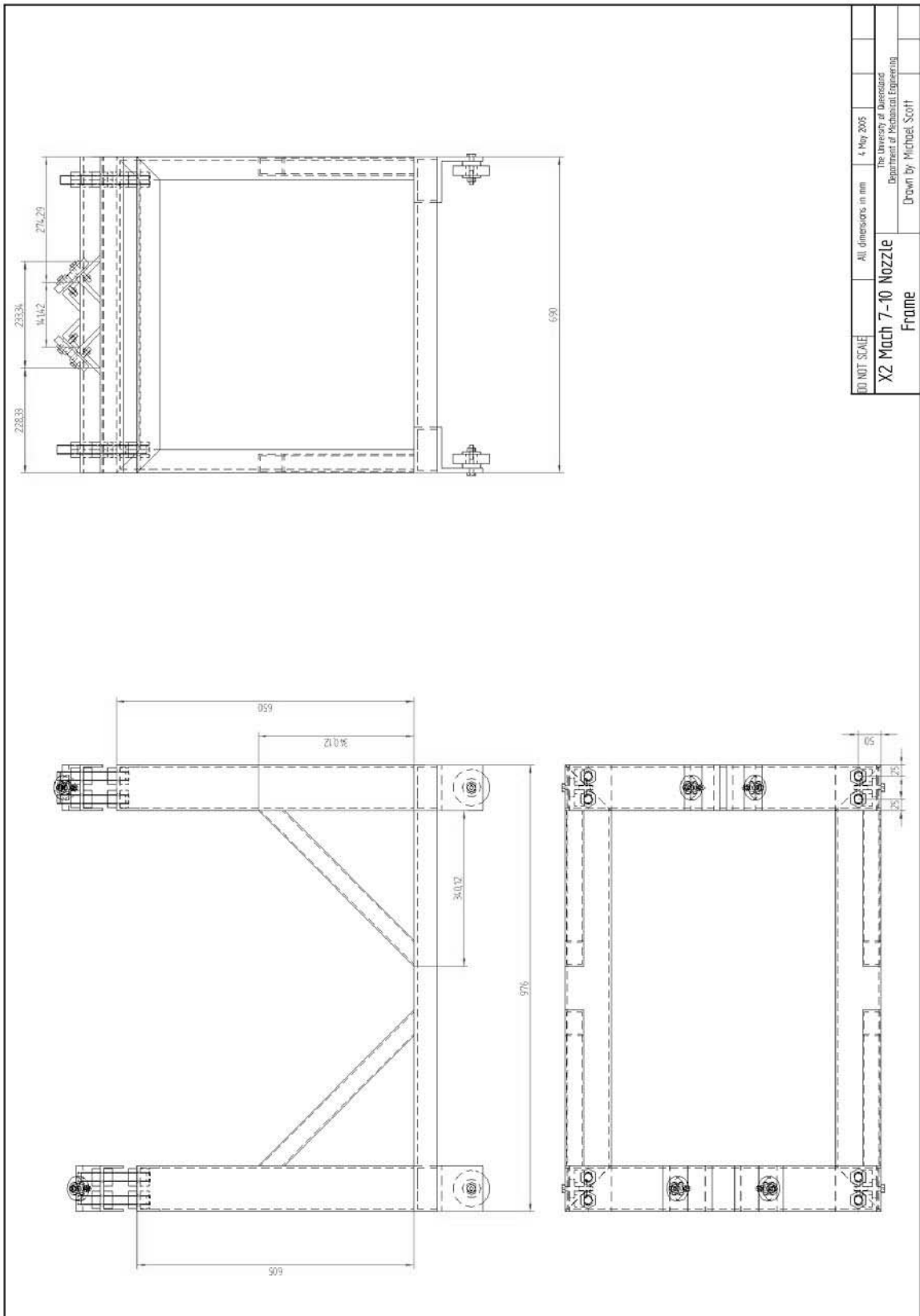
EO NOT SCALE	All dimensions in mm	19 April 2005	
The University of Queensland Department of Mechanical Engineering			
X2 Mach 7-10 Nozzle		Section 1	
		Drawn by: Michael Scott	



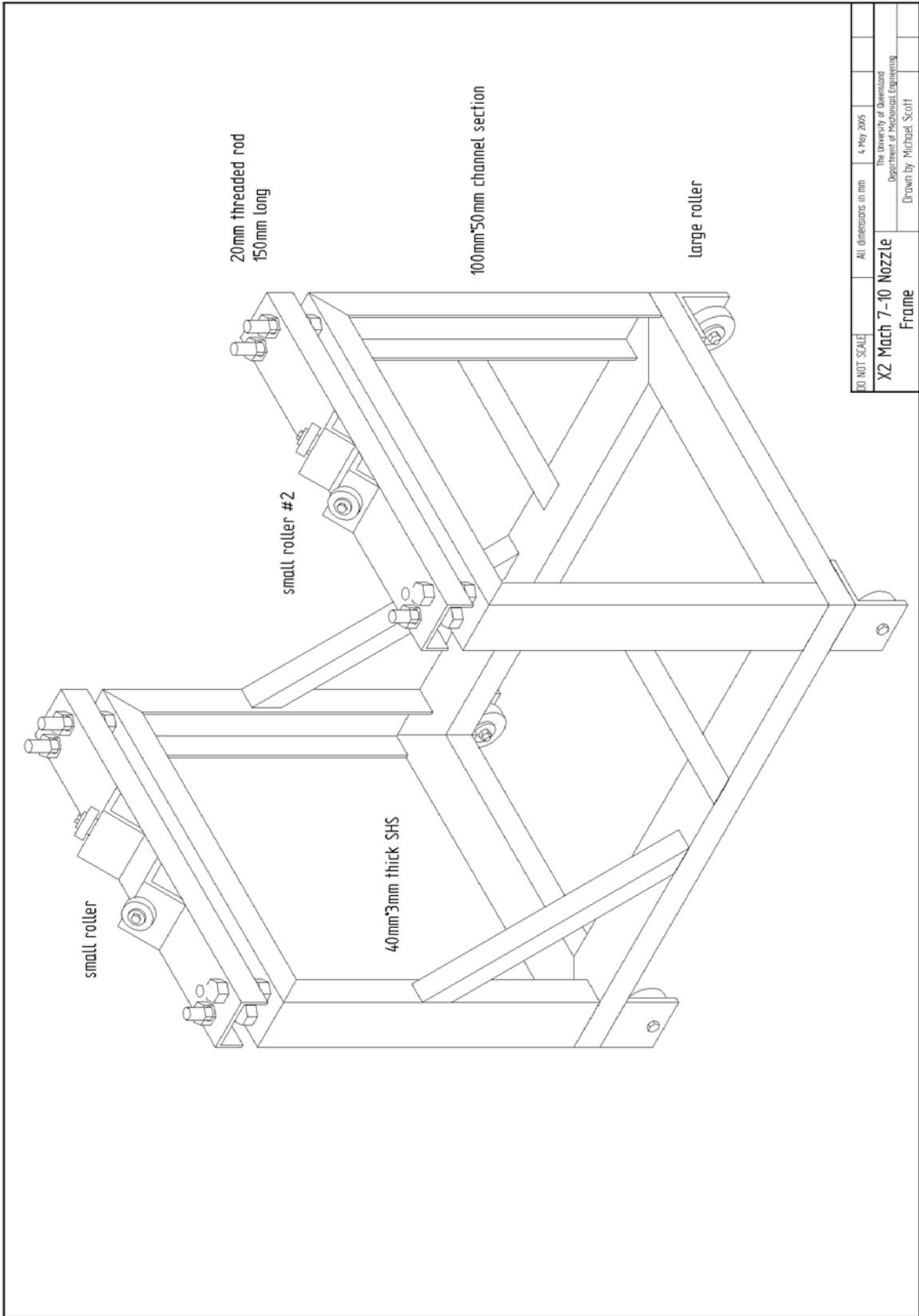


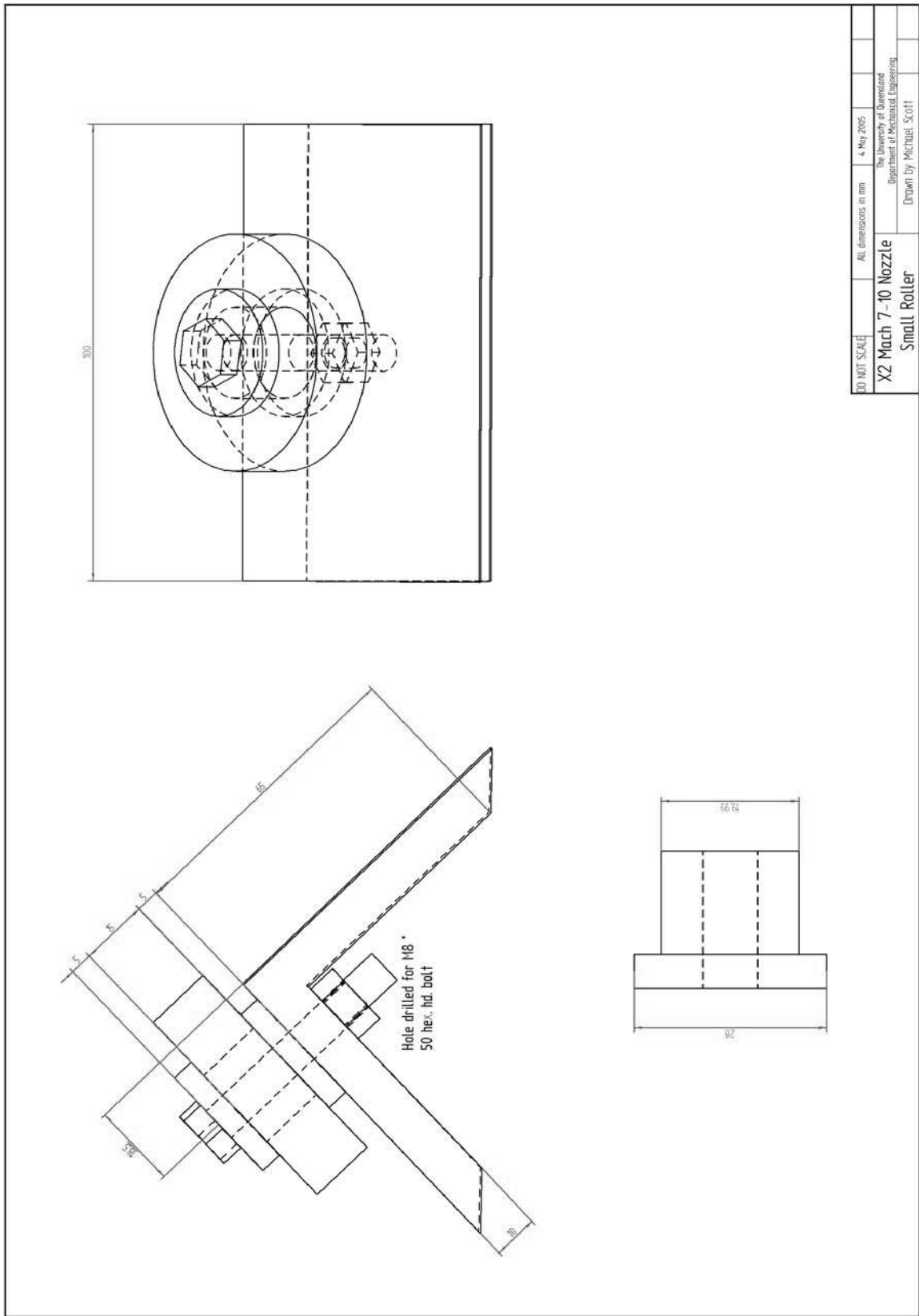


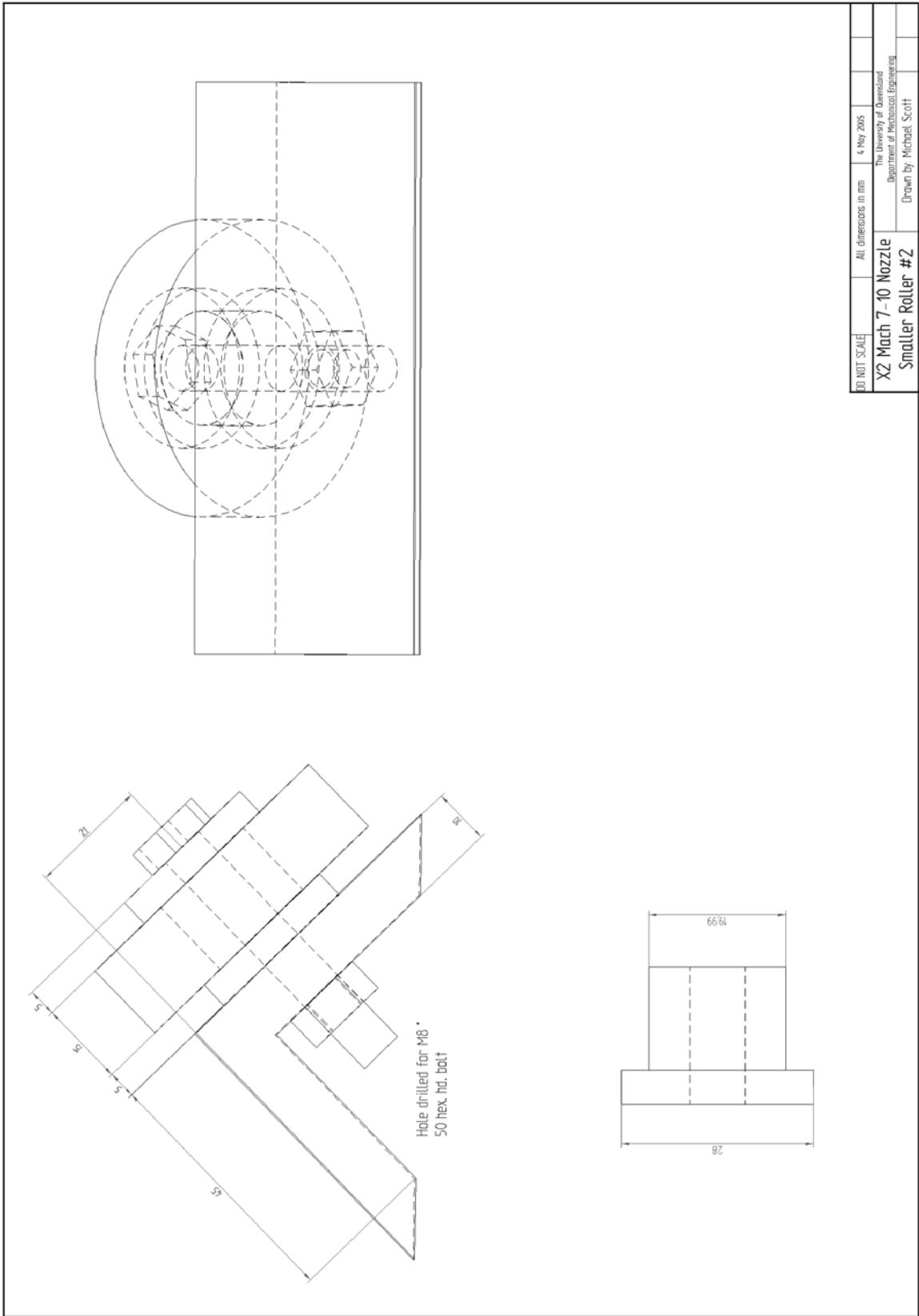
DO NOT SCALE	All dimensions in mm	19 April 2005		
X2 Mach 7-10 Nozzle			The University of Queensland Department of Mechanical Engineering	
Drawn by: Michael Scott				



DD NOT SCALE	All dimensions in mm	4 May 2005
X2 Mach 7-10 Nozzle Frame		
The University of Queensland Department of Mechanical Engineering Drawn by Michael Scott		







3D NOT SCALE	All dimensions in mm	4 May 2005	
X2 Mach 7-10 Nozzle		The University of Queensland Department of Mechanical Engineering	
Smaller Roller #2		Drawn by Michael Scott	